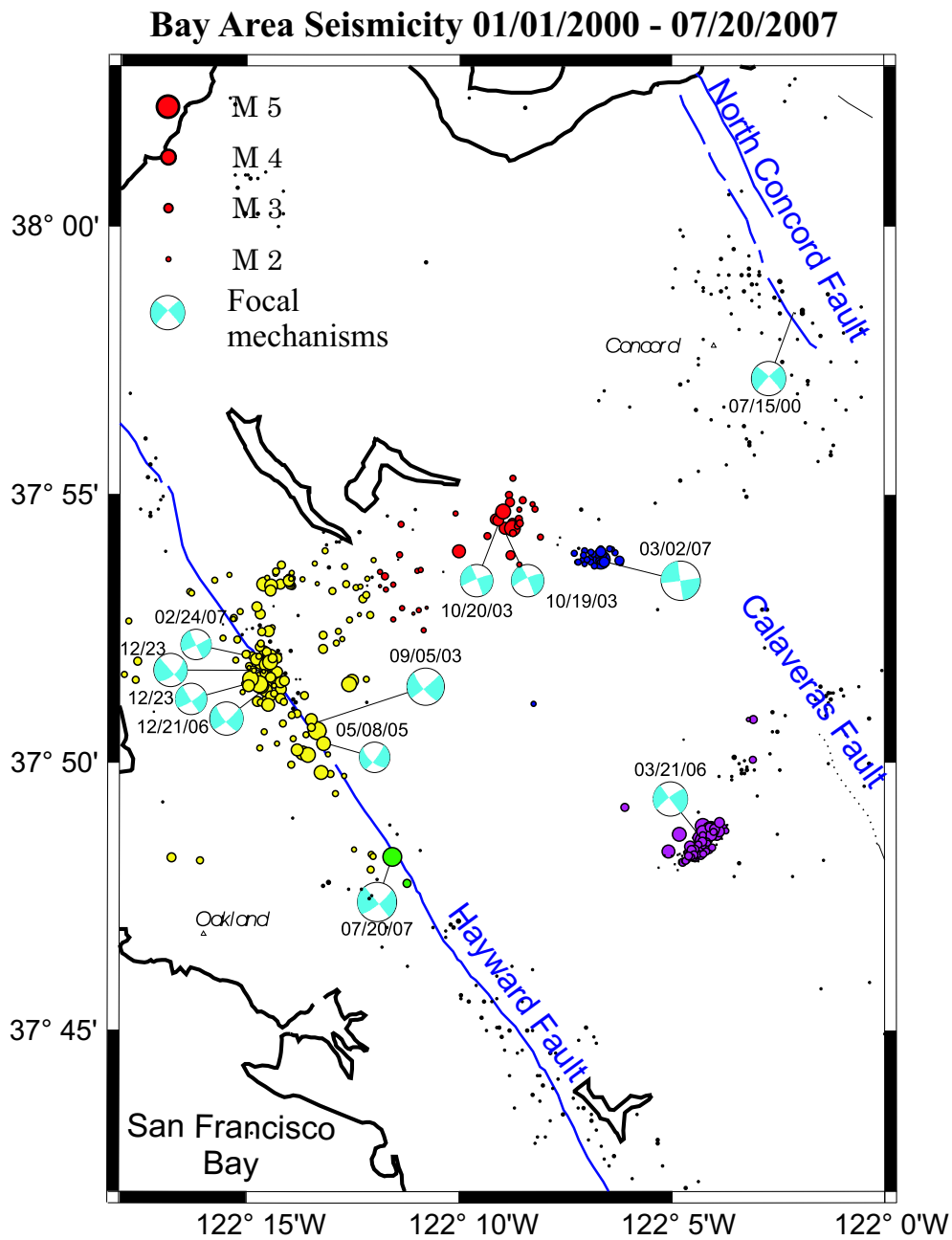


# Berkeley Seismological Laboratory



**Annual Report  
July 2006 - June 2007**

**Berkeley Seismological Laboratory**  
**Annual Report**  
**July 2006 - June 2007**

#### Cover Picture

Earthquakes along and near the Hayward Fault from 2000 to the present. The July 20, 2007 event is indicated in green, and black dots indicate background seismicity. Other recent clusters along and near the Hayward Fault are marked in color, with the earthquakes from December 2006 in yellow. The Lafayette event, which occurred on the evening of March 1, 2007, and its aftershocks are denoted in dark blue. The earthquake on the morning of July 20, 2007 occurred farther southeast along the Hayward Fault than the events in the sequence which occurred around Christmas, 2006. It was felt widely throughout the Bay Area and jolted many residents awake. Its mechanism is typical for strike-slip along the Hayward Fault. Although there have been many small events along the Hayward Fault over the past few years, in 1868 the Hayward Fault hosted the first good-sized earthquake to occur in the Bay Area in a relatively heavily populated area.

# Contents

<b>1</b>	<b>Director's Report</b>	<b>1</b>
1.1.	Background and Facilities . . . . .	1
1.2.	Highlights of 2006-2007 . . . . .	3
1.3.	BSL staff news . . . . .	5
1.4.	Acknowledgements . . . . .	6
<b>2</b>	<b>Research Studies</b>	<b>7</b>
2.1.	Kinematic Models of Repeating Earthquakes . . . . .	8
2.2.	Accelerating Moment Release in Areas of High Stress? Preliminary Results . . . . .	11
2.3.	Do repeating earthquakes talk to each other? . . . . .	14
2.4.	Segmentation in Episodic Tremor and Slip All Along Cascadia . . . . .	17
2.5.	A New Spectral Ratio Method Using Narrow Band Coda Envelopes: Evidence for non-Self-Similarity in the Hector Mine Sequence . . . . .	20
2.6.	Evolution of Tremor Activity at Cholame, CA . . . . .	23
2.7.	Regional Analysis of $L_g$ Attenuation: Comparison of 1D Methods in Northern California . . . . .	25
2.8.	A simple method for simulating microseism H/V spectral ratio in 3D structure . . . . .	27
2.9.	Broadband Modeling of 3D velocity structure in the San Francisco Bay Area . . . . .	29
2.10.	Inversion of the Teleseismic Observations for the Velocity Structure Within the Santa Clara Valley Basins . . . . .	31
2.11.	Observations of Infragravity Waves at the Endeavour Ocean Bottom Broadband Seismic Station (KEBB) . . . . .	33
2.12.	Identifying Isotropic Events Using an Improved Regional Moment Tensor Inversion Technique . . . . .	35
2.13.	Recalibrating $M_L$ for CISN . . . . .	37
2.14.	The Orinda Events: Complexity in Small Events . . . . .	39
2.15.	Using 1906 Simulations to Assess Performance of Northern California Networks . . . . .	41
2.16.	Scanning of Unusual Seismicity in the Mendocino Triple Junction Region . . . . .	43
2.17.	ElarmS AlertMap: ShakeMap-Based Analysis of Earthquake Early Warning Results . . . . .	45
2.18.	Parkfield-Hollister Electromagnetic Monitoring Array . . . . .	48
2.19.	Creep on the Rodgers Creek Fault Identified Using PS-InSAR . . . . .	51
2.20.	Asymmetric motion across the San Francisco Bay Area faults. Implications on the magnitude of future seismic events. . . . .	53
2.21.	A Decade of InSAR Observation across the Creeping Segment of the San Andreas Fault . . . . .	55
2.22.	Indian Plate Motion, Deformation, and Plate Boundary Interactions . . . . .	57
2.23.	Hidden Dykes detected on Ultra Long Period seismic signals at Piton de la Fournaise volcano? . . . . .	59
2.24.	The Fate of the Juan De Fuca Plate: Implications for a Yellowstone Plume Head . . . . .	61
2.25.	Non-linear 3D Born Shear Wave Tomography in Southeastern Asia . . . . .	64
2.26.	Inferring composition and temperature of the upper mantle from interpretation of long period seismic data and global attenuation measurements . . . . .	67
2.27.	Q Constraints on Upper Mantle Temperature . . . . .	70
2.28.	Applying the Spectral Element Method to Tomography: Crustal Effects . . . . .	72
2.29.	Travel time analysis of Sdiff, SKS and SKKS phases . . . . .	74
2.30.	Locating Scatterers in the Mantle Using Array Analysis of PKP Precursors from an Earthquake Doublet . . . . .	76
2.31.	Test of Innermost Inner Core Anisotropic Models . . . . .	78
2.32.	GPS exploration of the elastic properties across and within the Northern San Andreas Fault zone and heterogeneous elastic dislocation models . . . . .	80

<b>3 BSL Operations</b>	<b>85</b>
3.1. Berkeley Digital Seismic Network . . . . .	86
3.2. California Integrated Seismic Network . . . . .	97
3.3. Northern Hayward Fault Network . . . . .	103
3.4. Parkfield Borehole Network (HRSN) . . . . .	111
3.5. Bay Area Regional Deformation Network . . . . .	120
3.6. Northern California Earthquake Data Center . . . . .	129
3.7. Data Acquisition and Quality Control . . . . .	139
3.8. Northern California Earthquake Monitoring . . . . .	148
3.9. Outreach and Educational Activities . . . . .	154
<b>Glossary</b>	<b>156</b>
<b>Appendix I Publications, Presentations, and Panels 2006-2007</b>	<b>158</b>
<b>Appendix II Seminar Speakers 2006-2007</b>	<b>169</b>
<b>Appendix III Organization Chart 2006-2007</b>	<b>171</b>

# Chapter 1

## Director's Report

As I was working on the introduction to this Annual Report, in the evening of October 30th, 2007, the San Francisco Bay Area - including my desk at home - was shaken by the strongest temblor since the  $M$  6.9 1989 Loma Prieta earthquake. It felt exactly as John Mitchell described in his impressions from the great Lisbon earthquake of 1755: "a tremulous vibration followed by a wave-like undulation", but was generally a mild experience. Promptly, our real-time earthquake notification system indicated that it had occurred east of Alum Rock in the South Bay, and that its moment magnitude was  $M_w$  5.4. The shaking was felt widely, from Carson City in Nevada and Yosemite in the East, to Thousand Oaks near Los Angeles in the South and to Eureka in the North. Fortunately, nobody was hurt in this quake and the damage was very minor, surprisingly so. Owing to our real time estimation of rupture directivity, it quickly became apparent that the rupture propagated to the south-west, concentrating the strongest shaking in a sparsely populated area. This was in contrast to what was experienced last July, when an earthquake smaller by an order of magnitude, the  $M_w$  4.2, July 20th, 2007 Oakland earthquake, sent objects flying off shelves in Berkeley and San Francisco. The latter earthquake occurred in the heart of the urban area, and the rupture propagated to the north. These recent examples illustrate the complexity of earthquake ruptures, and how important it is to provide rapid and accurate information not only on the hypocentral location and the magnitude, but also on rupture directivity, which can significantly influence the distribution of the shaking. The near surface three-dimensional geometry of basins and the basement topography also play a role in amplifying or reducing local shaking, and the larger the earthquake, the more important this becomes. The ability to provide this kind of information in quasi-real time is the result of efforts that have been pursued at BSL for the last 15 years, progressively translating research developments into the operational environment. The Alum Rock earthquake was a perfect "dry run" test for our northern California real time system, operated jointly with the US Geological Survey at Menlo Park, and helped identify a few small issues with telemetry and

hard-wired parameters in a real life, yet benign situation.

This earthquake also served to assess the performance of the Earthquake Early Warning system currently being developed (see section 2.17.), which successfully detected the earthquake and determined its magnitude to within 0.3 magnitude units.

During the night and days following the earthquake, members of our staff also spent considerable time providing information to the media - another regular activity which sets the BSL apart from most other Organized Research Units on the Berkeley Campus.

### 1.1. Background and Facilities

The Berkeley Seismological Laboratory (BSL), formerly the Berkeley Seismographic Station (BSS), is the oldest Organized Research Unit (ORU) on the UC Berkeley campus. Its mission is unique in that, in addition to research and education in seismology and earthquake-related science, it is responsible for providing timely information on earthquakes (particularly those that occur in northern and central California) to the UC Berkeley constituency, the general public, and various local and state government and private organizations. The BSL is therefore both a research center and a facility/data resource, which sets it apart from most other ORUs. A major component of our activities is focused on developing and maintaining several regional observational networks, and participating, along with other agencies, in various aspects of the collection, analysis, archival, and distribution of data pertaining to earthquakes, while maintaining a vigorous research program on earthquake processes and Earth structure. In addition, the BSL staff spends considerable time on public relations activities, including tours, talks to public groups, responding to public inquiries about earthquakes, and, more recently, World-Wide-Web presence (<http://seismo.berkeley.edu/>).

UC Berkeley installed the first seismograph in the Western Hemisphere at Mount Hamilton (MHC) in 1887. Since then, it has played a leading role in the operation of state-of-the-art seismic instruments and in the development of advanced methods for seismic data analysis

and interpretation. Notably, the installation, starting in 1927, of Wood-Anderson seismographs at 4 locations in northern California (BKS, ARC, MIN and MHC) allowed the accurate determination of local earthquake magnitude ( $M_L$ ) from which a unique historical catalog of regional earthquakes has been maintained to this day, providing crucial input to earthquake probabilities studies.

Over the years, the BSS continued to keep apace of technological improvements. The first centrally telemetered network using phone lines in an active seismic region was installed by BSS in 1960. The BSS was the first institution in California to operate a 3-component "broadband" system (1963). Notably, the BSS played a major role in the early characterization of earthquake sources using "moment tensors" and source-time functions, and made important contributions to the early definitions of detection/discrimination of underground nuclear tests and to earthquake hazards work, jointly with UCB Engineering. Starting in 1986, the BSS acquired 4 state-of-the-art broadband instruments (STS-1), while simultaneously developing PC-based digital telemetry, albeit with limited resources. As the telecommunication and computer technology made rapid progress, in parallel with broadband instrument development, paper record reading could be completely abandoned in favor of largely automated digital data analysis.

The current modern facilities of BSL have been progressively built over the last 16 years, initiated by significant "upgrade" funding from UC Berkeley in 1991-1995. The BSL currently operates and acquires data, continuously and in real-time, from over 60 regional observatories, housing a combination of broadband and strong motion seismic instrumentation installed in vaults, borehole seismic instrumentation, permanent GPS stations of the Bay Area Regional Deformation (BARD) network, and electromagnetic sensors. The seismic data are fed into the BSL real-time processing and analysis system and are used in conjunction with data from the USGS NCSN network in the joint earthquake notification program for northern California, started in 1996. This program capitalizes on the complementary capabilities of the networks operated by each institution to provide rapid and reliable information on the location, size and other relevant source parameters of regional earthquakes. In recent years, a major emphasis in BSL instrumentation has been in densifying the state-of-the-art seismic and geodetic networks, while a major ongoing emphasis in research has been the development of robust methods for quasi-real time automatic determination of earthquake source parameters and predicted strong ground motion, using a sparse network combining broadband and strong motion seismic sensors, as well as permanent geodetic GPS receivers. A recent emphasis has been the development of "earthquake early warning" capabilities.

The backbone of the BSL operations is a regional net-

work of now close to 30 digital broadband and strong motion seismic stations, the Berkeley Digital Seismic Network (BDSN), with continuous telemetry to UC Berkeley. This network provides the basic regional data for the real-time estimation of location, size and rupture parameters for earthquakes of M 3 and larger in central and northern California, within our Rapid Earthquake Data Integration (REDI) program and is the Berkeley contribution to the California Integrated Seismic Network (CISN). It also provides a fundamental database for the investigation of three-dimensional crustal structure and its effects on regional seismic wave propagation, which is ultimately crucial for estimating ground shaking for future earthquakes. Most stations also record auxiliary temperature/pressure channels, valuable in particular for background noise quality control. Complementing this network is a  $\sim 25$  station "high-resolution" network of borehole seismic sensors located along the Hayward Fault (HFN) and under the Bay Area bridges, operated jointly with the USGS/Menlo Park and linked to the Bridge Safety Project of the California Department of Transportation (Caltrans). The latter has facilitated the installation of sensor packages at 15 bedrock boreholes along 5 east bay bridges in collaboration with Lawrence Livermore National Laboratory (LLNL). A major science goal of this network is to collect high signal-to-noise data for micro-earthquakes along the Hayward Fault to gain insight into the physics that govern fault rupture and its nucleation. The BSL is also involved in the operation and maintenance of the 13 element Parkfield borehole seismic array (HRSN), which is providing high quality data on micro-earthquakes, clusters and most recently tremors, and provides an important reference for the San Andreas Fault Observatory at Depth (SAFOD). Since April 2002, the BSL is also involved in the operation of a permanent broadband ocean bottom station, MOBB, in collaboration with MBARI (Monterey Bay Aquarium Research Institute).

In addition to the seismic networks, the BSL is involved in data archival and distribution for the permanent geodetic BARD Network as well as the operation, maintenance, and data processing of 22 out of its 70+ sites. Whenever possible, BARD sites are collocated with BDSN sites in order to minimize telemetry costs. In particular, the development of analysis methods combining the seismic and geodetic data for the rapid estimation of source parameters of significant earthquakes has been one focus of BSL research.

Finally, two of the BDSN stations (PKD, SAO) also share data acquisition and telemetry with 5-component electromagnetic sensors installed with the goal of investigating the possibility of detection of tectonic signals. In 2002-2003, automated quality control software was implemented to monitor the electromagnetic data.

Archival and distribution of data from these and other

regional networks is performed at the Northern California Earthquake Data Center (NCEDC), operated at the BSL in collaboration with USGS/Menlo Park. The data reside on a mass-storage device (current holdings  $\sim 10$  TerraBytes), and are accessible “on-line” over the Internet (<http://www.ncedc.org>). Among others, data from the USGS Northern California Seismic Network (NCSN), are archived and distributed through the NCEDC. The NCEDC also maintains, archives and distributes the ANSS/CNSS earthquake catalog.

Core University funding to our ORU currently provides salary support for 2 field engineers, one computer expert, 2 data analysts, 1 staff scientist and 2 administrative staff. This supports a diminishing portion of the operations of the BDSN and provides seed funding for our other activities. All other infrastructure programs are supported through extra-mural grants primarily from the USGS, NSF, and the State of California, through its Office of Emergency Services (OES). We acknowledge valuable recent contributions from other sources such as Caltrans and PEER, as well as our Earthquake Research Affiliates.

## 1.2. Highlights of 2006-2007

### 1.2.1 Research Accomplishments

Chapter 2 documents the main research contributions of the past year. Research at the BSL spans a broad range of topics, from the study of microseismicity at the local scale to global deep earth structure, and includes the use of seismological, geodetic, and remote sensing (InSAR) techniques. Productivity continues to be high: forty three papers in refereed journals, including two in *Nature*, have been published by BSL researchers in the last year, originating from 4 faculty members and their students, and one senior researcher.

The analysis of borehole microseismic data from the HRSN (Parkfield) network is continuing to provide exciting results. A highlight of this past year’s research has been a study by Doug Dreger and collaborators (2.1.), in which they have reconciled the difference in reported stress drop estimates for small earthquakes, by applying Doug’s finite source inversion method to microseism borehole observations. Bob Nadeau and collaborators (2.3., 2.6.) continue to analyze repeating earthquakes and tremor activity near Parkfield, finding intriguing patterns of changes in strain release associated with the M6 2004 Parkfield earthquake, and in particular a correlation between deep tremor activity and microseismicity in seismogenic zone above. On the other hand, Karl Kappler and collaborators (2.18.) show no clear precursory signal in electromagnetic data preceding or during the Parkfield earthquake.

Work on non-volcanic tremor in subduction zones has led Richard Allen to propose a relationship between the

recurrence period of these tremors and properties of the overriding plate, in particular topography (2.4.).

Richard Allen and his students have also continued to develop a methodology for earthquake early warning (2.17.), testing it in the framework of our real-time system. While the debate continues as to whether an earthquake knows when it starts how big it will become, an important by-product of this development is the ability to significantly speed-up the production of reliable “shake maps”.

Doug Dreger and his students and collaborators have also worked on a variety of regional source and structure topics. In particular, they have finalized a methodology using moment tensor inversion to characterize different seismic sources, and in particular distinguish those with a significant non-double couple component, such as would be the case for nuclear tests and mine collapses (2.12.). In particular, this methodology has proven very useful in assessing the nature of the Utah mine collapse of Aug 6, 2007 (e.g. <http://www.seismo.berkeley.edu/~peggy/Utah20070806.htm>). Concurrently, they have been testing crustal and basin models in the San Francisco Bay Area, and in particular the Santa Clara valley, using different approaches: microseismic noise (2.8.), 3D broadband waveform modeling using finite differences (2.9.), and inversion of teleseismic observations (2.10.). Finally, various approaches to determining the Lg attenuation structure in the San Francisco Bay Area have been compared, towards the determination of a robust model for this region (2.7.).

A number of studies focus on the seismicity and deformation in northern California. Peggy Hellweg 2.14. describes the unusual microearthquake sequence of October 2003 near Orinda, CA, while a recently begun study aims at characterizing moment tensors and spectra of slow events in the Mendocino region (2.16.). Using InSAR data, Roland Bürgmann and his group have been characterizing creep along the Rodgers Creek Fault (2.19.) and the San Andreas Fault (2.21.). Earthquake and ground shaking potential has been analyzed in different fashions. Using continuous GPS data accumulated over the last 10-15 years on the BARD network, Nicolas Houlié and I (2.20.) point out to the consequences of asymmetric rheology across the Bay Area faults. The performance capabilities of the northern California seismic networks have been assessed through simulations of a repeat of the 1906 earthquake (2.15.). A recently begun study is searching for evidence of accelerating seismic moment release in northern and southern California by modelling the evolution of stress and seismicity in the region (2.2.). A new method based on coda spectral amplitude ratios shows promise in distinguishing earthquake sources, with consequences on earthquake scaling (2.5.). Finally, magnitude accuracy within CISN will soon be improved with the implementation of a California-wide consistent set of

local magnitude ( $M_L$ ) station corrections (2.13.).

Moving away from California, continuous and campaign style GPS data have been used to constrain the motion and deformation of the Indian Plate (2.22.), while Nicolas Houlié and Jean-Paul Montagner (IPG paris, France) 2.23. propose a method to track the long term deformation response of a volcano to changes in pressure inside the magma chamber.

BSL researchers have also contributed to larger scale regional and global structure studies. Mei Xue and Richard Allen 2.24. used teleseismic body wave travel time tomography to investigate the fate of the subducted Juan de Fuca plate and its interaction with the Yellowstone plume head. Barbara Romanowicz and her group have been investigating new approaches to waveform tomography. With post-doc Aimin Cao, we have been testing a promising method combining the advantages of the path average approximation and those of 3D Born scattering on the case of radially anisotropic upper mantle structure in southeast Asia (2.25.). We are making progress towards a global upper mantle model using the spectral element method in the forward computation of 3D synthetics (2.28.). We have further documented the presence of strong lateral variations at the base of the mantle using diffracted waves (2.29.). Using an array stacking method, Aimin Cao has been able to localize scatterers most likely associated with remnant slabs in the lowermost mantle under North America (2.30.). With post-doc Fabio Cammarano, we have been working towards understanding the respective contributions of variations in temperature and composition in the upper mantle using seismic waveforms and mineral physics data as constraints (2.27., 2.26.). Finally, we continue to study the earth's inner core, and, this year, have assembled a high quality dataset of near antipodal PKP travel time data to test for the existence of an innermost inner core (2.31.).

### 1.2.2 Infrastructure and Earthquake Notification

A highlight of the past year has been the successful completion of the NSF funded project in collaboration with Tom VanZandt of Metrozet for the design and testing of new electronics for the STS-1 very broadband seismometer. This exceptional seismometer, installed at several hundred seismic stations around the world, and in particular at 10 of the BDSN sites, was developed in the 1970's but is no longer produced, raising concerns about its longevity and the need for a high quality replacement. The BSL developed a test-best and participated in the testing of successive iterations of electronics developed by Metrozet. The new electronics present several attractive features, in particular capabilities for remote calibration. After testing at UC Berkeley's Byerly vault, they were installed for further testing at Hopland (HOPS). They

are now ready for production.

The prototype earthquake early warning system developed by Prof. Richard Allen has been implemented in our real time system and is being tested and improved in this framework. It is already providing useful by-products, such as the ability to obtain reliable shake maps in just over a minute, compared to 4+ minutes in the operational system used by CISEN.

As in previous years, BSL's infrastructure development efforts have centered around several major projects:

- operation and enhancement of the joint earthquake notification system with USGS/Menlo Park.
- the continuing development of the California Integrated Seismic Network
- participation, at various levels, in three components of the national Earthscope program: the deployment in northern California of the *BigFoot* component of USArray, archival of borehole strainmeter data in the framework of the Plate Boundary Observatory (PBO), and the preparation for archival of the data from the San Andreas Fault Observatory at Depth (SAFOD).
- development of borehole networks at Parkfield and along the Hayward Fault
- operation and further enhancements of the BARD network of continuous GPS
- operation of the Northern California Earthquake Data Center

The main goal of the CISEN (see Section 3.2.) is to ensure a more uniform system for earthquake monitoring and reporting in California. The highest priority, from the point of view of emergency responders in California, is to improve the robustness of statewide real-time notification and to achieve a uniform interface across the State to the California OES and other emergency responders. This represents a major challenge, as the CISEN started as a heterogeneous collection of networks with disparate instrumentation, software systems and cultures. Much effort has gone over the past few years to develop coordinated software between southern and northern California and in northern California, between Berkeley and USGS/Menlo Park. These two institutions are joined together in the Northern California Earthquake Management Center (NCEMC). A highlight of the past year has been the long awaited retirement of the CUSP real-time earthquake timing system in Menlo Park. BSL staff continue to spend considerable efforts in organizational activities for CISEN, notably by participating in the CISEN Project Management Group (Neuhauser and Hellweg), which includes weekly 2 hour phone conferences, and the

Standards Committee (Neuhauser-chair, Hellweg, Lombard), which strives to define and coordinate software development tasks. Romanowicz and Hellweg serve on the CISN Steering Committee. Doug Neuhauser has also been serving on the CISN Steering Committee in the transition period following Lind Gee's departure in summer 2005. The CISN also represents California as a designated region of ANSS (Advanced National Seismic System) and the BSL is actively involved in planning activities for the ANSS.

The BSL concluded an agreement in June 2004 with IRIS to contribute 19 stations of the BDSN to USArray, while the experiment is deployed in California. This includes 17 existing stations and the two recently installed sites: GASB and MCCM. In the past year, BSL has continued to acquire telemetered data from these and other northern California USArray stations and to pay particular attention to the maintenance of those permanent sites which are part of USArray. As USArray moves out of California starting in Fall 2007, BSL has been preparing to take over 7 of the USArray sites. This involves transfer of site permits, preparation of BSL equipment (seismometers and dataloggers funded through FEMA and OSN grants) and securing new telemetry paths where needed.

The Parkfield borehole network (HRSN, see Section 3.4.) continues to play a key role in support of the Earthscope SAFOD (San Andreas Fault Observatory at Depth) drilling project, by providing low noise waveforms for events in the vicinity of the target drilling zone. In the past year, integration of the HRSN data streams into the NCSN triggering scheme has been completed, in support of researchers working on repeating micro-earthquakes. Also, the upgrade of the telemetry system has been completed. HRSN data are now telemetered over the USGS T1 line to Menlo Park and then on to Berkeley over the joint T1 line between the two institutions.

In the past year, the Northern Hayward Fault Network (NHFN, see Section 3.3.) has continued to expand. St. Mary's College station (SM2B) has been completed and four additional sites have been drilled, have down-hole packages, and are awaiting connection to dataloggers. This will bring the total number of borehole NHFN sites to 18. On-going network maintenance involves regular inspection of the collected seismic waveform data and spectra for nearby seismic events, and for noise samples, in order to assure that the instruments operate at maximum performance to capture the source spectrum of micro-earthquakes down to negative magnitudes.

The BARD continuous GPS (C-GPS) network (see Section 3.5.) has focused its efforts to convert three additional sites to acquire data at 1Hz sampling rate (up from the standard 15-30 sec rate), bringing to 15 the total number of stations upgraded, with the goal of using these data in complement to seismic data for real-time

earthquake notification. We have been working with our colleagues at the US Geological Survey in Menlo Park to establish a joint GPS real time data acquisition system and integrate it with our existing seismic earthquake notification system. We have been working with EB Parks, EBMUD and the Plate Boundary Observatory (PBO) of Earthscope, to acquire data from their GPS stations in real time. In exchange for real time data feeds from East Bay agencies, we can provide RTK (Real-Time Kinematic) data for land surveys that they perform.

The NCEDC (see Section 3.6.) continues archival and on-line distribution of data from expanding BDSN, NHFN, HRSN, BARD, Mini-PBO, and other networks and data collections in northern California and Nevada, including telemetered continuous data from USArray stations in northern California and vicinity. We are continuing to receive data from the SAFOD pilot hole and main hole and data from 15 SCSN (southern California) broadband sites as part of the CISN robust "backbone". In late 2006, we begun to archive and distribute a single unified northern California earthquake catalog, obtained in real-time from the NCEMC through database replication from the NCEMC's real-time systems. In the past year, the NCEDC has supported the NCEMC earthquake analysis by providing real-time access to earthquake parameters and waveforms for the CISN Jiggle earthquake review software, and has implemented software and procedures to read and archive continuous NCSN seismograms from tapes for the period 2001-2005, beginning the processing of these tapes.

### 1.3. BSL staff news

Changes in BSL staff in 2006-07 are as follows.

Cynthia Bresloff left BSL in June 2007 to pursue a career in GIS support at the Nature Conservancy and was replaced in August 2007 by Jennifer Taggart, who received her BS in geophysics from California Institute of Technology.

Kate Conner went on maternity leave in May 2007 and gave birth to baby boy Elliott Koenig Lewis on May 24, 2007. Eileen Evans worked as a student employee in the business office while Kate was on maternity leave.

Two graduate students associated with BSL completed their PhD's in the past year: Dennise Templeton and Akiko To. Akiko is now a post-doc at JAMSTEC and Dennise accepted a position at Lawrence Livermore National Lab. Junkee Rhie, who graduated in 2005 and stayed on as a post-doc for a year, joined the faculty of the University of Seoul, Korea, in July 2007. Post-doc Gareth Funning joined the faculty at the University of California, Riverside. Federica Marone completed her posdoc appointment at the end of November 06 and joined the research staff at the Paul Scherrer Institute (Switzerland). Chris Fuller worked as a postdoc with

Roland Bürgmann between July and December 06.

New arrivals have continued through the summer and early Fall of 2007. Huaiyu Yuan joined the global seismology group as a post-doc in early August. Chander Shaker Daula Vishwanath arrived in late June on a one year BOYSCAST postdoctoral fellowship. Isabelle Ryder was hired in January as a postdoc working in Roland Burgmann's group. New graduate students Shan Dou, Robert Porritt, Holly Brown Moore, and Amanda Thomas arrived in the summer of 2007. Angela Chung received her BS from EPS and is now working for the Lab as a Staff Research Associate.

Rich Clymer retired at the end of June and has come back to work part time as a retiree appointee to work on the HRSN maintenance and upgrade.

Student employee Tomasz Matlak graduated and left the BSL engineering lab to pursue his PhD in the Department of Mechanical Engineering. His brother Jozef is a freshman this year and has replaced his brother in the lab. Student employee Eric Winchell began working with the global seismology group in November 2006.

## 1.4. Acknowledgements

I wish to thank our technical and administrative staff, scientists and students for their efforts throughout the year and their contributions to this Annual Report. Individual contributions to activities and report preparation are mentioned in the corresponding sections, except for the Appendix section, prepared by Kate Conner, Kristen Jensen and Jennifer Taggart.

I also wish to specially thank the individuals who have regularly contributed to the smooth operation of the BSL facilities: Mario Aranha, Rich Clymer, Doug Dreger, John Friday, Jarrett Gardner, Peggy Hellweg, Nicolas Houlié, Bill Karavas, Alexei Kireev, Rick Lellinger, Pete Lombard, Rick McKenzie, Bob Nadeau, Doug Neuhauser, Charley Paffenbarger, Bob Uhrhammer, and Stephane Zuzlewski, and in the administrative office, Kristen Jensen, Kate Conner, Tina Barber-Riggins and Yolanda Andrade. I also wish to thank our undergraduate assistants, Angela Morrish Chung, Eileen Evans, Tomasz Matlak, Jozef Matlak, and Eric Winchell for their contributions to our research and operational activities.

I am particularly thankful to Jennifer Taggart and Peggy Hellweg, for their help in putting together this Annual Report.

The Annual Report of the Berkeley Seismological Laboratory is available on the WWW at [http://seismo.berkeley.edu/annual\\_report](http://seismo.berkeley.edu/annual_report).

## Chapter 2

# Research Studies

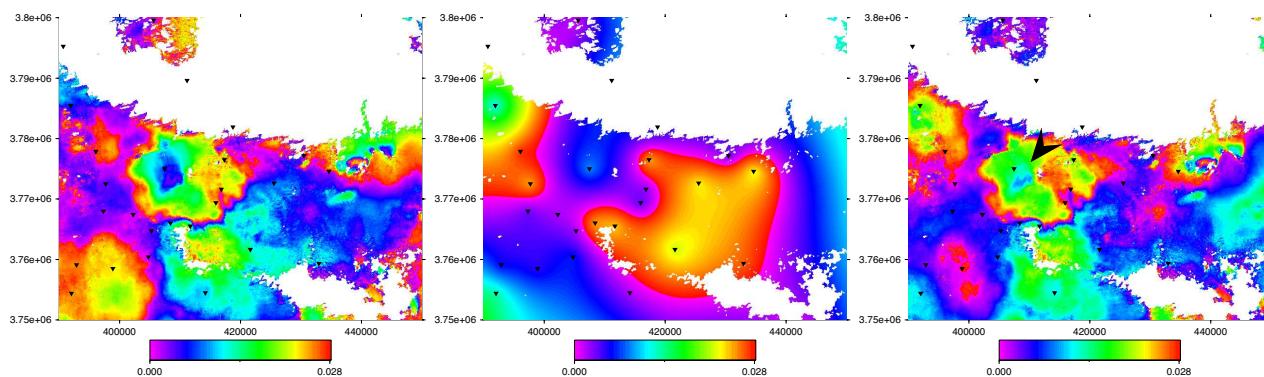


Figure 2.1: InSAR measurement (left), troposphere model inferred from GPS observations (center) and corrected InSAR scene (right). Thirty percent of the uplift detected (20 mm) in the San Gabriel Valley was constituted by a troposphere contribution located above the maximal uplift location. The methodology applied here has been automated on the BARD network. From *Houlié, Funning and Burgmann, in prep.*

## 2.1. Kinematic Models of Repeating Earthquakes

Douglas Dreger, Robert Nadeau, and Angela Chung

### 2.1.1 Introduction

On the Parkfield segment of the San Andreas Fault, repeating earthquake seismicity is observed with highly similar waveforms, suggesting that the events occur on the same patch of fault repeatedly (Nadeau *et al.*, 1995). Surrounding these repeating clusters are areas inferred to creep. A shallow cluster of such repeating events is the drilling target of the NSF EarthScope San Andreas Fault Observatory at Depth (SAFOD) experiment. Imanishi *et al.* (2004) studied waveforms and spectra for one of the SAFOD target events using data obtained from the SAFOD Pilot Hole, and determined a Mw 2.1 and a depth of 2.1 km. From their corner frequency measurements they find a static stress drop of 8.9MPa. On the other hand, Nadeau and Johnson (1998) proposed an asperity-loading model to infer that slip in each event was on the order of 6.6cm, and a stress drop of 240MPa. If a rigidity of 12 GPa, more appropriate for the shallow depth of the event is used, a stress drop of 100MPa is obtained with their method. The difference between 8.9 and 100 MPa bears directly on the nature of the faulting mechanics, whether frictional sliding or rock fracture processes are operating in these events. In this study we reconcile the difference in the reported stress drop estimates using a finite-source inverse method to determine the rupture area, slip distribution, spatially variable stress drop, and rupture velocity of the small repeating earthquakes.

### 2.1.2 Data and Methods

We use three-component 100Hz velocity records from the High Resolution borehole Seismic Network (HRSN) to determine the seismic moment rate functions at each station for a Mw2.1 event in the repeating cluster being targeted by the NSF SAFOD experiment. Figure 2.2 shows the location of the target events with respect to the HRSN, and Figure 2.2b shows the relative locations of the Mw2.1 repeating earthquakes, and a nearby Mw0.68 event used as an empirical Green’s function (eGf). The relative event locations are based on sub-sample precision waveform cross-correlation measurements and the double-difference relocation method, giving centroid locations within about 2m of each other. The smaller eGf is located about 10m away and is even within the very small radius inferred for a stress drop of 240MPa after Nadeau and Johnson (2004).

In Figure 2.3, the vertical component waveforms at station VCAB are compared for the Mw2.1 target and the Mw0.68 eGf, illustrating an extremely high degree

of waveform similarity. This level of waveform similarity is observed for all three components at all stations, and attests to the nearly collocated nature of the events as well as the similarity in their respective focal mechanisms. Together with the exceptional SNR, these events represent an ideal case for the empirical Green’s function method.

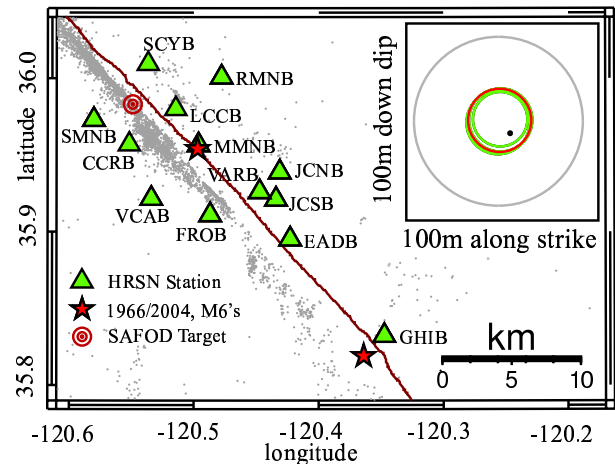


Figure 2.2: Map showing the locations of HRSN stations (inverted triangles), the SAFOD repeating target events (concentric circles), the locations of the 1966 and 2006 mainshock epicentres (stars), and background seismicity (gray dots). The inset shows a cross-sectional view of the relative locations of the repeating events (larger circles), and the Mw0.68 empirical Green’s function event (small circle). The size of the circles shows the respective areas of a 240MPa event. For comparison the large gray circle shows the inferred area for a 9MPa event.

To obtain the seismic moment rate functions at each station we employed a commonly used spectral domain deconvolution approach in which the complex spectrum of the eGf is divided out of the complex spectrum of the main event. Hough and Dreger (1994) and references therein give an overview of the method. The basic concept is that if the smaller eGf event is collocated and has the same radiation pattern as the larger event, then the common instrument response, propagation, attenuation and site effects are removed by the deconvolution process, resulting in the unfettered source spectrum. The inverse Fourier transform yields the pulse-like seismic moment rate function (Figure 2.3).

We performed deconvolutions separately on each of the three components at 8 or 9 of the HRSN stations depending on availability and SNR. Stations EADB and GHIB

(Figure 2.2) were omitted in all cases due to noisy channels. The remaining stations provide excellent azimuthal coverage of the repeating sequence (Figure 2.2). The moment rate functions may then be inverted for the spatial distribution of fault slip (Dreger, 1994).

In our application we used a 31 by 31 fault with dimensions of  $150 \times 150 \text{ m}^2$ , with a corresponding subfault size of  $4.8 \times 4.8 \text{ m}^2$ . The fault is assumed to have a strike of 137 and dip of 90. The size of the subfault was chosen to produce a temporally smooth kinematic process with respect to the sample rate of the data. A slip positivity constraint, and a smoothing operator minimizing the spatial derivative of slip were applied. The weight of the smoothing constraint was determined by trial and error by finding the smallest value that produced a smoothed model with close to the maximum fit to the data measured by the variance reduction.

In each inversion it is assumed that the rupture velocity is constant, and that the boxcar slip velocity function has a constant rise time. Using a grid search we tested rupture velocities of 0.2 to 2.3 km/s (8-100%), and rise times from 0.004 to 0.052 sec to find optimal values and to assess the resolution of the parameters.

## Results

In Figure 2.4 we show the slip model. This model has a rise time of 0.008 seconds, and a rupture velocity of 1.8 km/s (78% of the local shear wave velocity), the median from models within 2% of the peak fit. The allowable range in the kinematic parameters given this level of fit is 1.2-2.3 km/s (52-100% of the shear wave velocity) in rupture velocity, and 0.004 to 0.012 seconds for rise time. Within this population of solutions there is a tradeoff in the rise time and rupture velocity where long rise times are associated with fast rupture velocities (or short rupture times), and vice versa. It is notable that the obtained rise time is more consistent with a slip pulse rather than crack-like rupture, and the slip velocity inferred from the ratio of slip to rise time is 167 cm/s, consistent with values obtained for larger events. There is a dominant asperity in which the slip is found to be extremely concentrated, roughly circular with a diameter of about 40 m with a peak (8.6 cm) at the center, which is similar to the 6.6 cm inferred by *Nadeau and Johnson (1998)*.

Because the slip distribution is non-uniform, we use the method of *Ripperger and Mai (2004)*, shown to be consistent with static or dynamic elastic dislocation models, to determine the coseismic stress change (stress drop). This method maps the spatially variable slip on the fault to the spatially variable stress change, or stress drop. Results applied to the SAFOD target event are shown in Figure 2.4B. In regions of high slip, the stress change is positive indicating a stress drop during rupture. The method also determines the degree of stress increase (neg-

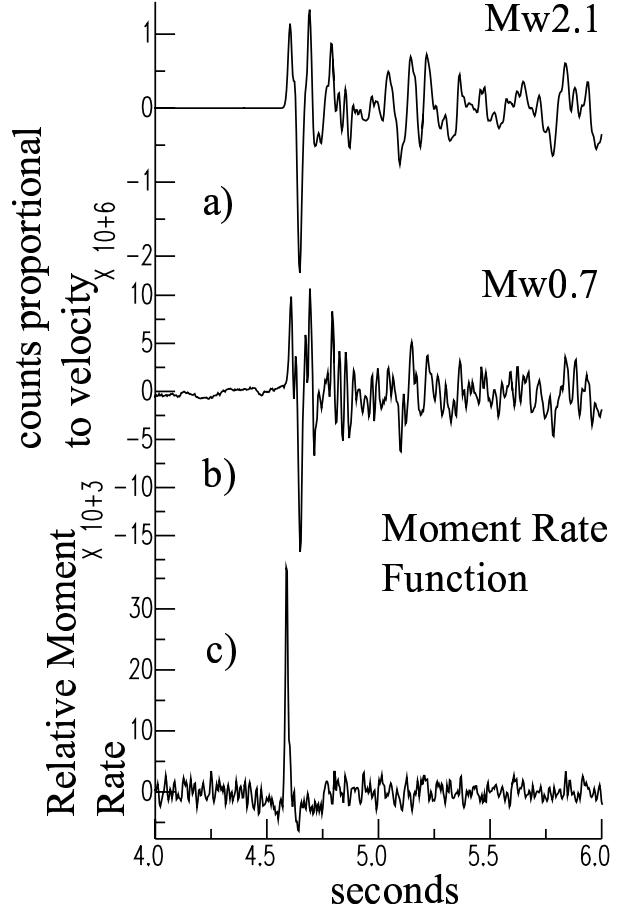


Figure 2.3: a) Vertical component waveform for the Mw2.1 event recorded at station VCAB. b) Vertical component waveform for the Mw0.68 eGf event recorded at station VCAB. c) The moment rate function obtained by deconvolving (b) from (a).

ative stress change) on the region surrounding the rupture. The model has a peak stress drop of 80 MPa, and averages ranging from 3.7-19.7MPa depending on how the average is calculated.

The very high stress drop we obtain for much of the rupture area of the SAFOD repeaters (Figure 2.4B) is at odds with more traditional spectrally-based estimates (e.g. *Imanishi et al., 2004*). However, the stress drop averaged from Figure 2.4B over areas with positive stress drop is only 11.6 MPa, which is close to the *Imanishi et al. (2004)* result. On the other hand, the spatially variable high stress drop we obtain is required to fit the shape of the moment rate functions, and the peak is closer to the estimate obtained using the method of *Nadeau and Johnson (1998)*. Thus, the finite-source results reconcile these disparate estimates of stress drop, illustrating that the two methods are apparently sensitive to different aspects of the rupture.

Assuming an average density of  $2000 \text{ kg/m}^3$ , hydro-

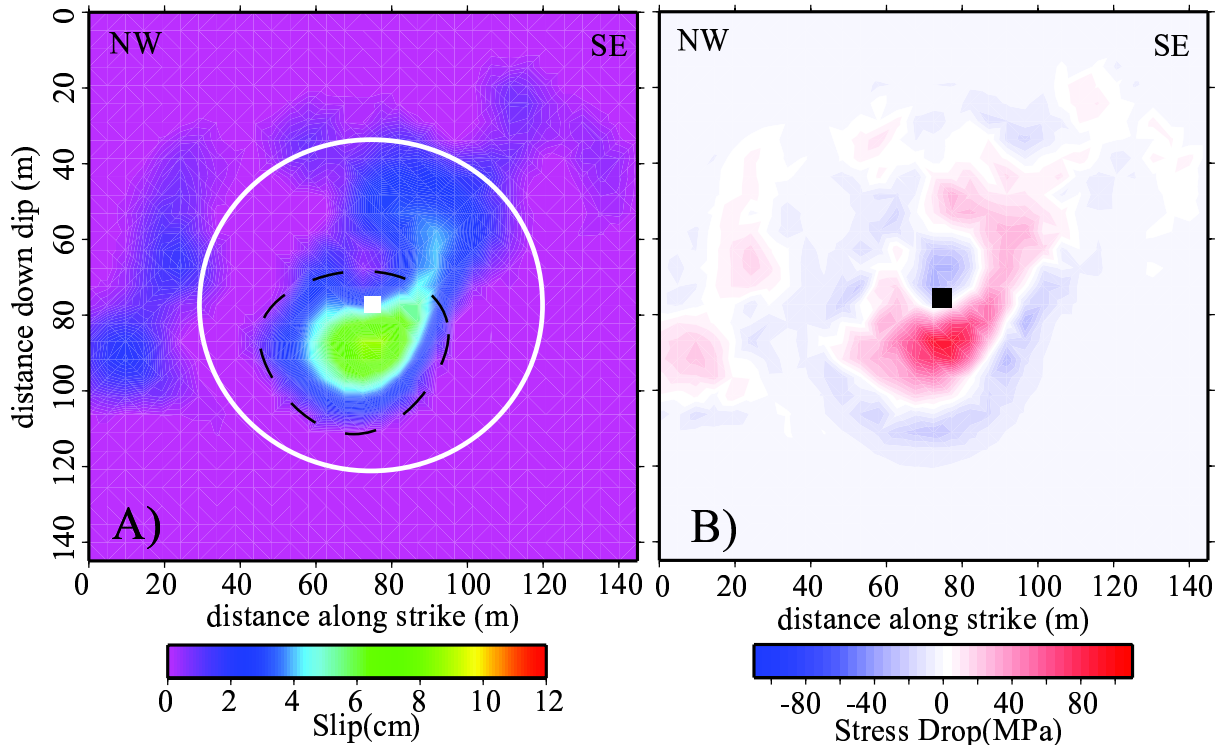


Figure 2.4: A) Slip distribution obtained by inverting moment rate functions from 9 HRSN stations. The hypocenter (white square) is in the center of the assumed rupture plane. The white circle shows the area of a 10MPa event. B) Stress drop obtained by applying the method of Ripperger and Mai (2004)

static pore pressure and a coefficient of friction of 0.4 gives a maximum frictional strength of only 7.8MPa at the depth of the events. On the other hand, it has been proposed that small dimension asperities with strength approaching that of intact rock can concentrate substantial stress levels (Nadeau and Johnson, 1998). High stress drop repeating earthquakes may represent those relatively isolated, small-scale, contact points where large stress concentrations can develop and be released on a fairly regular basis. The much larger fault areas of bigger earthquakes may be frictionally weak, but studded with sparsely distributed high strength asperities producing relatively low average stress-drops during large earthquake rupture.

### 2.1.3 Acknowledgements

This research was supported by the National Science Foundation (EAR-0510108 & EAR-0537641).

### 2.1.4 References

Dreger, D., Empirical Green's Function Study of the January 17, 1994 Northridge, California Earthquake, *Geophys. Res. Lett.*, 21, 2633-2636, 1994.

Hough, S. E., D. S. Dreger, Source Parameters of the

4/22/92 M6.1 Joshua Tree, California Earthquake and its Aftershocks: Empirical Green's Function Analysis of GEOS and TERRAscope Data, *Bull. Seism. Soc. Am.*, 85, 1576-1590, 1995.

Imanishi, K., W.L. Ellsworth and S.G. Prejean, Earthquake source parameters determined by the SAFOD Pilot Hole seismic array, *Geophys. Res. Lett.*, 31, L12S09, doi:10.1029/2004GL019420, 2004.

Nadeau, R. M., W. Foxall and T. V. McEvelly, Clustering and periodic recurrence of microearthquakes on the San Andreas Fault at Parkfield, California, *Science*, 267, 503-507, 1995.

Nadeau, R. M., and L. R. Johnson, Seismological studies at Parkfield VI: moment release rates and estimates of source parameters for small repeating earthquakes, *Bull. Seism. Soc. Am.*, 88, 790-814, 1998.

Nadeau, R. M., A. Michelini, R. A. Uhrhammer, D. Dolenc, and T. V. McEvelly, Detailed kinematics, structure and recurrence of micro-seismicity in the SAFOD target region, *Geophys. Res. Lett.*, 31, L12S08, doi:10.1029/2003GL019409, 2004.

Ripperger, J. and P. M. Mai (2004). Fast computation of static stress changes on 2D faults from final slip distributions, *Geophys. Res. Lett.*, Vol. 31, No. 18, L18610 10.1029/2004GL020594.

## 2.2. Accelerating Moment Release in Areas of High Stress? Preliminary Results

Aur lie Guilhem, Roland B rgmann, Andrew M. Freed (Purdue University), and Tabrez Ali (Purdue University)

### 2.2.1 Introduction

Several retrospective analyses have proposed that significant increases in moment release occurred prior to many large earthquakes of recent times. However, the finding of Accelerating Moment Release (AMR) strongly depends on the choice of several parameters (magnitude range, area being considered surrounding the events, time period prior to the large earthquake) and the AMR analysis may appear as a data-fitting exercise with no new predictive power. As AMR may relate to a state of high stress around the eventual next epicenter, it is interesting to compare the AMR results to models of stress accumulation in California. Instead of assuming a complete stress drop on all surrounding fault segments implied by the back-slip stress lobe method (*Bowman and King, 2001*), we consider that stress evolves dynamically, punctuated by the occurrence of earthquakes and governed by the elastic and viscous properties of the lithosphere (*Freed et al., 2007*). We generate several sensitivity tests of the method, as well as a first grid-search analysis for a few large events in Southern California. We also present here a comparison of a more general AMR analysis from 1965 to today with maps of Coulomb stress changes due to all  $M \geq 7.0$  since 1812, subsequent postseismic relaxation and interseismic strain accumulation.

### 2.2.2 The AMR concept and data

It has been found that an increase in the number of intermediate earthquakes occurs before a large event which produces a regional increase in the cumulative Benioff strain. This cumulative Benioff strain can be fit by a power law time-to-failure relation (*Bowman et al., 1998*) which has the following form:  $\epsilon(t) = A + B(tc - t)^m$

and

$$\epsilon(t) = \sum_{i=1}^{N(t)} \sqrt{E_i(t)}$$

where  $\epsilon(t)$  is the Benioff strain,  $N$  is the number of earthquakes considered,  $E$  is the energy of individual earthquakes,  $tc$  is the time of the large earthquake and  $A$  is the value of the Benioff strain when  $t=tc$ . The energy of each particular seismic event is defined as:  $\log(E) = 4.8 + 1.5M_s$

To quantify the AMR, we examine the ratio called  $c$ -value between the root-mean-square of a power-law time-to-failure function versus a linear fit to the cumulative energy of events. When the  $c$ -value is smaller than 0.7, we may consider a case of AMR. The cumulative Benioff strain is then better fit by a power law than by a linear trend.

In the case of using a circular search area for AMR, several parameters (magnitude range, area surrounding the events, time period prior to large earthquake) are required according to the choice of the mainshock studied and the AMR results depends on them.

We study the seismicity of southern California obtained from the ANSS catalog between 32N and 40N latitude since 1910 with a minimum magnitude 3.5. We extract events for AMR calculations following the systematic approach employed in previous studies. We use Nutcracker, a stress and seismicity analysis software to perform all the AMR calculations.

### 2.2.3 Grid search of AMR for three California earthquakes

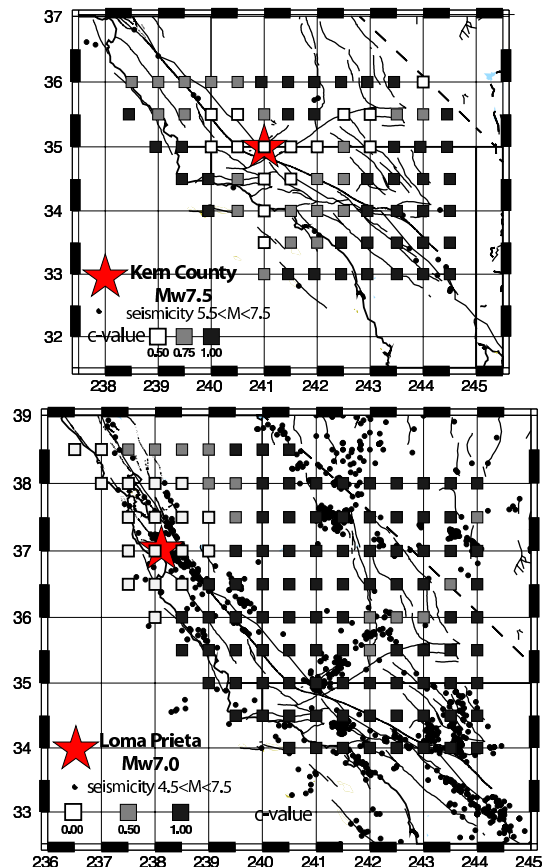


Figure 2.5: Grid search analysis of AMR for Kern County and Loma Prieta

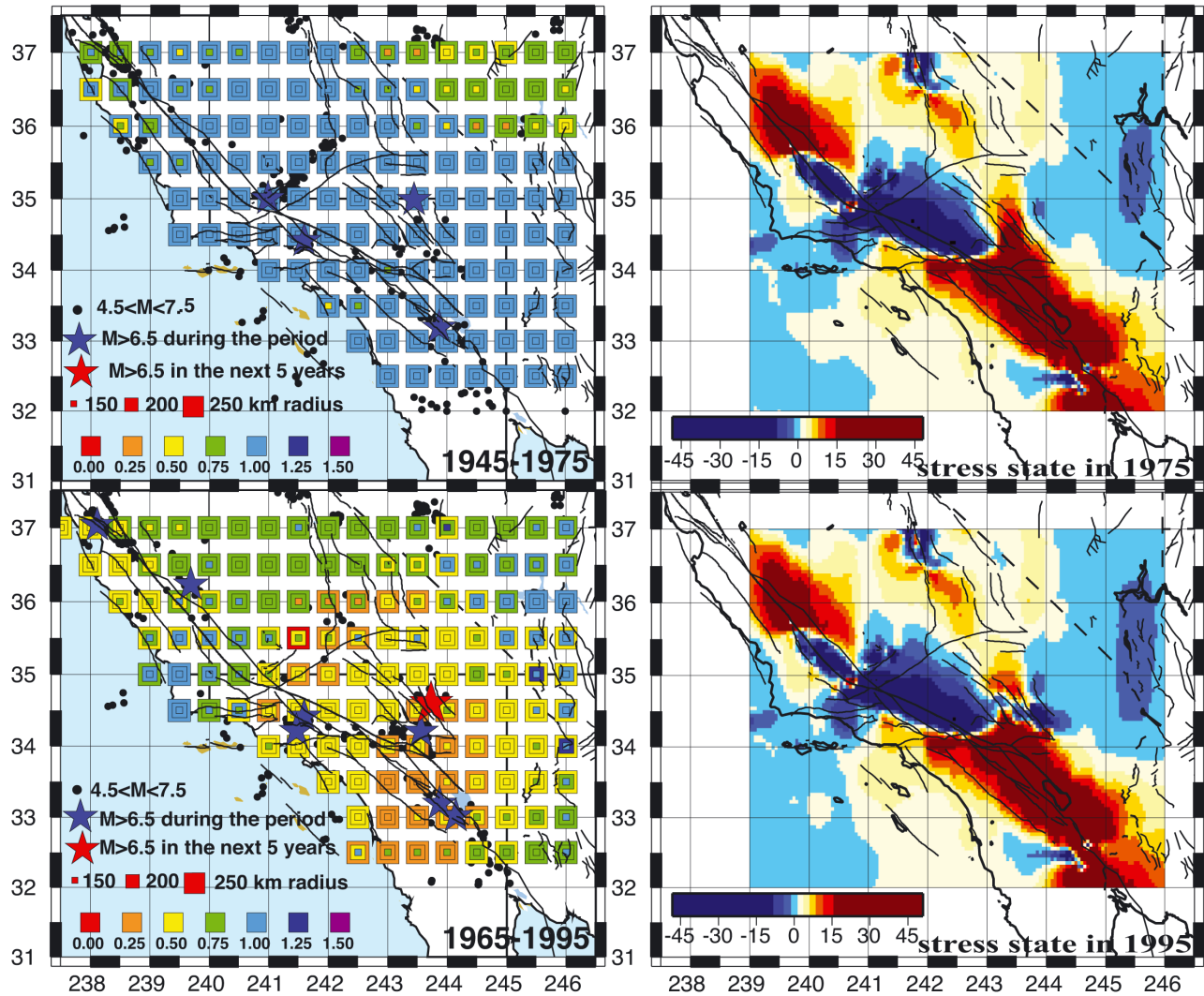


Figure 2.6: Examples of comparison of maps of c-values from AMR circular grid search and of state of stress (bars) for 1975 and 1995.

Figure 2.5 presents two different maps for two large earthquakes of California: Kern County in 1952 and Loma Prieta in 1989. Each map shows the  $c$ -values obtained by a grid search analysis over southern California using the same parameters used by *Bowman et al.* (1998): radius of the circular search, period of time and magnitude range. The location of the mainshock is indicated by the star; the seismicity used in the search is represented by black dots.

The first grid search analysis was done with the goal of testing the concept of AMR and to answer the question: Can one find other regions of small  $c$ -values with the same parameters outside of the mainshock area?

On the contrary, the two mainshocks are located in the main areas of small  $c$ -values at the time of the respective main shocks. The choice of AMR parameters made by Bowman does not result in other potential regions of apparent AMR. However we still have to adjust the three parameters according to the mainshock we study.

## 2.2.4 AMR grid search maps versus stress change maps

The AMR concept can be interpreted as a data-fitting exercise since there is no general relationship between the radius of the search, the magnitude range and the period of time before the mainshock according to its magnitude. However, based on the results of *Bowman et al.* (1998), the AMR circular search seems to be optimal between 150km and 250km around a magnitude 6.5-7.5 event. Figure 2.6 presents maps of  $c$ -values for a possible M7 event in southern California, using a 30-year period of time and three radii: 150km, 200km and 250km. The occurrence of large earthquakes during the tested period increases the  $c$ -value, meaning that there is no significant AMR at that time and location. Once the seismicity associated with this event is no longer included in the data set, the results are in better agreement with the seismicity. This is particularly the case for Loma Prieta in 1989 and for Hector Mine in 1999.

Figure 2.6 also presents a comparison between the AMR grid search results and models of stress change over southern California in order to evaluate if areas inferred to be highly stressed also exhibit significant evidence of accelerating seismicity. Rather than assuming a complete stress drop on all surrounding fault segments implied by the back-slip stress lobe (*Bowman and King*, 2001), we consider that stress evolves with time from contributions of coseismic, postseismic and interseismic processes, governed by the elastic and viscous properties of the lithosphere. This emphasizes the importance of postseismic relaxation processes in time-dependent stress transfer and resulting earthquake hazard. Except for the contributions from the largest earthquakes, there is no

large variation in the stress pattern with time. The AMR and stress change maps do not look similar when there are many large earthquakes in the periods of the AMR calculations. However, they present similar features in 1985 and 1995.

## 2.2.5 Discussion and future work

The present work shows the first grid search analysis done for AMR. Adjusting three major parameters of the AMR circular search (radius of the circular region, magnitude range of background seismicity and time period considered), the results of the AMR are positive for large earthquakes in southern California. The comparison of a more general AMR grid search over southern California and stress maps from 1965 to 2005 shows more variable results. The AMR is sensitive to the time and location of larger events during the period of time considered. If a large shock occurs near the beginning of the tested period, the  $c$ -value will be larger at the end of the period than if the major earthquake occurs later. More research has to be done especially in the direct comparison of the stress state with seismicity patterns. It would be interesting to remove all the aftershock sequences and test again the similarity between AMR and stress change in southern California. Also, the work should evolve from an AMR circular search to a direct evaluation of a correlation between areas of high stress and AMR.

## 2.2.6 References

- Bowman, D.D., G. Ouillon, C.G. Sammis, A. Sornette, and D. Sornette (1998), An observational test of the critical earthquake concept, *Journ. of Geophys. Res.*, 103, B10, 24,349-24,372.
- Bowman, D.D. , and G.C.P. King (2001), Accelerating seismicity and stress accumulation before large earthquakes, *Geophys. Res. Lett.*, 28, 4039-4042.
- Freed, A.M., S.T. Ali, and R. Bürgmann (2007), Evolution of stress in Southern California for the past 200 years from coseismic, postseismic and interseismic stress changes, *Geophys. Journ. Intern.*, 169, doi: 10.1111/j.1365-1246X.2007.03391.x.
- Hardebeck, J.L., K.R. Felzer, and A.J. Michael (2007), Rigorous observational tests contradict the Accelerating Moment Release hypothesis, unpublished manuscript.
- Nutcracker v.X.1.5,  
[geology/fullerton.edu/dBowman/Site/Downloads.html](http://geology.fullerton.edu/dBowman/Site/Downloads.html)

## 2.3. Do repeating earthquakes talk to each other?

Kate Huihsuan Chen, Roland Bürgmann, and Robert M. Nadeau

### 2.3.1 Introduction

What determines the timing of earthquake recurrences and their regularity is of fundamental importance in understanding the earthquake cycle and has important implications for earthquake probability and risk estimates. This question cannot be answered without statistically significant observations of recurrence properties in natural earthquake populations. Historical or paleoseismic data of recurring large earthquakes have thus provided limited information about the degree to which stress interactions between earthquakes may produce some of the variability in earthquake recurrence intervals. A detailed record of micro-earthquake data from the borehole High Resolution Seismic Network (HRSN) and surface Northern California Seismic Network (NCSN) network sites at Parkfield provides a unique opportunity to examine how fault interaction acts on the observed timing and aperiodicity of the repeating events. Taking advantage of a large number of repeating micro-earthquakes with precisely determined relative locations, we analyze the repeating-event catalog for empirical evidence of asperity interaction and then offer a conceptual model for the mechanics of such interaction. We consider 217 repeating-earthquake sequences (REQSs) ranging from  $M = -0.4$  to  $M = 3$  to study their recurrence behaviors in space and time. In this effort, we separate the effect of changes in recurrence intervals that stem from documented coherent accelerations of fault slip, such as have been observed in the mid-1990s and following the 2004 Parkfield earthquake, from those caused by local interactions.

### 2.3.2 Repeating earthquake sequences from NCSN and HRSN data

The NCSN has reliably located earthquakes to less than M 1 level since 1984, and most sites consist of short-period seismometers. During the period 1984-2004 ending before the Parkfield M6 mainshock, 30 M 1.3 - 3.0 NCSN-derived repeating sequences were identified with a total event number of 178 (Nadeau and McEvilly, 2004). With the higher level of detection of micro-earthquakes, the borehole High Resolution Seismic Network (HRSN) has revealed a larger number of repeating earthquakes ranging in magnitude from -0.4 to +1.7. Recording of the HRSN deep borehole sensors began in early 1987, but the original data acquisition system failed in 1998. In August 2001, the HRSN network was upgraded and three new borehole stations were installed to improve resolution of the structure, kinematics and monitoring capabilities in the SAFOD drill-path and target zone. During the period

1987-1998, 187 HRSN repeating sequences were identified with a total event number of 1123. With more sequences that repeat more frequently due to their smaller event size, the HRSN catalog significantly increases the amount of repeating data available for analysis and provides a better opportunity to examine recurrence properties.

### 2.3.3 Variation in recurrence intervals

The variability of recurrence intervals is represented by the coefficient of variation, COV, the standard deviation divided by the mean of recurrence intervals, and is determined using the events that occurred before the 2004 M6 Parkfield earthquake (filled circles in Figure 2.7). A COV of 0 implies perfect periodicity, while COV=1 implies Poissonian recurrence and COV of greater than 1 indicates temporal clustering. The locations and COVs of repeating earthquake sequences are shown by circles in Figure 2.7, where large circles indicate the REQSS from NCSN data. We find that 50% of the NCSN REQSS are characterized by a COV of less than 0.3, and 67% of these small COV REQSS correspond to zones of low background seismicity, suggesting that these quasi-periodic repeaters are more isolated in space. The aperiodicities of REQSS do not reveal a systematic dependence on depth or magnitude. Following the 29 September 2004, M6.0 Parkfield, California earthquake, a large number of postseismic repeats are observed in many of the 25 updated repeating sequences (1987 - Sept. 15, 2006, which are shown by crosses in Figure 2.7, Nadeau, 2007, unpublished data). The event chronologies and time evolution of inter-event time spans (recurrence intervals) for two clusters of REQSS are shown in Figure 2.8a and 2.8b, respectively. The events in the cluster in the upper panel (see location in Figure 2.7) reveal a similar pattern, whereas the events in the cluster in the lower panel appear more randomly distributed. We note that the range of separation distances among the REQSS in these two clusters are similar, but the magnitude differences in the upper cluster in Figure 2.8a range from M 0.24 - 0.95 ( $dM = 0.71$ ), whereas the lower cluster includes events from M 0.58 - 1.70 ( $dM = 1.12$ ). The larger size difference may play a role in the temporal interaction between the sequence events and requires further examination. We next evaluate how the appearance of temporal interaction correlates with separation distance and magnitude difference among all REQSS pairs.

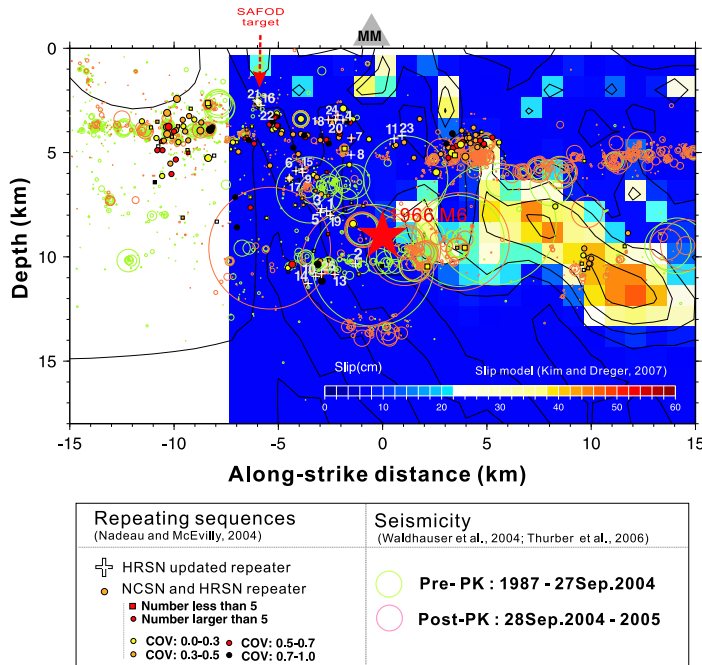


Figure 2.7: Along fault depth section showing the distribution of HRSN (1987 - 1998) and NCSN (1984 - 2004) repeating sequences (filled circles), background seismicity (1987-2005, open circles color coded for pre- and post-2004 earthquake), 1966 M6 hypocenter (red star), and their relationship to the slip distribution of the 2004 Parkfield mainshock (Kim and Dreger, 2007). Fill color/shades are keyed to the COV in recurrence interval. White crosses and numbers indicate the updated 25 HRSN repeating sequences.

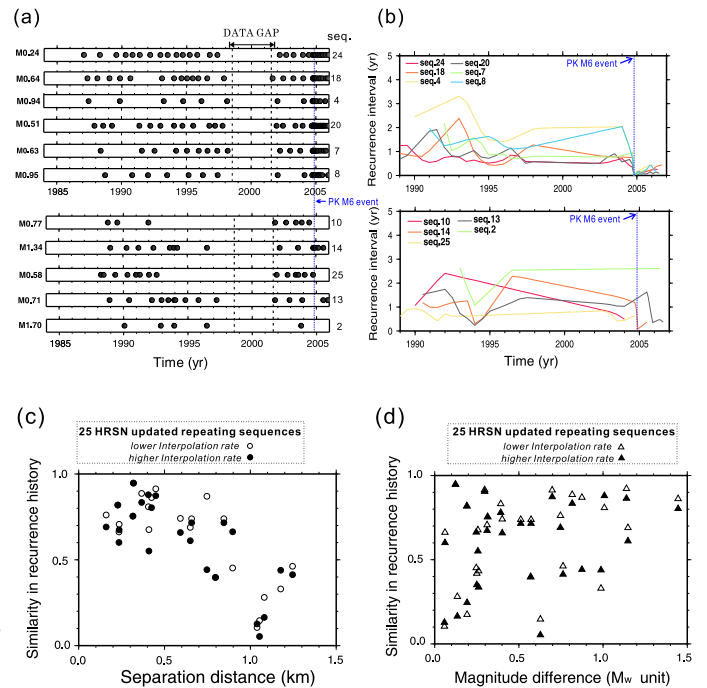


Figure 2.8: (a) Event chronology for two of the updated HRSN REQSs clusters (see white crosses with numbers in Figure 1 for locations). Note that in the upper panel, events rapidly recurred after the 2004 September Parkfield earthquake, which suggests a characteristically decaying afterslip pattern, whereas in the lower panel, the afterslip pattern is not clear. (b) Inter-event time spans (recurrence interval) as a function of time for each REQS in the two clusters. (c) Similarity in recurrence history (cross-correlation coefficient between the curves in (b)) between the 25 updated HRSN REQSs as a function of separation distance using different interpolation intervals. (d) Similarity in recurrence history curve as a function of magnitude difference (in Mw unit) by different interpolation rates. Filled symbols indicate the cross-correlation coefficients calculated by 0.5-yr and 0.1-yr interpolation intervals before and after the 2004 Parkfield earthquake respectively. Open symbols indicate the cross-correlation coefficients from 1-yr and 0.1-yr interpolation intervals before and after the 2004 Parkfield earthquake respectively.

### 2.3.4 Asperities interacting in time

To illustrate the temporal association between the neighboring REQSs, we have selected the 25 updated HRSN REQSs with more event repeats to calculate the similarity of recurrence interval curves (example shown in Figure 2.8b). We group the REQSs into pairs when the separation distance is less than 1.5 km and then calculate the cross-correlation coefficient between their recurrence curves by different interpolation intervals. Note that the different number of repeats of the REQSs lead to a different sampling rate of recurrence interval curves in Figure 2.8b, which requires interpolation into the same number of data points. High cross-correlation coefficient indicates a similar recurrence-interval history and implies stronger interaction in time and/or correlated slip-rate changes. Taking account of all 25 REQSs, in Figure 2.8c we show that when the separation distance is small, their recurrence histories appear to be similar. The relationship between recurrence history and magnitude difference, however, is unlikely to follow a linear pattern. Following the 29 September 2004, M6.0 Parkfield, California earthquake, a large number of postseismic event repeats occurred, where the sequences show extremely shortened recurrence intervals that gradually increase with time (upper panels in Figure 2.8a and 2.8b). This behavior is consistent with rapid afterslip adjacent to the coseismic rupture that is also evident in geodetic measurements (Johanson *et al.*, 2006; Johnson *et al.*, 2006; Murray and Langbein, 2006). However, this accelerated recurrence behavior is not obvious for some of the deeper repeating sequences we analyzed (e.g., seqs. 25, 10, 13, 2). Note that events in the seqs. 10 and 2 have not recurred since 2004 (lower panel in Figure 2.8a and 2.8b), suggesting that the Parkfield rupture somehow shut off these REQSs near the NW end of the rupture front, at least for the time being. A less pronounced, but widespread acceleration was also associated with a series of earthquakes with M greater than 4 and accelerated fault creep in the mid-1990s (also evident in the upper panels in Figure 2.8a and 2.8b).

### 2.3.5 Conclusions

The large population of characteristically repeating earthquakes at Parkfield provides a unique opportunity to study how these asperity ruptures interact with each other. Here we analyze M -0.4 ~ 3.0 repeating earthquake sequences to examine the variation of recurrence properties in space and time. We find that 67% of quasi-periodic repeating sequences (i.e., coefficient of variation in recurrence interval less than 0.3) correspond to zones of low seismicity, suggesting that these more regular repeating events are more isolated in space and from perturbing stress changes. We find that closely spaced repeating sequences show evidence of strong interaction in time, reflected in temporally clustered event recurrences.

The temporal correspondence appears to be a function of separation distance from nearby earthquakes rather than the relative size of the events. The response of the repeating events to the occurrence of larger earthquakes provides the clearest documentation of the interaction process. Accelerations of repeating sequences are associated with M 4 - 5 events that occurred in the mid-1990s and following the Parkfield earthquake when a large number of sequences exhibit accelerated recurrence behavior consistent with rapid afterslip following the mainshock. However, the characteristically decaying afterslip pattern is not obvious for some of the repeating sequences located close to the co-seismic slip area, suggesting either that the stress changes are very heterogeneous, or that the rupture erased or shut off some of the sequence source areas. Building on the above observations, we will be able to develop mechanical models that test the extent to which fault interaction in the form of static stress changes and transient postseismic fault creep produces the observed aperiodicity in the occurrence of these events, and furthermore, attempt to improve predictions of the times of future event repeats.

### 2.3.6 References

- Johanson, I. A., E. J. Fielding, F. Rolandone, and R. Bürgmann, Coseismic and postseismic slip of the 2004 Parkfield earthquake from space-geodetic data, in *Bull. Seism. Soc. Am.*, 96, 269-282, 2006.
- Johnson, K. M., R. Bürgmann, and K. Larson, Frictional properties on the San Andreas fault near Parkfield, California, inferred from models of afterslip following the 2004 earthquake, in *Bull. Seism. Soc. Am.*, 96, 321-338, 2006.
- Kim, A., and D. S. Dreger, Rupture process of the 2004 Parkfield earthquake from near-fault seismic waveform and geodetic records, in *Geophys. Res. Lett.*, submitted, 2007.
- Murray, J., and J. Langbein, Slip on the San Andreas Fault at Parkfield, California, over Two Earthquake Cycles, and the Implications for Seismic Hazard, in *Bull. Seis. Soc. Am.*, 96, S283 - S303, 2006.
- Nadeau, R.M. and T.V. McEvilly, Periodic Pulsing of Characteristic Microearthquakes on the San Andreas Fault, in *Science*, 303, 220-222, 2004.
- (Kate Chen has been a visiting scholar in BSL from March 2006 to May 2007) \* Department of Earth Sciences, National Cheng Kung University, Tainan, Taiwan

## 2.4. Segmentation in Episodic Tremor and Slip All Along Cascadia

Richard M Allen and Michael Brudzinski (Miami University)

### 2.4.1 Introduction

As oceanic plates subduct down into the mantle, friction on the interface with the overriding plate causes stick-slip behavior in the megathrust zone, pulling the upper plate down until it pops back up during a potentially devastating earthquake. Recent observations have also revealed slow slip episodes (SSE) that occur regularly on parts of the deeper plate interface with motion indicating release of accumulated strain (*Dragert et al., 2001; Lowry et al., 2001*). Their frequency and amount of slip ( $M_w \sim 6.5-7.5$ ) (*Melbourne et al., 2005*) imply they are a substantial portion of the interplate deformation budget. The duration of these episodes is much greater than earthquakes, yet they are accompanied by weeks of non-volcanic tremor (NVT) (*Obara, 2002; Rogers and Dragert, 2003; Szeliga et al., 2004*). As such, they represent another section of the strain rate continuum between earthquake and geologic time scales. Processes that govern ETS or potential relationships to major earthquakes and local geology remain unknown, although ETS has been proposed to impact the likelihood of megathrust earthquakes (*Mazzotti and Adams, 2004*).

### 2.4.2 ETS Observations

We utilize a new set of ETS information generated by automated identification of NVT and SSE at individual GPS and seismic stations that circumvents the need for dense networks (*Brudzinski and Allen, 2007*). We find NVT that correlate with SSE in several new locations along the subduction zone, particularly along central Cascadia. Corresponding seismic and GPS data availability ranges from 1 to 8 years, with 30 stations reporting SSE and 55 stations reporting NVT (Figure 2.9) of the over 300 stations that have been investigated with our automated techniques. It is clear that ETS occurs along the entire subduction zone, meaning that localized geological conditions special to a particular site are not controlling factors that prohibit ETS.

### 2.4.3 ETS Recurrence Intervals

While ETS is observed throughout the Cascadian subduction zone, the characteristics vary coherently along-strike revealing clear segmentation in the recurrence interval and relative timing of ETS events. First, there are 3 broad geographic zones with different recurrence intervals of ETS (Figure 2.9). The average interval across the Siletzia Zone ( $19 \pm 4$ ) is longer than those observed on Vancouver Island to the north ( $14 \pm 2$ ) and is nearly

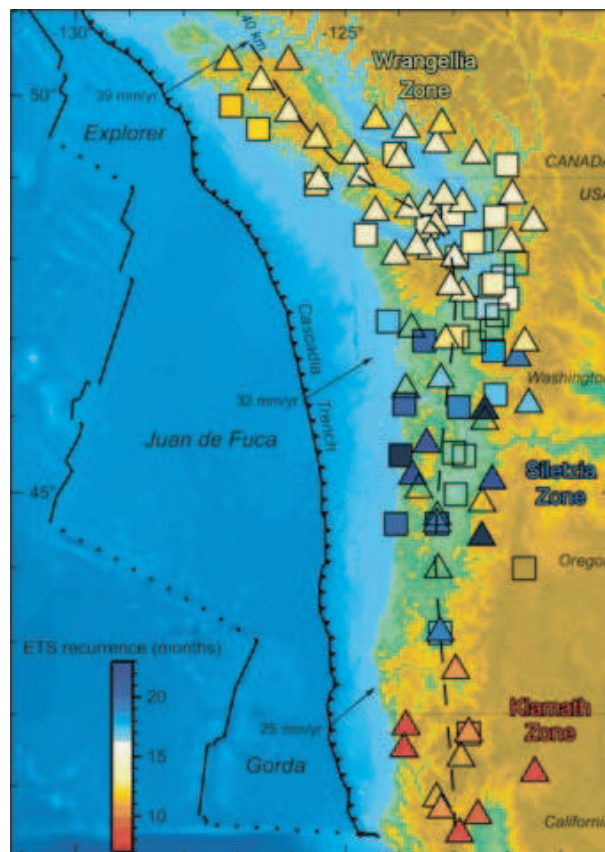


Figure 2.9: Map illustrating patterns in ETS along the entire Cascadia subduction zone. Colored basemap shows topography and bathymetry. Dashed line onshore marks 40 km depth contour of the subduction interface. Arrows and associated annotations show directions and speeds of subduction relative to North America. Locations of continuous GPS stations (squares) and broadband seismometers (triangles) which exhibit ETS are shown, with colors indicating the recurrence interval when multiple ETS events were observed. Recurrence intervals establish 3 zones that are labeled based on the continental terrane block they associate with.

twice as long as that from California to the south ( $10 \pm 2$ ). The broader geographic extent of our ETS measurements relative to previous studies allows us to identify that a coherent Wrangellia Zone extends from northern Vancouver Island down to  $\sim 47.5^\circ$  N, and that a Klamath Zone extends up from the southern end of the subduction zone to  $\sim 42.8^\circ$  N (Figure 2.9).

This pattern of recurrence intervals is not tied to the overall rate of subduction which drives the earthquake cycle as a whole. Overall convergence velocities decrease slowly from the north to the south (Figure 2.9), while the longest recurrence interval occurs in the middle of the subduction zone. We also find the 3 zones of relatively uniform recurrence intervals cannot be explained by age of the subducting plate, implying along strike variations in ETS are not due to temperature changes.

We suggest that the recurrence interval of ETS is related to properties of the overriding continental plate instead of the subducting oceanic plate. The age and temperature of the subducting plate likely has some impact on generating ETS, because initial work has shown SSE and/or NVT are prominent in other young, warm subduction zones like southwest Japan and Mexico (*Hirose and Obara, 2006; Larson et al., 2004; Lowry et al., 2001; Obara, 2002*). Yet the oceanic plates subducting beneath Cascadia are relatively uniform compared to the heterogeneity of the continental plate they dive beneath. In fact, the central Siletzia Zone with an  $\sim 18$  month recurrence interval corresponds to the relatively low lying and young Coastal Range Block of central and northern Oregon and southern Washington (mostly thick Siletzia terrane). The shorter-recurrence interval zones to the north (Wrangellia) and south (Klamath) correspond to older Pre-Tertiary blocks with higher topography consisting of a melange of old oceanic material with later silicic intrusion in a continental environment. Figure 2.10A shows how ETS recurrence intervals are inversely proportional to onshore fore-arc topography. Correlation of these continental blocks with along-strike patterns of ETS is also consistent with the observation that NVT appears to occur throughout the continental crust at depths above the interface with the subducting oceanic crust.

#### 2.4.4 ETS Segments

The zones of spatially coherent recurrence intervals (Figure 2.9) are further divided into segments where individual events recur over roughly the same location. While the average recurrence intervals of ETS are similar within a given zone, the relative timing between ETS events shows variation with location, a phenomenon that is particularly clear when comparing northern and southern Vancouver Island (*Dragert et al., 2004*). The extent of these segments is now emerging from the increased number of ETS observations. Figure 2.10B illustrates the phase shift in time between different segments by displaying the timing of ETS observations all along Cascadia, with horizontal lines estimating the along-strike extent of a given episode. Since these are station locations instead of source locations, we would expect the grey lines to extend on the order of 50 km beyond the actual source locations. Dashed vertical lines are approximate boundaries defined by events on either side that are

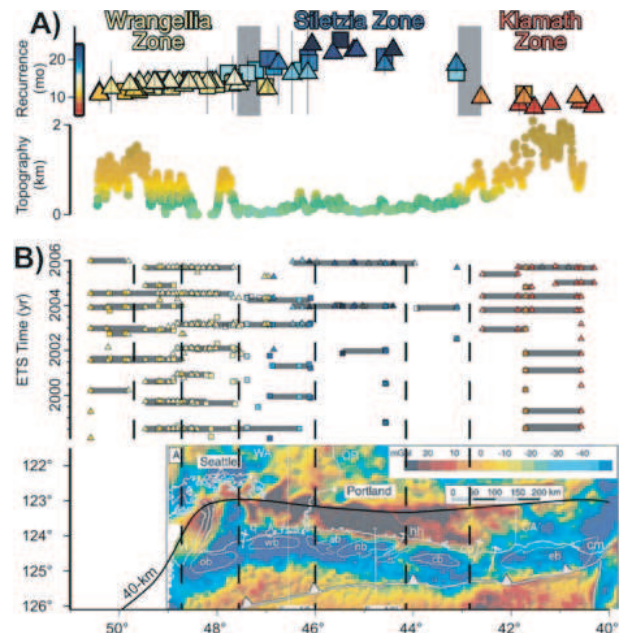


Figure 2.10: Plot of along strike patterns of ETS and upper plate features. (A) Top panel shows distinct variations in ETS recurrence with symbols as in Figure 2.9 and vertical bars show boundaries of observed intervals. Bottom panel shows topography above the 40 km depth contour of the subduction interface, in the middle of ETS observations. Topography is inversely correlated with ETS recurrence, roughly matching the primary continental terranes of different age and composition (Wrangellia, Siletzia, Klamath). (B) Top panel shows "phase" of ETS for 7 different segments along the subduction zone from ETS timing at individual stations. Horizontal grey lines connect stations that record ETS within a month of one another. Bottom panel shows color shaded gravity anomalies and locations of offshore fore-arc sedimentary basins (white lines), features which have been correlated with megathrust asperities on the subduction interface in recent global studies (*Wells et al., 2003*). Vertical dashed lines show apparent edges of ETS segmentation from currently available data that seem to correlate with megathrust segmentation from the 5 largest sedimentary basins. To deal with trench curvature, station latitudes are those when projected on to 40-km contour (black curve).

separated in time by over a month for greater than 50% of the episodes. We find 7 large segments with along-strike widths of 100-200 km (Figure 2.10B).

The largest segments of ETS occur immediately landward from the proposed locations of asperities on the Cascadia megathrust (*Wells et al., 2003*). The asperity locations are based on large, low gravity, sedimentary basins in the forearc that have been interpreted to indicate potential seismogenic segmentation at depth. Figure

2.10B shows the along-strike pattern of prominent fore-arc basins for comparison with the spatial extent of ETS segments. The apparent correlation between segmentation of the seismogenic zone and segmentation of the ETS zone suggests that effects of locking (or lack thereof) on the megathrust are transmitted to greater depths where slow slip is believed to occur (*Dragert et al.*, 2001). This spatially links megathrust structure and anticipated seismogenic behavior with ETS characteristics.

## 2.4.5 Discussion

A remaining question is whether upper plate structure controls plate interface behavior or vice versa. Both models have been proposed for fore-arc basins, with either basins developing in response to locking on the subduction interface (*Song and Simons*, 2003; *Wells et al.*, 2003) or thickness of the upper plate critical wedge controlling the frictional behavior on the plate interface (*Fuller et al.*, 2006). For ETS recurrence, the accreted terranes comprising the upper plate above ETS generate inherently sizable along-strike variations in structure, composition and age that are presumably more significant than long-term effects of ETS on upper plate structure. This supports an interpretation where variations in the Wrangelia, Siletzia, and Klamath blocks control behavior of the ETS source zone. A clue to how continental blocks could be responsible for differences in ETS recurrence is geochemical evidence that the different terranes have different fluid content (*Schmidt and Grunder*, 2006), which could trigger ETS via high pore fluid pressures (*Kodaira et al.*, 2004; *Obara*, 2002). An intriguing hypothesis is that different terrane composition affects rheology of the upper plate and hence the plate interface. For example, the Siletzia terrane would represent denser, stronger, more oceanic-like crust, while the Klamath terrane represents lighter, weaker, more continental-like crust. Such a scenario would suggest that the low-lying Siletzia region has a longer recurrence interval because the upper plate has the strength to accumulate strain for longer periods between SSE.

## 2.4.6 Acknowledgements

We relied heavily on data from PANGA, IRIS, USGS, CNSN, PNSN, BDSN, and EarthScope. R. Blakely, W.-P. Chen, B. Currie, K. Creager, C. DeMets, H. Deshon, W. Hart, S. Holtkamp, H. Kao, A. Lowry, W. McCausland, T. Melbourne, T. Niemi, W. Szeliga, B. Tikoff, C. Thurber, R. Wells, and an anonymous reviewer provided beneficial feedback. NSF provided support for MB (EAR-0642765, EAR-0510810) and RA (EAR-0643077, EAR-0539987). UW-Madison also provided support for MB and deployment of the OATS array.

## 2.4.7 References

- Brudzinski, M. and R.M. Allen, Segmentation in episodic tremor and slip all along cascadia, *Geology*, *35*, 907-910, doi: 10.1130/G23740A.1, 2007.
- Dragert, H., G.C. Rogers, J. Cassidy, H. H. Kao, and K. Wang, Episodic tremor and slip in northern Cascadia, *USGS Progress Report*, *04HQGR0047*, 1-6, 2004.
- Dragert, H., Wang, K. L., and James, T. S., A silent slip event on the deeper Cascadia subduction interface, *Science*, *292*, 1525-1528, 2001.
- Fuller, C. W., Willett, S. D., and Brandon, M. T., Formation of forearc basins and their influence on subduction zone earthquakes, *Geology*, *34*, 65-68, 2006.
- Hirose, H., and Obara, K., Short-term slow slip and correlated tremor episodes in the Tokai region, central Japan, *Geophysical Research Letters*, *33*, 5, 2006.
- Kodaira, S., Iidaka, T., Kato, A., Park, J. O., Iwasaki, T., and Kaneda, Y., High pore fluid pressure may cause silent slip in the Nankai Trough, *Science*, *304*, 1295-1298, 2004.
- Larson, K. M., Lowry, A. R., Kostoglodov, V., Hutton, W., Sanchez, O., Hudnut, K., and Suarez, G., Crustal deformation measurements in Guerrero, Mexico, *Journal of Geophysical Research-Solid Earth*, *109*, B04409, 2004.
- Mazzotti, S., and Adams, J., Variability of near-term probability for the next great earthquake on the Cascadia subduction zone, *Bulletin of the Seismological Society of America*, *94*, 1954-1959, 2004.
- Melbourne, T., Szeliga, W. M., Miller, M. M., and Santillan, V. M., Extent and duration of the 2003 Cascadia slow earthquake, *Geophysical Research Letters*, *32*, L04301, 2005.
- Obara, K., Nonvolcanic deep tremor associated with subduction in southwest Japan, *Science*, *296*, 1679-1681, 2002.
- Rogers, G., and Dragert, H., Episodic tremor and slip on the Cascadia subduction zone: The chatter of silent slip, *Science*, *300*, 1942-1943, 2003.
- Schmidt, M. E., and Grunder, A. L., Segmentation of the Cascade Arc Based on Compositional and Sr and Nd Isotopic Variations in Primitive Volcanic Rocks, *EOS Trans. Am. Geophys. Union*, *87*, T53G-02, 2006.
- Song, T. R. A., and Simons, M., Large trench-parallel gravity variations predict seismogenic behavior in subduction zones, *Science*, *301*, 630-633, 2003.
- Szeliga, W., Melbourne, T. I., Miller, M. M., and Santillan, V. M., Southern Cascadia episodic slow earthquakes, *Geophysical Research Letters*, *31*, L16602, 2004.
- Wells, R. E., Blakely, R. J., Sugiyama, Y., Scholl, D. W., and Dinterman, P. A., Basin-centered asperities in great subduction zone earthquakes: A link between slip, subsidence, and subduction erosion?, *Journal of Geophysical Research-Solid Earth*, *108*, 2507, 2003.

## 2.5. A New Spectral Ratio Method Using Narrow Band Coda Envelopes: Evidence for non-Self-Similarity in the Hector Mine Sequence

Kevin Mayeda, Luca Malagnini (Istituto Nazionale di Geofisica e Vulcanologia, Roma), William R. Walter (Lawrence Livermore National Laboratory)

### 2.5.1 Introduction

The use of local and regional S-wave coda is shown to provide stable amplitude ratios that better constrain source differences between event pairs. We first compared amplitude ratio performance between local and near-regional S and coda waves in the San Francisco Bay region for moderate-sized events, then applied the coda spectral ratio method to the 1999 Hector Mine mainshock and its larger aftershocks. We find: (1) Average amplitude ratio standard deviations using coda are 0.05 to 0.12, roughly a factor of 3 smaller than direct S-waves for  $0.2 < f < 15.0$  Hz; (2) Coda spectral ratios for the  $M_w$  7.0 Hector Mine earthquake and its aftershocks show a clear departure from self-similarity, consistent with other studies using the same datasets; (3) Event-pairs (Greens function and target events) can be separated by 25 km for coda amplitudes without any appreciable degradation, in sharp contrast to direct waves.

### 2.5.2 Amplitude Ratios

Do earthquakes scale self-similarly or are large earthquakes dynamically different than small ones? This question is important from a seismic hazard prediction point of view, as well as for understanding basic rupture dynamics for earthquakes. We test the extent to which narrowband coda envelopes can improve upon the traditional spectral ratio using direct phases, allowing a better comparison with theoretical models to investigate similarity. The motivation for using the coda is its stability relative to direct waves and its unique property of spatially homogenizing its energy (Mayeda *et al.*, 2003). Based on prior work on local and regional coda, we hypothesize that amplitude ratios of the same event-pair will be much more stable for coda than for direct S-waves. We tested this hypothesis by forming narrowband amplitude ratios for both wave types and compared their standard deviations for many event pairs. In practice, direct wave empirical Greens function studies have limited their data to co-located events with the same source mechanism. This, however, severely limits the useable amount of data, and if proven feasible, the coda's stability and minimal move-out will allow inclusion of more events that are separated in distance and not necessarily of the same focal mechanism. For both the coda and direct S-waves, we formed amplitude ratios for event pairs by simply subtracting the log10 amplitudes for each sta-

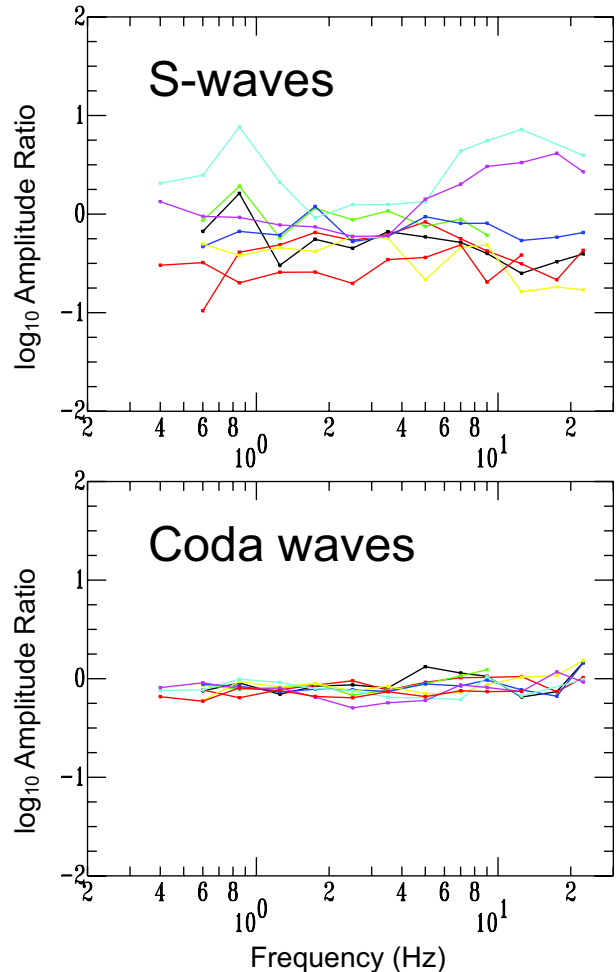


Figure 2.11: An example of amplitude ratios for a pair of events ( $M_w$  3.63 and 3.74) separated by 15.7 km in epicentral distance and identical depths of 7 km. Direct S-wave ratios (top) for 8 color-coded stations show significant scatter over the entire frequency range, whereas the coda wave amplitude ratios (bottom) are very stable from station to station.

tion that recorded the event pair. Since the site and path are the same for both events, the ratio should reflect the source differences in the frequency band. Figure 2.11 shows an example of direct wave amplitude ratios and coda wave ratios. Both events are roughly the same size and, as expected, the log10 average of the ratios is close to 0; however, the direct wave results are significantly more scattered. Using all available ratios, such as the example shown in Figure 2.11, we plot the amplitude ratio standard deviation versus event-pair offset for each frequency band (2.12). The coda amplitude ratios are roughly a factor of 3 smaller and do not show any appreciable increase with event separation, in contrast to the direct waves. This means that the use of the coda will allow for the inclusion of many more events in spectral ratios studies, whereas in direct wave studies, only those events that are virtually co-located are used. Equally important, the coda spectral ratios are significantly less scattered and thus source parameters, such as corner frequency, will be better constrained when we fit the observed data with theoretical source models, such as the commonly used omega-square model (*Aki, 1967; Brune, 1970*).

### 2.5.3 Application to the $M_w$ 7.0 Hector Mine sequence

Next, we turn our attention to local and regional recordings of the  $M_w$  7.0 1999 Hector Mine mainshock and 6 aftershocks ranging between  $M_w$  3.7 and 5.4. In this case we consider 6 broadband stations ranging between 60 and 700 km: GSC, PFO, MNV, CMB, TUC, and ELK. All the events have independent regional seismic moment estimates from full waveform inversion by *G. Ichinose* (pers. comm., 2006). As observed for San Francisco Bay Area events, the coda spectral ratios for Hector Mine events were very stable, with average standard deviations of less than 0.1 for all frequencies. Figure 2.13 shows all 6 ratios, assuming both simultaneous source model fits and individual ratio fits. In all cases the high frequency asymptote is significantly above the theoretically predicted value. This is consistent with a break in self-similarity and is inconsistent with a standard self-similar *Brune* (1970) style omega-square model. Our preferred interpretation is that the apparent stresses are systematically lower for the aftershocks than the mainshock. If all events have Brune-style spectra with an f-2 fall-off at high frequencies, this implies the corner frequency scaling is steeper than f-3 for self-similar, constant apparent stress scaling. More in-depth results of this study can be found in (*Mayeda et al., 2007*).

### 2.5.4 Acknowledgements

K. Mayeda was supported under Weston Geophysical subcontract No. GC19762NGD and AFRL contract No. FA8718-06-C-0024. Work by L. Malagnini

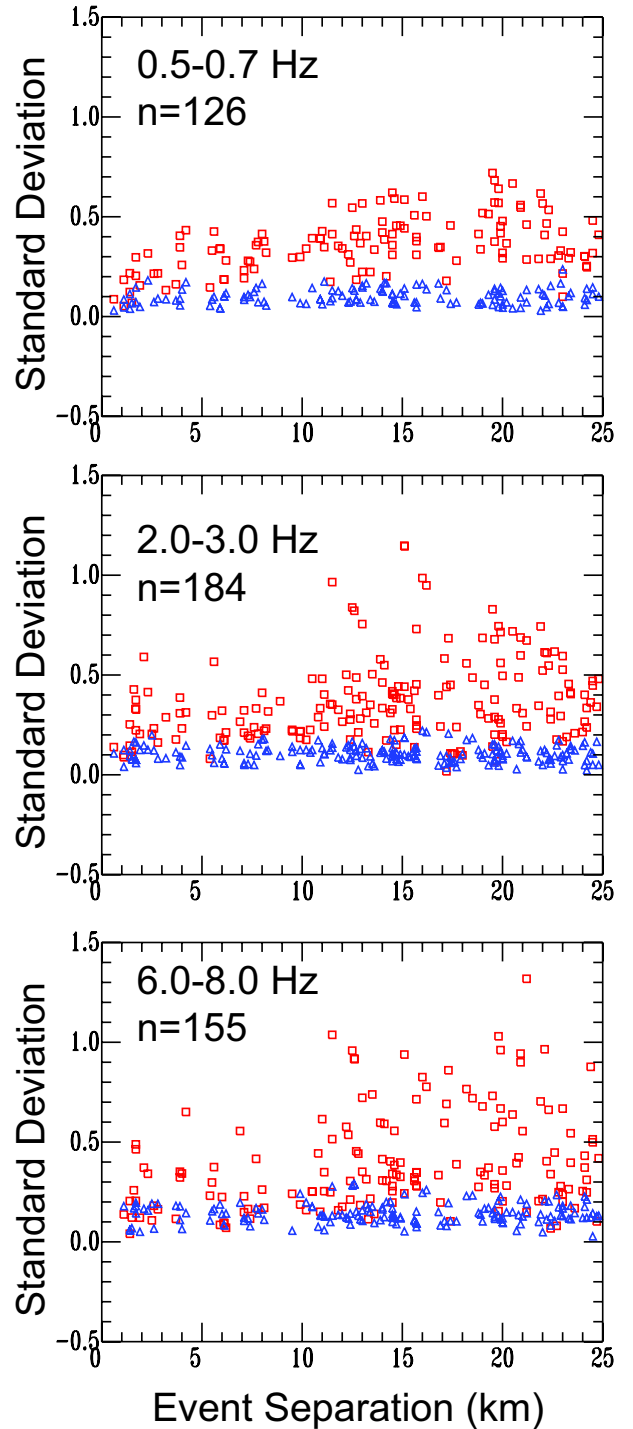


Figure 2.12: For event ratios that had at least 5 stations recording, we plot the amplitude ratio standard deviation versus event separation for coda (triangles) and direct waves (squares) for three frequency bands, 0.5-0.7 Hz (top), 2.0-3.0 Hz (middle), and 6.0-8.0 Hz (bottom). Note that the coda scatter shows almost no dependence upon distance, in sharp contrast with the direct waves and is roughly a factor of 3 smaller.

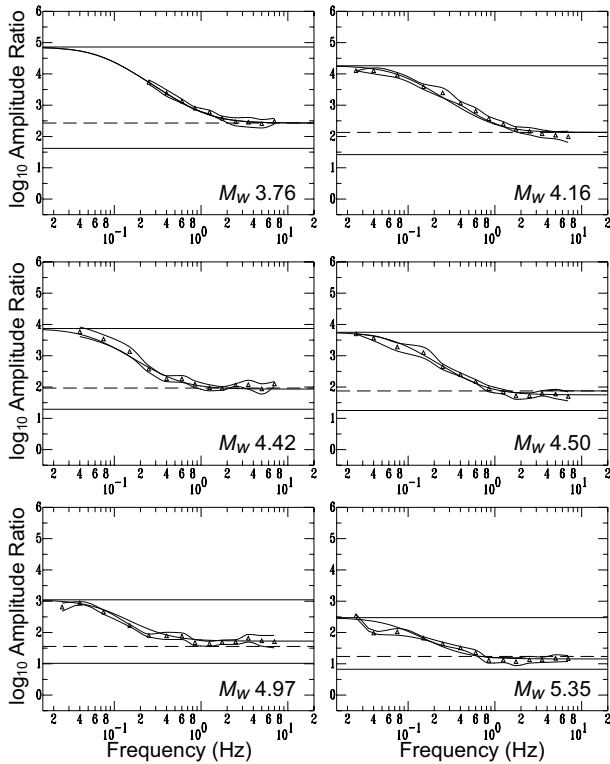


Figure 2.13: Spectral ratios for the Hector Mine mainshock relative to 6 aftershocks. In each figure, we show the low and high frequency asymptotes assuming constant apparent stress scaling as solid lines. Dashed lines show the case if the spectral fall-off were 1.5 rather than 2.0. However, observations worldwide are inconsistent with a fall-off of 1.5 and we are left to assume that the apparent stresses are systematically lower for the aftershocks than the mainshock, breaking similarity.

was performed under the auspices of the Dipartimento della Protezione Civile, under contract S4, ProCiv-INGV (2004-06), project: "Stima dello scuotimento in tempo reale e quasi-reale per terremoti significativi in territorio nazionale". Work by W.R. Walter was performed under the auspices of the U.S. Department of Energy by the University of California, LLNL under contract No. W-7405-Eng-48. This is LLNL contribution UCRL-JRNL-229275.

### 2.5.5 References

Aki, K. (1967), Scaling law of seismic spectrum. *J. Geophys. Res.* *72*, 1217-1231.

Brune, J. N. (1970), Tectonic stress and spectra of seismic shear waves from earthquakes, *J. Geophys. Res.* *75*, 4997-5009.

Mayeda, K., A. Hofstetter, J.L. O'Boyle, W.R. Walter (2003), Stable and transportable regional magnitudes

based on coda-derived moment-rate spectra, *Bull. Seismol. Soc. Am.*, *93*, 224-239.

Mayeda, K., L. Malagnini, W.R. Walter (2007), A new spectral ratio method using narrow band coda envelopes: Evidence for non-self-similarity in the Hector Mine sequence, *Geophys. Res. Lett.*, doi:10.1029/2007GL030041.

## 2.6. Evolution of Tremor Activity at Cholame, CA

Robert M. Nadeau

### 2.6.1 Introduction

Nonvolcanic tremor (NVT) activity (i.e., long-duration seismic signals with no clear P or S waves) may provide important clues to the rheology and processes responsible for the nucleation and seismic cycles of large earthquakes. Nonvolcanic tremors were first observed in subduction zones (i.e., thrust fault plate boundaries) (e.g., Obara, 2002; Rogers and Dragert, 2003), where fluids from subduction processes were believed to play an important role in generating these tremors. However, more recently, we have discovered NVT along the San Andreas Fault (SAF) (a transform plate boundary) near Cholame, CA, where subduction related fluids are not present (Nadeau and Dolenc, 2005).

### 2.6.2 SAF Tremors

Our discovery of NVTs beneath Cholame, CA is important for three reasons: 1) they occur along a transform rather than a subduction plate boundary zone, 2) no obvious source for fluid re-charge exists in the Cholame area to aid in tremor genesis, and 3) the highest level of tremor activity in the region occurs beneath the inferred epicentral region of the moment magnitude (M)  $\sim 7.8$  1857 Fort Tejon earthquake, whose rupture zone is currently locked.

### 2.6.3 Ongoing Activity

Nadeau and Dolenc (2005) found that changes in tremor and micro-earthquake rates at Cholame appeared to correlate. This suggests that deep deformation associated with the Cholame tremors (i.e., ETS) may also be stressing the shallower seismogenic zone in this area. Subsequent monitoring of the Cholame tremors has revealed further evidence for such stress-coupling. Of particular note have been the rate changes associated with the 22 December 2003, M6.5 San Simeon, CA and the 28 September 2004, M6 Parkfield, CA earthquakes (epicenters  $\sim 50$  km west and  $\sim 10$  km NW of Cholame, respectively) that have now been observed (Fig. 2.14).

Between 1 and 3 months before the Parkfield earthquake, tremor activity was relatively low, near pre-San Simeon levels. The activity then spiked between 20 and 22 days prior to the Parkfield mainshock. The relationship of this fore-tremor (FT) to the Parkfield mainshock is suggestive of coupling between deep stress changes associated with the tremors and stress changes in the shallower seismogenic zone leading to the Parkfield M6.0 mainshock.

More profound, however, has been the large and long lasting increase in overall tremor rates following the Parkfield event. Immediately following the the mainshock, tremor rates increased to unprecedented levels that persisted for several days. For several weeks following this period tremor rates remained extremely high but decayed rapidly (similar to the decay of aftershocks in the region). Then,  $\sim 80$  days after the mainshock, tremor rates appear to have entered into a new state where overall rates decay much more slowly and where the dominant pattern of activity exhibits a pattern of multi-scale quasi-periodic variation (i.e., with periodicities of  $\sim 75$  and 330 days). This pattern has persisted up to the time of this report, and it is not yet clear whether the rate behavior reflects solely the response of the tremor source region to stress from the Parkfield mainshock or if mainshock stresses have activated other tremor related processes (e.g., fluid migration or transient deformation).

In any case, the pattern of tremor rate behavior relative to the San Simeon and Parkfield events supports the argument that nearby moderate magnitude earthquakes can stimulate deep NVT activity and that such events may have a significant impact on the long-term evolution of NVT activity. In addition, because the Cholame segment of the SAF has an estimated earthquake recurrence time of 140 years (+93, -69) (WGCEP, 1995), and it is now over 140 years since the Fort Tejon event, future increases in SAF tremor activity may signal periods of more rapid stress change and an increased probability for the next large earthquake on the Cholame segment.

### 2.6.4 Acknowledgments

This research was supported by U.S. Geological Survey award nos. 06HQGR0167 and 07HQAG0014.

### 2.6.5 References

- Nadeau, R.M. and D. Dolenc, Nonvolcanic Tremors Deep Beneath the San Andreas Fault, *Science*, 307, 389, 2005.
- Obara, K., Nonvolcanic Deep Tremor Associated with Subduction in Southwest Japan, *Science*, 296, 1679-1681, 2002.
- Rogers, G. and H. Dragert, Episodic Tremor and Slip on the Cascadia Subduction Zone: The Chatter of Silent Slip, *Science*, 300, 1942-1943, 2003.
- Working Group on California Earthquake Probabilities (WGCEP), Seismic hazards in southern California: probable earthquakes, 1994 to 2024, *Bull. Seism. Soc. Am.*, 85, 379-439, 1995.

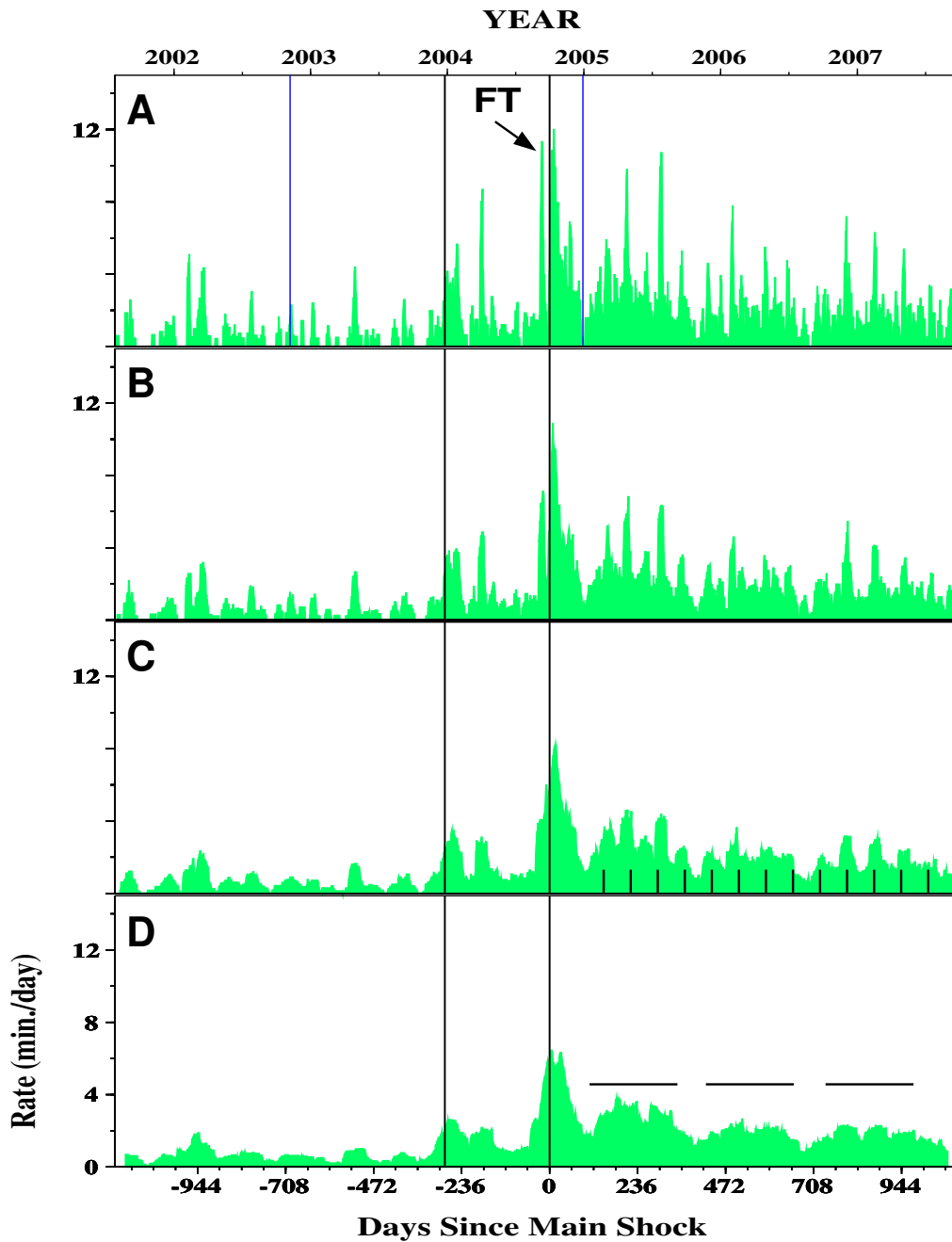


Figure 2.14: Activity rate history of nonvolcanic tremors detected by the borehole High Resolution Seismic Network (HRSN) at Parkfield (PF), CA. Histories span 2240 days (3 years 65 days prior to the PF mainshock to 2 years 349 days after the event). The number of minutes of tremor activity for each day is computed, yielding a time series of activity rates with sampling interval of 1 day. The time series is then smoothed with boxcars of 4 different window lengths (panel A, 7.5 days; B, 15 days; C, 30 days and D, 60 days) stepped at daily intervals with values plotted at the center of each window. This is done to help illustrate the multi-scale periodicity of the data. Black lines spanning all four panels are times of the 2003 and 2004 San Simeon and PF earthquakes. Black lines in panel 1 are times of the 2002 Denali M8.1 and 2004 Sumatra M9.3 earthquakes. Triggering of tremor activity from these global events appears to be relatively insignificant compared to triggering related to the San Simeon and PF events. FT refers to apparent fore-tremor event preceding the PF mainshock. Small vertical dashes (Panel C) are 75 day intervals approximating periodicity on this scale following the PF mainshock. Short horizontal lines (panel D) show the approximate 330 day rate pulses.

## 2.7. Regional Analysis of $L_g$ Attenuation: Comparison of 1D Methods in Northern California

Sean R. Ford, Douglas S. Dreger, Kevin Mayeda, William R. Walter (Lawrence Livermore National Laboratory), Luca Malagnini (Istituto Nazionale di Geofisica e Vulcanologia), William S. Phillips (Los Alamos National Laboratory)

### 2.7.1 Introduction

Understanding of regional attenuation  $Q^{-1}$  can help with structure and tectonic interpretation (Alegabi and Wyession, 2006; Benz *et al.*, 1997; Frankel, 1990), and correcting for the effects of attenuation can lead to better discrimination of small nuclear tests (e.g. Baker *et al.*, 2004; Mayeda *et al.*, 2003; Taylor *et al.*, 2002). Present threshold algorithms for event identification rely on  $Q$  models that are derived differently, and the models can vary greatly for the same region. In a recent submission to the Bulletin of the Seismological Society of America (Ford *et al.*, 2007) we characterize the difference between popular 1-D  $Q$  methods, and the difference within each method based on parameterization choice.

### 2.7.2 Data & Methods

The dataset consists of 158 earthquakes recorded at 16 broadband (20 sps) three-component stations of the BDSN between 1992 and 2004. The wide distribution of data parameters allows for sensitivity testing. We calculate  $Q_{Lg}$  by fitting the power-law model,  $Q_0 f^n$  using five different methods. The first two methods use the seismic coda to correct for the source effect. The last three methods use a spectral ratio technique to correct for source, and possibly site effects.

The coda normalization (CN) method uses the local shear-wave coda as a proxy for the source and site effects, thus amplitude ratios remove these two effects from the S-wave spectrum (Aki, 1980; Yoshimoto *et al.*, 1993). The coda-source normalization (CS) method uses the stable, coda-derived source spectra to isolate the path attenuation component of the  $L_g$  spectrum (Walter *et al.*, 2007). The two-station (TS) method takes the ratio of  $L_g$  recorded at two different stations along the same narrow path from the same event in order to remove the common source term (e.g., Chavez and Priestley, 1986; Xie and Mitchell, 1990). The reverse two-station (RTS) method uses two TS setups, where a source is on either side of the station pair in a narrow azimuthal window (Chun *et al.*, 1987). The two ratios are combined to remove the common source and site terms. The source-pair/receiver-pair (SPRP) method is the RTS method with a relaxation on the narrow azimuthal window requirement (Shih *et al.*, 1994).

### 2.7.3 Method Comparison

Since each method has a different data requirement it is improper to compare the methods with the full dataset. For example, the CN method will sample geology at all back-azimuths relative to a station, whereas the RTS method is restricted to a narrow azimuthal window aligned roughly along a pair of stations and events. In an attempt to normalize the dataset used for each method, we restrict the data to lie in a small region along the Franciscan block (Figure 2.15a). We implement all five methods to calculate  $Q_0 f^n$  in the region (Figure 2.15b). The populations are then smoothed with a two-dimensional gaussian kernel (Venables and Ripley, 2002) to produce an empirical distribution so that the 95% confidence region can be estimated. The grey region in Figure 2.15 represents a parameter space that fits all studies.

### 2.7.4 Acknowledgements

Figures were made with Generic Mapping Tools (Wessel and Smith, 1998).

### 2.7.5 References

- Aki, K. (1980). Attenuation of shear-waves in the lithosphere for frequencies from 0.05 to 25 Hz, *Phys. Earth Planet. Inter.* 21, 50-60.
- Alegabi, G. I., and M. E. Wyession (2006). Q(Lg) distribution in the basin and range province of the western United States, *Bull. Seism. Soc. Amer.* 96, 348-354.
- Baker, G. E., J. Stevens, and H. M. Xu (2004).  $L_g$  group velocity: A depth discriminant revisited, *Bull. Seism. Soc. Amer.* 94, 722-739.
- Benz, H. M., A. Frankel, and D. M. Boore (1997). Regional  $L_g$  attenuation for the continental United States, *Bull. Seism. Soc. Amer.* 87, 606-619.
- Chavez, D. E., and K. F. Priestley (1986). Measurement of frequency dependent  $L_g$  attenuation in the Great Basin, *Geophys. Res. Lett.* 13, 551-554.
- Chun, K., G. F. West, R. J. Kokoski, and C. Samson (1987). A novel technique for measuring  $L_g$  attenuation; results from Eastern Canada between 1 to 10 Hz, *Bull. Seism. Soc. Amer.* 77, 398-419.
- Ford, Sean R., Dreger, D.S., Mayeda, K., Walter, W.R., and Luca Malagnini (2007). Regional Analysis of  $L_g$  Attenuation: Comparison of 1D Methods in Northern California, submitted to *Bull. Seism. Soc. Amer.*
- Frankel, A. (1990). Attenuation of high-frequency shear waves in the crust: measurements from New York

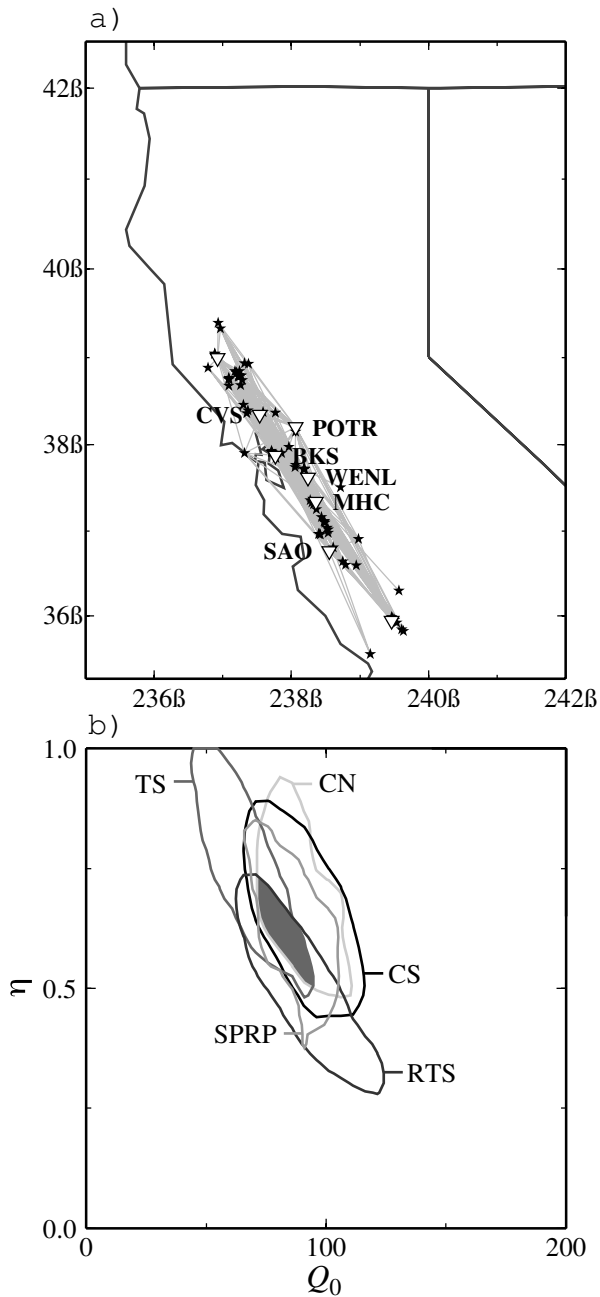


Figure 2.15: Method comparison. a) Map of the subset used in the comparison analysis. Data are in a small region near the San Francisco Bay Area, primarily along the Franciscan block. b) Power-law parameters and their empirical 95% confidence regions are given. The intersecting region is shaded grey.

State, South Africa, and Southern California, *J. Geophys. Res.* *95*, 17441-17457.

Mayeda, K., A. Hofstetter, J. L. O'Boyle, and W. R. Walter (2003). Stable and transportable regional magnitudes based on coda-derived moment-rate spectra, *Bull. Seis. Soc. Amer.* *93*, 224-239.

Shih, X. R., K. Y. Chun, and T. Zhu (1994). Attenuation of 1-6 s Lg waves in Eurasia, *J. Geophys. Res.* *99*, 23-23,875.

Taylor, S., A. Velasco, H. Hartse, W. S. Philips, W. R. Walter, and A. Rodgers, (2002). Amplitude corrections for regional discrimination, *Pure. App. Geophys.* *159*, 623-650.

Venables, W. N., and B. D. Ripley (2002). *Modern Applied Statistics with S*, Springer, New York.

Walter, W. R., K. Mayeda, L. Malagnini, and L. Scognamiglio (2007). Regional body-wave attenuation using a coda source normalization method: Application to MED-NET records of earthquakes in Italy, *Geophys. Res. Lett.* *34*, L10308.

Wessel, P., and W. H. F. Smith (1998). New, improved version of generic mapping tools released, in *American Geophysical Union, San Francisco*, Vol. 79, 579.

Xie, J., and B. J. Mitchell (1990). Attenuation of multiphase surface waves in the Basin and Range Province; Part I, Lg and Lg coda, *Geophys. J. Int.* *102*, 121-137.

Yoshimoto, K., H. Sato, and M. Ohtake (1993). Frequency-dependent attenuation of P and S waves in the Kanto area, Japan, based on the coda-normalization method, *Geophys. J. Int.* *114*, 165-174.

## 2.8. A simple method for simulating microseism H/V spectral ratio in 3D structure

Junkee Rhie and Douglas Dreger

### 2.8.1 Introduction

The understanding of 3D basin structure is very important in the estimation of damaging strong shaking. Since *Nakamura* (1989) first used ambient noise to estimate the site amplification, several techniques to delineate 3D basin structure using background noise have been developed. The advantage of the background noise approach is that ambient seismic noise is ubiquitous and continuous. It means that we don't need to wait for earthquakes or detonate expensive explosions for studying structure. *Dolenc and Dreger* (2005) showed that the frequency of the dominant H/V spectral peak (hereafter referred to as FDP) due to microseisms correlates with the thickness of the Santa Clara Valley (SCV). However, the synthetic FDPs for one dimensional models could not explain the observed shifts of the FDP. This result indicates that 2D and 3D wave propagation effects should be considered for the deep basins when their thickness is comparable to their size. In this study, we developed a simple method to compute FDP due to microseisms for 3D basin models and applied the new method to predict observed FDPs during Santa Clara Valley Seismic Experiment (SCVSE) (*Lindh et al.*, 1999).

### 2.8.2 Method

Microseisms are dominant seismic noise in the frequency range from 0.1 to 5 Hz and they are generated by pressure changes on the ocean bottom. Since understanding of the coupling mechanism between the ocean and sea floor is limited, the reliable simulation of the microseism wavefield is quite difficult. Fortunately, *Dolenc and Dreger* (2005) found that FDP is independent of the level of microseism excitations. This observation indicates that the H/V ratio is not dependent on the detailed source process of the microseisms because taking the H/V ratio inherently cancels the source effects and enhances the propagation effects. We have developed a simple method to simulate FDP due to microseisms or any continuous sources for given 3D velocity models. Our new method is tested by comparing the synthetic FDPs to observations from SCVSE (Figure 2.16). The method is very straightforward and consists of 5 steps. First, we compute Green's functions using a 3D finite-difference code (E3D; *Larsen and Schulz*, 1995). Here we assume a shallow (500m depth) vertical CLVD source as the source of the microseisms in the continental margin, and a simple Gaussian source time function is applied. Second, the Gaussian source time function is deconvolved from the

synthetics. Third, in order to reduce grid-dispersion effects (e.g. *Levander*, 1988) a low pass filter with a corner frequency of 0.8 Hz is applied to synthetics. Fourth, continuous monochromatic sine waves for discrete frequencies over the range from 0.025 to 0.8 Hz, with an interval of 0.025 Hz, are convolved with the low-pass filtered synthetic waveforms for each station. Finally, maximum amplitudes of convolved waveforms of three components for each frequency are taken in the time window after amplitudes become stable. The final horizontal maximum is determined by taking the geometric mean of two maximum horizontal amplitudes. In this study, the definition of the H/V spectral ratio is just the ratio of maximum vertical and horizontal amplitudes as a function of frequency. Since synthetic vertical and horizontal amplitudes are not stably varying with frequency, and sometimes abnormally small vertical amplitudes cause unrealistic peaks in the H/V ratio, the moving average over 5 adjacent data points is applied to the horizontal and vertical amplitudes before taking the H/V ratio.

### 2.8.3 Results and Discussion

We computed three FDPs for three different 3D Santa Clara Valley velocity models. The first model is the San Francisco Bay Area model from USGS (USGS Bay Area Velocity Model 05.1.0). The second model is the UC Berkeley (UCB) 3D model (*Stidham et al.*, 1999). The third model is a modified USGS model. In this modified velocity model, in order to enhance the effect due to the basin structure, we kept the velocity structure inside the basin, but assumed only 1D reference velocity structure for the regions outside of the basin. The comparison between synthetic and observed FDPs shows that FDPs for USGS and modified USGS models follow a similar depth dependent trend as observed FDPs, and their absolute values are in agreement as well (Figure 2.17). The synthetic FDPs for the UCB model show that FDP correlates with basin depth up to 2 km, but the correlation coefficient is not high and individual values are more scattered than in the case of the other models, especially for shallow depths. We also cannot match the observed shift of the trend in the observed FDP curve at around 2 to 3 km depth because the maximum thickness of the basin obtained in the UCB model is only 2 km.

The observation and synthetic results show that the variations in FDP are sensitive to the thickness of the basin up to a certain depth and then becomes stable. The simulation of the P-wave time delays from teleseis-

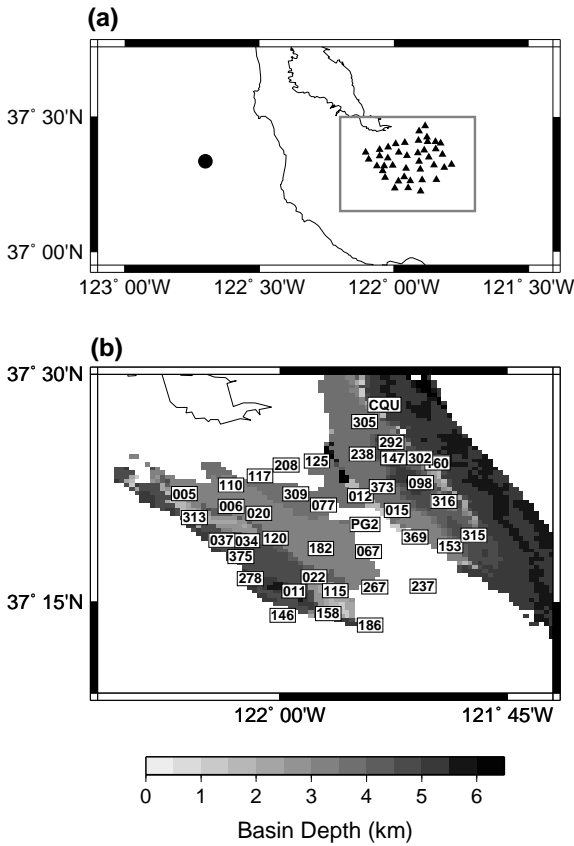


Figure 2.16: (a) The range of 3D models used for synthetic Green's function computation. Small triangles indicate the stations deployed during Santa Clara Valley Seismic Experiment (SCVSE). Solid circle represents assumed location of the microseism source. (b) The background shading indicates the depth of the Santa Clara Valley obtained from the 3D USGS velocity model

mic events for the USGS 3D velocity model at SCVSE stations shows a similar saturating trend as the FDPs for the USGS model (Dolenc et al., 2005). Synthetic time delay increases with increasing basin thickness up to a certain depth and then stabilizes. Since the P-wave time delay depends entirely on the mean velocity and thickness of the basin, this indicates that velocity contrast between the basin and the background medium is negligible at deeper depth, which is true for USGS 3D velocity model. In the case of the Santa Clara Valley model, FDP is only sensitive to the shallow structure, and the apparent thickness of the deeper part of the basin is much shallower than the model. It is likely due to the negligible velocity contrast in Santa Clara Valley model. But we still need more experiments to confirm which factor really controls the depth of the change in the depth-dependent trend of the FDP.

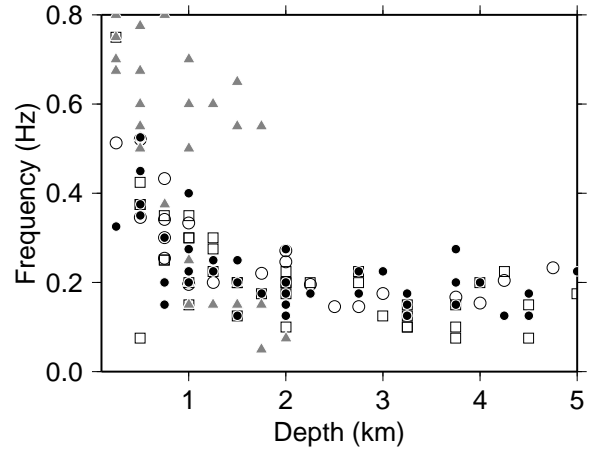


Figure 2.17: A comparison among observed (open circles) and three synthetic FDPs for USGS (Open squares), modified USGS (Solid circles) and UCB (Gray triangles), as a function of depth.

## 2.8.4 Acknowledgements

We thank the USGS and IRIS for providing the velocity model and seismic data. We also thank David Dolenc for providing his observed FDPs.

## 2.8.5 References

Dolenc, D., D. Dreger, and S. Larsen, Basin Structure Influences on the Propagation of Teleseismic Waves in the Santa Clara Valley, California, *Bull. Seism. Soc. Am.* 95, 1120-1136, 2005.

Dolenc, D., and D. Dreger, Microseisms observations in the Santa Clara Valley, California, *Bull. Seism. Soc. Am.* 95, 1137-1149, 2005

Larsen, S., and C. A. Schultz, ELAS3D: 2D/3D elastic finite difference wave propagation code, Technical Report No. UCRL-MA-121702, 19 pp, 1995.

Levander, A. R., Fourth-order finite-difference P-SV seismograms, *Geophysics* 53, 1425-1436, 1988.

Lindh, A. G., J. P. Eaton, M. O. Allen, J. H. Healy, S. W. Stewart, and L. Damerell, Calibration formulae and values for velocity seismometers used in the 1998 Santa Clara Valley, California seismic experiment, *U.S. Geol. Surv. Open-File Rept.* 99-434, 1999.

Nakamura, Y., A method for dynamic characteristics estimation of subsurface using microtremor on the ground surface, *QR Railway Tech. Res. Inst.* 30, 1, 1989.

Stidham, C., M. Antolik, D. Dreger, S. Larsen, and B. Romanowicz, Three-dimensional structure influences on the strong-motion wavefield of the 1989 Loma Prieta earthquake, *Bull. Seism. Soc. Am.* 89, 1184-1202, 1999.

## 2.9. Broadband Modeling of 3D velocity structure in the San Francisco Bay Area

Ahyi Kim, Douglas Dreger, and Shawn Larsen

### 2.9.1 Introduction

We performed 3D ground motion simulations for 9 recent moderate earthquakes in the San Francisco Bay Area to evaluate the USGS SF06 3D velocity model (Brocher et al., 2005; Jachens et al., 2005) in terms of modeling phase arrival timing, peak ground motion amplitudes, and general seismic waveforms. In addition, we performed forward modeling to obtain 3d structure modifications to improve the fit to available data.

### 2.9.2 Computational set up and 3D model used in the simulations

ID	Date	lon	lat	Strike	Dip	Rake	Depth	Moment	Mw
glt93016	01/16/1993	-121.455	37.028	331	83	166	7	2.40E+23	4.9
bol99230	08/18/1999	-122.686	37.907	115	49	69	8	7.25E+22	4.5
napa00247	09/03/2000	-122.414	38.377	60	75	18	11	3.74E+23	5
glt02134	05/14/2002	-121.6	36.967	212	87	-6	8	2.86E+23	4.9
dub03033	02/02/2003	-121.937	37.74	67	88	-19	14	1.36E+22	4.1
smar06166	06/15/2006	-121.492	37.102	360	78	-152	5	4.18E+22	4.4
glen06215	08/03/2006	-122.589	38.363	256	86	19	5	5.64E+22	4.4
hft07061	03/02/2007	-122.098	37.901	82	89	-1	14	2.77E+22	4.2
oak07202	07/20/2007	-122.18	37.8	321	89	168	5	2.52E+22	4.2

Figure 2.18: Table 1. Earthquake simulated in this study. Event ID and the source parameters are obtained from BSL Moment Tensor Catalog.

For the 3D waveform modeling, we used the elastic finite-difference code, E3D developed by Larsen and Schultz (1995). With the BSL cluster we can simulate ground motions throughout the greater San Francisco Bay Region to a maximum frequency of 0.5 Hz for models with a minimum wave speed of 500m/s. We have performed simulations of 9 Mw4.1-5.0 events using source parameters obtained from the BSL Moment Tensor Catalog (Figure 2.18:Table 1). Broadband seismic data was obtained from the Berkeley Digital Seismic Network (BDSN), and strong motion data was obtained from the USGS strong Motion Instrumentation Program (SMIP) and the California Geologic Survey (CGS) California Strong Motion Instrumentation Program (CM-SIP). The data was corrected to absolute ground velocity (cm/s). We compare synthetic and observed ground velocity in three passbands, namely 0.03-0.15Hz, 0.1-0.25Hz, and 0.1-0.5Hz.

### 2.9.3 Modeling results

From the 3D waveform simulations, we found that the USGS model explains important features of the overall waveforms very well, but the synthetics arrive earlier than the observations at all distances. The records

and synthetics were cross-correlated to determine the delay time (dt) for optimal alignment. (Figure 2.19). The cross-correlations of both P-waves and S-waves (Rodgers et al., 2007) show systematic delays indicating that on average the USGS 3D model is too fast.

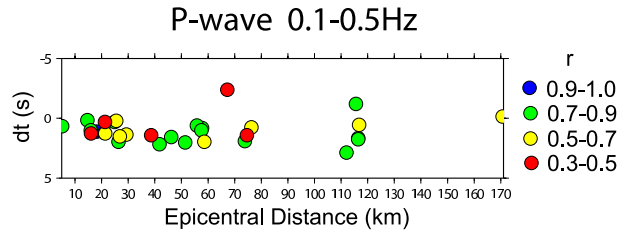


Figure 2.19: Delay time dt is estimated by cross-correlating the data and synthetic waveform pairs in 0.1-0.5Hz. The time axis is relative to the reported origin time.

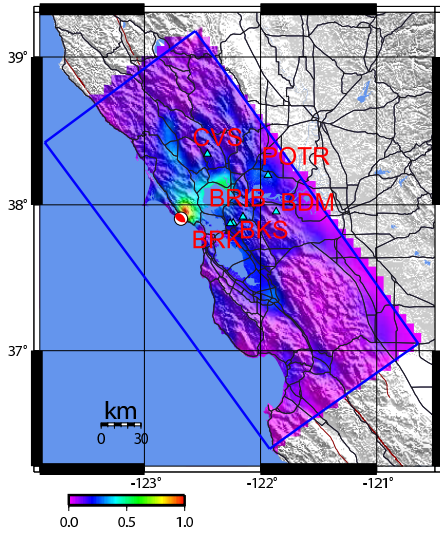
Figure 2.20 shows the synthesized PGV in the 0.1-0.5 Hz in map view, and waveform comparisons in the 0.03-0.15Hz, 0.1-0.25Hz and 0.1-0.5Hz passbands for the Boli-nas event. The synthetic PGV correlates well with the sedimentary basins and bedrock ridges, in that it is relatively larger in sedimentary basins and lower on bedrock ridges compared to what is computed with a 1D layered velocity structure and the same source parameters. For example, elevated shaking was observed in the distant Hollister valley as well as the San Francisco Bay region. The waveform comparison shows a very good fit in the 0.03-0.15 and 0.1-0.25Hz passband, except the POTR path. This west to east path crosses the northern San Francisco Bay area through the delta region, and evidently requires further model refinement. Waveform modeling of several paths crossing the region is ongoing.

### 2.9.4 References

Brocher, T. M., (2005). Empirical relations between elastic wave speeds and density in the Earth's crust, *Bull. Seism. Soc. Am.*, 95 No. 6, 2081-2092. Dreger D. and B. Romanowicz (1994). Source Characteristics of Events in the San Francisco Bay Region, USGS open-file report, 94-176, 301-309.

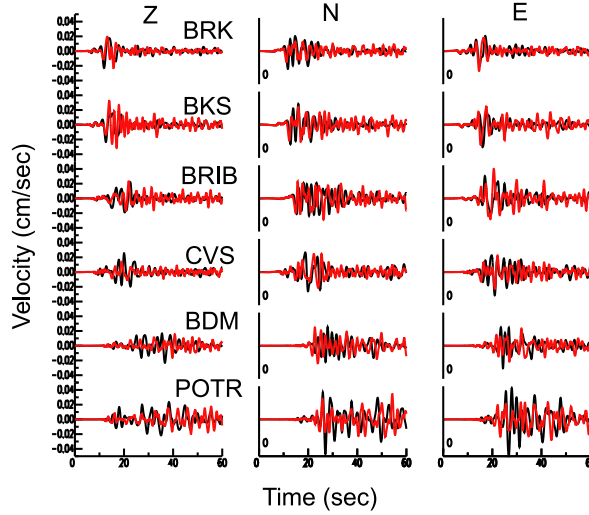
Jachens, R., R. Simpson, R. Graymer, C. Wentworth, T. Brocher (2006). Three-dimensional geologic map of northern and central California: A basic model for supporting ground motion simulation and other predictive modeling, 2006 SSA meeting abstract, *Seism. Res. Lett.*, 77, No.2, p 270.

### Boli99230 Mw4.5 PGV 0.1-0.5Hz

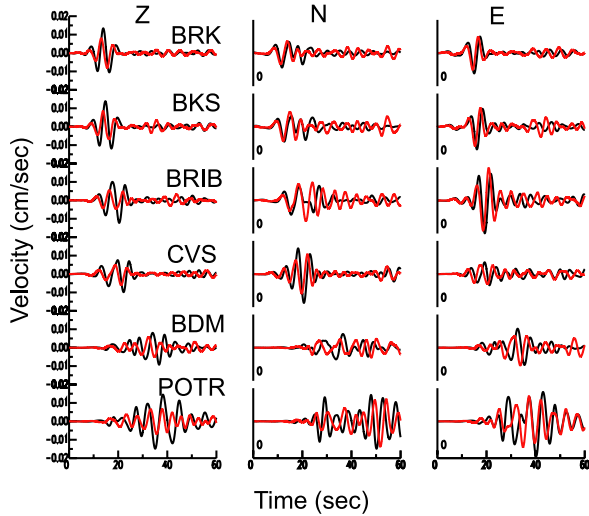


Normalized by Peak value 0.12(cm/sec)

### 0.1-0.5Hz



### 0.1-0.25Hz



### 0.03-0.15Hz

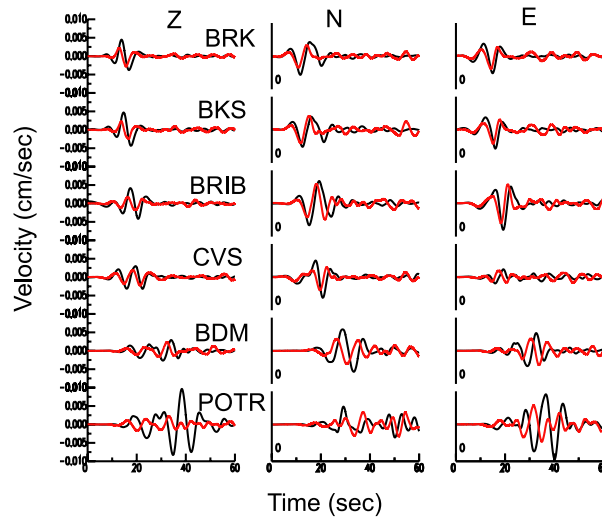


Figure 2.20: (Top left) Synthetic PGV ShakeMap for the Bolinas earthquake in 0.1-0.5Hz passband. Comparison between the data (black) and synthetics (red) in 0.1-0.5Hz (Top right), 0.1-0.25Hz (Bottom left), and 0.03-0.15Hz (Bottom right).

## 2.10. Inversion of the Teleseismic Observations for the Velocity Structure Within the Santa Clara Valley Basins

David Dolenc (now at U of Minnesota), Doug Dreger, and Shawn Larsen (LLNL)

### 2.10.1 Introduction

Previous analysis of the teleseismic data recorded by the 41-station seismic array in the Santa Clara Valley (SCV) (Dolenc *et al.*, 2005) showed strong correlations between basin depth reported in the USGS 3D seismic velocity model (ver. 2) (Jachens *et al.*, 1997) and different relative measures of ground motion parameters such as teleseismic arrival delays, P-wave amplitudes, and wave energy. The results suggested that the teleseismic dataset is sensitive to the basin structure and could therefore be used to improve the 3D velocity model.

We used teleseismic waveforms recorded by the SCV seismic array in an inversion to refine the USGS v2 model velocity structure within the SCV basins. To reduce the extremely large model space, we inverted only for the velocity structure within the basins while the basin geometry, as defined in the USGS v2 velocity model, was held fixed. The P- and S-wave velocities, and density in the basins were modeled as laterally uniform and with vertical gradients. The minimum S-wave velocity included in the model was 1 km/s.

### 2.10.2 Inversion

We followed the approach described by Aoi (2002). The observation equation is first linearized and then solved iteratively by singular value decomposition. Synthetic waveforms as well as sensitivity functions are needed to obtain the solution. We used the elastic finite-difference code E3D (Larsen and Schultz, 1995) to calculate the waveforms and obtain the sensitivity functions numerically, by taking the difference of waveforms from perturbed and unperturbed models.

The results of the inversion using the waveforms for the  $M_w=6.4$  Near Coast of Central Chile event are shown in Figure 2.21. The top two rows show the first 20 s of the waveforms as only this time window was used in the inversion. The bottom two rows show a 60 s time window. In addition to the P-wave, the pP-wave can be seen arriving just after the first 20 s. The results show that although the waveforms for only the first 20 s were used in the inversion, the final model also better describes the P-wave coda following the pP arrival.

Figure 2.22 compares the velocities in the SCV basins for the USGS v2 model (below station 238), initial, and final model after 3 iterations. Density and density gradient were not free parameters but were determined from P-wave velocity using the Nafe-Drake equation (Brocher, 2005).

### 2.10.3 Conclusions

The results suggest that the velocity structure in the SCV basins is slower than modeled in the USGS v2 velocity model. Additional tests showed that the inversion is stable and the final model is obtained in 3-4 iterations (Dolenc *et al.*, 2007). We started to test a more recent version of the USGS 3D velocity model (SF06) (Jachens *et al.*, 2006). We are also testing the stability of the inversion with additional free parameters that will enable us to model the velocity structure within the basins with a few layers with individual velocity gradients. We will also increase the grid spacing in our modeling to include slower velocities in the shallow parts of the basins.

### 2.10.4 Acknowledgements

Part of this work was supported by the USGS grants 99HQGR0057 and 00HQGR0048. The Hellman Faculty Fund is acknowledged for partial support.

### 2.10.5 References

- Aoi, S., Boundary shape waveform inversion for estimating the depth of three-dimensional basin structures, *Bull. Seism. Soc. Am.* 92, 2410-2418, 2002.
- Brocher, T. M., Empirical relations between elastic wavespeeds and density in the Earth's crust, *Bull. Seism. Soc. Am.* 95, 2081-2092, 2005.
- Dolenc, D., D. Dreger, and S. Larsen, Basin structure influences on the propagation of teleseismic waves in the Santa Clara Valley, California, *Bull. Seism. Soc. Am.* 95, 1120-1136, 2005.
- Dolenc, D., D. Dreger, and S. Larsen, Simultaneous inversion of the teleseismic, local, and microseism observations for the velocity structure within the Santa Clara Valley basins, *Seism. Res. Lett.* 78, 310, 2007.
- Jachens, R. C., R. F. Sikora, E. E. Brabb, C. M. Wentworth, T. M. Brocher, M. S. Marlow, and C. W. Roberts, The basement interface: San Francisco Bay area, California, 3-D seismic velocity model, *Eos Trans. AGU*, 78, F436, 1997.
- Jachens, R., R. Simpson, R. Graymer, C. Wentworth, and T. Brocher, Three-dimensional geologic map of Northern and Central California: A basin model for supporting earthquake simulations and other predictive modeling. *Seism. Res. Lett.* 77, 270, 2006.
- Larsen, S. and C. A. Schultz, ELAS3D: 2D/3D elastic finite-difference wave propagation code, Technical Report No. UCRL-MA-121792, 1995.

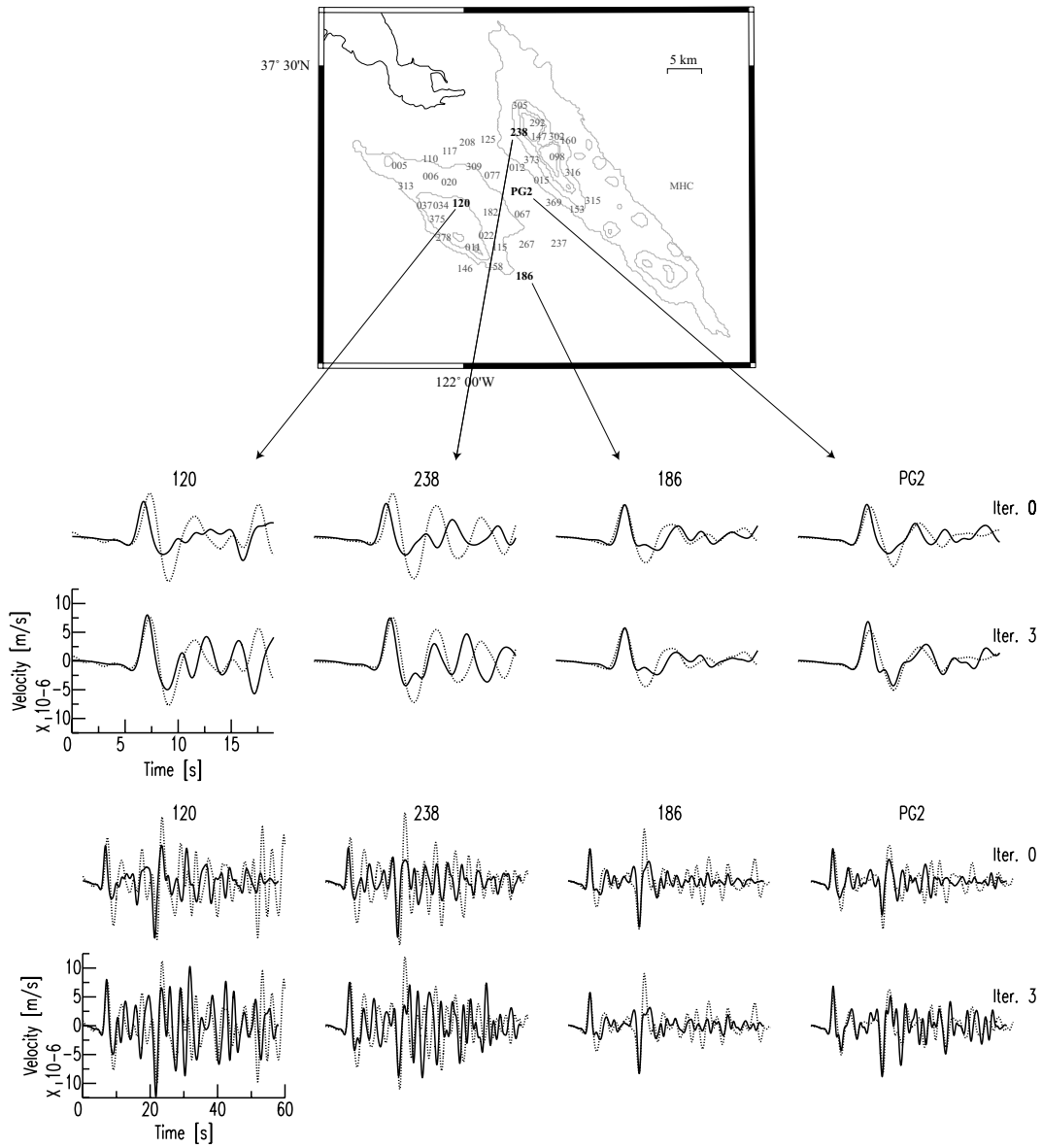


Figure 2.21: Results of the inversion for the  $M_w=6.4$  Near Coast of Central Chile event. Top two rows: The 20 s time window that was used in the inversion. Only four of the 38 stations that were used in the inversion are shown. The observed waveforms are shown for comparison (dotted). Bottom two rows: The longer time window (60 s) shows that final model also better describes the P-wave coda.

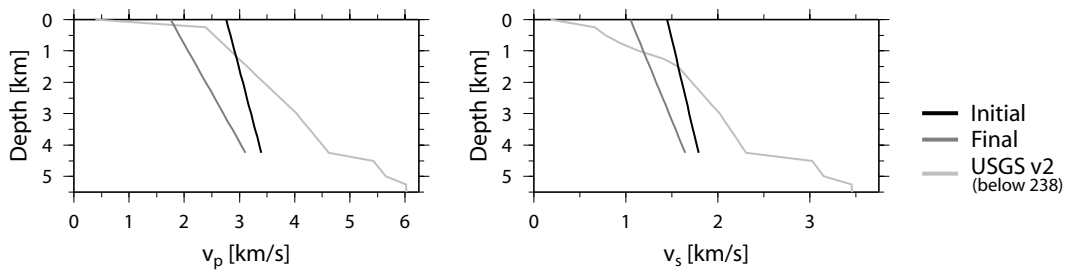


Figure 2.22: Velocities in the SCV basins for the USGS v2 model (below station 238), initial, and final model.

## 2.11. Observations of Infragravity Waves at the Endeavour Ocean Bottom Broadband Seismic Station (KEBB)

David Dolenc (now at U of Minnesota), Barbara Romanowicz, Paul McGill (MBARI), and William Wilcock (U of Washington)

### 2.11.1 Introduction

The long-period background noise observed at ocean bottom seismic stations is mainly due to deformation of the seafloor under the pressure forcing by long-period ocean surface gravity waves (infragravity waves; 0.002 to 0.05 Hz). Understanding the nature and characteristics of the coupling between infragravity waves and the solid earth is important for the study of infragravity wave generation and dissipation as well as for the study of the earth's hum and structure using non-seismic sources.

Station KEBB was installed 247 km offshore Vancouver Island at a water depth of 2376 m in August 2003 in collaboration between the University of Washington (UW), the University of Oregon, and the Monterey Bay Aquarium Research Institute (MBARI) as part of a three-year multidisciplinary experiment to monitor the linkages between the seismic deformation and hydrothermal fluxes on the northern Juan de Fuca plate. KEBB comprises a three-component broadband seismometer Guralp CMG-1T, sensitive over a wide frequency range, from 50 Hz to 2.8 mHz (360 sec), a recording, and a battery package. The seismometer is completely buried in the ocean floor sediments. The station is continuously recording data which were retrieved in August 2004 and September 2005.

### 2.11.2 Infragravity waves

Infragravity waves can be observed at KEBB in the period band from 30 to 400 sec. A comparison of the power spectral density (PSD) at KEBB, MOBB (ocean bottom station in Monterey Bay, CA; Romanowicz *et al.*, 2006), and YBH (land station in northern CA, one of the quietest BDSN stations) is shown in Figure 2.23. KEBB shows a noise hump for periods longer than 30 sec and MOBB for periods longer than 20 sec. The longer short-period cutoff value of the noise hump at KEBB is due to hydrodynamic filtering since KEBB is in deeper water (2376 m) than MOBB (1000 m). The two peaks observed at KEBB between 20 and 30 sec are due to instrumental noise and are present throughout the deployment. The long-period noise on the horizontal component is stronger at KEBB than at MOBB.

When compared to the energy of the short-period ocean waves recorded at local buoys, the low-frequency seismic noise is found to be mainly generated when the short-period ocean waves reach the coast, and not when the storm passes directly above KEBB (Figure 2.24).

Two types of modulation of the infragravity signal are observed at KEBB (Dolenc *et al.*, 2007b). A long-period modulation is best correlated with the energy of the 14-16 sec period ocean waves. The entire infragravity band signal is also modulated in phase with the tides.

### 2.11.3 Conclusions

Infragravity waves are generated in the nearshore region and are observed at KEBB only after they propagate from the shelf into deeper water and pass over KEBB. This agrees with the previous analysis of the MOBB data which also showed that the infragravity waves are generated in the nearshore region (Dolenc *et al.*, 2005). It sheds some light on the generation of the earth's low frequency "hum", confirming that coupling of infragravity waves with the solid earth occurs close to the shore (Rhie and Romanowicz, 2006). The long-period noise due to infragravity waves is unavoidable in shallow ocean bottom installations and postprocessing is needed to remove it from the seismic observations (Dolenc *et al.*, 2007a).

### 2.11.4 Acknowledgements

The KEBB deployment was funded by the W. M. Keck Foundation, MBARI, and UW.

### 2.11.5 References

- Dolenc, D., B. Romanowicz, D. Stakes, P. McGill, and D. Neuhauser, Observations of infragravity waves at the Monterey ocean bottom broadband station (MOBB), *Geochem., Geophys., Geosys.*, 6, Q09002, doi:10.1029/2005GC000988, 2005.
- Dolenc, D., B. Romanowicz, R. Uhrhammer, P. McGill, D. Neuhauser, and D. Stakes, Identifying and removing noise from the Monterey ocean bottom broadband seismic station (MOBB) data, *Geochem. Geophys. Geosys.*, 8, Q02005, doi:10.1029/2006GC001403, 2007a.
- Dolenc, D., B. Romanowicz, and W. Wilcock, Observations of infragravity waves at the Endeavour ocean bottom broadband station (KEBB), *Seism. Res. Lett.*, 78, 261, 2007b.
- Romanowicz, B., D. Stakes, D. Dolenc, D. Neuhauser, P. McGill, R. Uhrhammer, and T. Ramirez, The Monterey Bay broadband ocean bottom seismic observatory, *Annals of Geophysics*, 49, 607-623, 2006.
- Rhie, J. and B. Romanowicz, A study of the relation between ocean storms and the Earth's hum, *G-Cubed*, 7, doi:10.1029/2006GC001274, 2006.

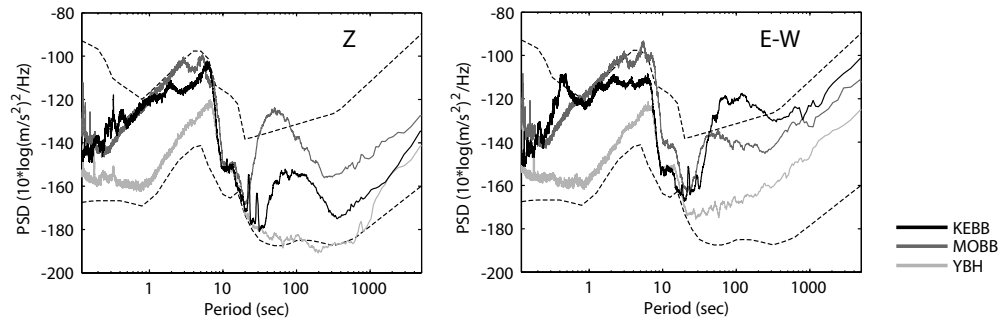


Figure 2.23: PSD at KEBB, MOBB, and YBH for the vertical (left) and horizontal (right) component on a stormy day (10/08/2003). The USGS high- and low-noise models for land stations are shown as dashed lines.

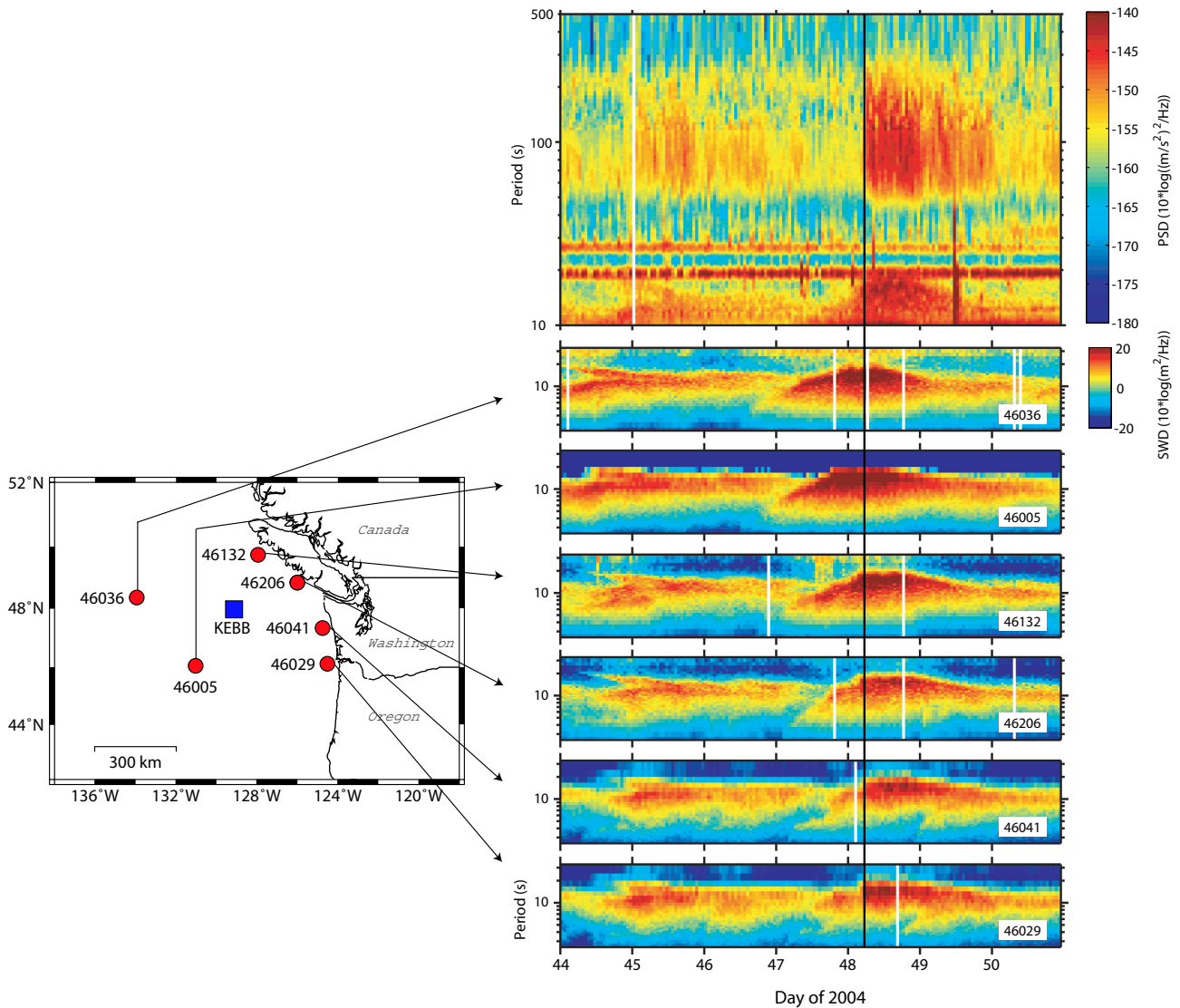


Figure 2.24: Top panel: PSD for the vertical KEBB component as a function of time (7 days) and period (10-500 sec). Bottom 6 panels: The spectral wave density of the ocean waves measured at the buoys. The storm observed on day 48 was approaching from the WSW direction. The change of the infragravity peak width (vertical black line) coincides with the time when the short-period ocean waves reach the coast and not when they pass above KEBB.

## 2.12. Identifying Isotropic Events Using an Improved Regional Moment Tensor Inversion Technique

Sean R. Ford, Douglas S. Dreger, William R. Walter (Lawrence Livermore National Laboratory)

### 2.12.1 Introduction

This research seeks to apply a regional distance complete moment tensor approach to tectonic and man-made seismic events in order to document performance in the ability to identify and characterize anomalous (non-double-couple) seismic radiation. Identification of events with demonstrably significant non-double-couple components can aid in discrimination and possibly yield determination (*Given and Mellman, 1986; Patton, 1988; Dreger and Woods, 2002*). As an initial application we calculate the full moment tensors of 17 nuclear tests at the Nevada Test Site (NTS), three collapses (two mine collapses and one explosion cavity collapse), and 12 earthquakes near the NTS.

We implement the time-domain full regional waveform inversion for the complete moment tensor (2nd rank tensor,  $M_{ij}$ ) devised by *Minson and Dreger (2007)* after *Herrmann and Hutcherson (1993)* based on the work of *Langston (1981)*. Data are collected for a total of 55 stations from the US National Seismic Network, IRIS/USGS, Berkeley Digital Seismic Network, Trinet, and the Lawrence Livermore National Laboratory (LLNL) network. We remove the instrument response, rotate to the great-circle frame, integrate to obtain displacement, and filter similarly to the synthetic seismograms.

### 2.12.2 Results

It is difficult to grasp the source-type from the standard focal mechanism plot. And decompositions of the deviatoric component are non-unique, where the DC and CLVD decomposition followed here could be replaced by two DCs (*Julian et al., 1998*). Following the source-type analysis described in *Hudson et al. (1989)* we calculate  $-2\epsilon$  and  $k$ , which are given by

$$\epsilon = \frac{-\hat{m}_1}{|\hat{m}_3|}$$

and

$$k = \frac{M_{ISO}}{|M_{ISO}| + |\hat{m}_3|}$$

where  $\hat{m}_1$ ,  $\hat{m}_2$  and  $\hat{m}_3$  are the deviatoric principal moments for the T, N, and P axes, respectively, and  $M_{ISO}$  is the isotropic moment where  $M_{ISO} = \text{trace}(M_{ij})/3$ .  $\epsilon$  is a measure of the departure of the deviatoric component from a pure double-couple mechanism, and is 0 for a pure

double-couple and  $\pm 0.5$  for a pure CLVD.  $k$  is a measure of the volume change, where  $+1$  would be a full explosion and  $-1$  a full implosion. We calculate the source-type plot parameters for 12 earthquakes, 17 explosions and three collapses (one cavity and two mine) and produce the source-type plot (Figure 2.25). The nuclear tests occupy the region where  $k > 0.25$ , the earthquakes cluster near the origin (with some interesting deviations), and the collapses plot almost exactly at  $(1, -5/9)$ , which is the location for a closing crack in a Poisson solid. The populations of earthquakes, explosions, and collapses separate in the source-type plot. These initial results are very encouraging and suggest a discriminant that employs the  $k$ ,  $-2\epsilon$  parameters.

### 2.12.3 Acknowledgements

Sponsored by the National Nuclear Security Administration, Office of Nonproliferation Research and Development, Office of Defense, Nuclear Nonproliferation. Contract No. DE-FC52-06NA27324. We thank Jeff Stevens for discussions regarding vanishing tractions at the free surface, Howard Patton for insights on the CLVD contribution to the explosion source, and Bruce Julian for the code to make the source-type plots. Figures were made with Generic Mapping Tools (*Wessel and Smith, 1998*).

### 2.12.4 References

- Dreger, D. and B. Woods (2002). Regional distance seismic moment tensors of nuclear explosions; seismic source mechanism through moment tensors, *Tectonophysics*, 356 (1-3), 139-156.
- Given, J. W. and G.R. Mellman (1986). Estimating explosion and tectonic release source parameters of underground nuclear explosions from Rayleigh and Love wave observations, Tech. rep., Sierra Geophysics Report No. SGI-R-86-126, Kirkland, WA.
- Herrmann, R. B. and K. Hutcherson (1993). Quantification of MLg for small explosion, Tech. rep., Phillips Laboratory Report PL-TR-93-2070.
- Hudson, J. A., R. G. Pearce, R. G., and R. M. Rogers (1989). Source type plot for inversion of the moment tensor, *J. Geophys. Res.*, 9 (B1), 765-774.
- Julian, B. R., A. D. Miller and G. R. Foulger (1998). Non-double-couple earthquakes; 1. Theory, Rev. *Geophysics*, 36 (4), 525- 549.
- Langston, C. A. (1981). Source inversion of seismic waveforms; the Koyna, India, earthquakes of 13 September 1967, *Bull. Seis. Soc. Amer.*, 71 (1), 1-24.

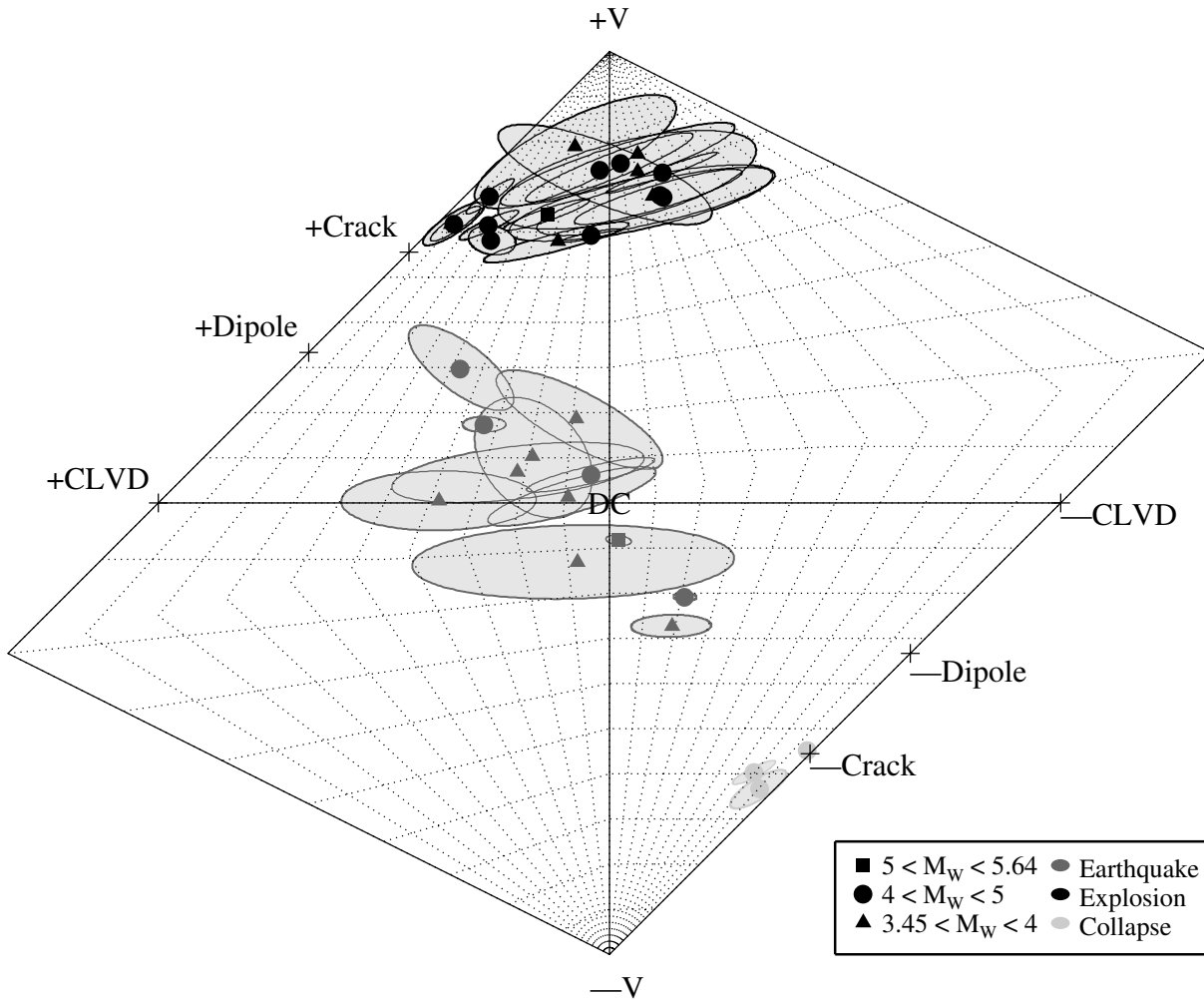


Figure 2.25: Source-type plot of the 12 earthquakes (blue), 17 explosions (red), 3 collapses (green), and their associated 95% confidence regions (shaded) analyzed in this study. The magnitude of the event is given by the symbol. The abscissa measures the amount of volume change for the source and the ordinate measures the departure from a pure DC.

Minson, S. and D. Dreger (2007). Improved seismic moment tensor inversion, submitted to *Geophys. J. Int.*

Muller, G. (1973). Seismic moment and long-period radiation of underground nuclear explosions, *Bull. Seis. Soc. Amer.*, 63 (3), 847-857.

Panning, M., D. Dreger and H. Tkalcic (2001). Near-source velocity structure and isotropic moment tensors; a case study of the long valley caldera, *Geophys. Res. Lett.*, 28 (9), 1815-1818.

Patton, H. J. (1988). Source models of the Harzer explosion from regional observations of fundamental-mode and higher mode surface waves, *Bull. Seis. Soc. Amer.*, 78 (3), 1133-1157.

Saikia, C. K. (1994). Modified frequency-wavenumber algorithm for regional seismograms using Filon's quadrature; modelling of Lg waves in Eastern North America,

*Geophys. J. Int.*, 118 (1), 142-158.

Sileny, J. (2004). Regional moment tensor uncertainty due to mismodeling of the crust, *Tectonophysics*, 383 (3-4), 133-147.

Sileny, J. and V. Vavrycuk (2002). Can unbiased source be retrieved from anisotropic waveforms by using an isotropic model of the medium?; Seismic source mechanism through moment tensors, *Tectonophysics*, 356 (1-3), 125-138.

Song, X. J., D. V. Helmberger and L. Zhao (1996). Broad-band modelling of regional seismograms; the basin and range crustal structure, *Geophys. J. Int.*, 125 (1), 15-29.

Wessel, P., and W. H. F. Smith (1998). New, improved version of generic mapping tools released, in American Geophysical Union, San Francisco, Vol. 79, 579.

## 2.13. Recalibrating $M_L$ for CISN

Robert Uhrhammer, Margaret Hellweg, Pete Lombard, Kate Hutton (Caltech), Egill Hauksson (Caltech), Allan Walter (USGS Pasadena), Dave Oppenheimer (USGS Menlo Park)

### 2.13.1 Research Objectives

*Richter* (1935) and *Gutenberg and Richter* (1942) developed the local magnitude scale using Wood-Anderson seismographs. *Richter* (1935) defined "local" magnitude as:

$$M_L = \log A - \log A_o(\Delta) + dM_L$$

where:  $M_L$  is the local magnitude estimate;  $\log A$  is the logarithm of the maximum trace amplitude  $A$  (in mm) recorded by a standard Wood-Anderson torsion seismograph;  $\log A_o(\Delta)$  is the logarithm of a standard event of magnitude zero at the same epicentral distance  $\Delta$  in km; and,  $dM_L$  is the station adjustment. The  $M_L$  estimate for an event is then the arithmetic average of the individual estimates from the Wood-Anderson seismographs that recorded the event.

In the past thirty years, the instrumentation with which we measure earthquakes has changed, and we can now process the data digitally. Nonetheless, we would like to continue to assign events with local magnitudes which are consistent with those that have been calculated in Northern and Southern California for the past 75 years.

### 2.13.2 Data Set

Initially, a set of approximately 100,000 waveforms from 255 candidate earthquakes recorded by 1160 horizontal channels (Station-Network-Channel-Location, or SNCL labels are used to describe each) from the AZ, BK, CI and NC networks were extracted. The candidate events were selected from the CISN 2000-2006 seismicity catalog by gridding the state into 50km square bins and selecting the largest  $M_L$  3+ event that occurred in each bin, and also (to obtain an adequate USArray data set) the largest  $M_L$  3+ event in 2006 (or second largest if the largest 2000-2006 event in the bin occurred in 2006). The SNCL channels included both broadband and strong motion instruments.

Local magnitude ( $M_L$ ) was calculated from each channel's trace by deconvolving the instrument response and convolving the response of a Wood-Anderson seismograph (*Uhrhammer et al.*, 1996). For each event, differences for all SNCL pairs were calculated, giving a dataset with more than 10 million differential observations. These differences were simultaneously inverted to determine a station adjustment for each SNCL,  $dM_L(\text{SNCL})$ , and a function describing the amplitude decay as a function of distance, called  $\log A_o$ .

### 2.13.3 Approach

Following a sequence of exploratory inversions, the data set was culled to remove events and SNCL's with fewer than 7 data each and to also remove data with event-SNCL distances greater than 500 km. The remaining differential data were then inverted simultaneously, via constrained linear least-squares, to determine the perturbations to the amplitude decay function ( $\log A_o$ ) and the adjustment ( $dM_L$ ) for each SNCL with the constraints: (1)  $\log A_o(100\text{km}) = -3$ ; and (2) the sum of the  $dM_L$ s for selected SNCLs with historical  $dM_L$  values = the sum of their historical  $dM_L$  values. This approach was taken to ensure consistency with past magnitudes determined in Northern and Southern California.

### 2.13.4 Amplitude Attenuation Function

The constrained linear least-squares perturbations to the  $\log A_o$  function were found to be very stable and well represented by a sixth order Chebyshev polynomial at hypocentral distances from 8 km to 500 km. At shorter distances, it is approximated by a line with a slope close to 2. In this study, we use hypocentral distance, rather than epicentral distance as originally used by *Richter* (1935), to accurately represent variation in the  $\log A_o$  attenuation function at close distances. This  $\log A_o$  form was adopted and a CISN  $\log A_o$  algorithm was developed and used in all subsequent inversions for the  $dM_L$  SNCL adjustments. A plot of the CISN  $\log A_o$  function is shown in Figure 2.26.

### 2.13.5 SNCL $dM_L$

Following another sequence of exploratory inversions, the data set was further culled to include only broadband data SNCLs. The final inversion used data from 217 earthquakes which occurred throughout California for 560 broadband horizontal channels from the AZ, BK, CI and NC networks. For each event, differences in  $M_L$  for all SNCL pairs were calculated, giving a dataset with 2607484 observations. These differences were simultaneously inverted to determine the  $dM_L$  station adjustment for each SNCL with the constraint:  $dM_L(\text{PAS.E}) + dM_L(\text{PAS.N}) + dM_L(\text{BAR.N}) + dM_L(\text{MWC.E}) + dM_L(\text{MWC.N}) + dM_L(\text{PLM.E}) + dM_L(\text{PLM.N}) + dM_L(\text{RVR.E}) + dM_L(\text{RVR.N}) + 1.5 * ( dM_L(\text{BKS.E}) + dM_L(\text{BKS.N}) + dM_L(\text{BRK.N}) + dM_L(\text{BRK.E}) + dM_L(\text{MHC.N}) + dM_L(\text{MHC.E}) ) = +0.943$  (the sum of the historical  $dM_L$  values at these stations). The 1.5 multiplier is used to equalize the weight-

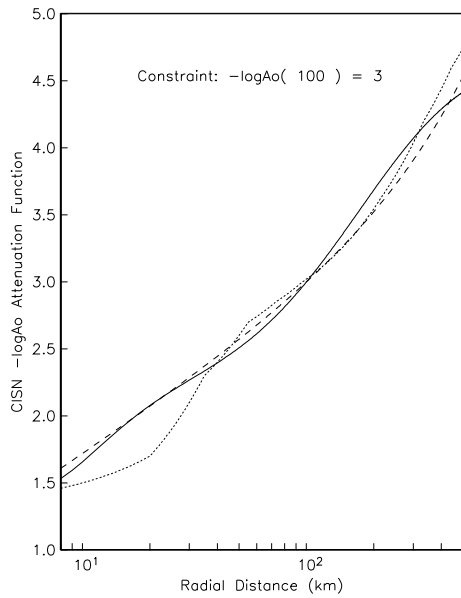


Figure 2.26: Comparison of the new CISN  $-\log A_o$  attenuation function (solid line) with those used in Northern California (short dashed line, *Richter*, 1935) and in Southern California (long dashed line, *Kanamori et al*, 1999). Note that distance is given from the hypocenter and not from the epicenter.

ing of the 6 BK SNCLs and the 9 CI SNCLs. A map of the CISN SNCL  $dM_L$  adjustments is shown in Figure 2.27.

### Significance of Findings

The state-wide  $\log A_o$  and station corrections for determining magnitudes will improve reporting for earthquakes in all of California on several counts. First,  $M_L$  was being calculated using only a subset of the currently existing broadband stations in both Northern and Southern California, as only they had been calibrated. In the past 10 years, many broadband stations and strong motion stations have been added to the networks. With the additional stations,  $M_L$  determination should become much more reliable. Second, until now Northern (*Uhrhammer et al*, 1996) and Southern California (*Kanamori et al*, 1999) have been using different  $\log A_o$  functions, with their attendant  $dM_L$  values for each SNCL. Thus different magnitudes were often determined by Northern or Southern California for an earthquake if it was near the boundary of the reporting regions, or for very large earthquakes in the other region. When the results of this project are implemented in the realtime and event review systems, this should no longer be the case.

### 2.13.6 Acknowledgements

Work on this project has been supported by the CISN funding of the California Governor's Office of Emergency Services under contract 6023-5 and the United States Geological Survey project 07HQAG0013.

### 2.13.7 References

Richter, C.F., An instrumental earthquake magnitude scale, *Bull. Seismol. Soc. Am.*, 25, 1-32, 1935.

Gutenberg, B. and Richter, C. F, Earthquake magnitude, intensity, energy and acceleration, *Bull. Seismol. Soc. Am.*, 32, 163-192, 1942.

Uhrhammer, R., Loper. S. J., Romanowicz, B., Determination of local magnitude using BDSN broadband records *Bull. Seismol. Soc. Am.*, 86, 1314-1330, 1996.

Kanamori, H., Maechling, P., Hauksson, E., Continuous Monitoring of Ground-Motion Parameters *Bull. Seismol. Soc. Am.*, 89, 311-316, 1999.

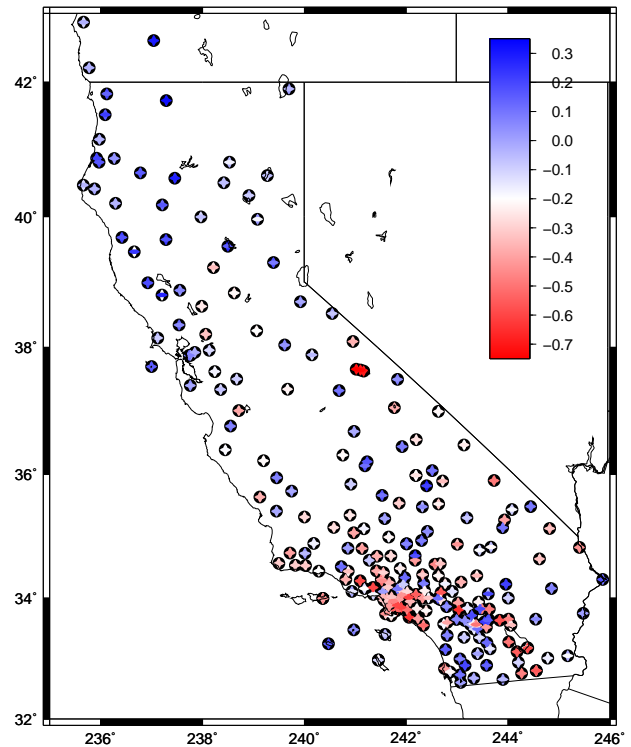


Figure 2.27: CISN  $dM_L$  adjustments for broadband stations in Northern and Southern California.

## 2.14. The Orinda Events: Complexity in Small Events

Margaret Hellweg

### 2.14.1 Introduction

Are small earthquakes like large earthquakes? Does their faulting involve the same physics? How small do aftershocks get, and where do they occur? Do they exhibit similar complexity to that observed in large events? These questions are difficult to answer, because small earthquakes and their tiny aftershocks are rare in our recordings.

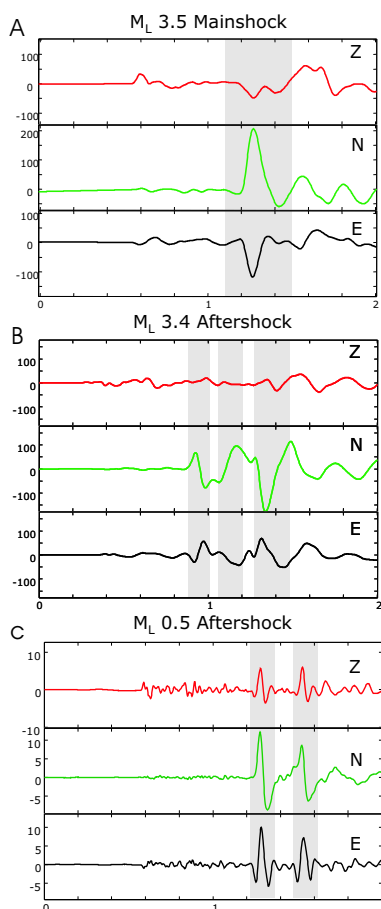


Figure 2.28: Example waveforms of (A) the mainshock, which is simple, and (B) the largest and (C) a small aftershock, which are complex. This is most easily seen in the S-waves (gray shading), which have more than one large arrival on B and C.

A sequence of small earthquakes near Orinda, California, occurred almost under the BSL's station BRIB (37.92 N, 122.15 W). At the surface, this station has a broadband seismometer and an accelerometer. As it is

also a borehole station of the Northern Hayward Fault network, it has a geophone and an accelerometer, each with 3-components, at a depth of 119 m. The borehole instruments are sampled at 500 sps. The sequence began on October 19, 2003, at 14:35:27 UTC, with an earthquake with  $M_d$  2.5. The mainshock (MS,  $M_L$  3.5, Figure 2.28A) followed about an hour later. Over the course of the next 3 months, there were more than 4000 aftershocks, with magnitudes ranging from -2.5 to 3.4.

### 2.14.2 Event Complexity

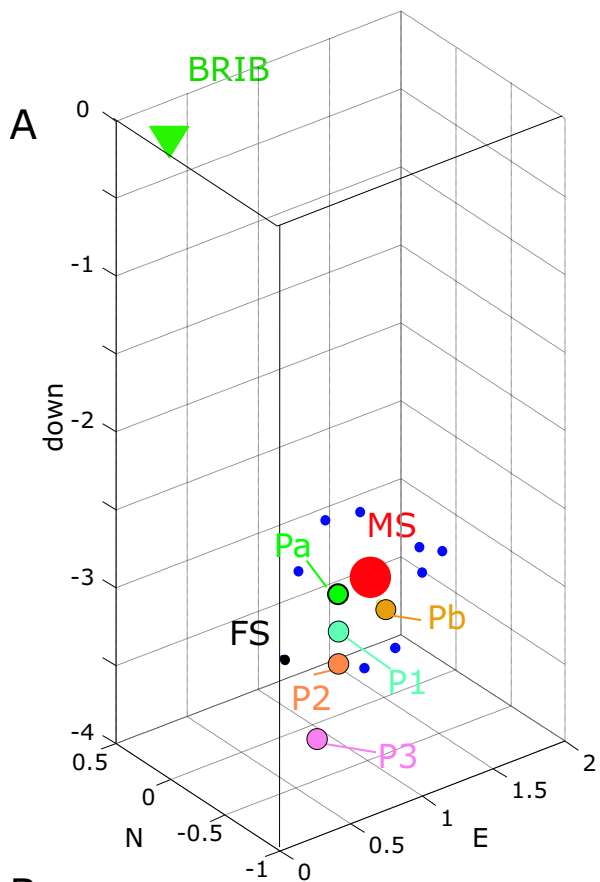
Most events in the Orinda sequence, like the MS, have classically simple waveforms, a single P pulse followed by a single S pulse (Figure 2.28A). However, many earthquakes of all sizes exhibit one of two types of complexity. In one type, several events of similar size occur within a very short interval, as a sort of "rapid-fire" burst (Hill *et al.*, 1990, Asch *et al.*, 1997). In the second type of complexity, more than one P-wave pulse arrives before the first S-wave (Figure 2.28 B, C). Using measurements from waveforms of a few events, we estimate the source location of the P-pulse of each subevent from its polarization (Plesinger *et al.*, 1986, Abercrombie, 1995) and its  $t_{s-p}$ .

As with the other events of the sequence,  $t_{s-p}$  values for the subevents lie between 0.58 and 0.7 s, and they are located within the cluster. Figure 2.29A shows as an example the locations of three subevents from the event in Figure 2.28B (P1, P2 and P3) and two subevents from the event in Figure 2.28C (Pa and Pb) in relationship to the mainshock (MS), the  $M_d$  2.5 foreshock (FS) and several aftershocks (small dots), as well as to the station BRIB. The distances are given in km. The table (Figure 2.29B) gives the spatial separation of the subevents and the intervals between them. It also gives the ratio of the subevent spacing to the values of  $v_P$  (4.1 km/s) and  $v_S$  (2.3 km/s) assumed for the source volume. The intervals between the subevents are consistent with the propagation of rupture at speeds around  $0.8 v_S$ .

### 2.14.3 Summary and Perspectives

Although the earthquakes of the Orinda sequence are small, their study contributes to understanding and defining earthquake hazard in Northern California. They occurred in an otherwise seismically quiet region of the Bay Area, between the Hayward and Calaveras faults. The only previous recent seismicity in the area occurred as a brief sequence in 1977 (Bolt *et al.*, 1977). Thus, this sequence offers the opportunity to learn more about

the seismicity and seismic hazard between the two faults. In addition, the many aftershocks provide data for improving the velocity structures between these two major faults, particularly at shallow levels. cursory comparisons between the Orinda and other nearby sequences with similarly sized mainshocks suggest that the Orinda sequence has produced many more aftershocks. Learning more about the physics at these earthquakes' sources will help understand why this is true.



**B**

Subevent-Pair	$\Delta t_p$ [s]	$\delta$ [km]	$\delta/v_p$ [s]	$\delta/v_s$ [s]	$(\delta/v_s)/\Delta t_p$
P2-P1	0.092	0.195	0.048	0.085	0.92
P3-P2	0.259	0.465	0.113	0.202	0.78
Pb-Pa	0.25	0.363	0.089	0.158	0.63

Figure 2.29: Locations (from P-wave polarization and  $t_{s-p}$ ) of the  $M_L$  2.5 foreshock (FS), the mainshock (MS) and the P-wave pulses of the largest aftershock (P1, P2, P3) and a small aftershock exhibiting complexity (Pa, Pb).

seismicity on the San Andreas fault in southern California. *J. Geophys. Res.*, 100, 24003-24014, 1995.

Asch, G., K. Wylegalla, M. Hellweg, D. Seidl, and H. Rademacher, Observations of Rapid-Fire Event Tremor at Lascar Volcano, Chile, *Annali di Geofisica*, 39, p. 273-282, 1996.

Bolt, B., J. Stifler and R. Uhrhammer. The Briones Hills Earthquake Swarm of January 8, 1977, Contra Costa County, California. *Bull Seismol. Soc. Am.*, 67, 1555-1564, 1977.

Hill, D.P., W.L. Ellsworth, M.J.S. Johnston, J.O. Langbein, D.H. Oppenheimer, A.M. Pitt, P.A. Reasenberg, J.L. Sorey and S.R. McNutt, The 1989 Earthquake Swarm Beneath Mammoth Mountain, California, An Initial Look at the 4 May through 30 September Activity, *Bull. Seis. Soc. Am.*, 80, 325-339, 1990.

Plesinger, A., M. Hellweg and D. Seidl, Interactive high-resolution polarization analysis of broadband seismograms. *J. Geophysics*, 59, p. 129-139, 1986.

#### 2.14.4 References

Abercrombie, R.E., Earthquake locations using single-station deep borehole recordings: Implications for micro-

## 2.15. Using 1906 Simulations to Assess Performance of Northern California Networks

Margaret Hellweg, Peter Lombard, John Boatwright (USGS), Howard Bundock (USGS), Hamid Haddadi (CGS)

### 2.15.1 Introduction

Emergency responders depend on real time data products such as earthquakes' locations and their magnitudes. ShakeMaps (Wald *et al* 1996) are also critical tools for estimating the impact of large and great earthquakes on society. These products can only be as reliable as the seismic systems which record and transmit ground shaking. We test the real time ShakeMap capabilities of the seismic networks in Northern California Seismic System (NCSS) (USGS Menlo Park, network code: NC; UC Berkeley, network code BK; the California Geological Survey, network code CE; USGS Strong Motion Program, network code NP). These networks have a large number of freefield strong motion stations; however, only about 160 of them, mostly in the San Francisco Bay Area, report data in real time. Thus only these stations can contribute to initially produced ShakeMaps.

### 2.15.2 ShakeMap Scenarios

Boatwright and Bundock (2005) produced a new Modified Mercalli intensity map in the form of a ShakeMap for the 1906 San Francisco earthquake reviewing all intensities reported in the Lawson report (Lawson *et al*, 1908; Figure 2.30A). We use this as a reference for the quake's actual ground motion to compare with ShakeMaps produced using subsets of the real time strong motion stations in Northern California from the BK, NC and NP networks. Ground motion for each site is taken from Graves (2006) synthetic ground motions for a 1906-type event ( $M_w$  7.8, epicenter 2 mi W of San Francisco, rupture from San Jose to Cape Mendocino) and fed into ShakeMap.

Figure 2.30B shows the ShakeMap which would result if all 160 real time stations in the NCSS were able to transmit their data reliably to the datacenter where the ShakeMap is produced. Two things stand out in comparison with Figure 2.30A: The high level of ground shaking around the Bay Area and the extremely low estimate of shaking along the northern segment of the San Andreas Fault, where there are few stations. The latter factor can be somewhat alleviated by introducing the extent of fault rupture (Figure 2.30C). This information may be available within an hour of the quake, either from finite fault inversions or from the distribution of aftershocks. The estimated relatively slow decay of ground motion with distance from the fault is caused by the attenuation relationship currently used in ShakeMap (Boore *et al*, 1997).

Figure 2.30B may be considered a "best case scenario",

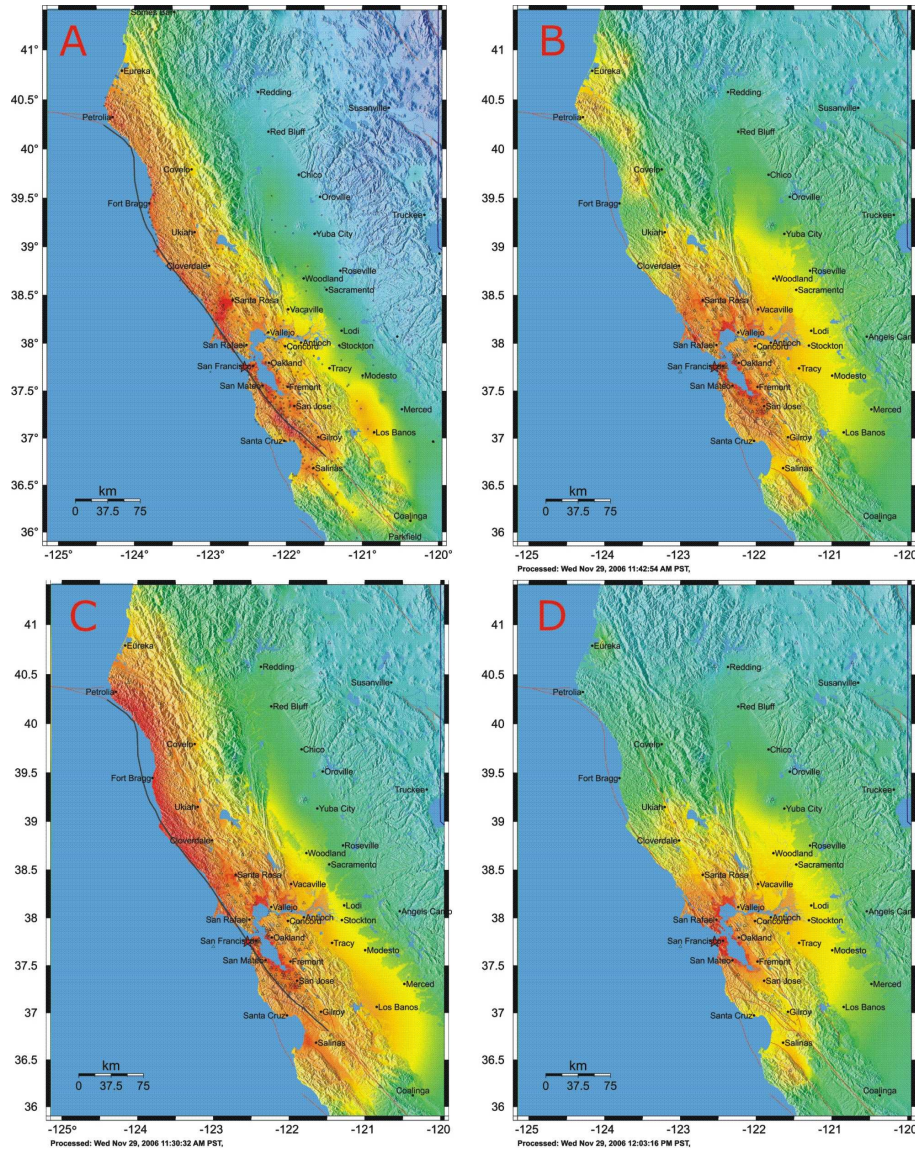
with all real time stations reporting. The 1906 earthquake produced strong shaking. If the data center at the USGS Menlo Park were incapacitated, no data from the NC and NP networks would be available. In this case, the only data to constrain the initial ShakeMap would come from the 27 BK strong motion sites (Figure 2.30D).

### 2.15.3 Conclusions

We simulate the performance of the Northern California Seismic System (networks NC, NP and BK) of the California Integrated Seismic Network for the case of a repeat of the 1906 earthquake to assess its ability to produce reliable ShakeMaps. Among the many factors that influence the robustness of the system are reliability of telemetry from individual stations and nodes, as well as of the data center. Even with the correct location and magnitude for the earthquake and with all 160 real time strong motion instruments reporting ground motions, it is still critical to estimate the fault length to produce a usable ShakeMap.

### 2.15.4 References

- Boatwright, J. and H. Bundock, Modified Mercalli intensity maps for the 1906 San Francisco earthquake plotted in ShakeMap format. *USGS Open-File Report, OF 2005-1135*, 2005.
- Boore, D. M., W. B. Joyner, and T.E. Fumal, Equations for Estimating Horizontal Response Spectra and Peak Accelerations from Western North American Earthquakes: A Summary of Recent Work, *Seism. Res. Lett.*, 68, 128-153, 1997.
- Graves, R., Broadband Ground Motion Simulations for Earthquakes in the San Francisco Bay Region, *Seismol. Res. Lett.*, 77, 275, 2006.
- Lawson, A., G. K. Gilbert, H. F. Reid, J. C. Branner, H.W. Fairbanks, H. O. Wood, J. F. Hayford and A. L. Baldwin, The California Earthquake of April 18, 1906: Report of the State Earthquake Investigation Commission, 1908.
- Wald, D. J., V. Quitoriano, T. H. Heaton, H. Kanamori, C. W. Scriver, and C. B. Worden, TriNet ShakeMaps: Rapid Generation of Instrumental Ground Motion and Intensity Maps for Earthquakes in Southern California, *Earthquake Spectra*, 15, 537-556, 1996



PERCEIVED SHAKING	Not felt	Weak	Light	Moderate	Strong	Very strong	Severe	Violent	Extreme
POTENTIAL DAMAGE	none	none	none	Very light	Light	Moderate	Moderate/Heavy	Heavy	Very Heavy
PEAK ACC.(%g)	<.17	.17-1.4	1.4-3.9	3.9-9.2	9.2-18	18-34	34-65	65-124	>124
PEAK VEL.(cm/s)	<0.1	0.1-1.1	1.1-3.4	3.4-8.1	8.1-16	16-31	31-60	60-116	>116
INSTRUMENTAL INTENSITY	I	II-III	IV	V	VI	VII	VIII	IX	X+

Figure 2.30: *Boatwright and Bundock* (2005) ShakeMap (A) and scenario ShakeMaps for assessing network performance (B-D). (A) The ShakeMap compiled by *Boatwright and Bundock* (2005) from the Lawson report (1908) provides a baseline against which to assess the initial ShakeMaps which would be computed from ground motion measured in a similar earthquake, if it were to occur today. (B) ShakeMap for 160 real time stations in Northern California from the BK, NC and NP networks. The initial ShakeMap would be ready within 10 minutes after an earthquake occurs. The hypocenter and magnitude are assumed to be the same as in 1906, however the length of the fault rupture is not known. (C) For this ShakeMap the same data is used as for (B), but in addition to hypocenter and magnitude, the extent of fault rupture is also used. Strong shaking is now also predicted along the Coast. (D) Maps (B) and (C) represent best cases for real time reporting. If telemetry to and from USGS Menlo Park is interrupted, ShakeMaps from UC Berkeley would be based only on the 27 stations of the sparse BK network.

## 2.16. Scanning of Unusual Seismicity in the Mendocino Triple Junction Region

Aur lie Guilhem, Douglas S. Dreger, and Robert M. Nadeau

### 2.16.1 Introduction

Anomalous seismic activity with wide-ranging behavior has been detected in the vicinity of the Mendocino Triple Junction (MTJ) and offshore transform faults. Among those unusual earthquakes are non-volcanic tremors, repeating earthquakes and slow-rupture or low-stress-drop earthquakes. These unusual events, together with 'typical' earthquakes, provide clues regarding the mechanics of faulting in the offshore region. One difficulty in the study of seismicity of the region is that the events located far offshore may go undetected or they may have poor locations with large uncertainty. Another difficulty is that there is a class of events that have either low stress drop or have slow rupture processes that make typical detection difficult. We present here preliminary results of a low-frequency continuous waveform scanning method to detect and locate events in the offshore region as well as compute the seismic moment tensor.

### 2.16.2 Unusual seismic events in Mendocino area

The Mendocino Triple Junction is a structurally and seismically complex region where the North American, the Pacific and the Juan de Fuca-Gorda plates intersect. The triple junction at Mendocino is the junction of the northern part of the San Andreas fault, the Cascadia subduction zone and the Mendocino Transform fault. Several unusual seismic events have been recorded in this area, including non-volcanic tremors, repeating earthquakes and slow/low-stress-drop earthquakes (Figure 2.31).

Thus far we have concentrated our efforts on the slow earthquakes or low-stress-drop earthquakes. This class of events is identified by a large discrepancy ( $\geq 0.5$ ) between the moment magnitude  $M_w$  and the local magnitude  $M_L$ , where  $M_w$  is larger. Based on the Berkeley Moment Tensor catalog, at least 18 slow earthquakes have occurred and have been recorded between 1992 to the present with a  $M_w$  range between 4.0 and 6.8. Smaller slow earthquakes may have occurred, but they have not been detected. Analyses show that some of the slow earthquakes have stress drops of 0.4 bar when the stress drop for a normal earthquake is between 10 and 100 bars. Whereas the corner frequency of a  $M_L \approx M_w \approx 4$  earthquake is about 2Hz, for a slow event ( $M_L=4$  and  $M_w=5$ ) the corner frequency is on the order of 0.1Hz, which is more appropriate for a  $M_w 6.5+$  event.

A catalog of relocated events shows a sequence of four

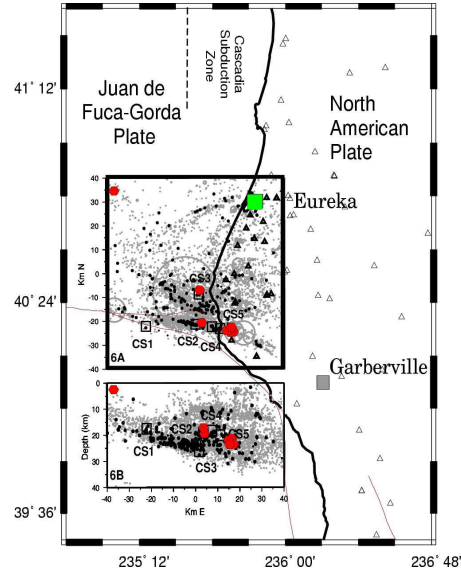


Figure 2.31: Map of the unusual seismic activity in Mendocino region. The green square is a BDSN station (JCC), the triangles are NCSN stations. Seismicity (gray points) has been relocated with hypoDD using the NCSN stations. Red circles are few slow earthquakes and small black circles show repeating earthquake seismicity.

low-stress-drop earthquakes which occurred in 1997 and 1999. All have a very similar location in latitude and longitude, but their depth varies in a range of 4 km. Because they are located at the same place on the Mendocino transform fault and also because they have about the same moment magnitude, these four events may appear as potential repeating slow-earthquakes.

Using a cross-correlation analysis with two of these four events as references, we have scanned about 6 years, between 2000 and the end of 2006, of continuous broadband data recorded at four stations of the Berkeley network (ORV, MOD, WDC and YBH) and filtered between 0.02 and 0.05 Hz. We run the cross-correlation analysis for the three components at each station and we study all the hits giving at least 60% of similarities with the references and seen at, at least, 3 stations.

We obtained a large number of hits due to large teleseisms. Because of the large S-P arrival time of the teleseisms, a positive result in the cross-correlation occurred for either the P-waves or S-waves. With this method, we have not detected any additional slow earthquakes in the

Mendocino transform fault that we did not know about. This result may also be due to the choice made in the references.

### 2.16.3 Detection, localization and moment tensor solution for an offshore slow earthquake

Previous studies (Dreger *et al.*, 1998 and Tajima *et al.*, 2002) have investigated the capability of a sparse broadband network, the Berkeley Digital Seismic Network (BDSN), at monitoring a region located outside the network, and tested the feasibility of a new automated moment-tensor determination system that continuously monitors seismic waveforms from the same network.

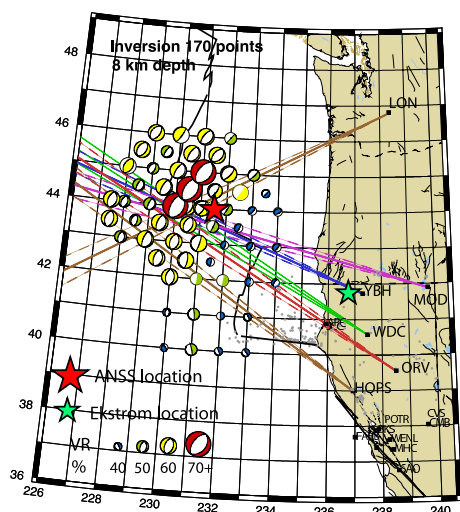


Figure 2.32: Low-frequency study of an offshore slow earthquake. Association of azimuthal rotation and seismic moment tensor grid search in the localization of an unusual event. The lines indicated the rotation axes plus or minus 3 degrees for each station.

Before using the moment and scanning method for events in Mendocino Triple Junction region, we need to test its feasibility for a recorded slow-earthquake. We have decided to apply it to a slow/low-stress drop event in December 2000 extracted from Goran Ekström’s catalog. Ekström analysed and located it onshore in Northern California (Figure 2.32). However a first triangulation analysis of seismic records between 0.02 and 0.05 Hz from a few stations of the BDSN network (YBH, MOD, WDC, ARC and ORV) has given an offshore location. Despite the difficulty of identifying the body waves, analyses of P and Rayleigh wave particle motion have been done and were used in order to determine the azimuth between the seismic stations and the event. Such an azimuthal analysis has confirmed an offshore location (lines from seismic stations on Figure 2.32).

However, the uncertainty on location that we obtained is relatively large and depends on the quality of the stations used. We have completed our research by a grid search analysis of the seismic moment tensors using ORV, MOD, WDC and YBH to quantitatively locate the earthquake using the variance reductions from the computation. By this frequency waveform scanning and moment tensor grid search we are able to define a smaller area for the location of the event around the ridge segment between the Pacific and Gorda plates. Finally, the ANSS catalog location is similar to our location using this method, suggesting the potential success of a low-frequency continuous waveform scanning in locating events in the offshore region, as well as computing the seismic moment tensor. We also have to mention here that the moment tensor solutions indicate a high CLVD component with a normal mechanism which could be consistent with an explosion on the ridge segment. The ANSS catalog gives a  $M_b$  4.7 and a  $M_s$  3.9. With our method we have found a  $M_w$  between 4.4 and 4.5 for the best moment tensor solutions.

With the goal of better constraining the location and mechanism of the offshore events, it would be important to consider a better coverage of broadband stations in the future. In the case of the earthquake in 2000, very few broadband stations were continuously recording. Some part of the analysis has considered the records at a station in Washington state, LON station (Figure 2.32). Today, many more high quality stations are operating in many places along the coast and can be easily used.

### 2.16.4 Conclusion

We plan to implement the low-frequency continuous moment tensor scanning method in the Mendocino region. Such a method would improve the response time for rapid characterization of earthquake sources and tsunami hazard from offshore events.

### 2.16.5 Acknowledgements

Part of this work is supported by the National Science Foundation (NSF) grant NSF-EAR-0537641.

### 2.16.6 References

- Dreger, D.S., R. Uhrhammer, M. Pasyanos, J. Franck, and B. Romanowicz (1998), Regional and Far-Regional Earthquake Locations and Source Parameters Using Sparse Broadband Networks: A test on the Ridgecrest Sequence, *Bulletin of the Seismological Society of America*, vol. 88, 6, 1353–1362.
- Tajima, F., C. Megnin, D.S. Dreger, and B. Romanowicz (2002), Feasibility of Real-Time Broadband Waveform Inversion for Simultaneous Moment Tensor and Centroid Location Determination, *Bulletin of the Seismological Society of America*, vol. 92, 2, 739–750.

## 2.17. ElarmS AlertMap: ShakeMap-Based Analysis of Earthquake Early Warning Results

Gilead Wurman, Richard M. Allen and Peter Lombard

### 2.17.1 Introduction

Earthquake Early Warning (EEW) efforts at the Berkeley Seismological Laboratory have recently expanded to become part of a large statewide effort involving Caltech, SCEC, the USGS and Berkeley to evaluate EEW algorithm performance in California. As part of this effort we have been developing several diagnostic tools to assess the performance of the ElarmS EEW methodology being developed at UC Berkeley. One of these tools incorporates elements of ShakeMap (Wald *et al.*, 2005) to generate second-by-second maps of predicted shaking based on data available to ElarmS in that second. We term these products AlertMaps.

These maps are very useful in evaluating the overall performance of ElarmS (and potentially other EEW algorithms) because they provide an intuitive geospatial representation of the availability of data and the behavior of the ElarmS methodology at each point in time. We discuss the technical aspects of generating AlertMaps, and present several snapshots of the AlertMap generated for the 20 July 2007  $M_w$  4.2 Oakland Earthquake.

### 2.17.2 Generating ElarmS AlertMaps

Since February of 2006 we have been automatically executing the ElarmS algorithm for every event of  $M \geq 3$  in northern California (Wurman *et al.*, 2007). As this processing is performed without human input, we refer to the procedure as Non-Interactive (NI) processing. We currently produce AlertMap output as part of the NI processing, allowing us to evaluate the performance of ElarmS for every event, a task that was much more difficult before the development of the AlertMaps.

In the NI processing procedure, ElarmS produces plain-text output once per second for 60 seconds beginning at the event origin time. The output contains all the data available to ElarmS in that second, including peak ground motion observations for each station, as well as station triggers and associated parameters such as maximum predominant period ( $\tau_p^{max}$ ) and peak velocity or displacement ( $P_{d/v}$ ) for that station and channel. The output also includes the event information (location, origin time, magnitude and other metadata) for each event associated from the individual station data.

The AlertMap output is entirely derived from this plain-text timeslice data, which is converted to AlertMap output via a series of perl scripts. The first of these digests the ElarmS text output at each second and converts it to XML files formatted for use by ShakeMap (Wald *et*

*al.*, 2005). A ShakeMap subroutine then executes for each second of output, producing a raster of ground motion predictions on a regular grid of approximately  $2.5^\circ$  lat by  $4.2^\circ$  lon around the estimated epicenter of the event. In addition, ShakeMap produces an XML file of predicted ground motion at just under 400 broadband stations of the NCSN and BDSN networks. All these ground motion predictions are based on the event location and magnitude, as well as any observations of actual peak ground motion available in each second. Using present computing resources, this step takes approximately 10 seconds to produce a one second timeslice. Reducing this processing time is a matter both of dedicating more computing re-

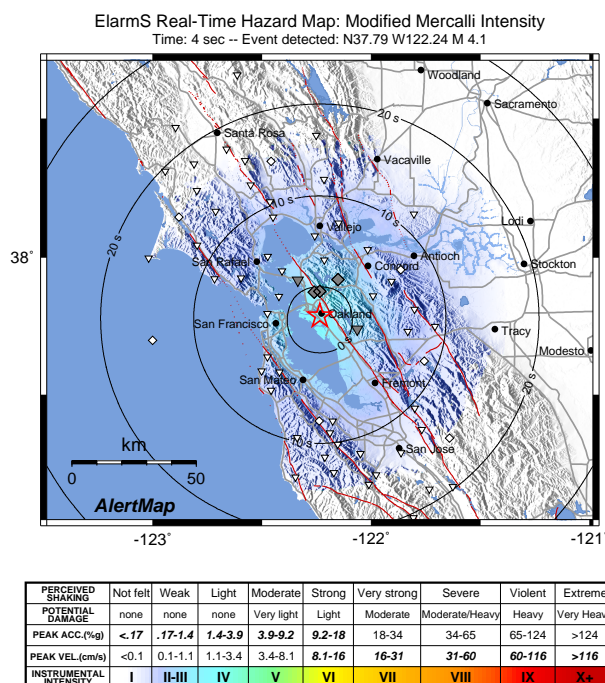
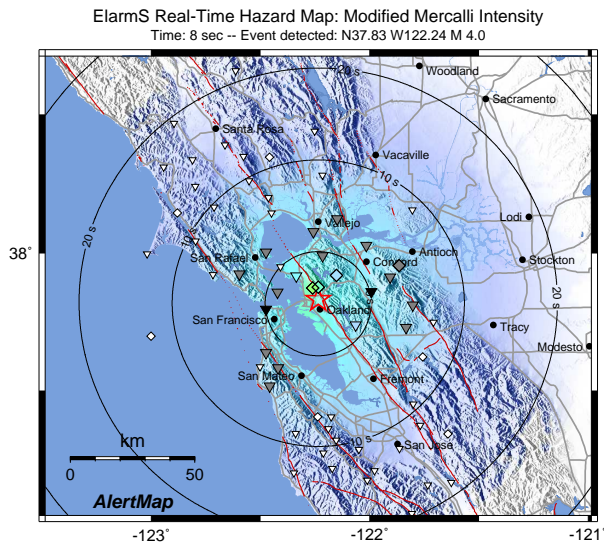


Figure 2.33: AlertMap frame for the 20 July 2007  $M_w$  4.2 Oakland earthquake, at 4 seconds after event origin. Color scale represents predicted MMI according to the scale at bottom. Circular contours represent time until onset of peak ground motion in seconds, based on a moveout of 3.75 km/s. Triangles represent strong-motion accelerometer stations, inverted triangles represent broadband velocity stations, and diamonds represent collocated installations. Larger grey stations have reported triggers at this time.



PERCEIVED SHAKING	Not felt	Weak	Light	Moderate	Strong	Very strong	Severe	Violent	Extreme
POTENTIAL DAMAGE	none	none	none	Very light	Light	Moderate	Moderate/Heavy	Heavy	Very Heavy
PEAK ACC.(%g)	<.17	.17-1.4	1.4-3.9	3.9-9.2	9.2-18	18-34	34-65	65-124	>124
PEAK VEL.(cm/s)	<0.1	0.1-1.1	1.1-3.4	3.4-8.1	8.1-16	16-31	31-60	60-116	>116
INSTRUMENTAL INTENSITY	I	II-III	IV	V	VI	VII	VIII	IX	X+

Figure 2.34: AlertMap for the Oakland event at 8 seconds after origin time. Black stations are those currently experiencing peak ground motions, and colored stations have reported peak ground motions according to the scale at bottom.

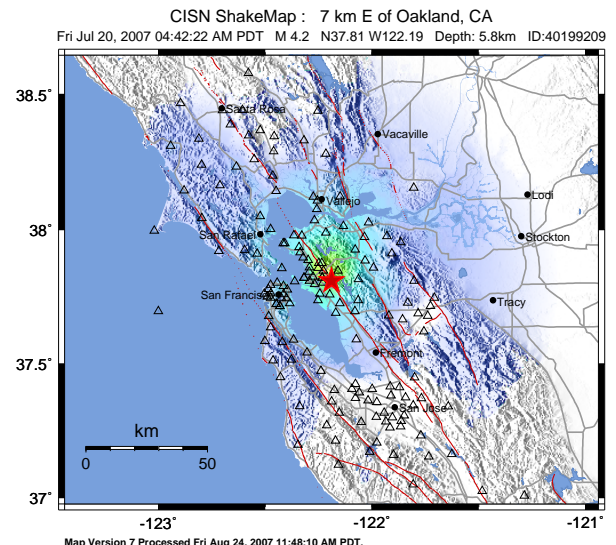
sources to the problem, and of simplifying the ShakeMap procedure and optimizing it to run in the minimum possible time.

When the ground motion grid files are available for all 60 seconds (less than 60 seconds if the event was not detected immediately) a script generates a Postscript map for each second, representing all the data and event parameters available in that second. Sixty of these maps are combined to produce an animation which presents the performance of ElarmS in an intuitive geospatial and temporal manner.

### 2.17.3 The 20 July 2007 Oakland Earthquake

On 20 July 2007 a  $M_w$  4.2 earthquake occurred in Oakland, CA and was detected by the ElarmS NI processing. Initial event detection occurred 3 seconds after event origin, and the first magnitude estimate of M 4.1 was available one second later, or 4 seconds after origin. The magnitude estimate over the following 10 seconds varied between 4.0 and 4.3, eventually stabilizing on M 4.2 15 seconds after event origin.

Figure 2.33 shows the AlertMap at 4 seconds after origin, the time of the first magnitude estimate of M 4.1. Note the magnitude and location are recorded in the title



PERCEIVED SHAKING	Not felt	Weak	Light	Moderate	Strong	Very strong	Severe	Violent	Extreme
POTENTIAL DAMAGE	none	none	none	Very light	Light	Moderate	Moderate/Heavy	Heavy	Very Heavy
PEAK ACC.(%g)	<.17	.17-1.4	1.4-3.9	3.9-9.2	9.2-18	18-34	34-65	65-124	>124
PEAK VEL.(cm/s)	<0.1	0.1-1.1	1.1-3.4	3.4-8.1	8.1-16	16-31	31-60	60-116	>116
INSTRUMENTAL INTENSITY	I	II-III	IV	V	VI	VII	VIII	IX	X+

Figure 2.35: ShakeMap produced by USGS for the Oakland event. Color scale represents observations of MMI at stations (triangles) and is interpolated for all points between stations.

of the map. The color scale represents the predicted modified Mercalli intensity (MMI) at all points based only on the event location and magnitude. At this time no stations have reported peak ground motions, so no bias correction has been applied to the empirical ground motion prediction equations (*Newmark and Hall, 1982; Boore et al., 1997; Wald et al., 1999; Boatwright et al., 2003*). The grey symbols represent stations which have reported triggers at this time, and the circular contours show the time in seconds until the onset of strongest ground motions (assuming a moveout speed of 3.75 km/s). At this time the epicenter location is somewhat south of the true location, and by looking at the map it becomes apparent that this is due to the fact that only stations to the north of the event have triggered at this time, leading to temporarily poor azimuthal coverage for this time period. This problem is eliminated in the following few seconds.

By the time 8 seconds have passed since the origin, the location has stabilized and several stations have reported observations of peak ground motion (Figure 2.34). The stations which have reported peaks are color-coded according to the corresponding MMI in this map, while stations currently experiencing peak ground shaking are filled in black. The observations of peak ground motion are used to compute a bias to the ground motion prediction equations, altering the predicted ground motions around the epicenter. Note that Oakland has already

experienced peak ground motion (in fact it had already experienced the peak even 4 seconds after the origin), and San Francisco is just beginning to experience peak ground motion. However, much of the remaining Bay Area receives as much as 10 to 15 seconds warning. We find that the performance of ElarmS depends primarily on the density and distribution of stations around the source, so that the warning time for an event of this size would be comparable to that for a larger event ( $M_w \sim 7$ ) if it were to nucleate in the same area.

An additional benefit to using ShakeMap algorithms to generate AlertMaps is this makes direct comparison between ElarmS predictions and the actual ShakeMap for each event. Figure 2.35 shows the ShakeMap for this event produced by USGS. A comparison between the ShakeMap and the AlertMap frames shows that even the first available ground motion predictions (Figure 2.33), which are based entirely on the event location and magnitude, are very similar to the observations shown in the ShakeMap. The availability of actual peak ground motion observations in Figure 2.34 helps to refine these predictions further.

## 2.17.4 Conclusions

We are currently generating an animated AlertMap for the first 60 seconds of each event of  $M \geq 3$  in northern California. These AlertMaps allow us to assess simply and quickly the performance of ElarmS for each of these events. The information presented in these maps is organized in an intuitive geospatial manner which is immediately familiar to users of ShakeMap, allowing for easy direct comparison between ElarmS predicted ground motions and actual observed ground motions represented in the regular ShakeMap product.

## 2.17.5 Acknowledgements

We thank Dave Wald for helpful discussions relating to ShakeMap. This work was funded by USGS/NEHRP Grants 05HQGR0074 and 06HQAG0147.

## 2.17.6 References

Boatwright, J., H. Bundock, J. Luetgert, L. Seekins, L. Gee, and P. Lombard, The dependence of PGA and PGV on distance and magnitude inferred from northern California ShakeMap data, *Bull. Seismol. Soc. Am.*, *93*, 2043-2055, 2003.

Boore, D.M., W.B. Joyner, and T.E. Fumal, Equations for estimating horizontal response spectra and peak accelerations from western North American earthquakes: A summary of recent work, *Seismol. Res. Lett.*, *68*, 128-153, 1997.

Newmark, N.M., and W.J. Hall, Earthquake spectra and design, *Geotechnique*, *25*, 139-160, 1982.

Wald, D.J., V. Quitoriano, T.H. Heaton, and H. Kanamori, Relationship between peak ground acceleration, peak ground velocity, and modified Mercalli intensity for earthquakes in California, *Earthquake Spectra*, *15*, 557-564, 1999.

Wald, D.J., B.C. Worden, V. Quitoriano, and K.L. Pankow, ShakeMap®Manual: Technical manual, users guide, and software guide, *Tech. Methods 12-A1*, U.S. Geol. Surv., Reston, VA, 2005.

Wurman, G., R.M. Allen, and P. Lombard, Toward earthquake early warning in northern California, *J. Geophys. Res.*, *112*, B08311, doi:10.1029/2006JB004830, 2007.

## 2.18. Parkfield-Hollister Electromagnetic Monitoring Array

Karl Kappler, H. Frank Morrison, Gary D. Egbert

### 2.18.1 Introduction

The primary objective of the UC Berkeley electromagnetic (EM) monitoring array is to identify EM fields that might be associated with earthquakes. For an overview of the sites and instruments see *Kappler et al. 2006*. We have continued to analyze the data from the Parkfield-Hollister (PKD-SAO) electromagnetic monitoring array taken during the four-year time window January 2002 to December 2005. We stress that although the data have been collected since 1996, large gaps in data acquisition due to lack of funding for array maintenance, together with incomplete documentation of when array sensors were swapped out and/or repaired, has made it difficult to examine small variations in parameters derived from array data. The focus this year has been on identifying those components of the EM fields observed which are coherent with natural micropulsations of earth's magnetosphere. The residuals obtained by removing this known natural source reflect the EM activity which is incoherent with the dominant natural fields. The method of separation is based upon projecting the observed data onto the eigenvectors of the robust estimated spectral density matrix (SDM).

### 2.18.2 Data Analysis

We point out that there are several regions in our four year window where robust estimates of the SDM could not be calculated, as this procedure [*Egbert 1997*] relies upon having at least two observatories operating; on several occasions either one or both of the observatories were not operational, or at least one group of channels (electric or magnetic) at a single site were down. Since there are many disjoint time windows to analyze, and our primary interest is identifying any variation in EM fields which may possibly be associated with the M6 Parkfield 2004 earthquake, we focused first on the days [137-299], 2004. This 163-day window features no swapping of instruments, auxiliary power supplies, or data loggers. Signal-to-noise ratios for all primary array channels are very good, with the exception of Hy at SAO, which was slightly degraded. This slight degradation did not significantly impact our robust SDM estimates. The SDM is estimated in each frequency band from a multivariate time-series of band averaged Fourier coefficients, having dimension  $N \times M$ , when  $N$  is the number of array channels, and  $M$  is the number of time windows which were Fourier transformed out of a day's data (typically 898 for Periods 4-30s). The actual robust SDM estimate is calculated as per the iterative method of *Egbert 1997*, resulting in a

collection of 25 covariance matrices, (one matrix for each frequency band) for each of our 163 days. In order to compress and display this data, we reduce each SDM to a list of its four dominant eigenvalues. These are calculated in units of signal to noise ratio. For all data presented in this summary we consider the array to be comprised of the eight primary channels, 100m electrodes and horizontal magnetometers. Figure 2.36 is a plot of these daily eigenvalues.

Since the dominant eigenvector on one day is not necessarily collinear, or even approximately collinear with the dominant eigenvector calculated on some other day, Figure 2.36 is subject to variation resulting from the fact that it was made by simply ordering the eigenvalues in descending fashion. The lack of guaranteed day-to-day continuity in eigenvalues suggests that a time series plot obtained by plotting daily eigenvalues of the SDM is difficult to interpret physically. This motivates us to look at the prevailing modes of the eigenvector decomposition. A two-week window comprising days 137-151 was sub-selected, and each day's dominant eigenvectors were averaged according to the ranks of their corresponding eigenvalues. In this we obtain four dominant average modes. These modes are simply linear combinations of array channels, which tend to exhibit coherence, on average. By calculating daily the power observed in each mode, we obtain the following time series:

It is apparent from Figure 2.37 that the third eigenvalue shows a weekly period, implying that most of the power in this mode can be attributed to cultural noise. At least some of the unusual noise in the highest frequency band of the third eigenvalue seems to have dispersed into the fourth, and possibly other average modes. This may suggest that signal of this period is not coherent with typical cultural noise. The two dominant modes of the SDM are normally associated with the plane-wave natural micropulsation sources [*Egbert 1989*]. We suggest that any signals associated with seismic activity along the fault – should they exist – are unlikely to be coherent with the MT source-field. As a method of looking more closely at the recorded time-series, we calculate residual fields by subtracting off the contributions of these natural fields. We select a method of residual calculation that uses sensors at a remote site to predict fields at PKD, where the intersite transfer function itself is calculated as an average over the two week interval (days 137-151). Our residual calculation intentionally uses no Parkfield data, except in the transfer function calculation, which is performed over a time-window distant from the earthquake, ensuring that the residuals will not unintentionally iden-

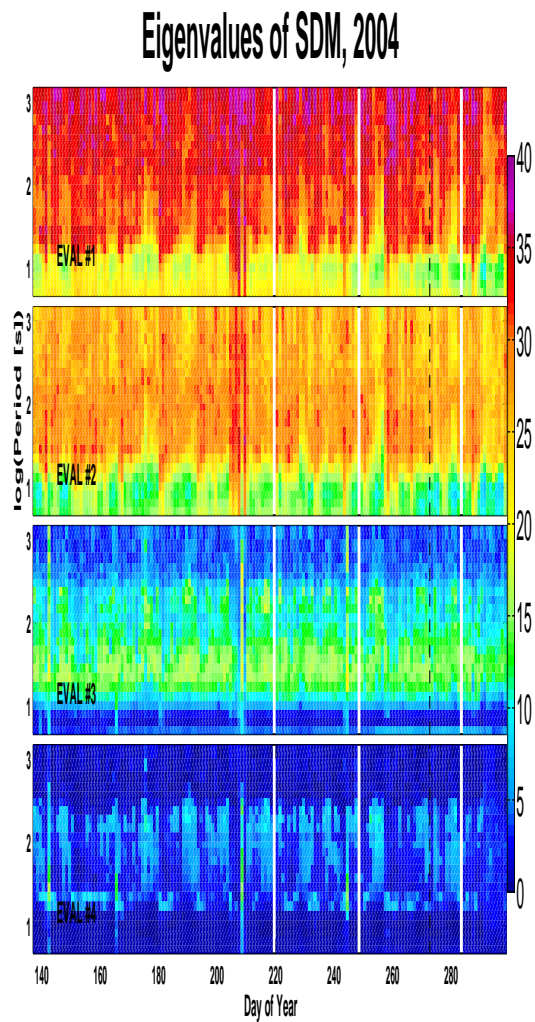


Figure 2.36: Eigenvalues of the SDM, the y-axis is  $\log(\text{Period (s)})$ , and the x-axis is day-of-year. The color bar represents units ( $10 \cdot \log_{10}(\text{SNR})$ ). Note the variation in amplitude in the highest frequency of the third eigenvalue.

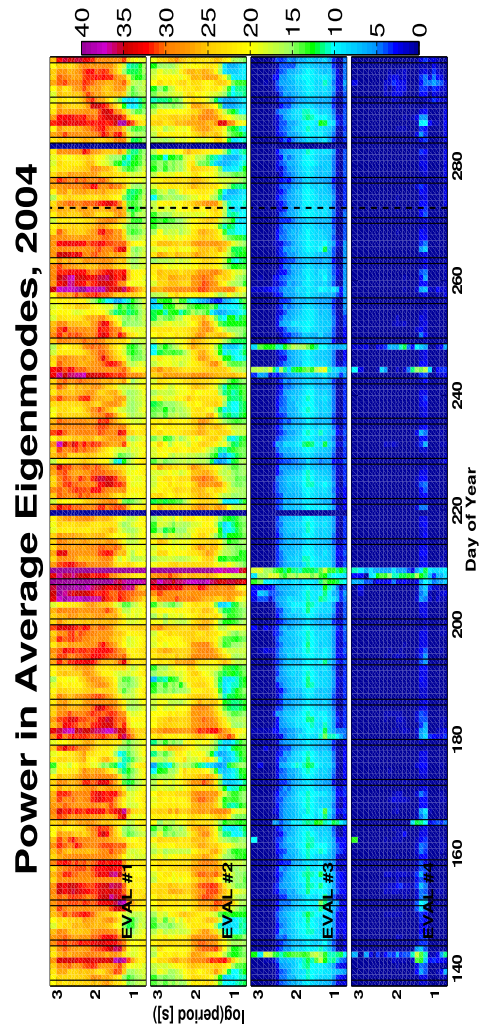


Figure 2.37: Power observed in dominant modes of the SDM. Note the large increase in power around days 205-210, which correspond to a major solar storm. Sundays are marked with thin black vertical lines, and the earthquake with the thick black dashed line

tify the signature of an EM process at work only at PKD by lumping such a signature in with the predicted signal. We use a method based on the average eigenmodes calculated from the SDM, which is essentially a method of similar triangles. Recall that an eigenvector of the SDM is simply a linear combination of array channels.

$$EV_k = \sum_{i=1}^{N_{PKD}} p_{i,k} P_i + \sum_{i=1}^{N_{SAO}} s_{i,k} S_i \quad (2.1)$$

where  $s_{i,k}$ ,  $p_{i,k}$  are scalar coefficients for the  $k^{th}$  eigenmode, and  $P_i$ ,  $S_i$  are array data for SAO and PKD respectively. The index of summation  $N_{site}$  reflects the number of channels operating at the site. Numeric values for the  $p_{i,k}$  and  $s_{i,k}$  are fixed during the calculation of the  $k^{th}$  average eigenmode, and yield the fixed PKD to SAO component ratio:

$$PS_k = \frac{\sum_{i=1}^{N_{PKD}} p_{i,k}^2}{\sum_{i=1}^{N_{SAO}} s_{i,k}^2} \quad (2.2)$$

Now choosing an eigenmode, i.e. fixing  $k$  (we thus omit further reference to  $k$ ), we can project actual SAO data onto the chosen mode, observing a set of coefficients:

$$\sum_{i=1}^{N_{SAO}} [s_i^{obs}]^2 \quad (2.3)$$

We then predict the PKD data assuming the existence of a complementary vector, collinear with  $\sum p_i P_i$  obeying the ratio:

$$\frac{\sum_{i=1}^{N_{PKD}} p_i^2}{\sum_{i=1}^{N_{SAO}} s_i^2} = \frac{\sum_{i=1}^{N_{PKD}} [p_i^{pred}]^2}{\sum_{i=1}^{N_{SAO}} [s_i^{obs}]^2} \quad (2.4)$$

By solving for the predicted PKD signal for the first two eigenmodes, and subtracting from the recorded PKD data, we obtain residual fields.

Figure 2.38 illustrates the signal (predicted) and residual fields for the sensor Hy (oriented N-S) at PKD for three months around the earthquake. We choose to show the band at a period of 85s because this period is in the midst of the band where magnetic anomalies were reported by *Fraser-Smith et al.* We see that no significant variation is evident in either the natural fields or in the local residual fields.

### 2.18.3 Future Work

This year we plan on a statistical analysis of the residuals for all bands over the 163 day time window. Any bands showing statistically significant variation around the time of the earthquake will be expanded in the time window to a four-year analysis in order to better gauge the time-scale on which the outliers are significant. Special attention will be paid to the residuals in the so-called MT "dead-band", near our high frequency cutoff. Since

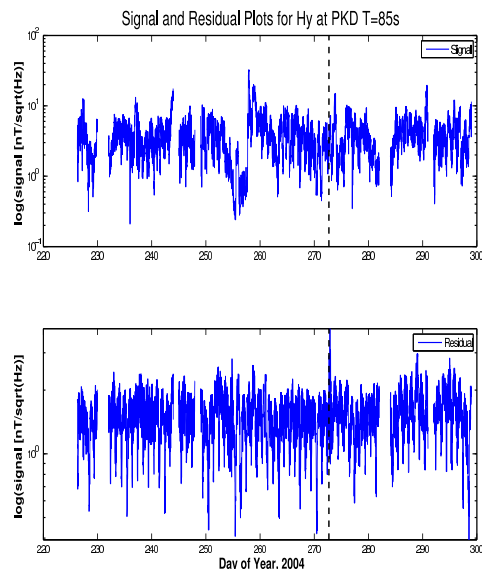


Figure 2.38: Magnetic Fields Calculated from SAO (a) and Residual Magnetic fields from subtracting predicted fields from observed data (b)

there is very little natural signal or cultural noise in this band (Figures 2.36 and 2.37), it would be the band in which anomalous signals ought to stand out most readily if they were present.

### 2.18.4 References

- Egbert, G.D., Booker, J.R., (1989), Multivariate Analysis of Geomagnetic Array Data 1. The Response Space, *Journal of Geophys. Res.* V94 No.B10 pp14227-14247
- Egbert G. D. (1997), Robust multiple-station magnetotelluric data processing, *Geophys. J. Int.* 130 pp475-496
- Fraser-Smith, A. C., Bernardi, A., McGill, P. R., Ladd, M. E., Helliwell, R. A., and Villard, O. G., 1990, Low-frequency magnetic field measurements near the epicenter of the Ms 7.1 Loma Prieta Earthquake, *Geophys. Res. Lett.*, 17, 1465-1468
- Kappler, K., Egbert, G.D., Morrison, H.F., Parkfield-Hollister Electromagnetic Monitoring Array, *BSL Annual Report*, 2006
- Kappler, K. Egbert, G.D., Morrison, H.F., Long-Term Analysis of ULF electromagnetic fields at Parkfield CA, *in progress*

## 2.19. Creep on the Rodgers Creek Fault Identified Using PS-InSAR

Gareth Funning, Roland Bürgmann and Alessandro Ferretti (TRE, Milan)

### 2.19.1 Introduction

Deformation in the northern San Francisco Bay Area is dominated by a series of sub-parallel strike-slip faults. Existing GPS observations provide some constraint on the slip rates of these faults, however these have only limited resolution for resolving shallow fault behavior, such as brittle creep. We use Permanent Scatterer InSAR (PS-InSAR) data to dramatically increase the density of surface deformation observations. We find a discontinuity in observed surface velocities across the Rodgers Creek fault, around Santa Rosa and further north, consistent with shallow creep at rates of up to 6 mm/yr (Funning *et al.*, 2007). The creeping segments are located in areas of local transtension, suggesting that lowered normal stresses may play a role in the distribution of creep. The existence of creep could significantly reduce expected moment release in future earthquakes on the Rodgers Creek fault, and thus has implications for seismic hazard assessment.

### 2.19.2 Data

For this study we use data acquired by the European Space Agency satellites ERS-1 and ERS-2 between 1992 and 2001. The North Bay region is covered in its entirety by a single descending track scene (track 342, frame 2835), and in total 30 useable images were acquired over this frame in the study interval. Permanent scatterers (PS) were identified using the method of Ferretti *et al.* (2001), and a best linear line-of-sight (LOS) velocity estimated for each. In total, 71000 PS were identified (Figure 2.39a).

On a regional scale, the velocity field obtained by PS-InSAR shows the deformation due to accumulation of strain on the major strike-slip faults. In Figure 2.39a this is represented by a color change from red to blue from west to east, signifying an eastward increase in velocity of  $\sim 10$  mm/yr towards the satellite. This is consistent with right-lateral shear across the fault system (e.g. Bürgmann *et al.*, 2006). More locally, steps in LOS velocity across faults represent shallow creep on those structures. We can identify such features for the Hayward and, we argue below, Rodgers Creek faults.

### 2.19.3 Estimating creep rate from velocity profiles

In the vicinity of Santa Rosa, we observe a step in velocity across the Rodgers Creek fault. We investigate this feature, which we interpret as representing surface fault creep, by plotting cross-fault profiles through our reduced

PS-InSAR dataset at 5 km intervals (Figure 2.39b,c). To estimate fault offset rates, we fit parallel straight lines to windows of datapoints on either side of the fault, and calculate the separation between them. The gradients of the lines reflect the regional component of deformation, along with any residual error in satellite orbital position, and are used to detrend the profiles. Assuming pure right-lateral strike-slip motion, we then convert the LOS velocities to creep rates, propagating the uncertainties of the measurements through the calculation.

We obtain rates which peak at  $6.0 \pm 0.6$  mm/yr immediately north of Santa Rosa (profile G-G'), and die off to the north and south. It is possible that the southernmost profile (H-H') appears less step-like than when plotted in plan view (Figure 2.39b) due to the fault bend at Santa Rosa. These rates, which represent the averages over an 10 year interval, are comparable with the estimate of 4.3 mm/yr recently obtained from alignment array measurements at site RC1 (Figure 2.39b) which do not overlap in time with our measurements.

### 2.19.4 Discussion

Significant creep is observed over a 25 km zone north of Santa Rosa, but not further south – in our dataset or by other workers, raising the question of the cause of this along-strike change in fault behavior. One potential factor is fault geometry – if slip were transferred eastwards to the Maacama fault, north of Santa Rosa, there would be a  $\sim 8$  km releasing stepover consistent with an unclamping of the Rodgers Creek fault. Further targeted PS-InSAR and GPS studies may allow us to determine where this slip transfer occurs, and thus to quantify the importance of this effect.

### 2.19.5 Acknowledgements

This work was supported by grants from the Department of Energy and the USGS-NEHRP external program. SAR data are copyrighted by the European Space Agency and were obtained via the WInSAR consortium.

### 2.19.6 References

- Bürgmann, R., G. Hilley, A. Ferretti, and F. Novali, Resolving vertical tectonics in the San Francisco Bay area from GPS and permanent scatterer InSAR analysis, *Geology*, 34, 221–224, 2006.
- Ferretti, A., C. Prati, and F. Rocca, Permanent scatterers in SAR interferometry, *IEEE Trans. Geosci. Remote Sensing*, 39, 8–20, 2001.

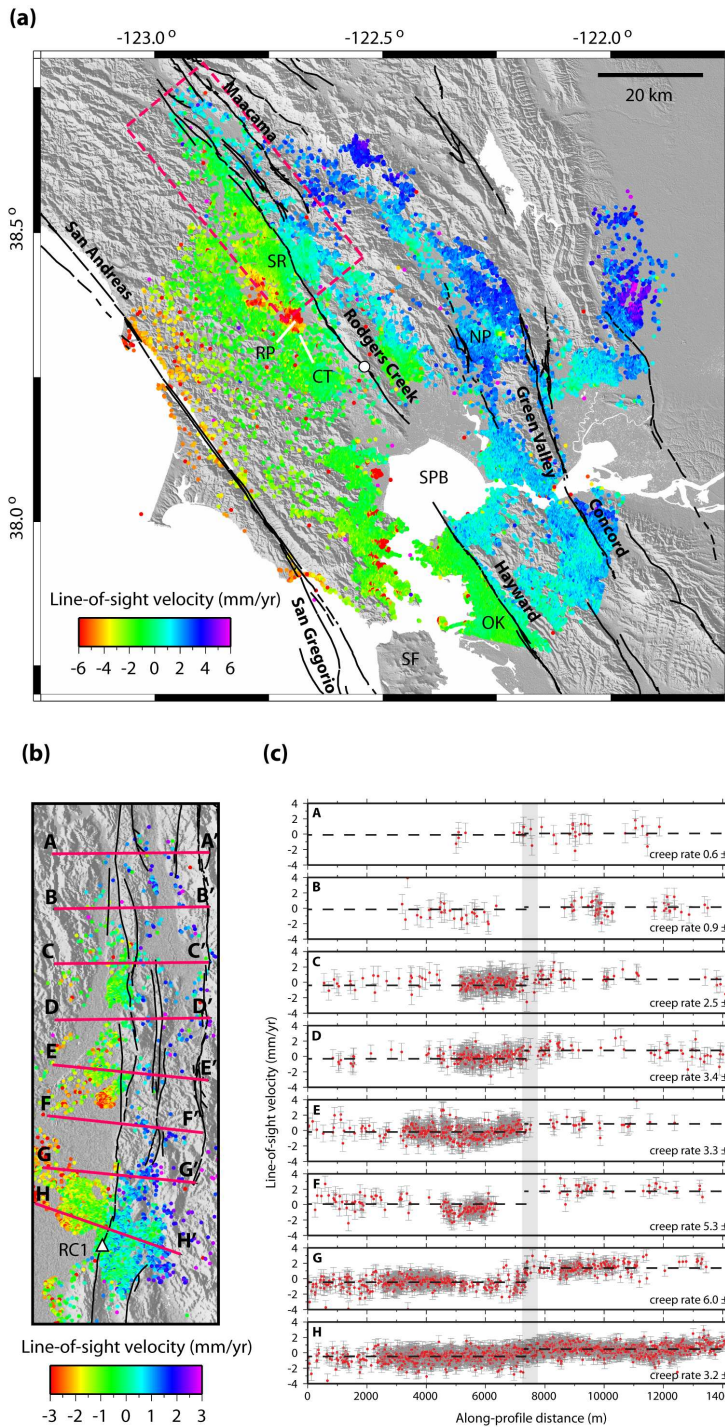


Figure 2.39: PS-InSAR evidence for creep on the Rodgers Creek fault. (a) Regional surface velocity field. Solid lines show mapped active faults. Dashed box shows location of (b). [SR: Santa Rosa, RP: Rohnert Park, CT: Cotati, NP: Napa, SF: San Francisco, OK: Oakland, SPB: San Pablo Bay] (b) Detail of velocities in the Santa Rosa area. Note change in color palette. Locations of 15 km-long fault-perpendicular profiles are shown. White triangle indicates location of alignment array RC1. (c) Profiles of PS-InSAR data across the Rodgers Creek fault near Santa Rosa. Red points signify PS velocity measurements within 2.5 km of the profile line; error bars indicate  $1\sigma$  uncertainties. Black dashed line indicates the best average linear fit to velocities from a range of windows either side of the fault. Gray box indicates the approximate location of the fault.

## 2.20. Asymmetric motion across the San Francisco Bay Area faults. Implications on the magnitude of future seismic events.

Nicolas Houlié and Barbara Romanowicz

### 2.20.1 Introduction

The San Francisco Bay area is one of the tectonically most deformed areas in the world. This deformation is the result of relative motion of the Pacific (PAC) and North-America (NAM) plates. A large part of the strain (75%) is accommodated along structures lying in a 50 km wide land stripe. At least two major seismic events ( $M_w \geq 6.5$ ) are expected along the San Andreas (SAF) and Hayward faults (HAY) within the next decades. Triggering effects between the two seismic events may not be excluded (Lienkaemper *et al.*, 1997). The last major event in the area occurred in 1989 (Loma Prieta event) (Segall and Lisowski 1990, Dietz and Ellsworth 1990). The velocity field after this large event was perturbed (Argus and Lyzenga 1994) and the microseismicity significantly increased since then in the southern portion of the San Francisco Bay Area (SFBA) (ANSS catalog). As the prediction of the next event is based on the estimation of the energy accumulated along active faults (acceleration along the fault, landslides, hydrogeological features). Our study area will be limited in this work to the San Francisco Bay Area (SFBA).

Here we test the potential asymmetry of the motion along the San Andreas and San Gregorio faults. The asymmetry of the motion is a unique opportunity to link the velocity models used in seismic tomography and moment tensor inversions with geodetic observations, by investigating the rigidity of the PAC oceanic crust. The asymmetry was already mentioned both by geodesists (Lisowski, M., 1991) and by seismologists Le Pichon *et al.*, 2005) but never tested in the SFBA on a real geodetic dataset. We evaluate the velocity field in the light of this hypothesis. We discuss the implications of the new location of the strain peak from the perspective of a future event. Additionally we provide some elements on the geometry of tectonic features in the San Pablo Bay region.

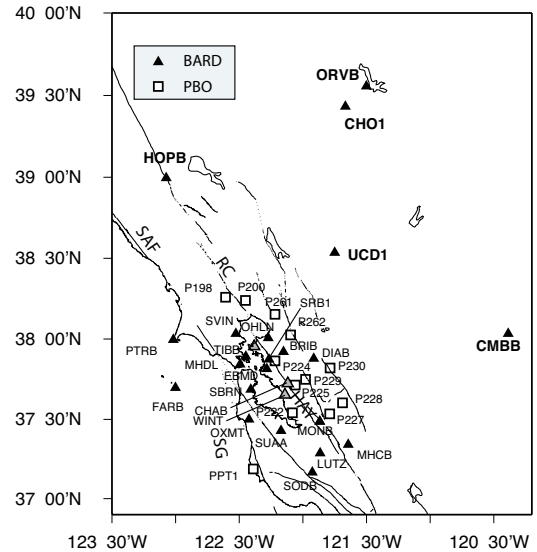


Figure 2.40: Map of the permanent GPS benchmarks of the BARD (black triangles) and PBO (white squares) networks. The sites HCRO (Hat Creek Radio Observatory), PKDB (Parkfield, CA), SAOB (San Andreas Geophysical Observatory) and YBHB (Yreka Blue Horn Mine, CA) are located outside the map.

### 2.20.2 Data and data processing

The BARD network is a permanent GPS network comprising 40 GPS sites, installed since 1994 in Northern California (Romanowicz *et al.*, 1994). Some of these sites have been transferred to the Plate Boundary Observatory (PBO), but not all. The receivers operating are mainly Ashtech (Z-12 and  $\mu Z$ ) and Trimble receivers (TR4000) with Choke Ring antennas. During the last two years, the network was upgraded, replacing the old receivers (mostly Ashtech Z-12) by Trimble NETRS with high-rate capabilities. The BARD network is streaming data to the Berkeley Seismological Laboratory in real-time (from 1s to 15s) (Romanowicz *et al.*, 1994). All the data are archived at the Northern California Earthquake Data Center (NCEDC, <http://www.ncedc.org>) (Neuhauser *et al.*, 2001). Today, the BARD network has operated long enough to provide high accuracy velocities in the San Francisco Bay Area (Blewitt and Lavallée, 2002).

All the data have been processed by using the GAMIT/GLOBK tool suite (King and Bock, 2006, Herring, 2005). We have adjusted all the 4018 daily solutions using five reference sites (BAY1, GOLD, JPLM, PPT1,

VNDP) that are present in our dataset and included in the ITRF2000 release (Altamimi *et al.*, 2002). The adjustment of the whole dataset of daily solutions was successfully completed by minimizing the shifts between the ITRF velocities and our solutions.

### 2.20.3 Results

Both asymmetric and symmetric deformation models are able to fit the GPS observations in the azimuth N55. We confirm that the transverse compressive component of the deformation across the Hayward fault is negligible. The location of the strain measurable from the GPS observations in the SFBA and its related shear stress rate have a direct impact on the expected time-recurrence of large earthquake in the Bay Area (Thatcher, 1990). We argue that discriminating between the two models is necessary in order to better integrate the GPS observations into constraints on the seismic cycle deduced from the monitoring of the seismic events and long-term geological evidences.

### 2.20.4 References

Altamimi, Z., P. Sillard, and C. Boucher (2002), ITRF2000: A New Release of the International Terrestrial Reference Frame for Earth Science Applications, *J. Geophys. Res.*, 107(B10), 2114, doi:10.1029/2001JB000561.

Argus, D., and G. Lyzenga (1994), Site velocities before and after the Loma Prieta and Gulf of Alaska earthquakes determined from VLBI, *Geophys. Res. Lett.*, 21(5), 333–336.

Blewitt, G., and D. Lavallée (2002), Effect of annual signals on geodetic velocity, *J. Geophys. Res.*, 107(B7), 2145, doi:10.1029/2001JB000570.

Dietz, L., and W. Ellsworth (1990), The October 17, 1989, Loma Prieta, California, earthquake and its aftershocks: Geometry of the sequence from high-resolution locations, *Geophys. Res. Lett.*, 17(9), 1417–1420.

Herring, T. (2005), *GLOBK: Global Kalman Filter VLBI and GPS Analysis Program, version 10.2*.

King, N., M. Murray, W. Prescott, R. R. Clymer, and B. Romanowicz (1994), The bay area regional deformation (bard) permanent gps array, in *Eos Trans. AGU, Fall Meet. Suppl*, S42B-09.

King, R., and Y. Bock (2006), *Documentation of the GAMIT software*, MIT/SIO.

Le Pichon, X., C. Kreemer, and N. Chamot-Rooke (2005), Asymmetry in elastic properties and the evolution of large continental strike-slip faults, *J. Geophys. Res.*, 110(B03405), doi:10.1029/2004JB003343.

Lienkaemper, J., J. Galehouse, and R. Simpson (1997), Creep response of the Hayward fault to stress changes caused by the Loma Prieta earthquake, *Science*, 276, 2014–2016.

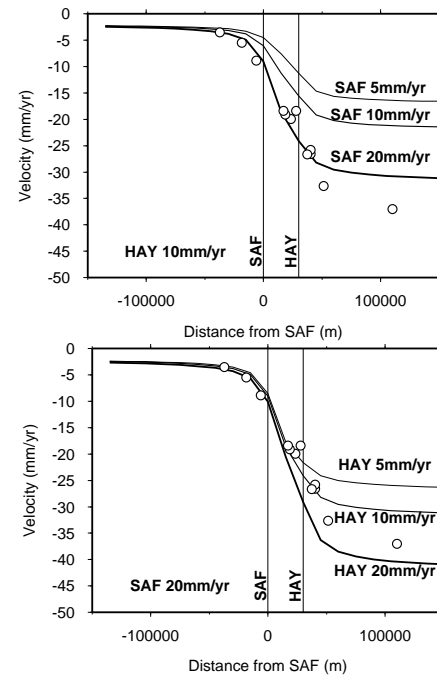


Figure 2.41: Validation of the asymmetric hypothesis of motion across SAF and HAY faults. Both locking depths are equal to 10 km. We combine the velocity fields associated with SAF and HAY. By varying the velocity along the Hayward (top) and San Andreas fault (bottom), keeping the other velocity fixed, we have determined the slip velocities of the HAY and SAF are respectively equal to 10 and 20 mm/yr. Some additional residuals are visible at the UCD1 site. This residual velocity could be explained by different sources such as the interseismic deformation related to Calaveras or Greenville faults.

Lisowski, M., J. Savage, and W. Prescott (1991), The Velocity Field Along the San Andreas Fault in Central and Southern California, *J. Geophys. Res.*, 96(B5), 8369–8389.

Neuhauser, D., D. Oppenheimer, S. Zuzlewski, L. Gee, M. Murray, A. Basset, W. Prescott, and B. Romanowicz (2001), Collaborative projects at the northern California earthquake data center (ncedc), *Eos Trans. Am. Geophys. Union*, 82(47).

Romanowicz, B., D. Neuhauser, B. Bogaert, and D. Oppenheimer (1994), Accessing northern California earthquake data via Internet, *Eos Trans. Am. Geophys. Union*, 75(23).

Segall, P., and M. Lisowski (1990), Surface Displacement in the 1906 San Francisco and 1989 Loma Prieta Earthquakes, *Science*, 250, 1241–1243.

Thatcher, W. (1990), Present-day crustal movements and the mechanics of cyclic deformation, in *The San Andreas Fault system, California*, vol. 1515, pp. 189–205.

## 2.21. A Decade of InSAR Observation across the Creeping Segment of the San Andreas Fault

Isabelle Ryder and Roland Bürgmann

### 2.21.1 Introduction

The San Andreas Fault system stretches from the southern California border 1,100 km northeastwards right up to the Mendocino triple junction offshore northern California. For much of its length, the fault is locked, displaying no significant offset between large seismic events. The parts of the fault that ruptured during the 1857  $M_w$  7.9 Fort Tejon earthquake and the 1906  $M_w$  7.9 San Francisco earthquake are examples of portions of the fault that are locked. In between these two rupture zones lies the 170 km-long creeping segment, from now on abbreviated CSAF. Various types of surface measurement in the last three decades or so have amply demonstrated that creep occurs along this section, with estimated creep rates up to 34 mm/year (*Burford and Harsh, 1980; Lisowski and Prescott, 1981; Schulz, 1982; Schulz, 1989; Titus et al., 2005*). Since the discovery of creep at the Cienega Winery by Tocher in 1960 (*Tocher, 1960*), the CSAF has essentially become the world's type locality for fault creep: no other fault section is known to creep along such a great length, nor at such a high rate. Several other faults in the San Andreas Fault system have well-documented creep, for example the Calaveras Fault (e.g. *Rogers and Nason, 1971; Johanson and Bürgmann, 2005*) and the Hayward Fault (e.g. *Savage and Lisowski, 1993; Simpson et al., 2001*), but the rates are less than 10 mm/year. Why some faults creep while others are locked is not known. It is, however, important to study this question. Collectively, the creeping faults in the San Francisco Bay region constitute a major part of the San Andreas Fault system; if we are to know the system well enough to predict earthquakes, then we need to understand the mechanics of creep. In this project we use Interferometric Synthetic Aperture Radar (InSAR) measurements covering almost a decade to record spatial variations in creep rate along the CSAF. We then invert these surface data for shallow creep rates and deep slip rates on the fault.

### 2.21.2 InSAR Observations

We use SAR data from the European ERS-1 and ERS-2 satellites acquired between May 1992 and January 2001 to construct interferograms across the CSAF. Processing was carried out using the Caltech/JPL software ROI-PAC (*Rosen et al., 2004*), with a bridge unwraping algorithm. Topographic effects were removed using a 90 m digital elevation model derived from Shuttle Radar Topography Mission (SRTM) data (*Farr and Kobrick, 2000; Rodriguez et al., 2006*). Agriculture in the

Salinas valley and the San Joaquin basin results in temporal decorrelation in many of the interferograms, and steep topography, particularly on the northeast side of the fault, leads to geometrical decorrelation. Collectively, these zones of incoherence lead to isolated patches in the unwrapped interferograms. Figure 2.42 shows a stack of twelve interferograms which can be unwrapped consistently across the fault. The stacking process increases the signal-to-noise ratio above that of individual interferograms, so that a more robust identification of spatial variations in creep rate can be made. The stack assumes a linear velocity for each pixel. The fault is clearly delineated by the abrupt offset running northwest to southeast across the stack image. The displacement gradient near the fault is much greater than would be expected for a fault locked to the bottom of the seismogenic layer (about 12-15 km in this region), implying that significant shallow slip occurred during the decade of observation. The positive range change on the southwest part of the image is enhanced in the Salinas Valley. We surmise that this enhancement is due to subsidence caused by aquifer discharge in this highly agricultural area. The area of > 10 mm/year positive range change in the southeast quadrant of the stack exactly coincides with the town of Coalinga and the nearby oil fields. It is possible that this range change anomaly is due to pumping of oil. The agreement of our 9-year creep rate with estimates obtained by other workers over earlier and/or longer periods of time show that creep rate on the years to decadal time scale has been approximately constant over the last 30 years. If there was any increase in creep rate as a result of either the 1857 Fort Tejon or the 1906 San Francisco earthquake, then presumably the rate has now levelled off.

### 2.21.3 Inversion for Creep Rate

To obtain an idea of the distribution of creep rate, we perform inversions using both the InSAR stack and GPS velocities. The CSAF is well-covered by continuous (Plate Boundary Observatory) and campaign GPS sites. Initially, separate InSAR and GPS inversions are carried out, as preliminaries to a joint inversion. The InSAR stack is downsampled by a factor of 20 in the north and east directions. Slip is constrained to be positive (i.e. right-lateral), and an upper bound of 40 mm/year on the slip rate is imposed. In the joint inversion, a maximum shallow creep velocity of 33 mm/year occurs in the centre of the segment, and to first order tapers off on either side, more rapidly to the south than to the north. This mirrors

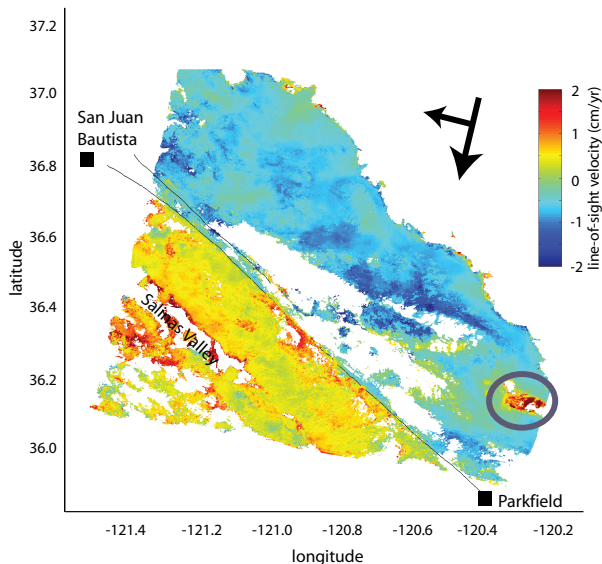


Figure 2.42: Stack of 12 descending ERS interferograms made from SAR scenes acquired between May 1992 and January 2001. Colours show range change, which is the surface displacement in the line of sight between the satellite and the ground. Red is positive range change, i.e. motion away from the satellite. Arrows show satellite ground track (towards south-southwest) and look direction (towards west-northwest). Fault traces for the CSAF and Calaveras Fault are marked. The line-of-sight offset rate across the fault is 10 mm/year, which is equivalent to a right lateral displacement rate of 32 mm/year. Grey ellipse in bottom right outlines area of suspected subsidence, possibly related to oil pumping near Coalinga. Subsidence may also be occurring in the agricultural Salinas Valley.

the pattern illustrated in Figure 3 of Titus et al. (2005), which is a compilation of surface geodetic slip rate estimates from different workers since the 1970s. Shallow creep rate falls to very low values ( $< 10$  mm/year) around Parkfield. Intermediate depth creep rates reach a maximum of 38 mm/year just north of centre, tapering off to the north, and decreasing before rising again towards Parkfield. The deep slip rate is about 35 mm/year.

### 2.21.4 Future Work

The other key aspect of deformation along the CSAF that needs to be studied is the temporal variation of surface displacement and, by implication, of creep rate on the fault. Preliminary work has been started using a Persistent Scatterer approach, to construct displacement

time series at individual points on the ground. This relatively new technique identifies individual radar scatterers that remain coherent over a long period of time (years to decades). In addition, time series from Plate Boundary Observatory GPS points are being studied to look for variations in creep rate over time, and possible correlations in time between features at different points along the fault. Building a detailed picture of both spatial and temporal variations should help us understand the mechanics, as well as the kinematics, of creeping fault zones.

### 2.21.5 Acknowledgements

This project is funded by NSF grant number EAR-0337-308. All SAR data is from the European Space Agency (ESA).

### 2.21.6 References

- Burford, R.O. and P.W. Harsh, Slip on the San Andreas fault in central California from alignment array surveys, *Bull. Seism. Soc. Am.*, *70*, 1233–1261, 1980.
- Johanson, I.A. and R. Bürgmann, Creep and quakes on the northern transition zone of the San Andreas fault from GPS and InSAR data, *Geophys. Res. Lett.*, *32*, L14306, 2005.
- Lisowski, M. and W.H. Prescott, Short-range distance measurements along the San Andreas fault system in central California, 1975 to 1979, *Bull. Seism. Soc. Am.*, *71*, 1607–1624, 1981.
- Rogers, T.H. and R.D. Nason, Active fault displacement on the Calaveras fault zone at Hollister, *Seism. Soc. Am. Bull.*, *61*, 399–416, 1971.
- Savage, J.C. and M. Lisowski, Inferred depth of creep on the Hayward fault, central California, *J. Geophys. Res.*, *98*, 787–793, 1993.
- Schulz, S.S., G.M. Mavko, R.O. Burford and W.D. Stuart, Long-term fault creep observations in central California, *J. Geophys. Res.*, *87*, 6977–6982, 1982.
- Schulz, S.S., Catalog of creepmeter measurement in California from 1966 through 1988, *USGS Open File Report*, *89*, 65, 1989.
- Simpson, R. W., J.J. Lienkamper and J.S. Galehouse, Variations in creep rate along the Hayward fault, California, interpreted as changes in depth of creep, *Geophys. Res. Lett.*, *28*, 2269–2272, 2001.
- Titus, S.J., C. DeMets and B. Tikoff, New slip rate estimates for the creeping segment of the San Andreas fault, *Geology*, *33*, 205–208, 2005.
- Tocher, D., Creep on the San Andreas fault – creep rate and related measurements at Vineyard, California, *Bull. Seism. Soc. Am.*, *50*, 396–404, 1960.

## 2.22. Indian Plate Motion, Deformation, and Plate Boundary Interactions

Edwin (Trey) Apel, Roland Bürgmann, and Paramesh Banerjee (Wadia Institute of Himalayan Geology)

### 2.22.1 Introduction

We use 1867 GPS-measured velocities to geodetically constrain Indian plate motion and intra-plate strain to examine plate boundary deformation and plate interactions around the Indian plate. Our solution includes 14 GPS velocities from continuously recording stations from within the stable Indian plate interior which are used to estimate the rotation parameters of the Indian plate. These refined plate motions estimates allow for the rigorous analysis of the India-Eurasia convergence zone where we estimate convergence to be 5-10% higher than previous geodetic estimates (e.g., *Paul et al.*, 2001; *Socquet et al.*, 2006a). Dense station coverage along the Himalayan range front allows us to rigorously test boundary parameterizations and develop a preferred plate boundary model. In our preferred model the Himalayan range front accumulates  $\sim 50\%$  of the India-Eurasia convergence with as much as 25 mm/yr of slip accumulation along some segments.

We use a block modeling approach to incorporate both rigid block rotation and a first-order model of near-boundary elastic strain accumulation effects in a formal inversion of the GPS velocities. The robust plate motion parameters for Eurasia, Australia, and India allow for the rigorous testing of variable plate boundary geometries and considerations of models that include smaller microplates within the plate boundary zones. These models allow us to further illuminate patterns in the interseismic strain accumulation along the Indian plate boundaries including Himalayan range front.

### 2.22.2 GPS Velocities

Our primary data in this study is a solution of 164 stations, including 42 campaign style sites from central and northwestern India and 14 CGPS from India's continental interior stations that we processed. The earliest campaign data were collected in 1995, but most sites were first occupied in 2001. Occupations have been repeated every year since although some stations have been lost. Each survey-style station was occupied for 4-6 days continuously, once a year. Processing details can be found in (*Banerjee and Bürgmann*, 2002). Selected, globally distributed IGS sites were used to define an ITRF00 reference frame.

In addition to our own analysis we integrate GPS-station velocities from published work along the Himalayans, throughout China, and Southeast Asia. We integrate a large number of published solutions (*Apel et al. and references therein*, 2006b) with our own solution.

These velocities were combined with our solutions by rotating them into a common reference frame. We combine velocities published in an ITRF00 reference frame into our own solution by minimizing the misfit at collocated stations. After the combination we compare our combined solution the published values to estimate misfit. For most sites the RMS is  $\sim 1-2$  mm/yr, well within the 95% confidence intervals for these sites.

### 2.22.3 Plates and Blocks

Plate boundary locations are critical for characterizing GPS velocities and the plate kinematics of a particular region. While some plate boundaries in the Indian region are well defined by active fault traces, youthful geomorphology, and abundant local seismicity, others appear more diffuse and ambiguous. We draw on the distribution and kinematics of 20th century seismicity, local geology, and mapped faults, and the GPS velocity itself to define our block model boundaries. Within this paper the term plate (and microplate) refers to the rigid, coherent, lithospheric entity defined by faults, seismicity etc. The term block is the specific implementation of these data into a parameterized set of variables within our block model (e.g. *Apel et al.*, 2006a).

We define our blocks as rigid entities on a spherical earth bounded by dislocations in an elastic halfspace and invert for poles and rates of rotation that minimize the misfit to the GPS velocities using the block modeling code by Meade and Hager (2005). Because our inversion combines rigid block rotation with elastic strain accumulation effects, the parameterization of the block boundary geometry is critical. Geometry of the block boundaries is based heavily on seismicity and adopted from plate reconstructions (*Replumaz and Tapponnier*, 2003) and prior analyses (*Socquet et al.*, 2006a; *Reilinger et al.*, 2006; *Simons et al.*, 2007; *Meade*, 2007; *Thatcher*, 2007) or adjusted as indicated by the geodetic data.

### 2.22.4 Results

Some block motions are well defined and vary little within our model. The Eurasian block, Australian block, and Indian block rotation parameters are defined primarily by the sites that lie within the stable interior and are affected very little by plate boundary strain. With respect to Eurasia the pole of rotation for the Indian plate is located at  $23.641 \pm 0.979^\circ\text{N}$   $8.732 \pm 4.402^\circ\text{E}$  with an angular rotation rate of  $0.359 \pm 0.012^\circ$  Myr<sup>-1</sup> (Figure 2.43). Relative poles shown in Figure 2.43 illustrate the consistency of our solution.

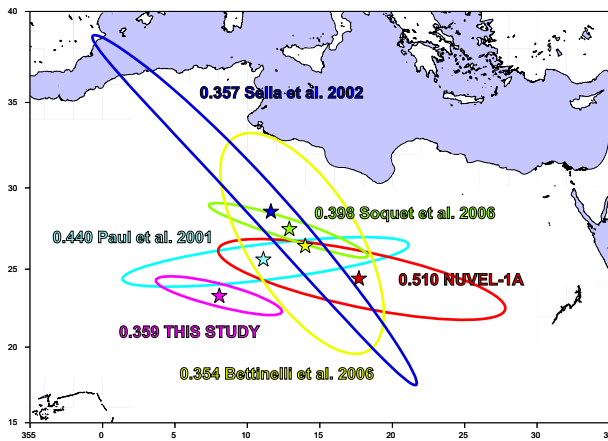


Figure 2.43: Relative plate poles of India's motion with respect to Eurasia. Values that precede the reference are the poles' magnitude measured in deg/My with a counter-clockwise positive convention.

Along the Himalayan Range Front we estimate IND-EUR convergence to vary from 34-41 mm/yr from  $\sim 76^\circ$  -  $91^\circ$  east longitude (Figure 2.44, inset). We parameterize the Himalayan front with four main blocks defined by the major geologic features like the Indus-Zangbo suture, Gulu rift, and Karakorum fault. As much as 25 mm/yr of contraction is accommodated by the Himalayan thrust (Figure 2.44). Our model, along the front, fit the data quite well. Some systematic misfit with the Himalayan blocks may be related to unmodeled east-west extension.

## 2.22.5 References

Apel, E. V., R. Bürgmann, G. Steblov, N. Vasilenko, R. King, and A. Prytkov, Independent active microplate tectonics of northeast Asia from GPS velocities and block modeling, *Geophysical Research Letters*, 33, L11303, doi:10.1029/2006GL026077, 2006a.

Apel, E., R. Bürgmann, and P. Banerjee, Geodetically constraining Indian plate motion and implications for plate boundary deformation, [seismo.berkeley.edu/annual\\_reports/ar05\\_06/node19.html](http://seismo.berkeley.edu/annual_reports/ar05_06/node19.html), 2006b.

Banerjee, P., and R. Bürgmann, Convergence across the northwest Himalaya from GPS measurements, *Geophysical Research Letters*, 10.1029/2002GL015184, 2002.

Meade, Brendan, Mechanics of the India-Asia Collision Zone, *Geology*, 35, p. 81-85, 2007.

Meade, B. J., and B. H. Hager, Block models of crustal motion in southern California constrained by GPS measurements, *Journal of Geophysical Research*, 110, B03403, 10.1029/2004JB003209, 2005.

Paul, J., Bürgmann, R., Gaur, V. K., Bilham, R. Larson, K. M., Ananda, M. B., Jade, S., Mukal, M., Anupama, T. S., Satyal, G., Kumar, D., The motion and ac-

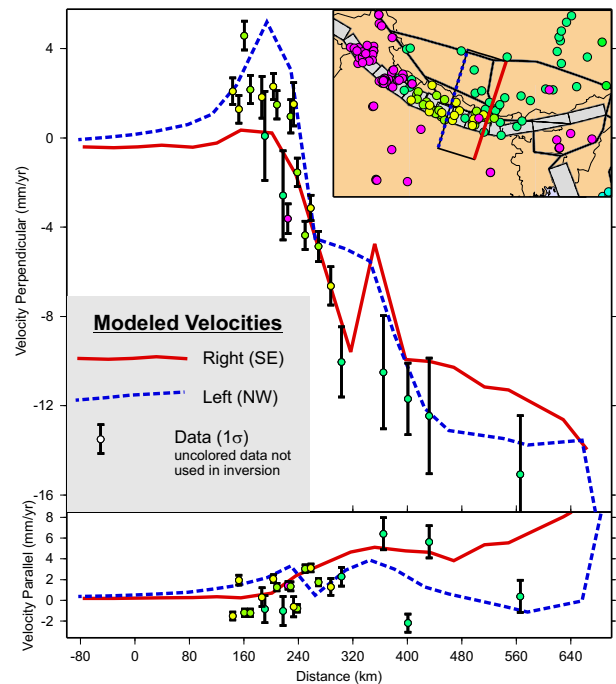


Figure 2.44: Velocity profile of measured and predicted velocities in Tibet. The inset figure shows the block configuration used in the inversion. GPS stations are colored according to source.

tive deformation of India, *Geophysical Research Letters* 28(4), 2001.

Reilinger R., et al., GPS constraints on continental deformation in the Africa-Arabia-Eurasia continental collision zone and implications for the dynamics of plate interactions, *Journal of Geophysical Research*, 111, B05411, doi:10.1029/2005JB004051, 2006.

Replumaz A., and P. Tapponnier, Reconstruction of the deformed collision zone Between India and Asia by backward motion of lithospheric blocks, *Journal of Geophysical Research*, 108 (B6), 2285, doi:10.1029/2001JB000661, 2003

Simons W. J. F., et al., A decade of GPS in Southeast Asia: Resolving Sundaland motion and boundaries, *Journal of Geophysical Research*, 112, B06420, doi:10.1029/2005JB003868, 2007.

Socquet, A., Vigny, C., Chamot-Rooke, N., Simons, W., Rangin, C. and Ambrosius, B., India and Sunda plates motion and deformation along their boundary in Myanmar determined by GPS, *Journal of Geophysical Research*, 111, B05406, 10.1029/2005JB003877, 2006a.

Thatcher W., Microplate model for the present-day deformation of Tibet, *Journal of Geophysical Research*, 112, B01401, doi:10.1029/2005JB004244, 2007.

## 2.23. Hidden Dykes detected on Ultra Long Period seismic signals at Piton de la Fournaise volcano?

Nicolas Houlié and Jean-Paul Montagner (IPG Paris, France)

### 2.23.1 Introduction

Both the magma feeding system geometry and the total volume of magma injected in the volcanic edifices still remain poorly known. This constitutes one of the main limitations for a better understanding and prediction of volcanic eruptive events. However, while the existence of a magma chamber is still debated on several volcanoes, it is often observed on paleovolcanoes around the world (Gudmundsson, 2002). The tracking of magma in motion within the volcanic feeding system is thus a key challenge of modern volcano-seismology. The Réunion island was created by the Réunion hotspot and is the most recent island of the Mascarene chain. Piton de la Fournaise is one of the two stratovolcanoes located on the eastern part of Réunion Island (France). Following the quiescent period between 1992 and 1998, the volcano has been quasi continuously active since the March 1998 event. The quality of the erupted basalts has been constant during the last two centuries and was described as “steady state basalt” (Albarède et al., 1997). The geometry of the magma feeding system is still debated. Some authors suggest that the magma feeding system is complex and composed of small magma reservoirs (Lénat and Bachèlery, 1990) but the large deformations of the whole volcano cannot be explained by such small subsurface sources (Houlié, 2005). It is now generally agreed that there is an upper magma chamber located (we will refer to this magma chamber as P2 (Aki and Ferrazzini, 2001)) at sea level (Nercessian et al., 1996; Sigmundsson et al., 1999; Aki and Ferrazzini, 2001). The volume of the upper magma chamber is estimated to be  $5 \cdot 10^{-8} m^3$ . Gravimetry measurements made along an East- West profile across the volcano have been used to locate the upper magma chamber (Lesquer, 1990). Its location is coincident with the observed seismicity (Nercessian et al., 1996; Battaglia et al., 2005). The proposed volume of the magma chamber is large enough (radius  $\sim 500$  m) to deform the whole volcano far away from the summit and west of the Enclos Fouqué, as is observed (Houlié, 2005). On the other hand, while the proposed size for the magma chamber is in agreement with geochemical measurements, it would be undetectable to seismic imaging. The migration of fluid coming out of this upper magma chamber and circulating inside the edifice can be detected by deformation at the surface. The use of long period (LP) or very long period (VLP) seismic events ( $0.2 Hz \leq f \leq 0.5 Hz$ ) has been successfully applied to several volcanoes (Chouet, 1988) in order to investigate fluid circulation inside several vol-

cano edifices. We present seismological evidence for a long-term response of the volcano to the deformation induced by changes in pressure inside the magma chamber located at sea level (Houlié and Montagner, 2007). The seismic signals are associated with the main eruptive events and recorded in the  $10^{-3} - 10^{-2} Hz$  frequency range.

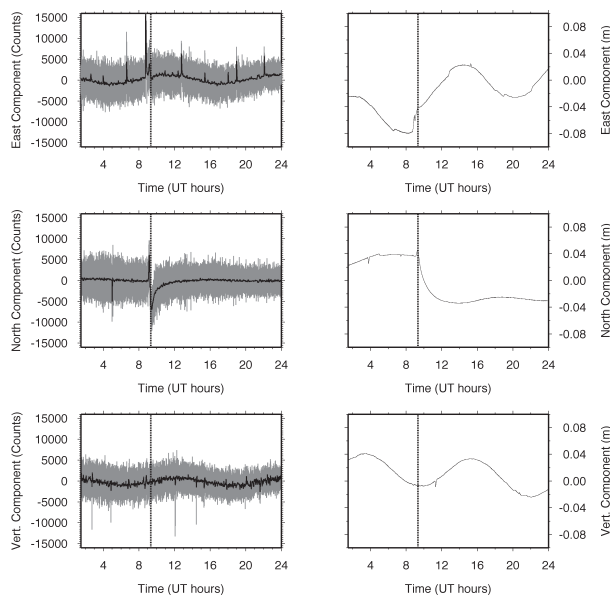


Figure 2.45: March 27th 2001. Left: GEOSCOPE data, in counts (the data are filtered by using a lowpass filter of  $10^{-2} Hz$ ). The three components of the LH channel (the sampling rate is equal to 1 s) are plotted. A deformation is detected by the broadband seismometer on the two horizontal components of the seismogram. Right: After deconvolving the instrument response, the displacement on the Northern component is equal to  $\sim 65 mm$ . Right column is displacement (in meters). The time of the eruptive event is indicated by a grey vertical line.

### 2.23.2 Results

The estimation of volume change  $\Delta V$  and its location using a broadband seismometer data is still approximate in the case of the Piton de la Fournaise and the volumes estimated here are constituting an upper bound limit. We are aware that this approach is simplistic but we believe that it is justified by the fact that the Mogi’s model is still routinely used in volcano observatories to determine

the pressure change in the edifice. A large number of deformation models are available in the literature (Yang and Davis, 1986; Gudmundsson, 1987). Some additional experiments will be necessary to discriminate the relative contributions of tilt and displacement during the transfer of magma out of the upper reservoir. The transient deformations extend over a region larger than 10 km across and with a typical duration of 500-1000 s. The similar pattern of deformation observed suggests that the source of the events has been stable over the last 15 yr. Large scale deformations were already suggested based on GPS benchmark time-series located on the western part of the Enclos Fouqué. We also confirm here that the EastWest displacement of the GPS benchmark 1B80 (Figure 2.46) could be related to the magma chamber pressure state and not to the slip along a discontinuity located along the border of the Enclos Fouqué, as previously suggested (Houlié, 2005). The GPS station located at the summit of the edifice constitutes a complementary tool to detect the long-term deformation episodes ( $T > 6$  months). The GPS receivers at the summit are only sensitive to the long-term component of the deformation of the magma chamber. Due to their location above the source, their sensitivity is reduced to the vertical component accuracy of the GPS (15 mm) (Houlié, 2005). The variability of the signal on the eastern component of RER suggests that it might be possible to locate the source of the over/under pressure provided that an additional broadband seismometer survey takes place.

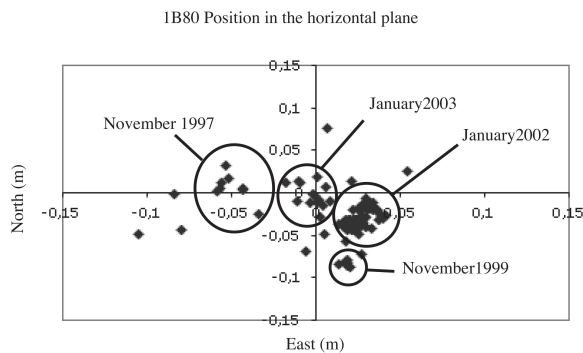


Figure 2.46: Displacement of the site 1B80 during 1997-2002 period. The shear modulus  $\mu$  is estimated to be 1.95 GPa at the Piton de la Fournaise. This low value is similar to the one used in Hawaii (Rubin and Pollard, 1987) to model the injection of basalt at Kilauea volcano. Figure from Houlié (2005). Data: OVPF/IPGP.

### 2.23.3 References

Aki, K., Ferrazzini, V., 2001. Comparison of Mount Etna, Kilauea, and Piton de la Fournaise by a quantitative modeling of their eruption histories. *J. Geophys.*

*Res.* 106 (B3), 40914102.

Albarède, F., Luais, B., Fitton, G., Semet, M., Kaminiski, E., Upton, B.G.J., Bachelery, P., Cheminée, J.L., 1997. The geochemical regimes of Piton de la Fournaise volcano (Réunion) during the last 530,000 years. *J. Petrol.* 38, 171201.

Gudmundsson, A., 1987. Formation and mechanics of magma reservoirs in Iceland. *Geophys. J. R. Astron. Soc.* 91, 2741.

Gudmundsson, A., 2002. Emplacement and arrest of sheets and dykes in central volcanoes. *J. Volcanol. Geotherm. Res.* 116, 279298.

Houlié, N. and Montagner, J.-P., Hidden Dykes detected on Ultra Long Period (ULP) seismic signals at Piton de la Fournaise volcano, 261, 1-2, 10.1016/j.epsl.2007.04.018, *Earth Planetary Science Letters* (2007).

N. Houlié, Mesure et Modélisation de données GPS de volcans. Applications à des études de déformation à diverses échelles et à la tomographie des panaches atmosphériques., Ph.D. thesis, Institut de Physique du Globe de Paris (2005).

Nercessian, A., Hirn, A., Lépine, J.C., Sapin, M., 1996. Internal structure of piton de la fournaise volcano from seismic wave propagation and earthquake distribution. *J. Volcanol. Geotherm. Res.* 70, 123143.

Sigmundsson, F., Durand, P., Massonnet, D., 1999. Opening of an eruptive fissure and seaward displacement at piton de la fournaise volcano measured by radarsat satellite radar interferometry. *Geophys. Res. Lett.* 26, 533536.

Yang, X., Davis, P.M., 1986. Deformation due to a rectangular elastic tension crack in an elastic half-space. *Bull. Seismol. Soc. Am.* 76, 865881.

## 2.24. The Fate of the Juan De Fuca Plate: Implications for a Yellowstone Plume Head

Mei Xue and Richard M. Allen

### 2.24.1 Introduction

In the Pacific Northwest, the Juan de Fuca plate, a remnant of the Farallon plate, continues to subduct beneath the North American continent (Figure 2.47). To the east of the Cascadia subduction zone lies the Yellowstone hotspot track. The origins of this track can be traced back to the voluminous basaltic outpourings of the Columbia Plateau around 17 Ma (*Watkins and Baksi, 1974; Christiansen and McKee, 1978*). If these basalts are the result of a large melting anomaly rising through the mantle to the base of the North America continent, such as a mantle plume head, the anomaly would need to punch through the subducting Juan de Fuca slab. Here, we use teleseismic body wave travel time tomography to investigate the fate of the subducted slab and its possible interaction with a plume head.

### 2.24.2 Tomographic results and resolution tests

We use a dataset collected from the Oregon Array for Teleseismic Study (OATS) operating from May 2003 to May 2006. The OATS array extends northwest-southeast across Oregon from the coast to the McDermitt Caldera (Figure 2.47). The dataset was complemented by data from 9 permanent networks and a temporary deployment: Berkeley Digital Seismograph Network (BDSN), Cascade Chain Volcano Monitoring (CC), Global Seismograph Network (GSN), Laser Interferometer Gravitational-Wave Experiment (LIGO), Princeton Earth Physics Project-Indiana (PEPP), Pacific Northwest Regional Seismic Network (PNSN), USArray Transportable Network (TA), University of Oregon Regional Network (UO), the United States National Seismic Network (USNSN), and the temporary deployment of the Wallowa Mountains Experiment. A total of 52 stations were used (Figure 2.47). The data from seismic events with epicentral distance greater than  $30^\circ$  and magnitude 6.0 and above from July 19th, 2003 to Nov. 10th, 2004 were inspected for all stations. For the S-velocity inversion, a total of 95 events (Figure 2.47) with clear S and SKS phases were recorded at 45 stations and a total of 2148 rays were used. For the P-velocity inversion, a total of 78 events with clear P and PKiKP phases were recorded at 46 stations and a total of 2101 rays were used. We follow a similar inversion procedure as described in *Allen, et al., 2002*.

Here we present the vertical slices through our S- and P- wave velocity models along the OATS array where

both models have the highest resolution (Figure 2.48a and b). The better ray coverage available from shear-wave arrivals means the Vs model has greater resolution than the Vp model. We therefore focus on the Vs model. The most prominent feature in our tomographic models is the high velocity anomaly which dips  $\sim 46^\circ$  and extends down to a depth of  $\sim 400$  km. We interpret this feature as the subducted Juan de Fuca plate. Resolution tests show that we are able to resolve any slab to a depth of  $\sim 600$  km. The second prominent feature is the low velocity body immediately beneath the slab extending to a depth of at least  $\sim 575$  km. This layer has a similar geometry as the slab: a dip of  $\sim 50^\circ$  to the east and a thickness of  $\sim 75$  km. The amplitude of this low velocity anomaly is estimated to be up to  $\sim 3\%$  for Vs. Resolution tests show that the low velocity layer is required by data and is not an artifact of the inversion.

### 2.24.3 Proposed tectonic model

Using the relative plate motion between the Juan de Fuca plate and the North American Plate (HS3-NUVELIA), the estimated total length of the slab subducted to the east in the last 17 Ma is  $\sim 480$  km. This is less than the total imaged slab length of  $\sim 660$  km from the present trench in an east-west direction. Therefore, the bottom edge of the slab we observe today was east of the trench around 17 Ma. Assuming a similar slab geometry to today, the  $\sim 180$  km length of slab would reach a depth of  $\sim 60$  km, comparable to the likely thickness of the continental lithosphere. We propose that the absence of the slab below 400 km depth today is due to the arrival of the Yellowstone plume head around 17 Ma, which destroyed the Juan de Fuca slab at depths greater than the thickness of the continental lithosphere. As the plume head material would spread westward beyond the trench, possibly as far as the Juan de Fuca Ridge, traction with the subducting plate would then pull some plume head material down into the mantle. We image this material as the low velocity layer beneath the slab in our Vs model. The observed low Vs anomaly of up to 3% is comparable with what is expected for plume head material  $100\text{-}300^\circ\text{C}$  hotter than the surrounding asthenosphere. Finally, this hot remnant plume head material beneath the slab may be partly responsible for the absence of a Wadati-Benioff zone associated with the subduction of the Juan de Fuca plate (*Xue and Allen, 2007*).

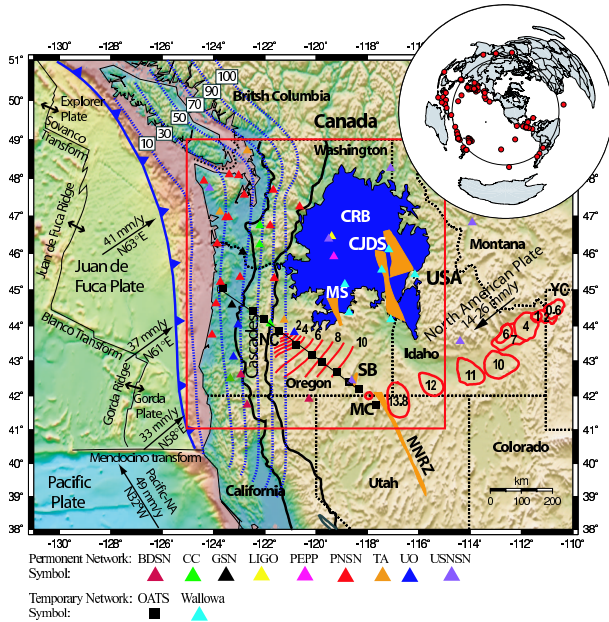


Figure 2.47: Tectonic map for the study region. Plate motions from HS3-NUVEL 1A are shown as black arrows (*Gripp and Gordon, 2002*). Blue dotted lines show the depth contours of the Juan de Fuca slab surface (*McCrorey et al., 2006*). The thick black lines delineate the Cascade Range. Age contours of initial rhyolitic volcanism along the Newberry track are shown in 1 Ma increments extending to the Newberry Caldera (NC) (*Jordan et al., 2004*). Major rhyolitic caldera centers along the Yellowstone track are shown with age in Ma extending to the Yellowstone Caldera (YC) (*Pierce and Morgan, 1992*). Both tracks initiate in the region of the McDermitt Caldera (MC), which is shown as a red circle. The Columbia River Basalt is shown in blue (12 to 17 Ma) (*Christiansen et al., 2002*). Dike swarms associated with the 17 Ma basaltic outpourings are shown in gold (*Camp and Ross, 2004*; *Christiansen and Yeats, 1992*): Chief Joseph Dike Swarm (CJDS), Monument Swarm (MS), Steens Basalt (SB), and Northern Nevada Rift Zone (NNRZ). The seismic stations used in this study are shown as triangles and squares with a total number of 52. Inset shows the distribution of the 95 events used in the inversion for the S-wave velocity model. The red square outlines the study region. The thick black line across OATS array indicates the location of the cross section shown in Figure 2.48

#### 2.24.4 Acknowledgements

We thank the people who assisted us in the deployment of OATS: Neal Lord, Lee Powell, Robert Pyzalski, Andrew Lockman, and William Unger from the University of Wisconsin; John Nabelek and Anne Trehu from Oregon State University, and all the land owners who hosted

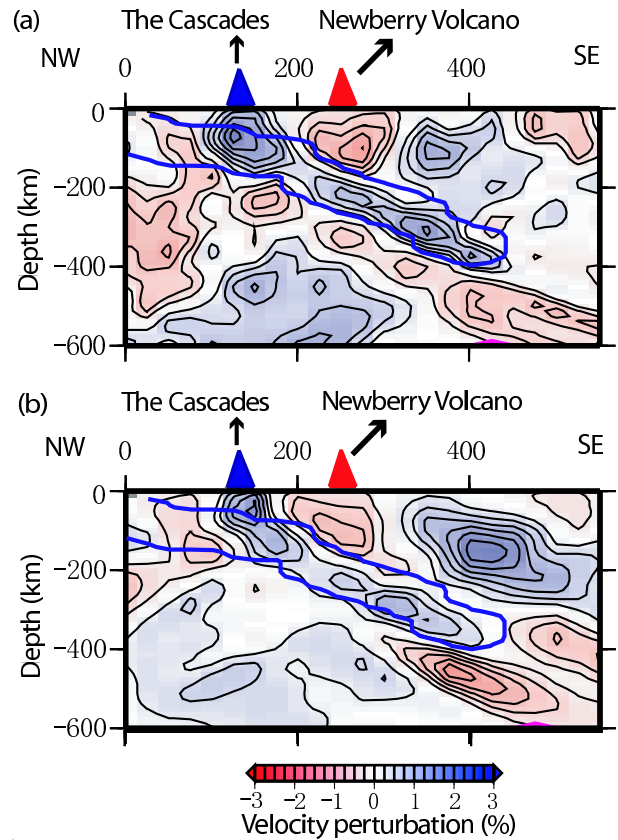


Figure 2.48: Vertical slices through the (a)  $V_s$  and (b)  $V_p$  models along the OATS line indicated in Figure 1. The envelope of the synthetic slab ending at 400 km depth is shown by the blue outline. The contour interval is 0.25% indicated by vertical lines in the color bar of the velocity scale. Zero contours are not shown. The locations of the Cascades and the Newberry Volcano are shown as blue and red triangles respectively.

our stations. We thank Gene Humphreys for allowing us using data from their deployment at Wallowa Mountain. We also use data from Berkeley Digital Seismograph Network, Cascade Chain Volcano Monitoring, Global Seismograph Network, Laser Interferometer Gravitational-Wave Experiment, Princeton Earth Physics Project-Indiana, Pacific Northwest Regional Seismic Network, USArray Transportable Network, University of Oregon Regional Network, and the United States National Seismic Network. The IRIS DMC provided seismic data. This work was supported by the NSF (EAR-0539987).

#### 2.24.5 References

Allen, R. M., et al., Imaging the mantle beneath Iceland using integrated seismological techniques, in *Journal of Geophysical Research-Solid Earth*, 107, 2325, doi:2310.1029/2001JB000595, 2002.

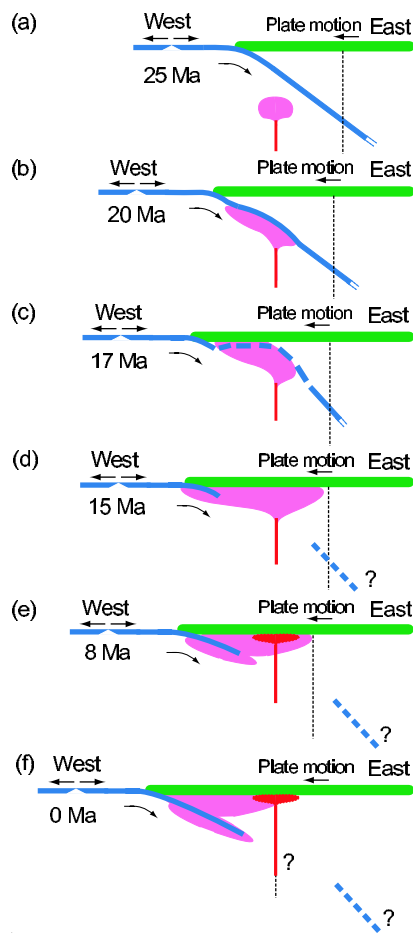


Figure 2.49: Proposed tectonic model for the interaction between the subducting Juan de Fuca Plate (blue) and the Yellowstone plume head (pink). Snapshots in time are shown as: (a) 25 Ma, the Yellowstone Plume is approaching the subducted Juan de Fuca plate; (b) 20 Ma, the plume head has intersected the Juan de Fuca plate and preferentially flowed westward along the base of the slab; (c) at 17 Ma, the plume head punched through the Juan de Fuca plate, destroyed a larger portion of the slab and caused the volcanism at the surface; (d) 15 Ma, the plume head material spreads out in a larger region at the base of the lithosphere; (e) 8 Ma, the subducting slab drags the remnant plume head material down into the mantle; (f) at present, the hot material from the remnant plume head has been brought to greater depth by the ongoing subducting slab. The vertical dashed line indicates the progression of the current Yellowstone caldera to the west. The red plume stem represents a hypothetical Yellowstone Plume since the arrival of the plume head (pink). Note: this model builds on the tectonic models proposed by Geist and Richards, 1993; Pierce, et al., 2000.

Camp, V.E., M.E. Ross, Mantle dynamics and genesis of mafic magmatism in the intermontane Pacific Northwest, *Journal of Geophysical Research-Solid Earth* 109, 2004.

Christiansen, R.L., E.H. McKee, Late Cenozoic volcanic and tectonic evolution of the Great Basin and the Columbia intermontane regions, in: R.B. Smith, G.P. Eaton, (Eds), *Cenozoic tectonics and regional geophysics of the western Cordillera 152*, Geological Society of America Memoir, Boulder, Colorado, pp. 283-311, 1978.

Christiansen, R.L., G.R. Foulger, J.R. Evans, Upper-mantle origin of the Yellowstone hotspot, *Geological Society of America Bulletin* 114, 1245-1256, 2002.

Christiansen, R.L., R.S. Yeats, Post-Laramide geology of the U.S. Cordilleran region, in: B.C. Burchfiel, P.W. Lipman, M.L. Zoback, (Eds), *The Cordilleran Orogen: Conterminous U.S. G-3*, Geological Society of America, Boulder, Colorado, 261-406, 1992.

Geist, D., M. Richards, Origin of the Columbia Plateau and Snake River Plain - Deflection of the Yellowstone plume, *Geology* 21, 789-792, 1993.

Gripp, A.E., R.G. Gordon, Young tracks of hotspots and current plate velocities, *Geophysical Journal International* 150, 321-361, 2002.

Jordan, B.T., A.L. Grunder, R.A. Duncan, A.L. Deino, Geochronology of age-progressive volcanism of the Oregon High Lava Plains: Implications for the plume interpretation of Yellowstone, *Journal of Geophysical Research* 109, doi:10.1029/2003JB002776, 2004.

McCrory, F.A., J.L. Blair, D.H. Oppenheimer, S.R. Walter, Depth to the Juan De Fuca Slab Beneath the Cascadia Subduction Margin A 3-D Model for Sorting Earthquakes, *U.S. Geological Survey, Data Series 91, Version 1.2*, 2006.

Pierce, K.L., W.J. Morgan, The track of the Yellowstone hotspot: Volcanism, faulting, and uplift, in: P.K. Link, M.A. Kuntz, P.L.B., (Eds), *Regional geology of eastern Idaho and western Wyoming 179*, Geological Society of America Memoir, 1-53, 1992.

Pierce, K.L., L.A. Morgan, R.W. Saltus, Yellowstone plume head: Postulated tectonic relations to the Vancouver slab, continental boundaries and climate, *USGS Open-File Report 00-498*, pp. 39, 2000.

Watkins, N.D., A.K. Baksi, Magnetostratigraphy and Oroclinal Folding of Columbia-River, Steens, and Owyhee Basalts in Oregon, Washington, and Idaho, *American Journal of Science*, 274, 148-189, 1974.

Xue, M. and R. Allen, The Fate of the Juan de Fuca Plate: Implications for a Yellowstone Plume Head, *Earth and Planetary Science Letters*, in Press.

## 2.25. Non-linear 3D Born Shear Wave Tomography in Southeastern Asia

Aimin Cao, Ahyi Kim, Mark Panning, and Barbara Romanowicz

### 2.25.1 Introduction

The crust and upper mantle in southeastern Asia is highly heterogeneous, presenting a challenge for path calibration, but it is well surrounded by earthquake sources, and a significant number of high quality broadband digital stations exist. Using a finite-frequency 2D approximation (NACT, Li and Romanowicz, 1995), we have already developed a 3D radially anisotropic model in a large region (longitude 30 to 150 degrees and latitude -10 to 60 degrees) from the existing long period waveform database in the range of 60 s to 400 s. The database was collected at Berkeley over the last 10 years for the construction of global mantle tomographic models (Li and Romanowicz, 1996; Megnin and Romanowicz, 2000; Gung et al., 2003; Panning and Romanowicz, 2004), and to it are added the data from 20 new events in the period up to to 2005.

A data set of 38826 3-component waveforms recorded at 169 stations from 393 events was used in the waveform inversion. The data have been processed with an automated algorithm, which removes glitches and checks for many common problems related to timing, poor instrument response, and excessively noisy windows. A weighting scheme has been applied to ensure even distribution of data across the region. The model is parameterized laterally in spherical spline level 6, which corresponds to lateral resolution of  $\sim 200$  km. And the corresponding radially anisotropic model is parameterized in the spline level 5, which corresponds to a lateral resolution of  $\sim 400$  km. In this study we will use a newly developed "non-linear" 3D Born approximation (N-Born) to refine the above NACT model (Panning et al., 2007).

### 2.25.2 Method and Results

The N-Born is modified from the standard 3D "linear" Born approximation (Capdeville, 2005) by including a "Path Average" term. This term allows the accurate inclusion of accumulated phase shifts which arise in the case when the wavepath crosses a spatially extended region with a smooth anomaly of constant sign. The linear 3D Born terms account for single scattering effects outside of the great circle path and are modeled according to the expressions of Capdeville (2005). Accounting for scattering outside of the great circle path is the one difference with our initial NACT approach.

Because the calculation of the 3D Born sensitivity kernels is very expensive computationally, we have to select a target subregion (longitude 75 to 150 degrees and latitude 0 to 45 degrees) (Figure 2.50). In order to further reduce

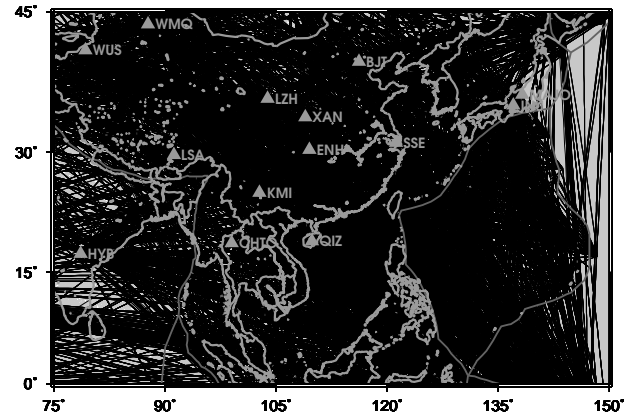


Figure 2.50: Raypath coverage in the subregion. The background grey raypath coverage is denoted for NACT and the black raypath coverage is for N-Born. Stations and events are required to be in the large region for the N-Born inversion, and so the N-Born raypath coverage is a subset of that of NACT.

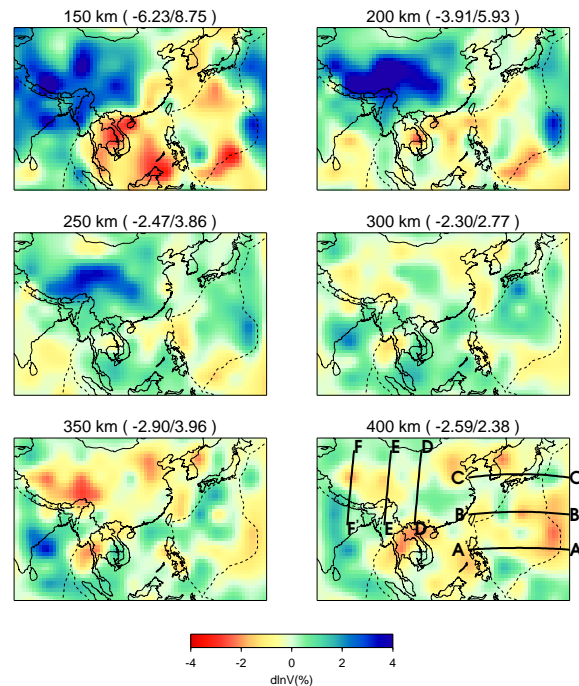


Figure 2.51: N-Born shear velocity model derived using the N-Born approximation in the subregion.

the intensity of the computation, we require that both events and stations must be in the large region, and only the ray paths along the minor arcs are selected. We calculated 3D Born sensitivity kernels for 162 events using the computing facilities (Jacquard) of the National Energy Research Scientific Computing Center ([www.nersc.gov](http://www.nersc.gov)). When we generate synthetics for the N-Born inversion, we use N-Born (Panning et al., 2007) in the subregion and NACT outside of the subregion.

Our starting model is the NACT model in the large region. We expand its radially anisotropic ( $\xi$ ) model from spherical spline Level 5 to Level 6, to conduct the conformal lateral parameterization for both isotropic and anisotropic inversion. We apply the N-Born approximation in the forward modeling part and calculate linear 3D Born kernels in the inverse part, and the adopted damping scheme for isotropic and radially anisotropic models is the same as that used in the NACT inversion.

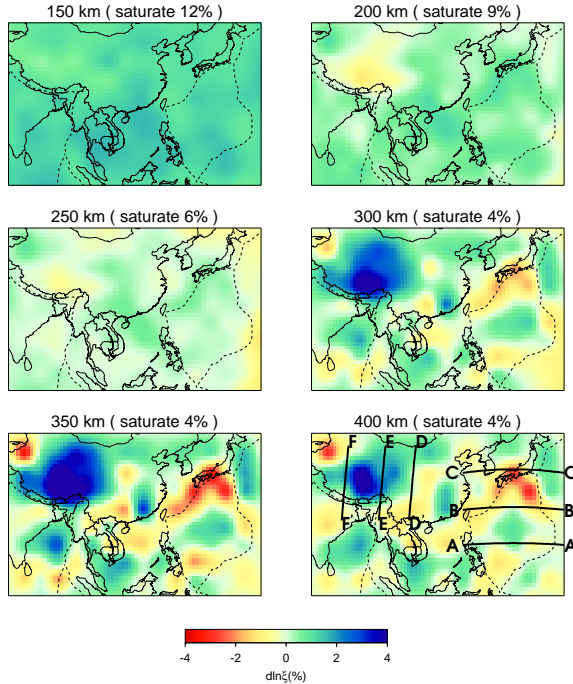


Figure 2.52: Radially anisotropic model of  $\xi$  ( $\xi = \frac{V_{SH}^2}{V_{SV}^2}$ ) in the subregion. Values are shown relative to an isotropic model ( $\xi=1.0$ ) with the anisotropy of the starting model above 220 km included. Blue regions represent regions where  $V_{SH} > V_{SV}$  and red regions where  $V_{SV} > V_{SH}$ .

Our N-Born shear velocity isotropic and anisotropic models are shown in Figure 2.51 and 2.52, respectively. Both N-Born and NACT derived models can fit waveforms very well, with up to  $\sim 83\%$  variance reduction (depending on the choice of damping). While the models agree in general, there are some notable differences be-

tween them in detail. For example, beneath the Tibetan plateau, the N-Born model shows a stronger fast velocity anomaly in the depth range 150 km to 250 km, which disappears at greater depth. This indicates that there is no delamination of lithosphere beneath the plateau, as has been suggested by some authors. More importantly, the N-Born anisotropic model can recover well the downwelling structure associated with subducted slabs (e.g., around Phillipine plate) (Figure 2.51). Beneath the Tibet plateau, radial anisotropy shows  $V_{SH} > V_{SV}$  (Figure 2.52) at depths of 300 km to 400 km, which implies horizontal rather than vertical flow and may help us to distinguish between end member models of the tectonics of Tibet.

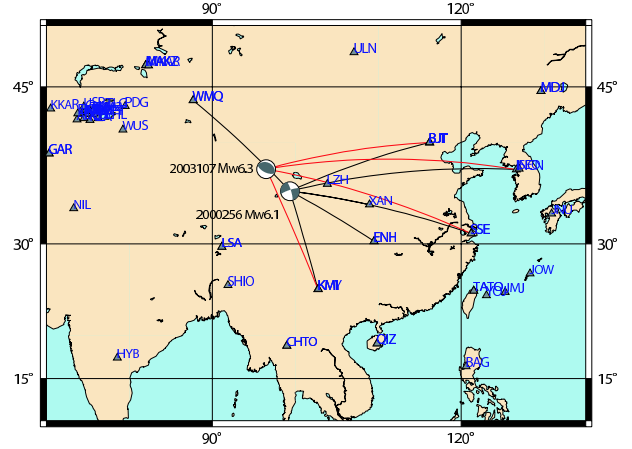


Figure 2.53: Event 2000256 (9/12/2000, Mw6.1), 2003107 (4/17/2003, Mw6.3) and IRIS station distributions. Source 2000256 (9/12/2000, Mw6.1) is used to obtain the velocity structures.

In order to refine the velocity structure beneath the region of our study, we perform forward waveform modeling with the method of frequency-wave number integration (FKI). Broadband seismograms are downloaded from IRIS and corrected to absolute ground velocity (cm/sec). We show 2 event locations of events 2000256 (9/12/2000, Mw6.1) and 2003107 (4/17/2003, Mw6.3), and the IRIS station distributions (Figure 2.53). We start with the 2000256 event, for which the continental ray paths are dominant, to obtain the 1D velocity structure between the source and each receiver. Broadband data are bandpass filtered at 0.005-0.05Hz. We used the Harvard CMT solution for the source parameters, and the starting model is a 1D layered average crustal velocity structure derived from CRUST2.0. Using the best velocity model we can obtain (Figure 2.54), we compute Green's functions and perform the moment tensor analysis for two ranges of frequency (0.01-0.05Hz and 0.005-0.03Hz). Then, we select the event 2003107, for which we have similar ray paths as for event 2000256, to per-

form the moment tensor analysis using Green's function obtained from our 1D simulation. We find a moment tensor solution in good agreement with the CMT solution, whereas the solution obtained using the PREM reference model is very poor. While this example was chosen because we expect that we can use Harvard CMT solutions for  $M > 6$  events as good references, this indicates that the additional regional modeling effort is worthwhile and will lead to better moment tensor solutions for smaller events in the area when we extend the modeling to higher frequencies (0.02-0.05Hz).

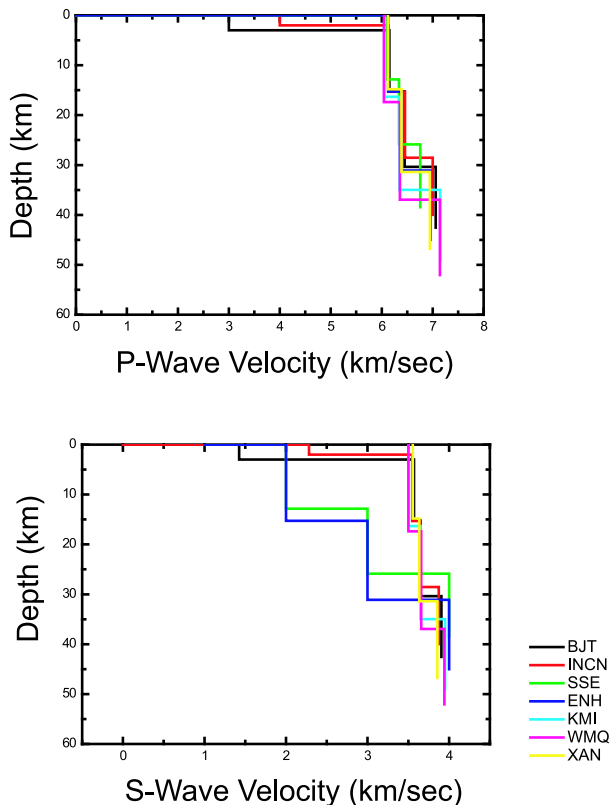


Figure 2.54: Best P-wave and S-wave velocity structures for the paths between event 2000256 and IRIS stations obtained from 1D forward modeling.

### 2.25.3 References

Capdeville, Y., An efficient Born normal mode method to compute sensitivity kernels and synthetic seismograms in the Earth, *Geophys. J. Int.*, 163, 639-646, 2005.

Gung, Y., B. Romanowicz, and M. Panning, Anisotropy and lithospheric thickness, *Nature*, 422, 707-711, 2003.

Li, X. D. and B. Romanowicz, Comparison of global waveform inversions with and without considering cross branch coupling, *Geophys. J. Int.*, 121, 695-709, 1995.

Li, X. D. and B. Romanowicz, Global mantle shear velocity model developed using nonlinear asymptotic coupling theory, *J. Geophys. Res.*, 101, 22,245-22,273, 1996.

Megnin, C. and B. Romanowicz, The 3D shear velocity structure of the mantle from the inversion of body, surface and higher mode waveforms, *Geophys. J. Int.*, 143, 709-728, 2000.

Panning, M. and B. Romanowicz, Inferences on flow at the base of Earth's mantle based on seismic anisotropy, *Science*, 303, 351-353, 2004.

Panning, M. and Y. Capdeville, and B. Romanowicz, Do first order 3D Born finite-frequency kernels improve modeling of surface waveforms? *Geophys. J. Int.*, submitted, 2007.

## 2.26. Inferring composition and temperature of the upper mantle from interpretation of long period seismic data and global attenuation measurements

Fabio Cammarano and Barbara Romanowicz

### 2.26.1 Introduction

Knowledge of the thermal and compositional structure of the upper mantle is essential to understanding the evolution of our planet. Direct constraints on shallow upper mantle chemical composition and temperatures are given by mineralogy and the geochemical signature of outcropping rocks. Overall, these data give a good idea of the ranges of temperatures and compositions expected in the first 200km. In general, there is a consensus that the average composition should not be far from the less depleted peridotites we sample, and therefore close to the "pyrolite" composition proposed by Ringwood (Ringwood, 1975). Shallow upper mantle T are consistent with those expected by a mantle adiabat with a potential T at surface of  $1300^{\circ}\text{C}$  ( $\pm 50^{\circ}\text{C}$ ). Also, melting conditions of peridotite rocks with depth (see, for example, the KLB1N solid curve by Hirschmann, 2000) are never fully reached, as indicated by seismic observations. This limits the maximum T we expect in the upper mantle. Below 200km, the best constraints on temperatures and compositions come from interpretations of seismic observations based on mineral physics. Recently, interdisciplinary studies which combine current knowledge of material properties at high P and T and geophysical observations are providing important insights into the nature of the upper mantle.

In a recent paper, (Cammarano and Romanowicz, 2007), we found that long period seismic waveforms require a high gradient of shear velocity between 250 and 350 km. Although some variations between continent and oceans are still seen until  $\sim 300\text{km}$ , the feature we observed is clearly global and raises questions about the average thermal or compositional structure of the upper mantle. In that paper, we discussed the thermal and compositional feature based on the family of PREF models and applying a pressure and temperature-dependent Q model, developed by the previous work of one of us (Cammarano *et al.*, 2003). Also, we showed that the  $V_S$  gradient with depth would require a value of  $G'$  (i.e. the pressure derivative of shear modulus) for olivine equal to 2.5 (experimental olivine  $G'$  are between 1.2 to 1.6) to make possible to explain such a feature without modifying the thermal or compositional structure of the upper mantle and we argued that an enrichment in garnet component with depth is the most plausible explanation.

Here, we refine our interpretation by testing two thermoelastic models (PEPI03, Cammarano *et al.*, 2003 and

LARS07, updated by *Stixrude and Lithgow-Bertelloni*, 2005) and the Faul and Jackson Q model (Faul and Jackson, 2005), discussed also in the preview report. We use the same 3-D  $V_S$  model obtained by inverting with respect to PREF, but we invert for T using the two average pyrolitic models coupled with the Faul and Jackson Q model at a given grain size and reference period at 150s. We test effects of grain size and extremely different activation volumes ( $V^*$ ) on the interpretation. Resulting 3-D structures are averaged and the  $\langle Q_S \rangle$  profile is compared with observations (the same of the previous report). Effects of variations in dry composition are tested using the LARS07 model. We model composition from harzburgite (1) to MORB (0). Pyrolite is given by a  $\sim 17\%$  of MORB component (0.17). In this report, we show uniquely average properties of the 3-D models.

### 2.26.2 Results

The two thermoelastic models for the same pyrolitic composition gave similar results in terms of thermal structure in the first 400km (Figure 2.55, second panel from the right) when coupled to the same P-T dependent Q model and assuming a given constant grain size and reference period (see Figure 2.55). Some differences between the two models appear in the first 150km. The two models differ in the transition zone as well, because of the large uncertainties on the shear properties of wadsleyite and ringwoodite. Here, we do not discuss further those features. Instead, we focus on the interpretation of the  $dV_S/dz$  gradient between 250 and 350km. Both pyrolite models (PEPI03 and LARS07) imply a negative thermal gradient to explain the  $V_S$  model required by seismic data (Figure 2.55). However, the consistent average Q structure predicted by those models attains very high values around 350km (Figure 2.55, third panel from the right) and we tested that the resulting  $\langle Q \rangle$  model is not consistent with the seismically observed global attenuation. Reducing the grain size, as expected, has the overall effect of reducing the temperatures to explain the same  $V_S$  structure, but the thermal gradients stay almost the same. We tested that even for a constant grain-size of 1mm, the resulting Q is still too high ( $Q_S \sim 450$ ) for both thermoelastic models at 350 km. The average density and  $V_P$  structures that are consistently determined by the mineral physics models are also plotted in Figure 2.55. The observed discrepancies are due to the different relative variations of  $V_S$  compared to density

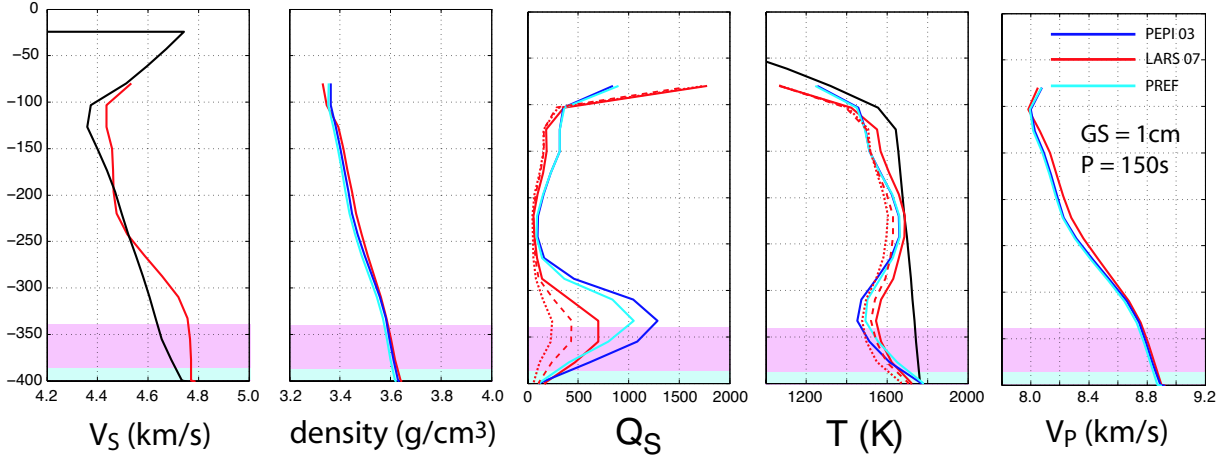


Figure 2.55: Comparison of thermal interpretation using PEPI03 and LARS07 pyrolitic models plus P-T and GS dependent Q model. Solid lines refer to GS=1cm, dashed for GS=1mm and dotted  $V^* = 0.6 \times 10^{-5}$ . Color scheme is given in the legend. Reference period is 150s. Starting  $V_S$  and thermal (adiabatic) model are in black

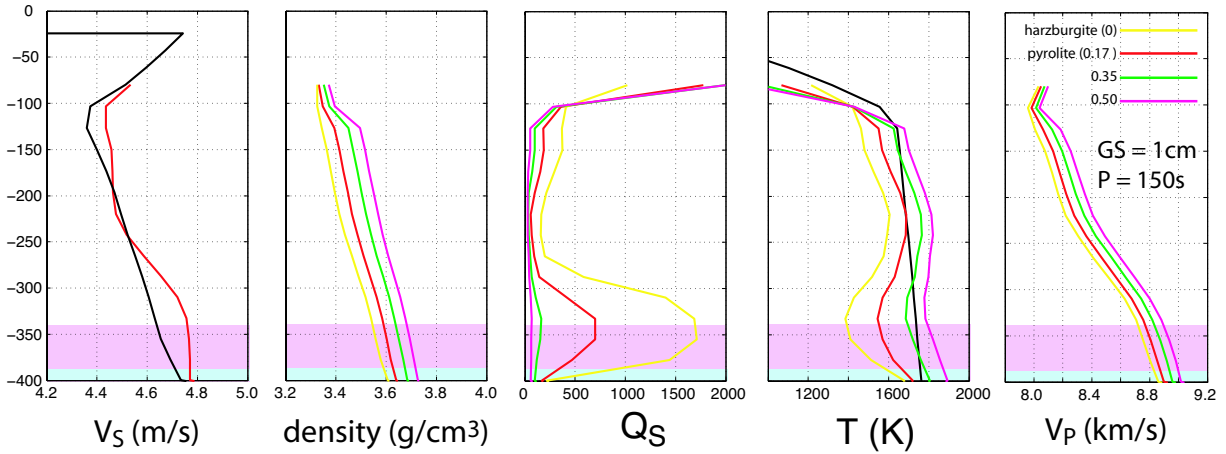


Figure 2.56: Comparison of thermal interpretation for 4 different compositions using LARS07 model plus P-T and GS dependent Q model at constant GS of 1cm and reference period of 150s. Color scheme is given in the legend. Starting  $V_S$  and thermal (adiabatic) model are in black

and  $V_P$  (heterogeneity ratios) between the two mineral physics models. Note, however, that variations in density are extremely small compared to the variations expected when interpreting the same  $\langle V_S \rangle$  model with variations in composition (compare density panels in Figure 2.55 and 2.56). We do not plot the similar indirect effects on  $V_P$  and density for a thermal interpretation when using different grain sizes. Alternatively to the discussed negative thermal gradient, an increase in grain size has been invoked to explain the isotropic features below 250km (Faul and Jackson, 2005). In our case, we found that such explanations would get a  $\langle Q_S \rangle$  structure that does not fit the seismic observations. The largest variations

in thermal interpretation are obtained when varying the pressure dependence of the Q model, i.e. the activation volume  $V^*$  (see also previous report). For example, by using a  $V^* = 0.6 \times 10^{-5}$ , we found that a thermal explanation characterized by an overall cold upper mantle ( $< T > \sim 1500K$ ) and a negative thermal gradient below 250km is now feasible. In spite of the low average T, the low  $V^*$  keeps the  $Q_S$  values small enough in hot areas to get a  $\langle Q_S \rangle$  consistent with observed seismic attenuations (Figure 2.55). Note, however, that  $Q_S$  values may be too low at some depths ( $\sim 20$ ) compared to what is inferred seismically. In Figure 2.56, we show the different thermal interpretation using the LARS07 model

for 4 compositions. If we assume an adiabatic  $1300^{\circ}\text{C}$  geotherm, it is possible to explain the  $V_S$  gradient with a compositional variation with depth. The required compositional gradient may be estimated visually by looking at what depth the thermal profiles for different compositions cross the mantle adiabat (Figure 2.56). We observe an increase from 17% of MORB component mixed with harzburgite (that is the value of an average pyrolite) at 250km until 35% at  $\sim 350\text{km}$ .

### 2.26.3 Conclusions

The combination of uncertainties on elastic and anelastic properties of mantle minerals together with long period seismic data and observed global attenuation measurements provide an important constraint on the nature of the upper mantle above 400km depth. In a previous paper, we found that adiabatic pyrolite is not compatible with seismic observations. One of the most striking features that is not reconcilable with such simple structure is the high  $V_S$  gradient we found globally below 250km (Cammarano and Romanowicz, 2007). Here we refine our interpretation by adding testing of predicted  $\langle Q_S \rangle$  structures against observations and investigating the effects of two mantle thermoelastic models. We found that a purely thermal interpretation would be possible only for low values of activation volume in order to be compatible with the  $\langle Q_S \rangle$  measurements and would imply a cold UM ( $T \sim 1500\text{K}$ ) and a negative thermal gradient below 250km, on average, at the global scale. A compositional explanation, more dynamically feasible in our opinion, would be more consistent with an adiabatic (potential T of  $1300^{\circ}\text{C}$ ) thermal structure and predicts a significant enrichment in garnet component with depth. By using the Stixrude 2007 model, we estimate a doubling of MORB component with respect to pyrolite around 350km depth. Test on the dynamical evolution of this C or T structure and other studies on 3-D Q structure and including constrain from density are required to clearly discriminate between the two possibilities.

### 2.26.4 References

Cammarano F., Goes S., Vacher P. and Giardini D., Inferring upper mantle temperatures from seismic velocities, *PEPI*, 138, 197-222, 2003.

Cammarano F. and B. Romanowicz, Insights into the nature of the transition zone from physically constrained inversion of long-period seismic data, *PNAS*, 104, 9139-9144, 2007

Faul, U.H., and I. Jackson, The seismological signature of temperature and grain size variations in the upper mantle, *Earth Planet. Sci. Lett.*, 234, 119-134, 2005.

Hirschmann, M.M., Mantle solidus: experimental constraints and the effects of peridotite composition., *Geochem. Geophys. Geosyst.*, 1, paper 2000GC000070, 2000.

Ringwood, A.E., Composition and Petrology of the Earth's Mantle, McGraw and Hill, New York, 1975.

Stixrude, L. and C. Lithgow-Bertelloni, Thermodynamics of mantle minerals: 1. Physical properties, *Geophys. J. Int.*, 162, 610-632, 2005.

## 2.27. Q Constraints on Upper Mantle Temperature

Fabio Cammarano and Barbara Romanowicz

### 2.27.1 Introduction

Imperfections in the crystalline structure of any mineral govern deformation and viscoelastic relaxation (anelasticity) at seismic frequencies. The study of different creep mechanisms and their mutual relevance at different P-T conditions (e.g., *Frost and Ashby* 1982) is useful in understanding the possible physical mechanisms that may also be responsible for seismic attenuation (i.e. at much higher frequencies). Recently, accurate experimental data of shear attenuation for mantle minerals at seismic frequencies (e.g., *Jackson et al.* 2002) are starting to provide a better understanding of such phenomena. A grain-boundary sliding mechanism seems compatible with laboratory experiments. Temperature and grain-size dependence for olivine polycrystalline samples have been accurately measured and modeled (*Faul and Jackson*, 2005). Pressure dependence, represented by activation volume, remains mostly unknown, however.

Within the Earth, viscoelastic relaxation causes dissipation and dispersion of seismic waves, or what is commonly referred to as intrinsic attenuation. Seismic attenuation mostly affects the amplitude of the waveforms. However, other effects related to the 3-D elastic structure of the Earth (focusing, scattering) and noise in the data make it difficult to retrieve information on the intrinsic attenuation structure of the Earth (see for a review, *Romanowicz*, 1998). Nevertheless, observations of attenuation of free oscillation and surface waves constrain the radial (1-D) attenuation profile of the Earth's upper mantle well enough, in spite of the well known discrepancy between the two datasets.

Here we use the modified Burgers model defined by *Faul and Jackson* (2005) to predict the quality factor ( $Q_S$ ) for a range of simple thermal and grain-size structures for the shallow upper mantle (down to 400 km). We assume the QL6 (*Durek and Ekström*, 1996) attenuation profile below that depth. We computed the  $Q_S$  values as a function of harmonic degree for fundamental and overtone spheroidal and toroidal modes, assuming a background reference velocity model. We found no distinguishable effects when testing two alternative velocity models (PREM *Dziewonski and Anderson*, 1980 and inverted PREM *Cammarano and Romanowicz*, 2007), indicating a weak sensitivity to the background velocity model used. We compared predicted values with seismic observations. Here, we show only comparisons with fundamental spheroidal modes (0S). We used five different compilations (see figure 2.58) based on attenuation of free oscillations and surface waves. Note that we do not

consider here the discrepancy between the two types of observations. We defined a misfit function as

$$\frac{1}{N_\ell} \sum_{\ell=1}^{N_\ell} \left| \frac{q_o - q_s}{q_o} \right| \quad (2.5)$$

and we computed the total misfit for each given structure. Consistent with the frequency of surface waves, we used a reference period of 150s in the computations of  $Q_S$  profiles with the Faul and Jackson model. The frequency dependence determined by their work is 0.27. Choosing a different period, within the band of surface waves, has a secondary effect on fitting observations compared to the unconstrained pressure dependence, as we shall discuss later.

### 2.27.2 Results

In order to highlight the characteristics of the trade-off between grain size and temperature, we show in figure 2.57 (top panel), the misfit values for isothermal structure from 100 to 400km for various constant grain sizes. We found that  $Q_S$  observations are much more sensitive to T than grain size, as shown by the contour lines in figure 2.57. Note that the “cold” structure of the lithospheric part does not affect measurements significantly. Indeed, we test that a negligible variation of the misfit pattern is obtained when using a standard 60My old oceanic geotherm for all thermal structures in the first 80km, plus a linear gradient in the 20km below to join the isotherms. The average temperature ( $\langle T \rangle$ ) of the upper mantle is very well constrained by seismic observations for a given grain size. For example, we found that a 1 mm grain size requires  $\langle T \rangle \sim 1500K$ , while a higher temperature ( $\sim 1600K$ ) is required around 1cm and slightly increases with coarser grain sizes. Subsequently, by giving a reference temperature at 100km of 1600K, more or less consistent with the temperature expected from a 60my old oceanic geotherm at that depth, we tested linear temperature gradients down to 400km, from  $-1.5^\circ/km$  to  $1.5^\circ/km$ , for various grain sizes (middle panel of figure 2.57). Again, we found that observations are able to discriminate between different thermal gradients with depth at given grain sizes. In general, positive gradients are required at grain sizes  $> 1cm$ , while negative ones are preferred for millimeter grain-sizes. There is an obvious trade-off, here not shown, between the Tref(100km) and the gradients below. A reference temperature of 1700K at 100km will be more compatible with positive thermal gradients. In particular, we found that an adiabatic  $1300^\circ C$  temperature is compatible with observations at

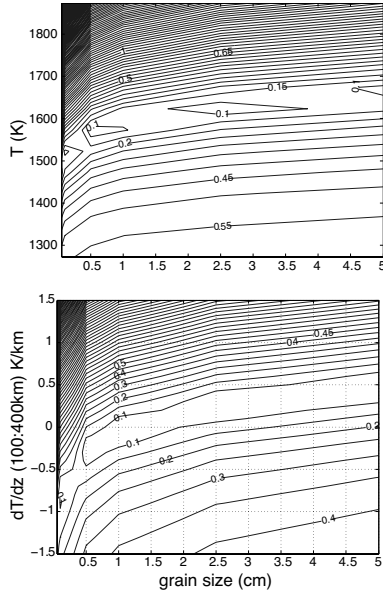


Figure 2.57: Misfit values to OS attenuation measurements for isothermal, constant grain-size upper mantle structure (right panel) and for linear thermal gradients from 100 to 400km (left panel). For left panel, reference temperature at 100km is 1600K.  $Q_S$  values are computed at period of 150s

1cm constant grain size. In figure 2.58, we give an example of  $Q_S$  depth profiles (top panel) and their predicted attenuation as a function of harmonic degree compared to OS measurements (bottom panel) for one best-fit model (grain size=2.5cm,  $dT/dz(K/km)=0.2$ , total misfit to OS attenuation measurements equal to 0.06) and one poorly fitting model (GS=2.5cm and  $dT/dz=0.8$ , misfit = 0.32). Note that because of the discrepancy between seismic observations, we are able to reach only minimum values of misfit equal to 0.06. In general, Q models based on T and GS structures do not have the first-order jump that characterizes seismic models around 220 km depth. Nevertheless, the fit to attenuation measurements can resolve between our different models. This preliminary result seems to point out that the constant increase in  $Q_S$  due to change in T or GS is sufficient to first order. Large uncertainties exist on the activation volume ( $V^*$ ). We tested the extreme values provided by Faul and Jackson, i.e.  $0.6$  and  $2 \times 10^{-5}$ , compared to  $1.2 \times 10^{-5}$  used in the model. Low values of  $V^*$  require negative thermal gradients, if Tref at 100km is set to 1600K. Conversely, very positive thermal gradients with depth are consistent with a high  $V^*$ . We anticipate that, in spite of the limitation imposed by  $V^*$  to interpret Q seismic observations, when P,T, GS dependent models are used together with elastic data at high P and T of mantle minerals for the interpretation of seismic data, we will be able to provide more constraints

on the temperature and composition structure of the upper mantle (see *Cammarano and Romanowicz 2007* and 2.26..

### 2.27.3 References

Cammarano F. and B. Romanowicz, Insights into the nature of the transition zone from physically constrained inversion of long-period seismic data, *PNAS*, 104, 9139-9144, 2007

Durek J.J. and G. Ekstrom, A radial model of anelasticity consistent with long period surface-wave attenuation, *Bull. Seis. Soc. Amer.*, 86, 144-158, 1996.

Dziewonski A.M. and D.L. Anderson, Preliminary reference Earth model, *Phys. Earth Planet. Int.*, 25, 297-356, 1981.

Faul, U.H., and I. Jackson, The seismological signature of temperature and grain size variations in the upper mantle, *Earth Planet. Sci. Lett.*, 234, 119-134, 2005.

Frost H.J. and M.F. Ashby, Deformation-Mechanism Maps: The Plasticity and Creep of Metals and Ceramics, 166 pp. Oxford: Pergamon Press, 1982.

Jackson I., J.D. Fitz Gerald, U.H. Faul and B.H. Tan Grain size sensitive seismic wave attenuation in polycrystalline olivine, *J. Geophys. Res.*, 107, B122360, 2002.

Romanowicz B., Attenuation tomography of the earth's mantle: A review of current status, *Pure and Applied Geophysics*, 153, 257-272, 1998.

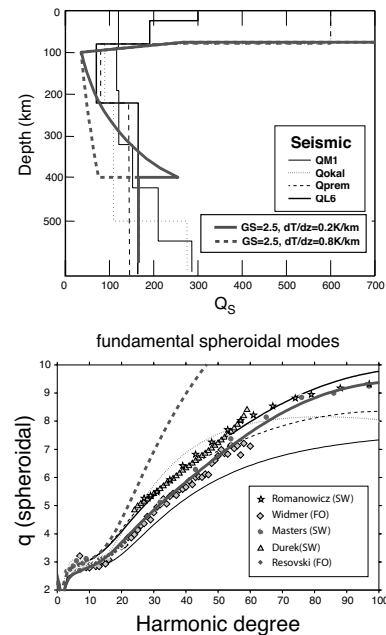


Figure 2.58: Examples of a good (solid red line) and a bad fit model (dashed).  $q$  is  $1000/Q_S$ . See text for details

## 2.28. Applying the Spectral Element Method to Tomography: Crustal Effects

Vedran Lekic and Barbara Romanowicz

### 2.28.1 Introduction

Crustal structure is characterized by large variations in topography/bathymetry of the surface and Moho, as well as by crustal velocity variations. While long period surface waves can be strongly affected by crustal structure, they lack the depth resolution necessary to constrain crustal thickness and velocity. Therefore, models of seismic velocities in the mantle depend on correcting the observed seismic waves for the effects of propagation through the crust. Typically, the effects of the crust are considered within the framework of normal mode summation and first order perturbation theory. One method, called the path average approximation (PAVA: *Woodhouse and Dziewonski, 1984*), assumes that the wave is only sensitive to structure along the great circle path joining the source with the receiver, and that this sensitivity is only a function of depth. Higher-order asymptotic approaches, such as non-linear asymptotic coupling theory (NACT: *Li and Romanowicz, 1995*), are capable of more accurately modeling the wave's actual sensitivity within the plane defined by the great circle path. However, in both approaches, the effects of crustal velocities are most often neglected, while the variations in Moho topography are considered as perturbations from an average Moho depth. On the other hand, the coupled Spectral Element Method (cSEM: *Capdeville et al., 2003*) is capable of fully accounting for 3D wave propagation through structure. Figure 2.59 illustrates that the differences between synthetic seismograms calculated using cSEM and NACT in a PREM mantle and realistic crustal structure can be large, especially on the transverse component. We explore the contamination of elastic models of the mantle that can result from such inadequacies in the forward modeling of crustal effects.

### 2.28.2 Synthetic Tests

In order to quantify the contamination of mantle models that can arise from the use of linear crustal corrections, we carry out a series of synthetic tests. Starting with PREM (*Dziewonski and Anderson, 1981*) and Moho topography and crustal velocities from CRUST2 (*Bassin et al, 2000*), we use the cSEM to generate a synthetic dataset of long-period (60 - 400 sec) transverse component waveforms for a set of 41 earthquakes and a realistic station distribution. Though restricted to first-orbit phases, the dataset provides good fundamental-mode and overtone coverage throughout Asia and the westernmost Pacific. Using the PAVA and NACT waveform modeling techniques, we correct the synthetic dataset for crustal

effects of CRUST2. We then invert the residual seismograms – which would ideally be very small – for mantle structure. Any retrieved mantle structure is contamination resulting from unmodeled crustal effects.

Figure 2.60 shows variations of isotropic shear speed obtained from an inversion of fundamental mode surface waves and overtones. The model explains 90 percent of the variance in the residual seismograms. Note the strong tectonic character of the mantle contamination. Mantle structure is artificially slow beneath continents, where linear crustal corrections underpredict the effects of crustal structure. Models developed using only transverse component higher modes and only fundamental mode surface waves are nearly identical to the model in Figure 2.60. Significant contamination of mantle structure extends to 100 km depth. Beneath Tibet, structure is different from surrounding mantle at a depth of 200 km.

In order to determine whether the contamination of mantle structure is the result of vertical smearing, we increase the depth parameterization by 5 cubic splines in the upper mantle – 2 in the crust. The retrieved model is substantially similar to that obtained previously, indicating that the mantle contamination is a feature of the waveforms, and not imposed by the parameterization.

Confronted with significant artifacts in mantle structure at depths as great as 200 km, we explore ways of compensating for the inadequacies of linear crustal corrections and minimizing the resulting contamination. Inversion for Moho and seafloor topography/bathymetry has been used in the construction of several global models (e.g. *Mégnin and Romanowicz, 2000*). Therefore, we invert for mantle velocity structure and Moho and seafloor topography simultaneously. The resulting model shows no significant contamination in the mantle while explaining the data as well as the model shown in Figure 2.60. However, the retrieved Moho and seafloor perturbations are inherently unphysical, since they result from inadequacies of linear crustal corrections and effects of 3D propagation in a laterally inhomogeneous crust.

### 2.28.3 Conclusion

Using a synthetic dataset of long period fundamental and high mode waveforms, we have quantified the contamination of mantle structure arising from the use of linear crustal corrections, which are inadequate at modeling the effects of crustal structure on waveforms, especially for the transverse component. Models derived using approximate forward modeling techniques may suffer from

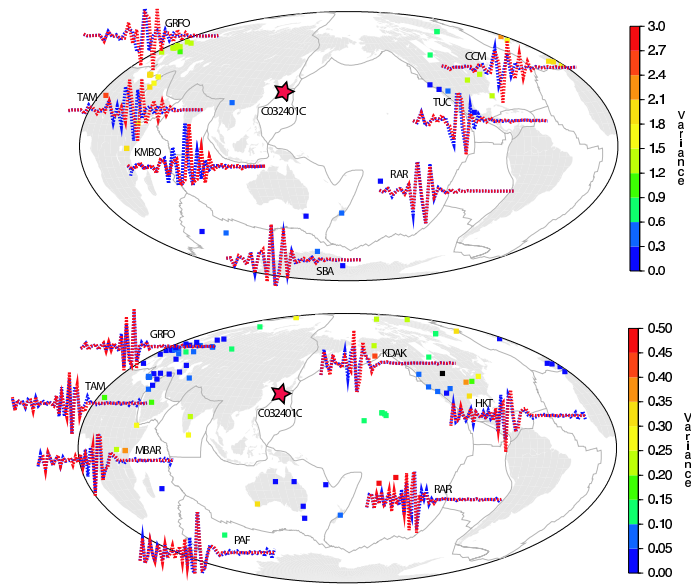


Figure 2.59: SEM (red) and NACT (blue) synthetic seismograms for the transverse (top) and vertical (bottom) component computed in a PREM mantle and a realistic crustal structure. The star denotes the event while stations squares are colored according to variance between the two synthetics.

artifacts at depths of 0 - 100 km. that arise from unmodelled crustal effects. Under Tibet, the contamination may extend to 200 km. These artifacts can be eliminated by inverting for Moho and seafloor topography/bathymetry; however, the retrieved perturbations are unphysical. In this study, we have examined the effects of linear crustal corrections, in which a single set of kernels is used. A much more accurate, though computationally heavy, approach involves non-linear crustal corrections, in which laterally varying structure kernels are considered along each path (e.g. *Montagner and Jobert, 1988*).

### 2.28.4 Acknowledgements

This research was supported by National Science Foundation grant NSF/EAR-0308750 and a National Science Foundation Graduate Fellowship held by VL.

### 2.28.5 References

Bassin, C., Laske, G. and G. Masters, 2000. The Current Limits of Resolution for Surface Wave Tomography in North America. *EOS Trans AGU 81*, F897.  
 Capdeville, Y., E. Chaljub, J.P. Vilotte and J.P. Montagner, 2003. Coupling the spectral element method with a modal solution for elastic wave propagation in global Earth models. *Geophys. J. Int.*, 152, 34-66.  
 Dziewonski, A.M. and D.L. Anderson, 1981. Preliminary reference Earth model. *Phys. Earth and Planetary*

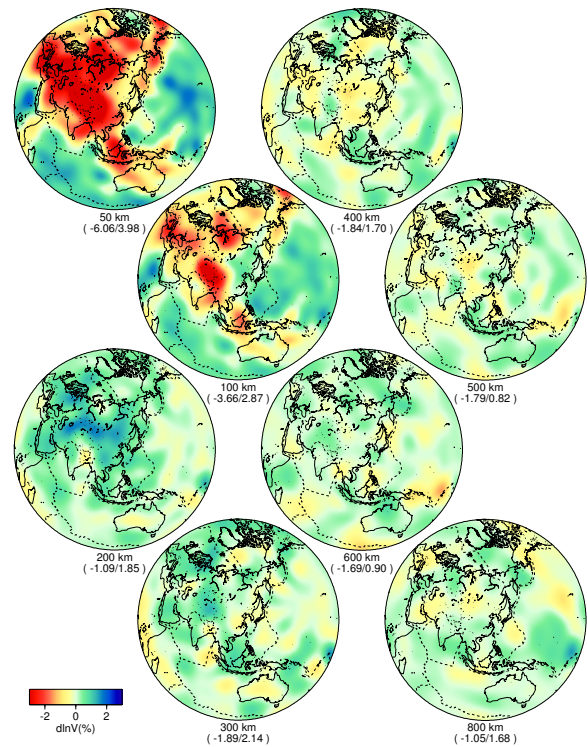


Figure 2.60: Isotropic shear wave speed model derived from synthetic transverse-component long-period fundamental mode surface wave and overtone waveforms. The starting model is a 1D mantle model with 3D crustal structure. Note the depth extent and tectonic nature of the retrieved artificial structure. Accounting for perturbations in Moho topography in the inversion removes this contamination.

*Int.*, 25, 297-356.

Li, X.D. and B. Romanowicz, 1995. Comparison of global waveform inversions with and without considering cross-branch modal coupling, *Geophys. J. Int.*, 121, 695-709.

Montagner, J.-P. and N. Jobert, 1988. Vectorial tomography, II, Application to the Indian Ocean. *Geophys. J. R. Astron. Soc.* 94, 309-344.

Megnin, C. and B. Romanowicz, 2000. The three-dimensional shear velocity structure of the mantle from the inversion of body, surface and higher-mode waveforms. *Geophys. J. Int.*, 143, 709-728.

Woodhouse, J.H. and A.M. Dziewonski, 1984. Mapping the upper mantle: three dimensional modeling of Earth structure by inversion of seismic waveforms. *J. Geophys. Res.* 89, 5953-5986.

## 2.29. Travel time analysis of Sdiff, SKS and SKKS phases

Akiko To and Barbara Romanowicz

### 2.29.1 Introduction

Global shear velocity tomographic models show two large-scale low velocity structures, so-called superplumes, in the lower mantle, under Africa and under the mid-Pacific. Sharp lateral velocity changes have been documented for some parts at the borders of the superplumes (e.g. *Wen, 2001, To et al., 2005, He et al., 2006*). We evaluate the distribution and amplitude of the anomalies given by a tomographic model for the D'' layer around the Pacific region by measuring travel times of Sdiff, SKS and SKKS phases. We search for sharp lateral velocity changes, which have not been found yet, at the borders and also inside, according to tomographic models, the superplume.

### 2.29.2 Distribution of the measured Sdiff travel times

We collected 1796 SKS, 1729 SKKS and 3861 Sdiff travel times which sample the Pacific region. In order to measure the travel time anomalies, synthetic waveforms from the 1D model (PREM) are first created for each trace. The anomalies are obtained by taking the cross correlations between PREM synthetic and observed waveforms. The waveforms are bandpass filtered between 100 and 17 second.

Figure 2.61(a) shows a distribution of measured Sdiff travel time anomalies with respect to PREM. Travel time anomalies are plotted at the midpoints of the diffracting portions of the Sdiff phases. The anomaly distribution has a good correlation with the tomographic model in the D'' layer. The figure indicates that the S wave structure in the D'' layer primarily contributes to the observed Sdiff anomalies.

Figure 2.61 (b) through (d) show the Sdiff travel time anomalies with respect to azimuth or back azimuth for some selected events or stations. Observed travel times of SKS and SKKS phases and synthetic travel times of Sdiff, which are calculated by ray theory, are also plotted. Lack of correlations of the travel time anomalies between Sdiff and other phases indicates that the Sdiff travel time anomalies are due to heterogeneities within the lower mantle. This is because the paths of Sdiff and SKKS are close to each other in the upper mantle but they are different in the lowermost mantle. The paths of SKS and Sdiff are more separated compared to Sdiff and SKKS in the upper mantle; however, the lack of correlation between SKS and Sdiff travel time anomalies can still indicate if the Sdiff anomalies are caused by near source or station structure or the lower mantle structure.

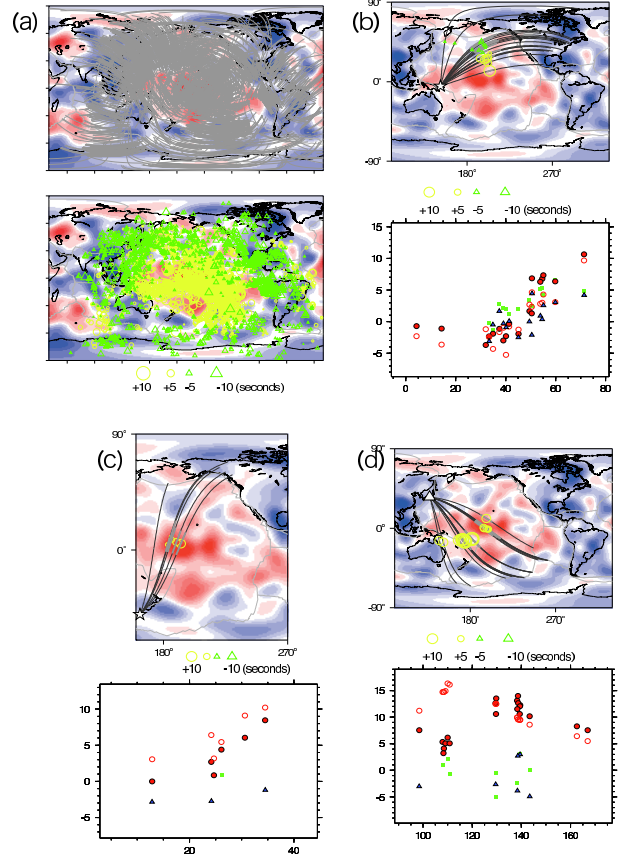


Figure 2.61: (a) Top panel: Distribution of diffracting portion of all the Sdiff paths whose travel time anomalies are measured. The background model is SAW24B16 (*Mégnin and Romanowicz, 2000*) at the depth of 2850km. Bottom panel: Sdiff travel time anomalies with respect to PREM is plotted at the midpoint of the paths. (b) (c) (d) Top panel: Sdiff travel time anomalies are plotted at the midpoint of the path. Diffracting portion of Sdiff waves are shown in thick gray lines. The back ground model is SAW24B16. The event locations are shown by stars. The station locations are shown by triangles. Bottom panel: Travel time anomalies of Sdiff (solid red circle), SKS (blue triangle) and SKKS (green square) phases with respect to azimuth or back azimuth. Synthetic travel time anomalies obtained by 1D ray theory for SAW24B16 are shown by open red circles.

Figure 2.61 (b) shows that trends of Sdiff travel time anomalies are well predicted in the Northern Pacific. The paths sample the border of the Pacific superplume. We

have previously reported that ray theory gives larger positive travel time anomaly estimations compared to a more exact method, such as the spectral element method, because of the lack of the finite frequency effects. With the finite frequency corrections, the positive anomalies of synthetic travel times become a few seconds smaller from what is shown in the figures. Figure 2.61(c) shows the data set with a rather steep change in Sdiff travel time anomalies with respect to azimuth, observed in the central Pacific. The paths sample inside the Pacific superplume. They indicate a possibility that the superplume is a gathering of multiple separated slow regions rather than a single big blob. Figure 2.61(d) shows one of the cases where the model over predicts the travel time anomalies.

### 2.29.3 Acknowledgements

The data were downloaded from IRIS DMC and CNSN.

### 2.29.4 References

Mégnin, C. and B. Romanowicz, The three-dimensional shear velocity structure of the mantle from the inversion of body, surface and higher-mode waveforms, *Geophys. J. Int.*, **143**, 709-728, 2000.

He, Y., Wen, L., and Zheng, T., Geographic boundary and shear velocity structure of the "Pacific anomaly" near the core-mantle boundary beneath western Pacific, *Earth Planet. Sci. Lett.*, **244**, 302-314, 2006.

To, A., B. Romanowicz, Y. Capdeville and N. Takeuchi, 3D effects of sharp boundaries at the borders of the African and Pacific Superplumes: observation and modeling, *Earth and Planet. Sci. Lett.*, **233**, 137-153, 2005

Wen, L., Seismic evidence for a rapidly varying compositional anomaly at the base of the Earth's mantle beneath the Indian Ocean, *Earth Planet. Sci. Lett.*, **194**, 83-95. 2001.

## 2.30. Locating Scatterers in the Mantle Using Array Analysis of PKP Precursors from an Earthquake Doublet

Aimin Cao and Barbara Romanowicz

### 2.30.1 Introduction

PKP precursors were first observed in the 1930's [Gutenberg and Richter, 1934], but it has taken more than sixty years to establish their origin. Array analyses of arrival times, slownesses, and spectra [Cleary and Haddon, 1972] have suggested that these precursors are scattered waves from the lower mantle rather than diffracted, reflected, or refracted waves from the core. Global simulations under the single and multiple scattering hypotheses have determined that small-scale, weak ( $< \sim 1\%$ ) heterogeneities distributed throughout the mantle likely contribute to the PKP precursor wave-trains, with perhaps a concentration in the lowermost mantle [Hedlin *et al.*, 1997].

Small-scale heterogeneities have important geodynamic significance in mantle convection. In particular, subducted slabs can survive for billions of years in the lower mantle due to incomplete mixing, and so regional distributions of small-scale heterogeneity in subduction or upwelling zones might help us sketch out local depth ranges of the mantle flow field and understand better the distribution and nature of heterogeneity. Given the fact that current resolution provided by seismic tomography is not high enough to image structures at scales of  $\sim 1-10\text{km}$ , locating and estimating the size and strength of individual scatterers responsible for PKP precursors provides a potential complementary approach.

Recent studies have derived general properties of the PKP precursor field from the analysis of high quality data from the global seismic network or from large aperture seismic arrays. The large aperture of the arrays considered prevented the use of standard array processing techniques such as the construction of vespagrams. Even when considering stacks across small-aperture arrays such as Norsar, these studies have primarily modelled stacks of the envelopes of the precursor train, and only in a statistical sense. In most cases, these authors have invoked the presence of partial melting associated with Ultra Low Velocity zones to interpret the large velocity contrasts ( $\sim 10\%$ ) necessary to explain the observed precursor amplitudes.

However, very few studies have attempted to locate individual scatterers in the mantle, because PKP precursors are usually weak and their arrivals overlap. Doornbos [1988] tried to locate the scattering regions using the NORSAR seismic array, but he pointed out that the uncertainty in the precursor slowness measurements was unknown. The arrival time of the onset of the precursor

train has also been used to try and locate the region of observed strong scattering. An added complication comes from the fact that there is ambiguity between source and receiver side scattering. In general, this is resolved indirectly, by comparing paths in different azimuths from the source or receiver side, and proposing an interpretation most compatible with all observations. Hedlin *et al.* showed that the ambiguity can be resolved in many regions of the lowermost mantle by inverting a global dataset of precursor average power estimates, in the framework of Rayleigh-Born scattering theory. Finally, even if the slowness and back-azimuth of a precursor can be precisely estimated using a small-aperture seismic array, it is also necessary to know if the precursor was scattered from PKPbc or PKPab on the receiver side or on the source side, in order to uniquely estimate the latitude, longitude, and depth of the corresponding scatterer. Since the amplitude of PKPbc is generally much larger than that of PKPab, it is often assumed that most of the scattering originates on the bc branch. However, until now, it was not possible to demonstrate that explicitly.

Doublet events, for which hypocenters, moment tensors, and source time history are basically identical, provide a powerful means to estimate repeatability of measurements of precursor slowness and back-azimuth. Fortunately, a very high quality earthquake doublet was reported recently [Zhang *et al.*, 2006]. Highly similar waveforms were recorded at 102 stations with a broad coverage of epicentral distances and azimuths, and the hypocenter separation of the two events was estimated to be less than  $1.0\text{km}$ . Further evidence of the unique quality of this doublet was obtained from the analysis of PP phases, which have identical waveforms in a time interval of at least 70 sec, and well into the PP coda. In this paper, we use this doublet to conduct array analyses of PKP precursors. Taking advantage of an effective stacking technique, we obtain clear and isolated doublet PKP precursors (Figure 1), which, we will argue, originate from individual scatterers in the mantle. The stability of the estimated slowness and back-azimuth enable us to obtain reliable locations of several of these scatterers in the lower mantle.

### 2.30.2 Data and Results

The high quality short-period Yellowstone Seismograph Array (YK) is a long-term primary array in the International Monitoring System (IMS) seismic network, act-

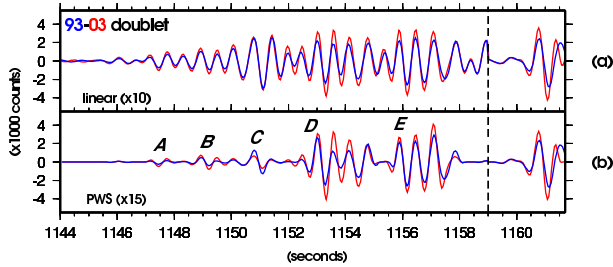


Figure 2.62: Stacked waveforms of 1993 (blue) and 2003 (red) doublet events filtered between 1 and 2 Hz. (a) Linear stacking. Waveforms before the dashed line are amplified 10 times. PKP precursor train is apparent, but all precursors are mixed together. (b) Phase Weighted Stacking (PWS). Waveforms before the dashed line are amplified 15 times. Individual precursors A, B, and C stand out. Precursors D and E are likely a mixture of scattered energy arriving sequentially from multiple scatterers. The PKIKP phase arrives after the dashed line.

ing as the backbone facility for nuclear explosion monitoring. The epicentral distance from YK to the doublet (1993.12.01.00:59:01.2,  $m_b = 5.5$ , depth=33 km; 2003.09.06.15:46:59.9,  $m_b = 5.6$ , depth=33 km in the PDE catalog) at SSI is  $\sim 137.8^\circ$ . 18 of all 19 stations at YK recorded very high signal-to-noise PKP precursors for both events. In order to enhance the precursor signals, we filtered the original seismograms in the frequency range of 1 to 2 Hz. Before stacking, we aligned traces with respect to PKIKP phases by means of cross-correlation and performed array-sided travel time corrections to remove the influence of heterogeneities just beneath the seismic array. We applied two different stacking methods: linear stacking (Fig. 1a) and Phase-Weighted Stacking (PWS) (Fig. 1b).

Based on ray tracing and the single-scattering assumption, we are able to locate the scattering regions responsible for the individual PKP precursors, using our precise measurements of slownesses, back-azimuths, and differential arrival times. Comprehensive consideration of the high quality differential arrival times, slowness, and back-azimuth deviations enables us to locate the mantle scatterers for precursors A, B, D, and E (Fig. 2). Precursors A and B are scattered at the CMB, while precursors D and E are scattered at  $\sim 420\text{km}$  and  $\sim 620\text{km}$  above the CMB, respectively.

### 2.30.3 References

Cao, A., and B. Romanowicz, Locating scatterers in the mantle using array analysis of PKP precursors from an earthquake doublet. *Earth Planet. Sci. Lett.*, 255, 22-31, 2007.

Cleary, J.R., and R.A. Haddon, Seismic wave scatter-

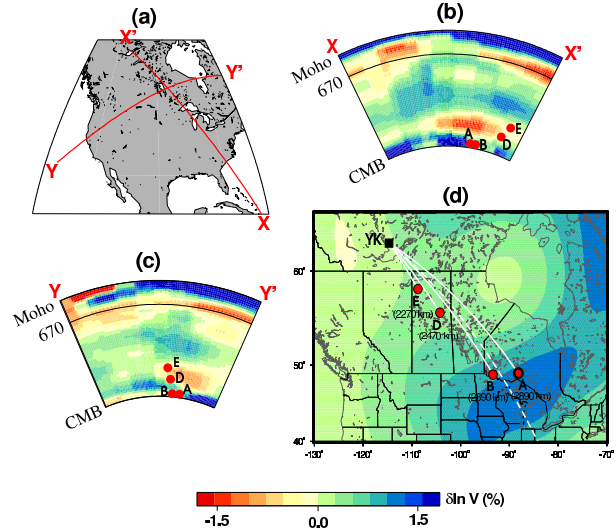


Figure 2.63: Distribution of seismic scatterers in the lower mantle. (a) Map view indicating the location of two vertical profiles in the region of our study. (b) and (c) Vertical cross-sections of the SAW24B16 shear wave tomographic model [Megnin and Romanowicz, 2000]. Profile XX' is along the great circle containing source and receivers, and profile YY' is perpendicular to it. Red dots show the projected locations of our constrained mantle scatterers into the cross-sections. (d) Map view of the distribution of seismic scatterers in the lower mantle. Black square denotes the Yellowknife seismic array (YK). Red dots indicate our located scatterers. Solid white lines are the horizontal projections of the ray paths of precursors. The dashed white line is part of the great circle from the sources in South Sandwich Islands (SSI) to YK. The background tomographic model shows the distribution of shear-wave velocity at a depth of  $2800\text{km}$ .

ing near the core-mantle boundary: a new interpretation of precursors to PKP, *Nature*, 240, 549-551, 1972.

Doornbos, D.J., Multiple scattering by topographic relief with application to the core-mantle boundary, *Geophys. J. Int.*, 92, 465-478, 1988.

Gutenberg, B., and C.F. Richter, On seismic waves: I, *Gerlands Beitr. z. Geophysik.*, 43, 56-133, 1934.

Hedlin, M.A., P.M. Shearer, P.S. Earle, Seismic evidence for small-scale heterogeneity throughout the Earth's mantle, *Nature*, 387, 145-150, 1997.

Megnin, C., and B. Romanowicz, The three-dimensional shear velocity structure of the mantle from the inversion of body, surface and higher-mode waveforms, *Geophys. J. Int.*, 143, 709-728, 2000.

## 2.31. Test of Innermost Inner Core Anisotropic Models

Aimin Cao and Barbara Romanowicz

### 2.31.1 Introduction

Since the first evidence for inner core anisotropy was presented [Morelli *et al.*, 1986; Woodhouse *et al.*, 1986], increasingly complex models have been proposed. It has been documented that anisotropy increases with depth in the inner core, and that it is much weaker in the quasi-eastern than in the quasi-western hemisphere. At the top of the inner core ( $< \sim 100km$ ), P-wave velocity may be isotropic and faster in the quasi-eastern hemisphere than in the quasi-western hemisphere.

The above complexity was questioned by several authors [Bréger *et al.*, 2000; Romanowicz *et al.*, 2002; Ishii *et al.*, 2002]. The complex lateral variations in P-wave velocity could be due to mantle, and possibly outer core, heterogeneity [Bréger *et al.*, 2000; Romanowicz *et al.*, 2002]. Ishii *et al.* (2002) suggested that there need not be an isotropic layer at the top of the inner core and that both body wave and normal mode observations can be explained by a model with constant anisotropy in the inner core.

More recently, the existence of an Innermost Inner Core (IMIC), within which the anisotropic characteristics are distinct, was proposed, respectively based on body wave [Ishii and Dziewonski, 2002] (hereafter referred to as ID02) and normal mode data [Beghein and Trampert, 2003] (hereafter referred to as BT03). However, the structures proposed are inconsistent: not only are the radii of the IMIC different ( $\sim 300km$  [ID02] versus  $\sim 400km$  [BT03]), but, more importantly, so are the slowest directions of anisotropy: in one model, the slowest direction is  $\sim 45^\circ$  with respect to the earth's spinning axis (ID02); the other is along the spinning axis (BT03). Cormier and Stroujkova (2005) tested the IMIC model of ID02 using PKIKP waveform modeling and suggested a much larger radius ( $\sim 500km$ ). Because the existence of the suggested IMIC is thought to be closely related to the early stages of inner core formation, it is important to try and clarify this inconsistency through further study.

The ID02 dataset is derived from the International Seismological Center (ISC) bulletins, and their study relies on the statistical analysis of a large noisy dataset. On the other hand, BT03 used normal mode data, the resolution of which decreases towards the center of the inner core. In this paper, we assemble a new dataset of absolute PKIKP (Fig. 2.64) travel time residuals, which are measured on high quality digital broadband seismograms recorded in global and local seismic networks (e.g., GSN, GEOSCOPE, and PASSCAL), to explore the seismic anisotropy in the central part of the inner core.

### 2.31.2 Data and Results

We systematically downloaded broadband vertical component seismograms ( $M_w > 6.0$ , depth  $> 0$  km) from the IRIS Data Management Center (DMC) corresponding to the epicentral distance range  $150^\circ$  to  $180^\circ$ , and for the time period 1990 to 2003, for which the relocated EHB event catalog is available [Engdahl *et al.*, 1998]. Thousands of seismograms recorded at global and regional networks were collected. Absolute PKIKP travel time residuals were measured with respect to the reference seismic model PREM, using relocated hypocenter and origin time as given in the EHB catalog, and correcting for ellipticity. We also conducted corrections for mantle heterogeneities using a P-wave global tomography model.

In order to test seismic models of ID02 and BT03, we calculate the predicted absolute PKIKP travel time residuals using the parameters of their respective anisotropic models [Cao and Romanowicz, 2007].

We divide our observations into four epicentral distance ranges (Fig. 2.65), corresponding to different depths of penetration of PKIKP in the inner core. In the epicentral distance range  $173^\circ$  to  $180^\circ$ , which corresponds to rays that sample the very center of the inner core, we confirm the trend observed by ID02, namely that the travel time residuals are maximum at intermediate angles  $\xi$ , decreasing both for polar ( $\xi \sim 0$ ) and for equatorial ( $\xi \sim 90^\circ$ ) paths. This means that the slowest P-wave velocity direction is not along the equatorial plane. This is why ID02 proposed the existence of an IMIC with a radius of  $\sim 300km$  and a slowest direction oriented at  $\sim 45^\circ$  with respect to the earth's rotation axis. However, our dataset indicates that the same trend is also present at shorter epicentral distances. More importantly, in the epicentral distance range  $165^\circ$  to  $180^\circ$ , neither the ID02 model nor the BT03 model can fit our observations. This fact suggests two possibilities: (1) there is an IMIC, but its anisotropic character is different from that in ID02 and BT03; (2) there is no IMIC.

First, we assume the existence of an IMIC. While keeping the upper layer anisotropic structure fixed, as given in ID02 (bulk constant anisotropy) and in BT03 (depth-dependent), respectively, we correct the observed PKIKP travel time residuals ( $\delta t'$ ) (Fig. 2.65) by subtracting  $\eta_0$  and  $\delta t_{upper}$  (contributed by the upper layer) and then invert for the anisotropic parameters A and B in the IMIC. It is clear that the constrained anisotropy in the IMIC strongly depends on the anisotropic structure in the upper layer of the inner core. If the upper layer has the bulk

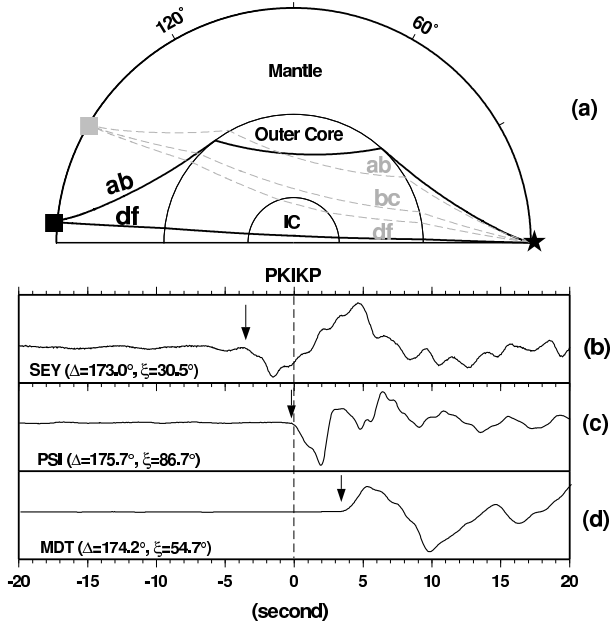


Figure 2.64: (a) Ray paths of PKIKP and PKP phases. The black solid line shows the ray path of PKIKP, which is used in this study. The event and stations are indicated by a star and squares, respectively. (b)-(d) Examples of PKIKP absolute travel time residual measurement.

constant anisotropic structure as used in ID02, the optimal IMIC radius inverted from our dataset is  $\sim 480\text{km}$ , and the corresponding variance reduction is 0.89. In contrast, the IMIC radius (300 km) suggested in ID02 is so small that the corresponding variance reduction is very low ( $\sim 0.3$ ). If the upper layer has the depth-dependent anisotropic structure as suggested in BT03, the optimal IMIC radius inverted from our dataset is  $\sim 530\text{km}$ , and the corresponding variance reduction is 0.94. Thus an IMIC with a depth-dependent anisotropic upper layer fits our dataset better. In both cases, the constrained IMIC radii are compatible with the radius suggested by *Cormier and Stroujkova* (2005) on the basis of PKIKP waveform modeling. In addition to the radius, the inverted IMIC anisotropic character is also strongly dependent on the upper layer anisotropy. The constrained slowest directions are  $\sim 50^\circ$  and  $\sim 55^\circ$ , when considering a ID02 or BT03 upper layer, respectively. And the constrained P-wave velocities along the axis of the earth’s rotation are 4.2% and 1.1% faster than that suggested in ID02, respectively.

Second, if there is no IMIC in the inner core, the variance reduction for a one-layer model is small (0.35). A constant anisotropy, one-layer, model can provide good fits to our observations in the epicentral distance range of  $165^\circ$  to  $170^\circ$ , but in other ranges, particularly from  $173^\circ$  to  $180^\circ$ , it does not (Fig.2.65). Both of the inverted

“two-layer” IMIC models fit our observations very well in the epicentral distance ranges of  $173^\circ$  to  $180^\circ$  and  $170^\circ$  to  $173^\circ$ . In the other two epicentral distance ranges ( $150^\circ$  to  $165^\circ$  and  $165^\circ$  to  $170^\circ$ ), however, the model with an upper layer as in BT03-1 fits our dataset better (Fig. 2). This suggests that the anisotropic structure in the upper part of the inner core most likely changes with depth.

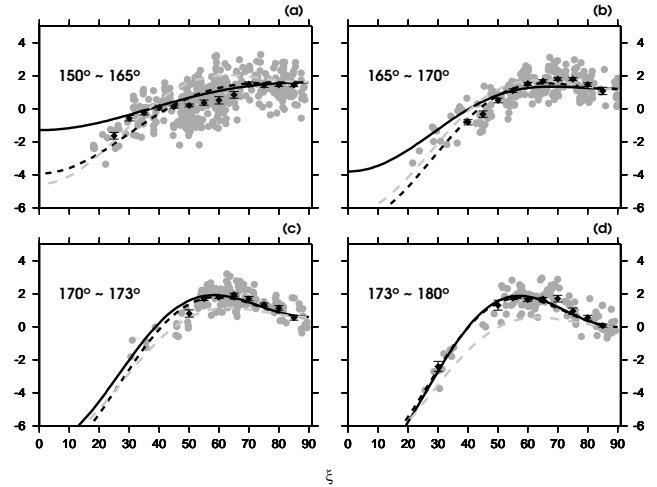


Figure 2.65: Theoretical PKIKP travel time residuals as a function of  $\xi$ , which include  $\delta t_{IMIC}$  (contributed by our inverted IMIC),  $\delta t_{upper}$  (contributed by the upper layer), and  $\eta_0$ . The solid and dashed black lines correspond to the best fitting IMIC models with a bulk constant (ID02-1) and a depth-dependent (BT03-1) anisotropic upper layer, respectively. The dashed grey line corresponds to a one-layer (i.e., no IMIC) anisotropic inner core model. The grey dots are data.

### 2.31.3 References

- Beghein, C., and J. Trampert, Robust normal mode constraints on inner core anisotropy from model space search, *Science*, 299, 552-555, 2003.
- Cao, A., and B. Romanowicz, Test of the innermost inner core models using broadband PKIKP travel time residuals. *Geophys. Res. Lett.*, 34, L08303, 2007.
- Ishii, M., and A.M. Dziewonski, The innermost inner core of the earth: evidence for a change in anisotropic behavior at the radius of about 300km, *Proc. Natl. Acad. Sci. U.S.A.*, 22, 14026-14030, 2002.
- Romanowicz, B., H. Tkalcic, and L. Bréger, On the origin of complexity in PKP travel time data from broadband records, in *Earth’s Core: Dynamics, Structure, Rotation*, V. Dehant and K. Creager Eds, *AGU Geodynamics Series*, 31, 31-44, 2002.

## 2.32. GPS exploration of the elastic properties across and within the Northern San Andreas Fault zone and heterogeneous elastic dislocation models

Romain Jolivet (Ecole Normale Supérieure de Paris), Roland Bürgmann and Nicolas Houlié

### 2.32.1 Introduction

The Northern San Francisco Bay Area (hereafter “North Bay”) is sliced by three major right-lateral strike-slip faults, the northern San Andreas Fault (SAF), the Rodgers Creek Fault (RCF) and the Green Valley Fault (GVF). The RCF represents the North Bay continuation of the Hayward fault zone and the GVF is the northern extension of the Concord fault. North of the juncture with the San Gregorio fault, geodetic and geologic data suggest a SAF slip rate of  $20\text{--}25 \text{ mm.yr}^{-1}$  (*d’Alessio et al., 2007, Lisowski et al., 1991*). Geodetically determined slip rates range from  $20.2 \pm 1.4 \text{ mm.yr}^{-1}$  (*d’Alessio et al., 2007*) to  $23 \pm 3 \text{ mm.yr}^{-1}$  (*Frey Mueller et al., 1999*). The remainder of the  $40 \text{ mm.yr}^{-1}$  of Pacific plate to Sierra Nevada Great Valley microplate motion is primarily accommodated by the RCF and the GVF.

Earthquake cycle deformation is commonly modeled assuming laterally homogeneous elastic properties in the Earth’s crust. First-order variations in rock elastic strength both across and within fault zones can, however, strongly impact inferences of fault slip parameters and earthquake rupture characteristics. Near Point Reyes, the SAF separates two different geologic terranes. On the east side of the fault is the Franciscan Complex, made of a mixture of Mesozoic oceanic crustal rocks and sediments, which were accreted onto the North American continent during subduction of the Farallon plate. On the west side of the SAF is the Salinian terrane, which is composed of Cretaceous granitic and metamorphic rocks, overlain by Tertiary sedimentary rocks and Quaternary fluvial terraces. *Prescott and Yu, 1986, Lisowski et al., 1991* describe an asymmetric pattern along a geodetically measured surface velocity profile across to SAF at Point Reyes, which can be explained by higher rigidities to the SW of the fault. *Le Pichon et al., 2005*, describes also an asymmetric pattern further north along the SAF, at Point Arena, but not at Point Reyes. *Chen & Frey Mueller, 2002*, rely on near-fault strain rates determined from trilateration and GPS measurements to infer a  $2\text{-km}$ -wide near-fault compliant zone (with 50% reduced rigidity) near Bodega Bay and Tomales Bay. Here we use densely spaced GPS velocities across the SAF to evaluate changes in elastic properties and within the SAF zone.

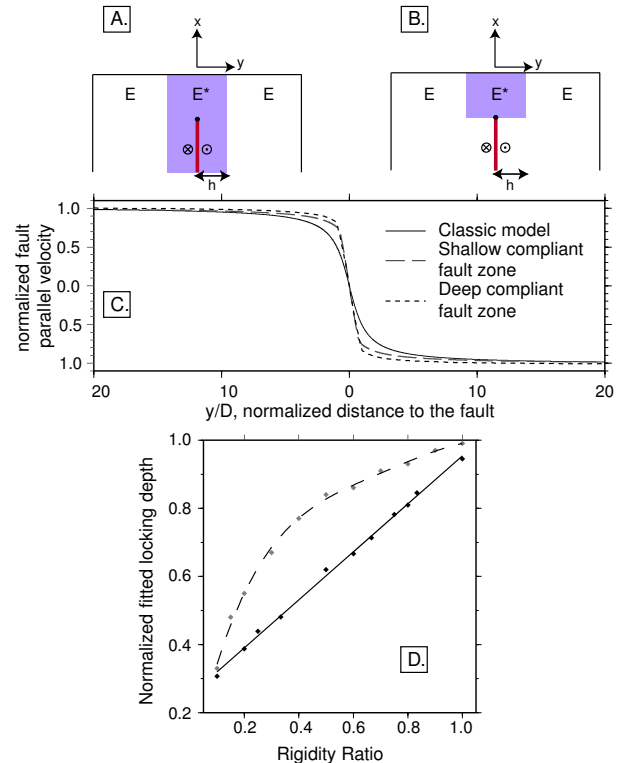


Figure 2.66: Model geometry of A. deep and B. shallow CFZM. The shaded area is the weak fault zone. C. Comparison between a 10 km locking depth classic screw dislocation model (continuous line), a 10 km locking depth Shallow CFZM (long-dashed grey line) and a 10 km locking depth Deep CFZM (dashed black line) with rigidity in the 2-km-wide fault zone being reduced by 80%. D. Locking depth determined by fitting velocity profiles (400 km long with a point spacing of 0.5 km) calculated with the CFZMs with the half-space equation 2.6. The grey dots are the best-fit locking depth for the deep CFZM and the dashed line is the corresponding polynomial fit. The black dots are the fitted locking depth for the shallow CFZM and the continuous line is the corresponding linear fit.

### 2.32.2 Heterogeneous Elastic Models

The classic way to interpret a GPS-derived velocity profile across a strike-slip fault is, assuming that the movement is only horizontal, to use the screw disloca-

tion model (*Savage and Burford, 1973*):

$$v(y) = \frac{v_{max}}{\pi} \operatorname{atan}\left(\frac{y}{D}\right) \quad (2.6)$$

Where  $v$  is the predicted fault-parallel velocity of a surface point at distance  $y$  from the fault and  $v_{max}$  is the far field velocity.  $v_{max}$  is also the slip rate on the dislocation below the locking depth  $D$ . This model assumes an infinite dislocation buried in a semi-infinite elastic medium. Next we consider laterally heterogeneous models that account for variation of elastic properties across and within the fault zone.

We first consider the model developed by *Le Pichon et al., 2005*, where the fault separates two elastic media, with different Young's modulus  $E_1$  and  $E_2$ . They consequently use a rigidity ratio,  $K$ , in the following equations:

$$y < 0 \Rightarrow V(y) = KV_{max} + \left(\frac{2KV_{max}}{\pi}\right) \operatorname{atan}\left(\frac{y}{D}\right) \quad (2.7)$$

$$y > 0 \Rightarrow V(y) = KV_{max} + \left(\frac{2(1-K)V_{max}}{\pi}\right) \operatorname{atan}\left(\frac{y}{D}\right)$$

Where  $V(y)$  is again the velocity at a distance  $y$  from the fault,  $V_{max}$  is the far field velocity,  $D$  the locking depth, and  $K = \frac{E_2}{E_1 + E_2}$  is the asymmetry ratio.

We also evaluate the deep Compliant Fault Zone Model (CFZM) developed in *Chen & Freymueller, 2002*, following *Rybicki and Kasahara, 1977*. A low rigidity fault zone is introduced between two elastic blocks (Figure 2.66).

This model (A. in Figure 2.66) is based on an infinitely deep weak fault zone. If we consider that the fault zone is weak because of damage caused by repeated earthquakes, this zone should not extend deeper than the locking depth. Therefore, we developed, using Finite Element Modeling (*Chéry et al., 2001*), a shallow CFZM (B. in Figure 2.66). Both models tend to localize the deformation close to the fault trace, but the shear is more localized in the shallow CFZM.

We tried to fit the computed velocity profiles obtained with both CFZMs with the classic screw dislocation model, to evaluate the trade-off between the rigidity ratio and the obtained best-fit locking depth. For both models, there is an inverse relationship between the rigidity ratio and the fitted locking depth (linear for the deep CFZM and curved for the shallow CFZM). As the difference between the CFZMs and the fitted classic models is smaller than the typical error obtained with geodetic data (typically  $1 \text{ mm.yr}^{-1}$ ), we cannot distinguish between a shallow locking depth and a compliant fault zone, relying only on geodetic data. Thus it is important to have independent constraints on the locking depth, for instance from the depth extent of microseismicity.

### 2.32.3 GPS velocities along the Northern San Andreas Fault

We collected GPS data in Bodega Bay and Tomales Bay, using 1996-2000 GPS measurements from *Chen & Freymueller (2002)* to calculate the velocities. We also used data from the Point Reyes profile, provided by the Bay Area Velocity Unification (BAVU), a compilation of the San Francisco bay area GPS velocities (*d'Alessio et al., 2005*). The data are processed using the GAMIT/GLOBK GPS analysis software. The site velocities are shown with respect to BARD continuous GPS station LUTZ in Figure 2.

A first analysis with a simple screw dislocation model, based on three parallel faults (SAF, RCF and GVF) provides a  $23 \pm 1 \text{ mm.yr}^{-1}$  slip rate on the SAF, with a  $14 \pm 2 \text{ km}$  locking depth, while the whole system is accommodating  $40 \text{ mm.yr}^{-1}$  of fault parallel displacement (we find a  $8 \pm 1 \text{ mm.yr}^{-1}$  slip rate on the RCF and  $9 \pm 1 \text{ mm.yr}^{-1}$  on the GVF)(Figure 2.67). *d'Alessio et al. (2007)* show that the velocity of the Farallon islands with respect to the Pacific plate is about  $2.9 \text{ mm.yr}^{-1}$  consistent with our modelled velocity field. But the half-space model velocity for the Farallon Island station is 4 to 5  $\text{mm.yr}^{-1}$  faster than the actual measured velocity. We next consider asymmetric models with a rigidity contrast across the SAF, fitting the data with the equation 2.8. We find that the modeled velocity profile better matches the Farallon Islands velocity with a 0.41 K ratio. Thus, we infer that the Salinian terrane has a rigidity 1.4 times higher than the Franciscan complex to the east of the SAF. Our results suggest an  $18 \text{ mm.yr}^{-1}$  slip rate on the SAF, with a  $10 \text{ km}$  locking depth. There is a significant trade-off between the inferred slip rate on the SAF and the rigidity contrast across the fault, with smaller rigidity contrasts leading to higher inferred slip rates.

The two networks across the SAF located further north, one in Tomales Bay and one in Bodega Bay, allow us to consider if the SAF represents a low-rigidity fault zone. Our preferred model for the Tomales Bay profile is a classic dislocation, with a  $21 \text{ mm.yr}^{-1}$  slip rate on the SAF, with a  $12 \text{ km}$  locking depth. We did not explore the corresponding trade-off but as our data set doesn't extend far away on both side of the fault, even using the PS-SAR data from *Funning et al., 2007*, the determined parameters are not well constrained. In Bodega Bay, our preferred model is based on a deep CFZM, with a  $28 \text{ mm.yr}^{-1}$  slip rate on the SAF, with a  $15 \text{ km}$  locking depth. The compliant zone is 40% weaker than the surrounding medium. But a classic homogeneous model with a  $24 \text{ mm.yr}^{-1}$  slip rate and a  $7 \text{ km}$  locking depth on the SAF satisfies the near-field data as well, as shown by the first-order trade-off between locking depth and the compliant fault zone rigidity contrast we found in the previous section. We prefer a  $15 \text{ km}$  locking depth and consequently introducing this deep CFZM because

of the microseismicity near the Point Reyes profile, assuming that there is no significant changes in the locking depth.

#### 2.32.4 Acknowledgements

This project was funded by the USGS National Earthquake Hazard Reduction Program (NEHRP). We would like to thank J. Freymueller for his help during the GPS survey. Thanks to R. Bürgmann for having me in his team during 6 months and to all the Berkeley Active Tectonics Group.

#### 2.32.5 References

d'Alessio, M. A., Johanson, I. A., Bürgmann, R., Schmidt, D. A. and Murray, M. H., Slicing up the San Francisco Bay Area: Block kinematics and fault slip rates from GPS-derived surface velocities, *J. Geophys. Res.*, *110*, B0640, 2007.

Chen, Q. and Freymueller, J. T., Geodetic evidence for a near-fault compliant zone along the San Andreas Fault in the San Francisco Bay Area, *J. Geophys. Res.*, *92*, 2002.

Chéry, J., Zoback, M. and Hassani, R., Rheology, strain and stress of the San Andreas Fault in Central and Northern California: A 3-d thermomechanical modeling study, *J. Geophys. Res.*, *106*, B08406, 2001.

Freymueller, J. T., Murray, M. H., Segall, P. and Castillo, D., Kinematics of the Pacific-North America plate boundary zone, northern California, *J. Geophys. Res.*, *104*, 7419-7442, 1999.

Funning, G. J., Bürgmann, R., Ferretti, A. and Fumagalli, A. Creep on the Rodgers Creek fault, northern San Francisco Bay area from 10 year PS-InSAR dataset. *submitted*, 2007.

Le Pichon, X., Kreemer, C. and Chamot-Rooke, N., Asymmetry in elastic properties and the evolution of large continental strike-slip faults, *J. Geophys. Res.*, *110*, B03405, 2005.

Lisowski, M., Savage, J. C. and Prescott, W. H., The Velocity Field Along the San Andreas Fault in Central and Southern California, *J. Geophys. Res.*, *96*, 8369-8389, 1991.

Prescott, W. H. and Yu, S. B., Geodetic measurement of horizontal deformation in the northern San Francisco Bay region, California, *J. Geophys. Res.*, *91*, 7475-7484, 1986

Savage, J. and Burford, R., Geodetic determination of relative plate motion in central California, *J. Geophys. Res.*, 1973

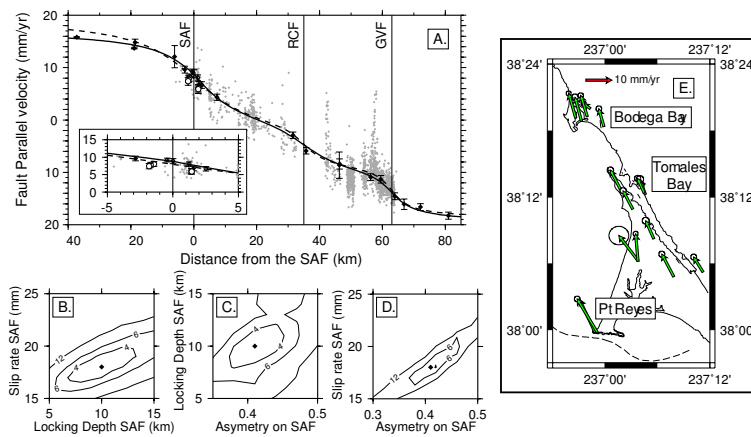


Figure 2.67: A. Best fit dislocation models for the Point Reyes profile. The black dots are the fault-parallel projected GPS velocities with their associated error bars. The grey dots are the PS-SAR data from (*Funning et al., 2007*). The dashed line is the best classic (elastic half-space) dislocation model. The continuous line is our preferred asymmetric model with a K ratio of 0.41 that better matches the observed velocity of the westernmost GPS site on the Farallon Islands. B. Trade off between the Locking Depth and the Slip Rate on the SAF. Contoured values are the sum of the weighted squared residuals divided by the number of data points C. Trade off between the Asymmetry Ratio and the Locking Depth on the SAF. D. Trade off between the Asymmetry Ratio and the Slip Rate on the SAF.



## Chapter 3

# BSL Operations

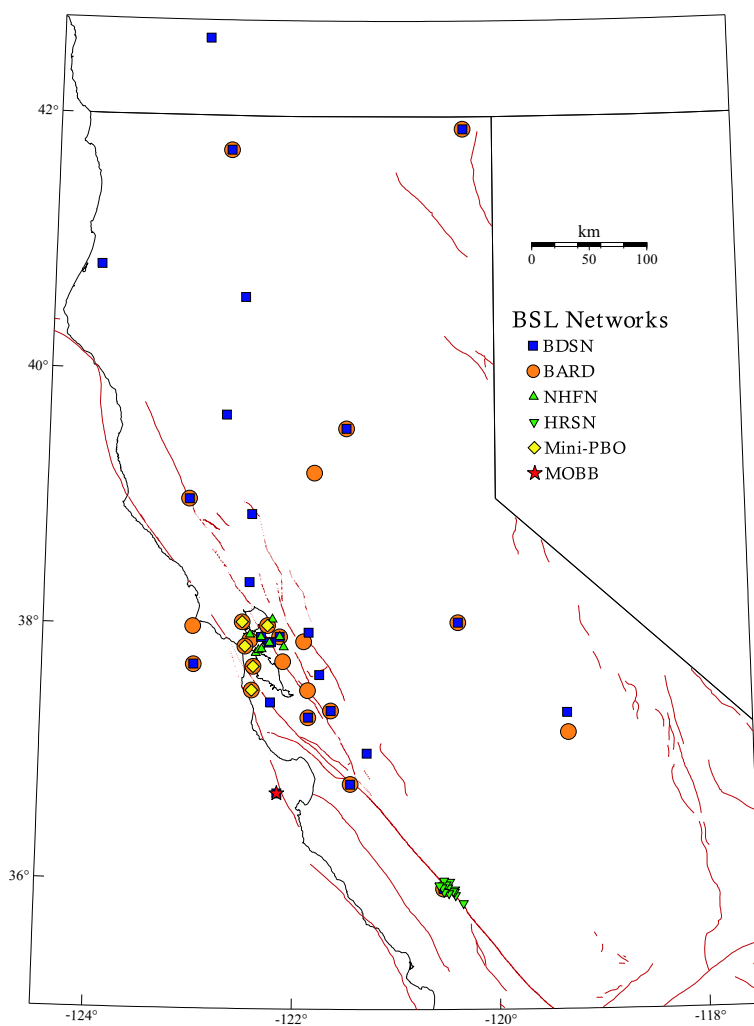


Figure 3.1: Map illustrating the distribution of BSL networks in northern and central California.

## 3.1. Berkeley Digital Seismic Network

### 3.1.1 Introduction

The Berkeley Digital Seismic Network (BDSN) is a regional network of very broadband and strong motion seismic stations spanning northern California and linked to UC Berkeley through continuous telemetry (Figure 3.2 and Table 3.1). The network is designed to monitor regional seismic activity at the magnitude 3+ level as well as to provide high quality data for research projects in regional and global broadband seismology.

Since 1991 the BDSN has grown from the original 3 broadband stations installed in 1986-87 (BKS, SAO, MHC) to comprise 27 stations, including an autonomous ocean-bottom seismometer in Monterey Bay (MOBB). We take particular pride in high quality installations, which often involve lengthy searches for appropriate sites away from sources of low-frequency noise, as well as continuous improvements in installation procedures and careful monitoring of noise conditions and problems. Thus, the focus of this year's technical efforts evolved to maintenance and repair, because of aging instruments, the desire for higher data rates, corrosion and outright equipment failure. Considerable engineering and research activities were also involved in a project to develop new electronics for the STS-1 seismometers (see Section 3.7.).

Further expansion of our network to densify the state-of-the-art strong motion/broadband seismic network and the joint earthquake notification system in this seismically hazardous region, one of BSL's long term goals, must be coordinated with other institutions and is contingent on the availability of funding.

Equally important, data quality and the integrity of the established network must be preserved and remain assured despite expansion. The first generation of broadband seismometers installed by BSL have been operating for almost 25 years. At the same time, the first generation of broadband dataloggers are entering their 16th year of service. These will both require continued vigilance and greater time commitment to both repairs and upgrades in the future.

### 3.1.2 BDSN Overview

Twenty-four of the BDSN sites are equipped with 3 component broadband seismometers and strong-motion accelerometers, and a 24-bit digital data acquisition system or datalogger. Two additional sites (RFSB and SCCB) consist of a strong-motion accelerometer and a 24-bit digital datalogger. The ocean-bottom station MOBB is equipped with a 3 component broadband seismometer. Data from all BDSN stations, except MOBB, are transmitted to UC Berkeley using continuous telemetry. In order to insure against data loss during utility dis-

ruptions, each site has a 3-day supply of battery power and is accessible via a dialup phone line. The combination of high-dynamic range sensors and digital dataloggers ensures that the BDSN has the capability to record the full range of earthquake motion for source and structure studies. Table 3.2 lists the instrumentation at each site.

Most BDSN stations have Streckeisen STS-1 or STS-2 three-component broadband sensors (*Wielandt and Streckeisen, 1982; Wielandt and Steim, 1986*). A Guralp CMG-3T downhole broadband sensor contributed by LLNL is deployed in a post-hole installation at BRIB. A Guralp CMG1-T is deployed at MOBB. The strong-motion instruments are Kinematics FBA-23, FBA-ES-T or MetroZet accelerometers with  $\pm 2$  g dynamic range. The recording systems at all sites are either Q330, Q680, Q730, or Q4120 Quanterra dataloggers, with 3, 6, 8, or 9 channel systems. The Quanterra dataloggers employ FIR filters to extract data streams at a variety of sampling rates. In general, the BDSN stations record continuous data at .01, 0.1, 1.0, 20.0 or 40.0, and 80 or 100 samples per second, although some sites send triggered data at the highest sampling rate using the Murdock, Hutt, and Halbert event detection algorithm (*Murdock and Hutt, 1983*) (Table 3.3). In addition to the 6 channels of seismic data, signals from thermometers and barometers are recorded at nearly every site (Figure 3.3).

In parallel with the upgrade of the broadband network, a grant from the CalREN Foundation (California Research and Education Network) in 1994 enabled the BSL to convert data telemetry from analog leased lines to digital frame-relay connections. The frame-relay network uses digital phone circuits that can support 56 Kbit/s to 1.5 Mbit/s throughput. Since frame-relay is a packet-switched network, a site may use a single physical circuit to communicate with multiple remote sites through the use of "permanent virtual circuits". Frame Relay Access Devices (FRADs), which replace modems in a frame-relay network, can simultaneously support multiple interfaces such as RS-232 async ports, synchronous V.35 ports, and ethernet connections. In practical terms, the upgrade to frame relay communication provides faster data telemetry between the remote sites and the BSL, remote console control of the dataloggers, additional services such as FTP and telnet to the dataloggers, data transmission to multiple sites, and the ability to communicate and transmit data from multiple instruments such as GPS receivers and/or multiple dataloggers at a single site. Today, 23 of the BDSN sites use frame-relay telemetry for all or part of their communications system.

As described in Section 3.7., data from the BDSN are

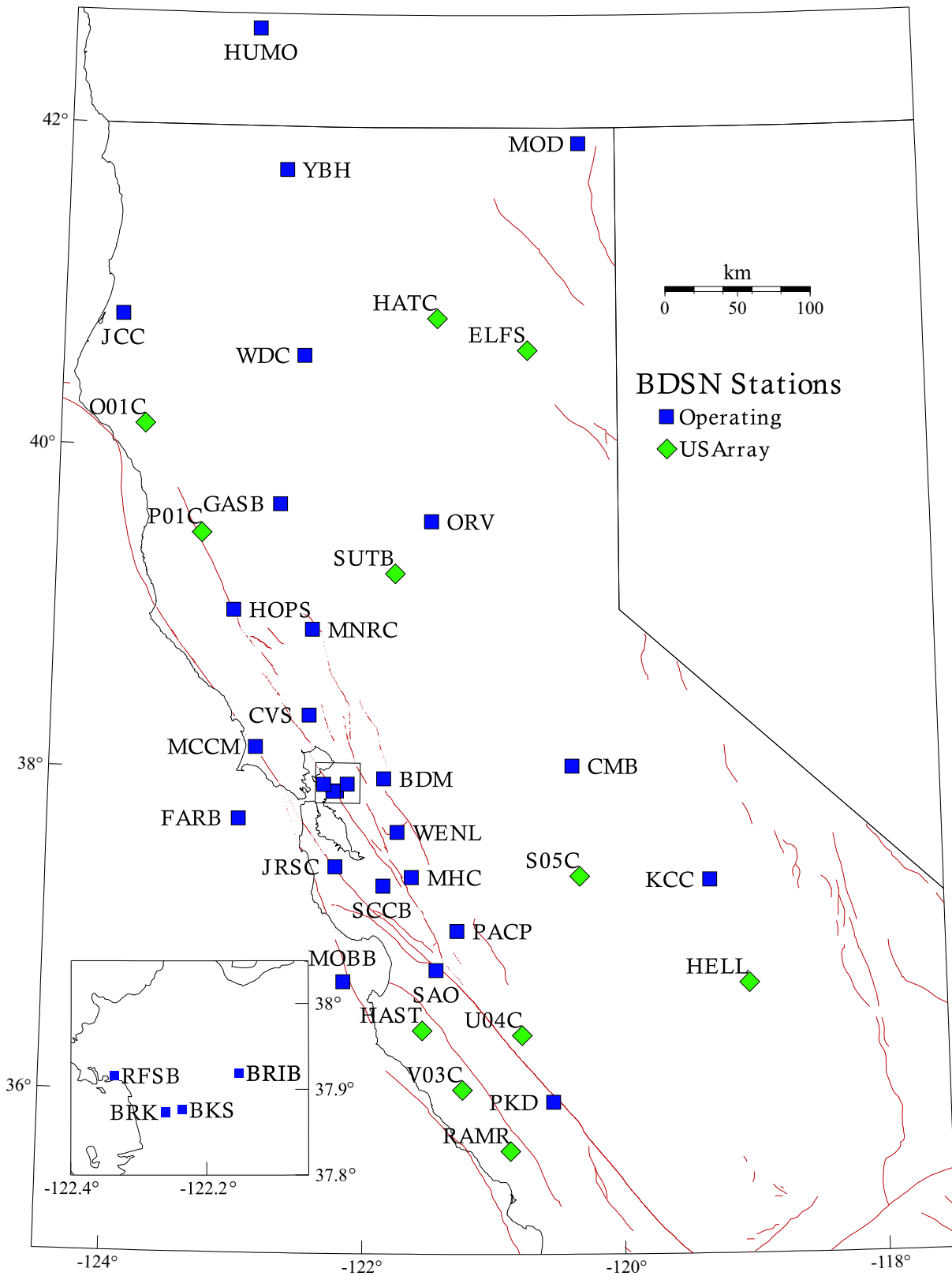


Figure 3.2: Map illustrating the distribution of BDSN stations (squares) in northern and central California. The diamonds indicate sites currently operated by USArray which we are monitoring as perspective future stations.

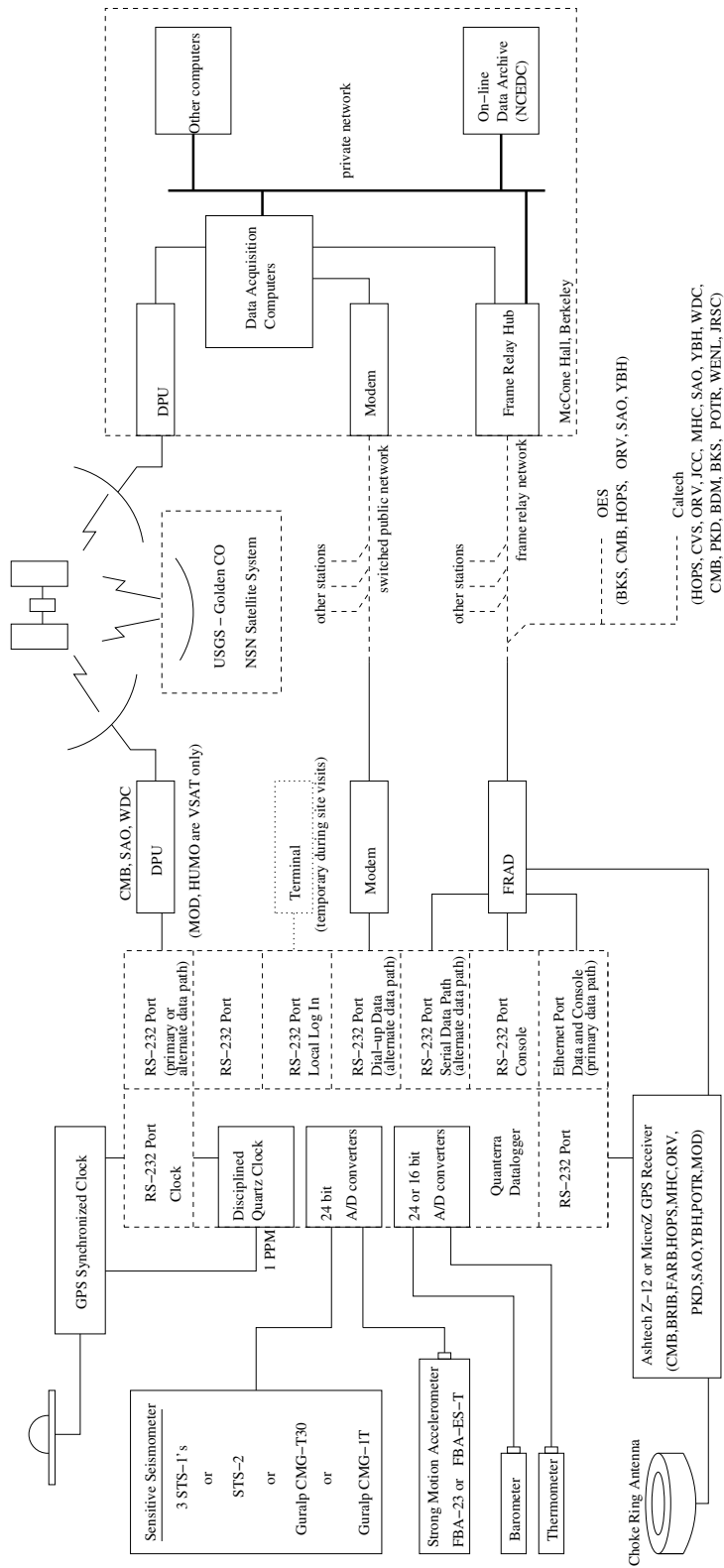


Figure 3.3: Schematic diagram showing the flow of data from the sensors through the dataloggers to the central acquisition facilities of the BSL.

Code	Net	Latitude	Longitude	Elev (m)	Over (m)	Date	Location
BDM	BK	37.9540	-121.8655	219.8	34.7	1998/11 -	Black Diamond Mines, Antioch
BKS	BK	37.8762	-122.2356	243.9	25.6	1988/01 -	Byerly Vault, Berkeley
BRIB	BK	37.9189	-122.1518	219.7	2.5	1995/06 -	Briones Reservation, Orinda
BRK	BK	37.8735	-122.2610	49.4	2.7	1994/03 -	Haviland Hall, Berkeley
CMB	BK	38.0346	-120.3865	697.0	2	1986/10 -	Columbia College, Columbia
CVS	BK	38.3453	-122.4584	295.1	23.2	1997/10 -	Carmanet Vineyard, Sonoma
FARB	BK	37.6978	-123.0011	-18.5	0	1997/03 -	Farallon Island
GASB	BK	39.6547	-122.716	1354.8	2	2005/09 -	Alder Springs
HOPS	BK	38.9935	-123.0723	299.1	3	1994/10 -	Hopland Field Stat., Hopland
HUMO	BK	42.6071	-122.9567	554.9	50	2002/06 -	Hull Mountain, Oregon
JCC	BK	40.8175	-124.0296	27.2	0	2001/04 -	Jacoby Creek
JRSC	BK	37.4037	-122.2387	70.5	0	1994/07 -	Jasper Ridge, Stanford
KCC	BK	37.3236	-119.3187	888.1	87.3	1995/11 -	Kaiser Creek
MCCM	BK	38.1448	-122.8802	-7.7	2	2006/02 -	Marconi Conference Center, Marshall
MHC	BK	37.3416	-121.6426	1250.4	0	1987/10 -	Lick Obs., Mt. Hamilton
MNRC	BK	38.8787	-122.4428	704.8	3	2003/06 -	McLaughlin Mine, Lower Lake
MOBB	BK	36.6907	-122.1660	-1036.5	1	2002/04 -	Monterey Bay
MOD	BK	41.9025	-120.3029	1554.5	5	1999/10 -	Modoc Plateau
ORV	BK	39.5545	-121.5004	334.7	0	1992/07 -	Oroville
PACP	BK	37.0080	-121.2870	844	0	2003/06 -	Pacheco Peak
PKD	BK	35.9452	-120.5416	583.0	3	1996/08 -	Bear Valley Ranch, Parkfield
RFSB	BK	37.9161	-122.3361	-26.7	0	2001/02 -	RFS, Richmond
SAO	BK	36.7640	-121.4472	317.2	3	1988/01 -	San Andreas Obs., Hollister
SCCB	BK	37.2874	-121.8642	98	0	2000/04 -	SCC Comm., Santa Clara
WDC	BK	40.5799	-122.5411	268.3	75	1992/07 -	Whiskeytown
WENL	BK	37.6221	-121.7570	138.9	30.3	1997/06 -	Wente Vineyards, Livermore
YBH	BK	41.7320	-122.7104	1059.7	60.4	1993/07 -	Yreka Blue Horn Mine, Yreka

Table 3.1: Currently operating stations of the Berkeley Digital Seismic Network. Each BDSN station is listed with its station code, network id, location, operational dates, and site description. The latitude and longitude (in degrees) are given in the WGS84 reference frame and the elevation (in meters) is relative to the WGS84 reference ellipsoid. The elevation is either the elevation of the pier (for stations sited on the surface or in mining drifts) or the elevation of the well head (for stations sited in boreholes). The overburden is given in meters. The date indicates either the upgrade or installation time.

acquired centrally at the BSL. These data are used for rapid earthquake reporting as well as for routine earthquake analysis (Section 3.2. and 3.8.). As part of routine quality control (Section 3.7.), power spectral density (PSD) analyses are performed weekly. Figure 3.4 shows a summary of the results for 2006 in comparison with other broadband stations operating in Northern California.

The occurrence of a significant teleseism also provides the opportunity to review station health and calibration. Figure 3.5 displays BDSN waveforms for a  $M_w$  8.1 deep focus earthquake in the Solomon Islands region on April 1, 2007.

BDSN data are archived at the Northern California Earthquake Data Center. This is described in detail in Section 3.6..

### Electromagnetic Observatories

In 1995, in collaboration with Dr. Frank Morrison, the BSL installed two well-characterized electric and magnetic field measuring systems at two sites along the San Andreas Fault which are part of the Berkeley Digital Seismic Network. Since then, magnetotelluric (MT) data have been continuously recorded at 40 Hz and 1 Hz and archived at the NCEDC (Table 3.4). At least one set of orthogonal electric dipoles measures the vector horizontal electric field,  $E$ , and three orthogonal magnetic sensors measure the vector magnetic field,  $B$ . These reference sites, now referred to as electromagnetic (EM) observatories, are co-located with seismographic sites so that the field data share the same time base, data acquisition, telemetry and archiving system as the seismometer outputs.

The MT observatories are located at Parkfield (PKD1, PKD) 300 km south of the San Francisco Bay Area,

### 2006 Vertical 30–60 sec Background Noise PSD

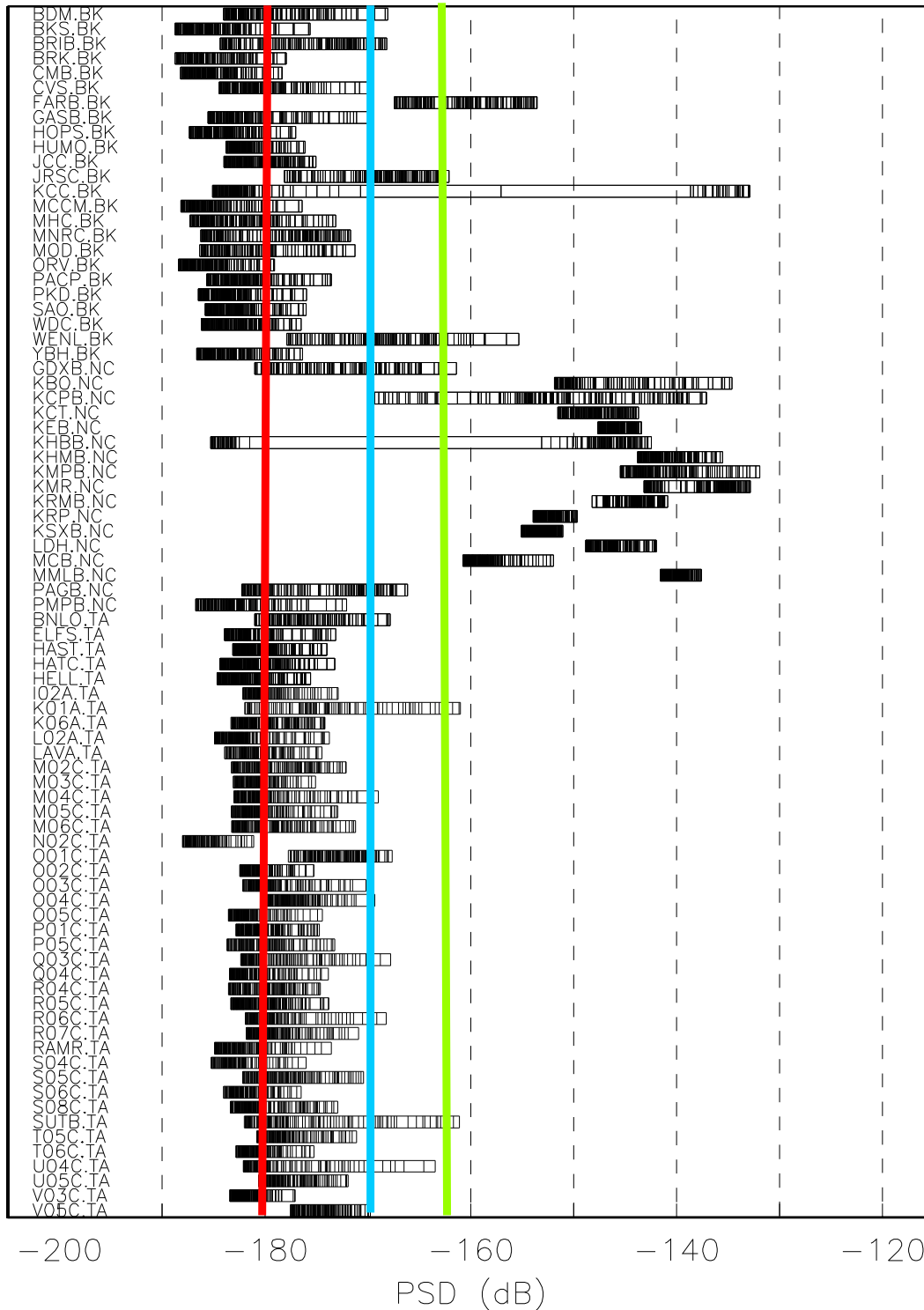


Figure 3.4: PSD noise analysis for vertical components of the broadband stations of the BK, NC and TA networks in Northern California, in the period range from 32-128 sec for the interval 1/1/2006-12/31/2006. The BK and TA stations have much lower noise levels than the NC stations because of the sensors. BRIB (situation in a shallow vault that is prone to tilting) and FARB (located on the Farallon Islands) stand out as sites with high noise levels. KCC is located in a overflow tunnel near a dam. When the water is running, it has high noise levels. HUMO (located in an abandoned mine) stands out as an exceptionally quiet site. The vertical lines indicate the average signal levels of events with  $M_L$  2.5, 3.5 and 4.5, respectively.

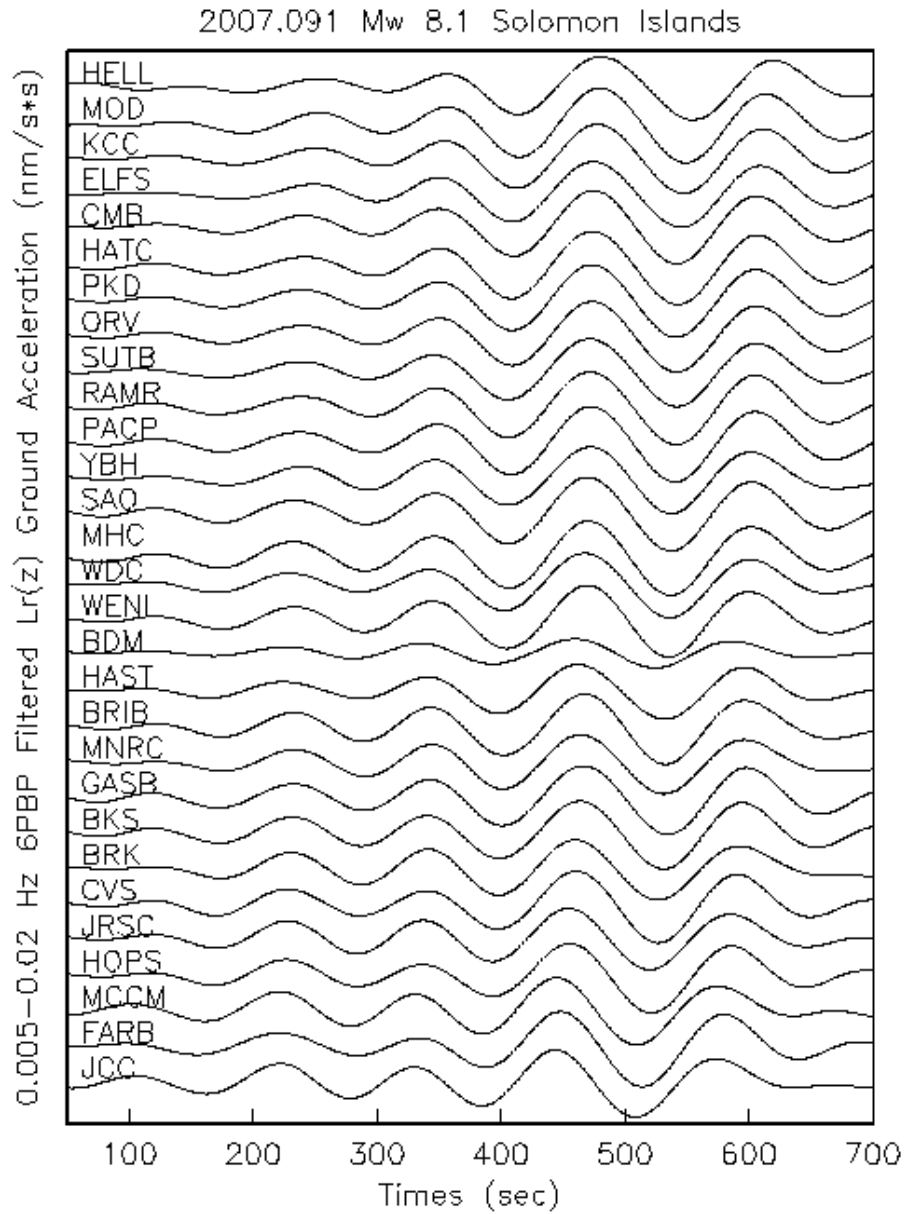


Figure 3.5:  $L_R(Z)$  vertical component broadband waveforms recorded across BDSN from the  $M_w$  8.1 teleseism which occurred on April 1, 2007, in the Solomon Islands at  $8.48^\circ$  S,  $156.98^\circ$  E. The traces are deconvolved to ground motion, scaled absolutely, and ordered from bottom to top by distance from the epicenter. For reference, the vertical distance between the traces is equivalent to  $500 \text{ nm/s}^2$ . The highly similar waveforms recorded across the BDSN provide evidence that the broadband sensors other than BDM are operating within their nominal specifications.

Code	Broadband	Strong-motion	datalogger	T/B	GPS	Other	Telemetry	Dial-up
BDM	STS-2	FBA-23	Q4120	X			FR	
BKS	STS-1	FBA-23	Q980	X		Baseplates	FR	X
BRIB	CMG-3T	FBA-23	Q980		X	Vol. Strain	FR	X
BRK	STS-2	FBA-23	Q680				POTS	
CMB	STS-1	FBA-23	Q980	X	X	Baseplates	FR	X
CVS	STS-2	FBA-23	Q4120	X			FR	
FARB	CMG-3T	FBA-23	Q4120	X	X		R-FR/R	
GASB	STS-2	FBA-ES-T	Q4120	X			R-FR	
HOPS	STS-1	FBA-23	Q980	X	X	Baseplates	FR	X
HUMO	STS-2	FBA-ES-T	Q4120	X			VSAT	X
JCC	STS-2	FBA-23	Q980	X			FR	X
JRSC	STS-2	FBA-23	Q680				FR	X
KCC	STS-1*	FBA-23	Q980	X		Baseplates	R-Mi-FR	X
MCCM	STS-2	FBA-ES-T	Q4120				VSAT	
MHC	STS-1	FBA-23	Q980	X	X		FR	X
MNRC	STS-2	FBA-ES-T	Q4120	X			None	X
MOBB	CMG-1T		GEOSense			Current meter, DPG	None	
MOD	STS-1*	FBA-ES-T	Q980	X	X	Baseplates	VSAT	X
ORV	STS-1	FBA-23	Q980	X	X	Baseplates	FR	X
PACP	STS-2	FBA-ES-T	Q4120	X			Mi/FR	
PKD	STS-2	FBA-23	Q980	X	X	EM	R-FR	X
RFSB		FBA-ES-T	Q730				FR	
SAO	STS-1	FBA-23	Q980	X	X	Baseplates, EM	FR	X
SCCB		MetroZet	Q730		X		FR	
WDC	STS-2	FBA-23	Q980	X			FR	X
WENL	STS-2	FBA-23	Q4120	X			FR	
YBH	STS-1 & STS-2	FBA-23	Q980	X	X	Baseplates	FR	X

Table 3.2: Instrumentation of the BDSN as of 06/30/2007. Except for PKD1, RFSB, SCCB and MOBB, each BDSN station consists of collocated broadband and strong-motion sensors, with a 24-bit Quanterra datalogger and GPS timing. The stations PKD1, RFSB and SCCB are strong-motion only, while MOBB has only a broadband sensor. Additional columns indicate the installation of a thermometer/barometer package (T/B), collocated GPS receiver as part of the BARD network (GPS), and additional equipment (Other) such as warpless baseplates or electromagnetic sensors (EM). The obs station MOBB also has a current meter and differential pressure gauge (DPG). The main and alternate telemetry paths are summarized for each station. FR - frame relay circuit, R - radio, Mi - microwave, POTS - plain old telephone line, VSAT - USGS ANSS satellite link, None - no telemetry at this time. An entry like R-Mi-FR indicates telemetry over several links, in this case, radio to microwave to frame relay. (\*) During part of 2006-2007 the STS-1s at these two stations were replaced by STS-2s

and Hollister (SAO), halfway between San Francisco and Parkfield (Figure 3.2). In 1995, initial sites were established at PKD1 and SAO, separated by a distance of 150 km, and equipped with three induction coils and two 100 m electric dipoles. PKD1 was established as a temporary seismic site, and when a permanent site (PKD) was found, a third MT observatory was installed in 1999 with three induction coils, two 100 m electric dipoles, and two 200 m electric dipoles. PKD and PKD1 ran in parallel for one month in 1999, and then the MT observatory at PKD1 was closed.

Data at the MT sites are fed to Quanterra dataloggers, shared with the collocated BDSN stations, synchronized in time by GPS and sent to the BSL via dedicated com-

munication links.

### 3.1.3 2006-2007 Activities

#### USArray

The BSL concluded an agreement with IRIS during 2003-2004 to contribute 19 stations of the BDSN to US-Array while the experiment is deployed in California. This included 17 existing stations: CMB, CVS, FARB, HOPS, HUMO, JCC, JRSC, KCC, MNRC, MOD, ORV, PACP, PKD, POTR, WDC, WENL, and YBH as well as the two new sites: GASB and MCCM.

The 19 BDSN sites provided USArray with a running start in northern California. In June of 2004, the BSL set

Sensor	Channel	Rate (sps)	Mode	FIR
Broadband	UH?	0.01	C	Ac
Broadband	VH?	0.1	C	Ac
Broadband	LH?	1	C	Ac
Broadband	BH?	20/40	C	Ac
Broadband	HH?	80/100	C	Ac/Ca
SM	LL?	1	C	Ac
SM	BL?	20/40	C	Ac
SM	HL?	80/100	C	Ac/Ca
Thermometer	LKS	1	C	Ac
Barometer	LDS	1	C	Ac

Table 3.3: Typical data streams acquired at BDSN stations, with channel name, sampling rate, sampling mode, and the FIR filter type. SM indicates strong-motion; C continuous; T triggered; Ac acausal; Ca causal. The LL and BL strong-motion channels are not transmitted over the continuous telemetry but are available on the Quanterra disk system if needed. The HH channels are recorded at two different rates, depending on the datalogger type. Q4120s provide 100 sps and causal filtering; Q680/980s provide 80 sps and acausal filtering.

Sensor	Channel	Rate (sps)	Mode	FIR
Magnetic	VT?	0.1	C	Ac
Magnetic	LT?	1	C	Ac
Magnetic	BT?	40	C	Ac
Electric	VQ?	0.1	C	Ac
Electric	LQ?	1	C	Ac
Electric	BQ?	40	C	Ac

Table 3.4: Typical MT data streams acquired at SAO and PKD, with channel name, sampling rate, sampling mode, and FIR filter type. C indicates continuous; T triggered; Ac acausal.

up the software necessary to exchange data with USArray and made modifications to the dataloggers to change the BH sampling rate from 20 Hz to 40 Hz. In this third year of USArray, the BDSN has continued to use the 40 Hz sampling rate for the BH channels.

During the station installation phase for northern and central California, the BSL collaborated with USArray to identify and permit sites that might be suitable as BDSN stations, several at UC reserves and field stations. The stations currently operating at Sutter Buttes, Hat Creek Radio Observatory, Eagle Lake Biological Field Station, Kirkwood Ski Area, Ben Lomond Conservation Camp, and at the summer home of a BSL staff member (M. Hellweg) in the Sierra Nevada foothills were established with support from BSL staff. Data from these sites (Figure 3.2) are being sent directly to the BSL as well as to the Array Network Facility. In addition, the BSL is monitoring data from several other USArray stations to evaluate their performance as possible future BDSN stations when USArray moves on across the country. In particular, noise comparisons are being conducted in different frequency bands for all BDSN and USArray stations in northern California (see Section 3.7. for further details).

### Station Upgrades, Maintenance and Repairs

Given the remoteness of the off-campus stations, BDSN data acquisition equipment and systems are designed, configured, and installed so that they are both cost effective and reliable. As a result, the need for regular station visits has been reduced. In 2006-2007 the focus of BSL's technical efforts went toward maintaining and repairing existing instrumentation, stations and infrastructure that was put in place during the early and mid 1990's . While expanding the data acquisition network remains one of the long term goals of BSL, it is equally important to assure integrity of the established network and preserve data quality.

The broadband seismometers installed by BSL are of the first generation and are now approaching 25 years in age. Concurrently, the first generation of broadband dataloggers are now 17 years old. Computer systems are retired long before this age, yet the electronics that form these data acquisition systems are expected to perform without interruption.

*SUTB:* During 2006-2007, the BSL has received support from the TA for operating permanent stations in northern California. The BSL has provided telemetry for this TA site for the past year and a half. Data are delivered to the BSL datacenter via a radio telemetry link to the BSL station ORV. Beyond the initial setup and deployment, this has involved maintaining the radio telemetry between the seismic site and the radio repeater - a distance of several kilometers. The radios inexplicably lost their connections and control programming several times during the past year. In each instance, they could

be reinitialized remotely from Berkeley, and telemetry resumed. Some of this year's support was used for equipment maintenance and to correct telemetry problems. BSL engineers visited both the radio installation and the seismic vault at the TA site, Sutter Buttes (SUTB), many times to maintain and troubleshoot network connectivity.

*KCC:* At station KCC (Kaiser Creek California) BSL engineers removed the STS-1 seismometers during 2006-2007 and installed an STS-2, and instrument consistent with the specifications of the TA. This provided the opportunity to use the three STS-1 components from Berkeley in the STS-1 electronics upgrade program (REF). During this testing, one of the STS-1 sensors was found to have reduced sensitivity. The instrument was repaired and is scheduled to be reinstalled before the winter of 2007, when the STS-2 is removed.

*WENL:* The BSL station WENL began operating in 1997. The equipment is installed in a high humidity adit used for storing and aging wine. BSL engineers replaced cables and the STS-2 seismometer this year after a reduction in the instrument's sensitivity (signal levels) was observed. Since WENL was installed, growth and development at the winery caused increases in the background noise levels over the past several years. A search for a suitable replacement site has begun.

*HOPS:* The BDSN station at Hopland, California, has been operating since October, 1994. The station is located approximately 100 miles northwest of Berkeley. During the current year, BSL engineers visited the station seven times to remove, repair, and replace seismometers and the geodetic GPS (BARD) receiver.

Actual repair of instruments in the field is difficult due to the nature of the sites, lack of test equipment, poor lighting, etc. In most cases, BSL engineers will remove failed equipment and replace it with a working spare in a single trip. The objective is to minimize the station down time. In the case of HOPS, which is close to the BSL, we elected to remove the equipment, return it to the Berkeley lab, repair it, and in at least one case, replace it the following day.

At HOPS, all three components of the STS-1 seismometers were found to have degraded sensitivity. Experience with the site, where similar problems have occurred in the past, led to the suspicion that the insulation on the connectors on the seismometer electronics had broken down. The connectors were replaced.

Later in the year, the prototype of the new STS-1 electronics (MetroZet) was installed at HOPS. As described elsewhere in this report, these electronics have the advantage of swept sign and step calibration functions over the network connection. The field operation of these electronics is currently being evaluated at HOPS.

*SAO:* At SAO, BSL engineers began rebuilding the seismometer vault in late summer of 2006. The area in front of the vault was excavated and re-graded to improve

drainage. A new concrete entrance was poured, and most importantly, a welded steel security door was added. The wooden door it replaced had been broken into on a number of occasions during the past ten years. A second steel door was hung on the outside to create a secure atrium and thermal buffer for the vault. As envisioned, future seismic instruments could be added in this atrium. Backfilling the entrance, final re-grading and cleanup of the site will be completed before the winter of 2007. SAO was built in 1966 and upgraded to first generation Quanterra broadband recording in early 1992.

*MCCM:* Two site visits were required to MCCM during the 2006-2007 year. During the first of these, a failed 12 vdc power supply was replaced. Later in the year, VSAT telemetry was restored during the second visit. A present, BSL engineers have developed a plan to improve continuous telemetry using digital radio link. Permits have been acquired for the installation of the necessary radios, repeater radios and infrastructure.

*YBH:* Station YBH was visited three times in the past year. Power at YBH is supplied by the local utility company. In this heavily forested area, it is BSL's obligation to keep the path to the power meter clear of fallen trees. One trip was necessary to remove fallen trees. In a later trip, BSL engineers replaced a failed data acquisition subsystem belonging to the CTBTO. The third trip was also necessary to resolve CTBTO telemetry issues. BSL's YBH station has been providing data to the CTBTO since 2002.

*HUMO:* BSL engineers visited the station at HUMO once during 2006-2007. This visit was necessary to repair and replace the power supply for the VSAT equipment. HUMO is the BDSN station furthest from Berkeley.

*OXMT:* The OXMT site has been providing borehole seismic and strain data, as well as geodetic GPS data, since February of 2004. This is a mountaintop site within 6 kilometers of the coast. During the past year, BSL engineers replaced a DC power supply which appeared to have failed due to weather-related problems.

*SBRN:* The site SBRN is a companion to OXMT and also provides borehole seismic and strain data, as well as geodetic GPS data. The site is within 100 meters of an elementary school. During the past year, the GPS monument and cover were vandalized and subsequently replaced by BSL engineers.

*RFSB:* BSL engineers made four trips to the Richmond Field Station (RFSB) during the past year. In two instances, the telemetry ports from the data logger were found not to be working, presumably as a result of a power surge or a nearby lightning strike. The other two trips were necessary to investigate and troubleshoot low signal levels on the surface accelerometer. Corroded connectors were found and replaced in each case. The RFSB site is within one kilometer of the San Francisco Bay.

*MONB:* The MONB site lies on an east/west ridge

north of San Jose, California. BSL operates a geodetic GPS and telemetry equipment there. In 2006-2007, BSL engineers installed radio equipment to consolidate data from future sites in the valley below. We expect to add at least one GPS site with data telemetry through MONB in the next year.

*SCCB:* During October of 2006, BSL engineers replaced the strong motion accelerometer at SCCB. The previous instrument (Kinematics FBA-ESP) was rendered unusable when the instrument enclosure was flooded during seasonal rain. A MetroZet accelerometer was installed in its place.

*ORV:* BSL engineers visited the station at ORV during the past year to replace the back up batteries. The replaced batteries were 15 years old and at end of their manufacturers specified lifetime.

*BRIB:* In March of 2007, BSL engineers installed a fiber optic local loop (between the telephone company demarcation and the instrument vault) at BRIB. The fiber optic data connections provide the advantage of electrical isolation from the telephone system, while concurrently allowing greater telemetry speeds and additional telemetry paths. This work was undertaken in part to support the Stanford/USGS electro-magnetic and magnetic monitoring equipment which was installed at BRIB during the past year. The Stanford/USGS instruments telemetry data to the BSL data center for archival.

*BDM:* The Quanterra data logger at Black Diamond Mine (BDM) froze several times during the past year and remained unresponsive. In each case, however, the data logger was rebooted remotely from Berkeley and did not require a site visit. At this time, BSL is permitting with the East Bay Regional Parks to add a geodetic GPS to the other instruments on site. As planned, the monument would be located within 100 meters of the seismometers.

### **The Monterey Bay Ocean Bottom Seismic Observatory (MOBB)**

The Monterey Ocean Bottom Broadband observatory (MOBB) is a collaborative project between the Monterey Bay Aquarium Research Institute (MBARI) and the BSL. Supported by funds from the Packard Foundation to MBARI, NSF/OCE funds and UC Berkeley funds to BSL, its goal has been to install and operate a long-term seafloor broadband station as a first step towards extending the on-shore broadband seismic network in northern California to the seaside of the North-America/Pacific plate boundary, providing better azimuthal coverage for regional earthquake and structure studies. It also serves the important goal of evaluating background noise in near-shore buried ocean floor seismic systems, such as may be installed as part of temporary deployments of “leap-frogging” arrays (e.g. Ocean Mantle Dynamics Workshop, September 2002).

BSL staff put significant effort in the development of

procedures to minimize instrumental noise caused by air circulation inside the seismometer package casing (see 2001-2002 and 2002-2003 BSL Annual Reports). These procedures were later applied to the preparation of 3 similar packages destined for installation on the Juan de Fuca plate in the framework of University of Washington’s Keck project.

This project follows the 1997 MOISE experiment, in which a three component broadband system was deployed for a period of 3 months, 40 km off shore in Monterey Bay, with the help of MBARI’s “Point Lobos” ship and ROV “Ventana” (Figure 3.6). MOISE was a cooperative program sponsored by MBARI, UC Berkeley and the INSU, Paris, France (*Stakes et al.*, 1998; *Romanowicz et al.*, 1999; *Stutzmann et al.*, 2001). During the MOISE experiment, valuable experience was gained on the technological aspects of such deployments, which contributed to the success of the present MOBB installation.

The successful MOBB deployment took place April 9-11, 2002 and the station is currently recording data autonomously (e.g. *Romanowicz et al.*, 2003). It comprises a 3 component very broadband CMG-1T seismometer system, a differential pressure gauge (DPG, *Cox et al.*, 1984) and a current meter. Data from the DPG are acquired with a sampling rate of 1 sps, and are crucial for the development and implementation of a posteriori noise deconvolution procedures to help counteract the large contribution of infragravity wave noise in the period range 20-200 sec. Procedures for removal of infragravity wave noise as well as signal generated noise have been developed.

Twenty “dives” involving the MBARI ship “Point Lobos” and ROV “Ventana” have so far taken place to exchange dataloggers and battery packages during the time period 04/10/02 to 06/30/07. In February 2004, the N/S component seismometer failed. It was temporarily replaced, from 05/19/04 to 07/09/04, by one of the Keck seismometer packages which was conveniently available at that time. The original seismometer was sent back to Guralp Systems Ltd. for repair and successfully reinstalled on 07/09/04.

The data collection from the broadband seismic system is fairly complete. However, there have been recurring DPG sensor as well as DPG data storage problems in the first two years of the MOBB operation. Well recorded DPG data are available since 03/18/2004.

The MOBB station is located close to the path of the MARS cable (Figure 3.6) which was deployed in the Spring of 2007. The connection of MOBB to the MARS cable will allow continuous, real-time data acquisition from this site. Developing the interface for the connection to MARS is the object of a recently funded NSF project. Work on this project commenced in the summer of 2007.

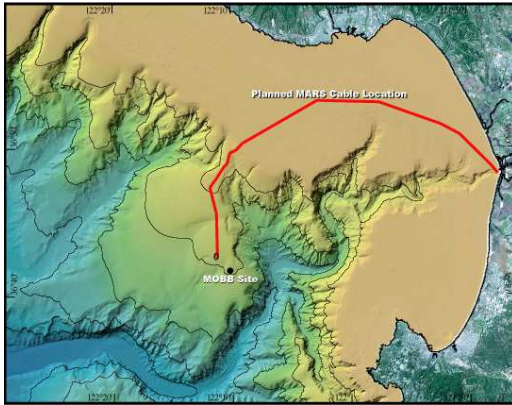


Figure 3.6: Location of the MOBB station in Monterey Bay, California, against seafloor and land topography. The path of the MARS cable is indicated by the solid line.

### 3.1.4 Acknowledgements

Under Barbara Romanowicz's general supervision, Peggy Hellweg and Doug Neuhauser oversee the BDSN data acquisition operations, and Bill Karavas heads the engineering team. John Friday, Jarrett Gardner, Rick Lellingner and Bob Uhrhammer contribute to the operation of the BDSN. Karl Kappler has been responsible for the operation of the EM observatories. Bill Karavas, Bob Uhrhammer, and Peggy Hellweg contributed to the preparation of this chapter.

The California Governor's Office of Emergency Services provided funding toward the development of sites MCCM and GASB as part of the CISN. The Incorporated Research Institutions in Seismology provided matching funds for the installation of MCCM. The CREST project provided a datalogger for GASB. Earthscope (USArray) provided funds towards telemetry of northern California TA stations through BSL and operation of joint BDSN/USArray stations.

MOBB is a collaboration between the BSL and MBARI, involving Barbara Romanowicz, Bob Uhrhammer, Doug Neuhauser and David Dolenc from the BSL, and Debra Stakes and Paul McGill from MBARI. The MBARI team also includes Steve Etchemendy (Director of Marine Operations), Jon Erickson, John Ferreira, Tony Ramirez and Craig Dawe. The MOBB effort at the BSL is supported by UC Berkeley funds. MBARI supports the dives and data recovery. The MOBB seismometer package was funded by NSF/OCE grant #9911392.

The Earthscope Transportable Array provides support for telemetry and maintenance of the 19 BDSN stations from which the BSL supplies data to the USArray efforts.

### 3.1.5 References

- Cox, C., T. Deaton and S. Webb, A deep-sea differential pressure gauge, *J. Atm. Ocean. Tech.*, *1*, 237-245, 1984.
- Crawford W. C., and S. C. Webb, Identifying and removing tilt noise from low-frequency (<0.1 Hz) seafloor vertical seismic data, *Bull. Seis. Soc. Am.*, *90*, 952-963, 2000.
- Murdock, J., and C. Hutt, A new event detector designed for the Seismic Research Observatories, *USGS Open-File-Report 83-0785*, 39 pp., 1983.
- Romanowicz, B., D. Stakes, J. P. Montagner, P. Tarits, R. Uhrhammer. M. Begnaud, E. Stutzmann, M. Pasyanos, J.F. Karczewski, S. Etchemendy, MOISE: A pilot experiment towards long term sea-floor geophysical observatories, *Earth Planets Space*, *50*, 927-937, 1999.
- Romanowicz, B., D. Stakes, R. Uhrhammer, P. McGill, D. Neuhauser, T. Ramirez and D. Dolenc, The MOBB experiment: a prototype permanent off-shore ocean bottom broadband station, *EOS Trans. AGU*, Aug 28 issue, 2003.
- Stakes, D., B. Romanowicz, J.P. Montagner, P. Tarits, J.F. Karczewski, S. Etchemendy, D. Neuhauser, P. McGill, J-C. Koenig, J.Savary, M. Begnaud and M. Pasyanos, MOISE: Monterey Bay Ocean Bottom International Seismic Experiment, *EOS Trans. AGU*, *79*, 301-309, 1998.
- Stutzmann, E., J.P. Montagner et al., MOISE: a prototype multiparameter ocean-bottom station, *Bull. Seism. Soc. Am.*, *81*, 885-902, 2001.
- Wielandt, E., and J. Steim, A digital very broad band seismograph, *Ann. Geophys.*, *4*, 227-232, 1986.
- Wielandt, E., and G. Streckeisen, The leaf spring seismometer: design and performance, *Bull. Seis. Soc. Am.*, *72*, 2349-2367, 1982.
- Zürn, W., and R. Widmer, On noise reduction in vertical seismic records below 2 mHz using local barometric pressure, *Geophys. Res. Lett.*, *22*, 3537-3540, 1995.

## 3.2. California Integrated Seismic Network

### 3.2.1 Introduction

Advances in technology have made it possible to integrate separate earthquake monitoring networks into a single seismic system as well as to unify earthquake monitoring instrumentation. In California, this effort began in the south with the TriNet Project. There Caltech, the California Geological Survey (CGS), and the USGS combined efforts to create a unified seismic system for southern California. With major funding provided by the Federal Emergency Management Agency (FEMA), the California Governor's Office of Emergency Services (OES), and the USGS, the TriNet project provided the opportunity to upgrade and expand the monitoring infrastructure, combining resources in a federal, state and university partnership. In 2000, the integration effort expanded to the entire State with the formation of the California Integrated Seismic Network (CISN, see 2000-2001 Annual Report). To this end, UC Berkeley and the USGS Menlo Park and Pasadena offices joined forces with Caltech and the CGS. The CISN is now in the seventh year of collaboration and its sixth year of funding from the OES.

### 3.2.2 CISN Background

#### Organization

The organizational goals, products, management, and responsibilities of the CISN member organizations are described in the founding MOU and in the strategic and implementation plans. To facilitate activities among institutions, the CISN has formed three management centers:

- Southern California Management Center: Caltech/USGS Pasadena
- Northern California Earthquake Management Center: UC Berkeley/USGS Menlo Park
- Engineering Strong Motion Data Center: California Geological Survey/USGS National Strong Motion Program

The Northern and Southern California Management Centers are operating as twin statewide earthquake processing centers serving information on current earthquake activities, while the Engineering Strong Motion Data Center has the responsibility for producing engineering data products and distributing them to the engineering community.

The Steering Committee, made up of two representatives from each core institution and a representative from

OES, oversees CISN projects. The position of chair rotates among the institutions; Jeroen Tromp is currently the chair of the Steering Committee.

An external Advisory Committee represents the interests of structural engineers, seismologists, emergency managers, industry, government, and utilities and provides review and oversight. The Advisory Committee is chaired by Stu Nishenko of Pacific Gas and Electric Company. It last met in August 2006. Agendas from the meetings and the resulting reports may be accessed through the CISN Web site (<http://www.cisn.org/advisory>). The next meeting is planned for September 2007.

The Steering Committee has formed other committees, including a Program Management Group to address planning and coordination, a Strong Motion Working Group to focus on issues related to strong-motion data, and a Standards Committee to resolve technical design and implementation issues.

In addition to the core members, other organizations contribute data that enhances the capabilities of the CISN. Contributing members of the CISN include: University of California, Santa Barbara; University of California, San Diego; University of Nevada, Reno; University of Washington; California Department of Water Resources; Lawrence Livermore National Lab; and Pacific Gas and Electric.

#### CISN and ANSS

The USGS Advanced National Seismic System (ANSS) is being developed along a regionalized model. Eight regions have been organized, with the CISN representing California. David Oppenheimer of the USGS represents the CISN on the ANSS National Implementation Committee (NIC).

Over the past 8 years, ANSS funding in California has been directed primarily to the USGS Menlo Park to expand the strong-motion instrumentation in the San Francisco Bay Area. As a result, more than 100 sites have been installed or upgraded, significantly improving the data available for ShakeMaps.

As the ANSS moves forward, committees and working groups are being established to address issues of interest. BSL faculty and staff have been involved in several working groups of the Technical Integration Committee, including Doug Dreger, Pete Lombard, Doug Neuhauser, Bob Uhrhammer, and Stephane Zuzlewski.

#### CISN and OES

The California Governor's Office of Emergency Services has had a long-term interest in coordinated earthquake monitoring. The historical separation between

northern and southern California and between strong-motion and weak-motion networks resulted in a complicated situation for earthquake response. Thus, OES has been an advocate of increased coordination and collaboration in California earthquake monitoring and encouraged the development of the CISN. In FY01/02, Governor Gray Davis requested support for the CISN, to be administered through OES. Funding for the California Geological Survey, Caltech and UC Berkeley was made available in spring 2002, officially launching the statewide coordination efforts. Following the first year of funding, OES support led to the establishment of 3-year contracts to the UC Berkeley, Caltech, and the California Geological Survey for CISN activities. The first multi-year award covered activities in 2002-2005. The second year of the three-year contract for 2006-2008 has just been completed. Past CISN-related activities are described in previous annual reports.

### 3.2.3 2006-2007 Activities

The CISN funding from has OES supported a number of activities at the BSL during the past year.

#### Collaboration with USArray

In late 2003, the CISN concluded a memorandum of agreement with the Incorporated Research Institutions in Seismology (IRIS) covering the duration of the USArray project in California. As a result, data from 19 stations operated by the BSL and 41 stations operated by Caltech are contributed to USArray’s travelling array (TA) during its California deployment. The BSL has also provided accelerometers for use at TA sites which are of interest as future BDSN stations. We monitor the data from these stations in real time, and use the data in ShakeMaps and moment tensors. In addition, data from these TA stations have been included in our development of new parameters that are valid statewide for determining  $M_L$  (see Research Study 2.13.). The collaboration between the BSL and USArray is discussed more fully in Sections 3.1. and 3.7., including the telemetry the BSL provides for the two USArray stations RAMR and SUTB. The TA will move out of California during the Fall of 2007.

#### FEMA Hazard Grant Mitigation Program Funds

The San Simeon and Parkfield earthquakes highlighted the sparseness of high quality instrumentation in northern California, outside of the Bay Area. Although the Parkfield event occurred in a very densely instrumented region, many of accelerometers operated there by the CGS are primarily analog, and the data were not available until several days after the event. Thus, in both these Central California events, the initial ShakeMaps were poorly constrained, because there were few digital instruments in the area with real-time communications.

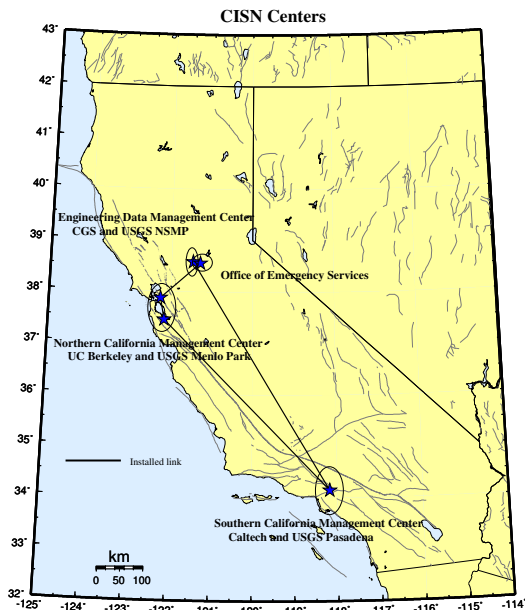


Figure 3.7: Map showing the geographical distribution of the CISN partners and centers. The communications “ring” is shown schematically with installed links (solid lines).

As a result of the San Simeon earthquake and other disasters, FEMA made funds available to OES under the Hazard Grant Mitigation Program (HGMP). The BSL, Caltech, and CGS submitted joint applications for funds to two of these programs, which were funded in August 2005 and May 2006. With funds from these two projects, seismic equipment has been purchased for four new stations, which will be chosen from the USArray TA stations currently deployed in California. One set was installed at the USArray station RAMR near the epicenter of the San Simeon event in September 2007 after the removal of the TA equipment. We monitor and use data from other TA stations in routine processing, and expect to take over HAST, just north of the San Simeon epicenter, and P01C, along the Northern California coast. The fourth site for FEMA equipment remains to be chosen.

#### Northern California Earthquake Management Center

As part of their effort within the CISN, the BSL and the USGS Menlo Park are implementing the new generation of the northern California joint notification system. Section 3.8. describes the operations of the existing Management Center and reports on the design and implementation progress.

In order to move ahead with plans for restructuring the northern California earthquake monitoring system, the USGS Menlo Park and BSL have been improving their

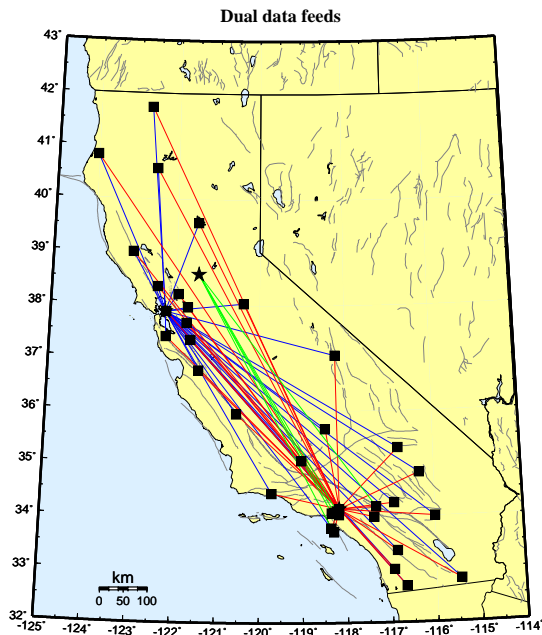


Figure 3.8: Map showing the 30 stations selected to send data directly to the Northern and Southern California processing centers, and the 5 stations that send data directly to the Engineering Data Center and the Southern California processing center.

communications infrastructure. At present, the BSL and the USGS Menlo Park are connected by two dedicated T1 circuits. One circuit is a component of the CISN ring, while the second circuit was installed in 2004-2005 (Figure 3.9) to support dedicated traffic between Berkeley and Menlo Park above and beyond that associated with the CISN.

The installation of the second dedicated T1 between Berkeley and Menlo Park freed up a frame-relay connection deployed by the BSL as part of the CalREN project in mid-1990s. The BSL has reconfigured this frame-relay circuit to serve as a second data acquisition link. BDSN data acquisition is now distributed between two frame-relay T1 circuits, eliminating what had been a single point of failure. An additional Permanent Virtual Circuit (PVC) has also been implemented at each BDSN site so that each station has connections to both T1s. This has improved the robustness of data acquisition at the BSL by providing redundancy in the incoming circuit.

In the long term, the BSL and USGS Menlo Park hope to be connected by high-bandwidth microwave or satellite service. Unfortunately, we have not yet been able to obtain funding for such an additional communication link.

### 3.2.4 Statewide Integration

BSL staff are involved in many elements of the statewide integration effort. The Standards Committee, chaired by Doug Neuhauser, continues to define and prioritize projects important to the development and implementation of the statewide earthquake processing system and to establish working groups to address them (see minutes from meetings and conference calls at <http://www.cisn.org/standards/meetings.html>).

*Dual Station Feeds:* Early in the existence of CISN, “dual station feeds” were established for 30 stations (15 in northern California and 15 in southern California) (Figure 3.8). The Northern California Earthquake Management Center (NCEMC) is using data from the Southern California stations to estimate magnitudes on a routine basis. A subset of these stations are being used for the moment tensor inversions, a computation that is sensitive to the background noise level.

*Data Exchange:* Pick exchange was initiated between the NCEMC and its Southern California counterpart in 2001-2002. The software CISN has developed to produce and exchange the reduced amplitude timeseries has also been completed. Currently, these timeseries are being exchanged at the NCEMC, but not yet statewide. Using a common format, the CISN partners continue to exchange observations of peak ground motion with one another following an event or a trigger. This step increases the robustness of generating products such as ShakeMap, since all CISN partners now exchange data directly with one another. This also improves the quality of ShakeMaps for events on the boundary between northern and southern California, such as the San Simeon earthquake, by allowing all data to be combined in a single map. Finally, this is a necessary step toward the goal of generating statewide ShakeMaps.

*The Software Calibration & Standardization:* CISN partners are working to standardize the software used for automatic earthquake processing and earthquake review, as well as to calibrate it. Currently, the software implemented in the NCEMC and in Southern California Management Center is very different. During the past year in the NCEMC, we have worked on preparing a version of the Southern California TriNet software for implementation as CISN Software in the NCEMC.

- **Magnitude:** Calibrating magnitude estimates has proven to be more difficult than originally anticipated. As described in 2003-2004, evidence indicates that there is a bias between the northern and southern California estimates of local magnitude  $M_L$ . Efforts to understand this issue have been hampered by the lack of a good statewide dataset. Bob Uhrhammer has selected data from 180 earthquakes distributed throughout the state and comprising recordings from 976 horizontal components

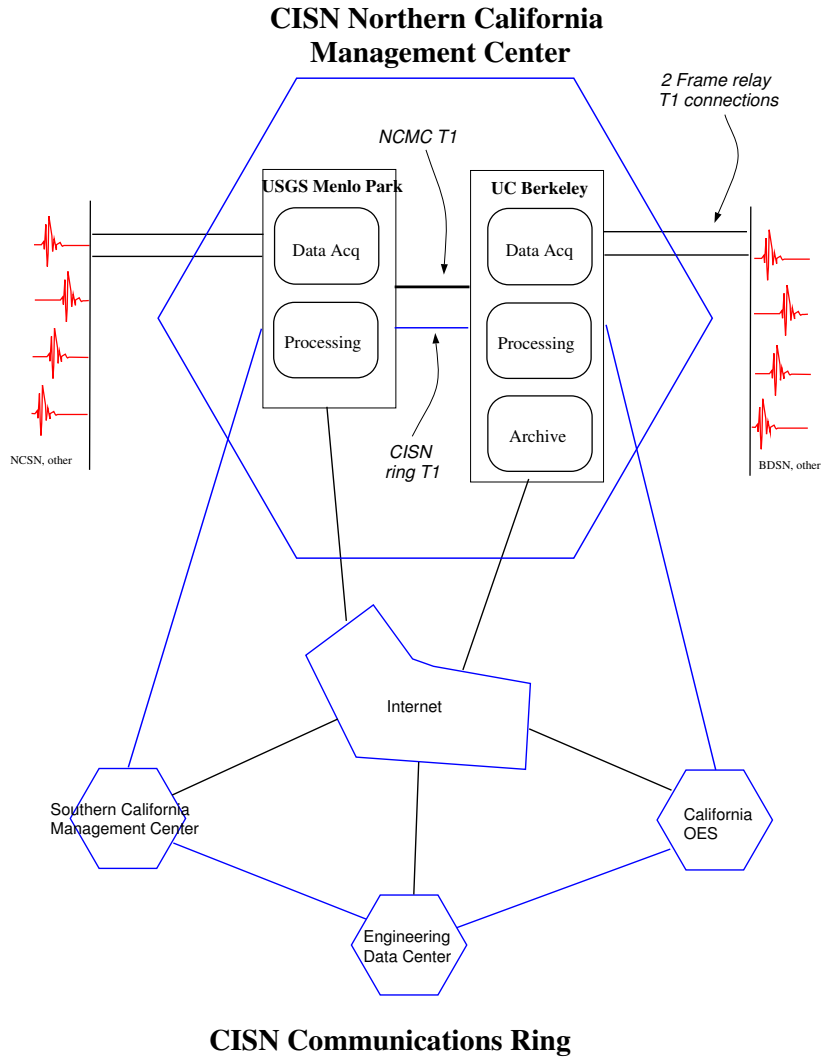


Figure 3.9: Schematic diagram illustrating the connectivity between the real-time processing systems at the USGS Menlo Park and UC Berkeley, forming the northern California Management Center, and with other elements of the CISN.

from the AZ, BK, CI and NC networks (see Research Study 2.13.). In January, we agreed on a  $\log A_o$  function suitable for statewide use. We are currently determining how to define station-specific corrections for  $M_L$  using differences for each station-component that has been recorded for a given event. The primary advantage of using this differencing method is that the results are independent of a reference station. A final component of the magnitude efforts is the determination of a magnitude reporting hierarchy. For the near future, each

region will continue to use its own preferences for magnitude reporting.

- ShakeMap: At present, ShakeMaps are generated on 5 systems within the CISN. Two systems in Pasadena generate “SoCal” Shakemaps; 2 systems in the Bay area generate “NoCal” Shakemaps; and 1 system in Sacramento generates ShakeMaps for all of California. The Sacramento system uses QDDS to provide the authoritative event information for northern and southern California.

The dearth of stations in the near source region of the 2003 San Simeon earthquake raised the issues of how to measure the quality of a ShakeMap and how to quantify the uncertainty. A subset of the Working Group has been working on this issue, based on the work of *Hok and Wald* (2003). *Lin et al* (2006) presented progress toward quantifying ShakeMap uncertainty. When the method is validated, we can use this information to determine a grade.

A second goal of this effort was to improve the robustness of ShakeMap generation and delivery by taking advantage of the fact that ShakeMaps are generated in the Bay Area, Pasadena, and Sacramento. Ongoing efforts in this direction will likely be based on the new USGS ShakeMap webpages at the National Earthquake Information Center.

- **Location Codes:** The CISN adopted a standard for the use of “location” codes (part of the Standard for the Exchange of Earthquake Data (SEED) nomenclature to describe a timeseries based on network-station-channel-location) in the late fall of 2003. USGS and UC Berkeley developers have modified the Earthworm software to support the use of location codes. After the transition at USGS Menlo Park away from the CUSP analysis system to *Jiggle* in late November, 2006, all networks in the CISN implemented location codes in their systems.
- **Metadata Exchange:** Correct metadata are vital to CISN activities, as they are necessary to insure valid interpretation of data. CISN is working on issues related to their reliable and timely exchange. The CISN Metadata Working Group compiled a list of metadata necessary for data processing and developed a model for their exchange. In this model, each CISN member is responsible for the metadata for its stations and for other stations that enter into CISN processing through it. For example, Menlo Park is responsible for the NSMP, Tremor, and PG&E stations, while Caltech is responsible for the Anza data. At the present time, dataless SEED volumes are used to exchange metadata between the NCEMC and the SCMC. The Metadata Working Group is developing a Station XML format for metadata exchange. This vehicle is expandable, and will probably allow exchange of a more comprehensive set of metadata than dataless SEED volumes, some which may be necessary for other systems, for example in V0 formatted data.
- **Standardization:** The CISN’s focus on standardization of software continues. For example, the BSL and the USGS Menlo Park are adapting the software running at the SCMC for use at the NCEMC

and are currently testing its various elements. The adoption of *Jiggle* in northern California in late November 2007, was the first step in the implementation of the new software. Current efforts are directed toward the implementation and testing of the complete system (see Section 3.8.).

### CISN Display

CISN Display is an integrated Web enabled earthquake notification system, designed to provide earthquake information for emergency response at 24/7 operations centers. First-responders, organizations with critical lifelines and infrastructure, and emergency responders are invited to register for an account at <http://www.cisn.org/software/cisndisplay.htm>.

The application provides users with maps of real-time seismicity, and automatically provides access to Web-related earthquake products such as ShakeMaps. CISN Display also offers an open source GIS mapping tool that allows users to plot freely available layers of public highways, roads and bridges, as well as private layers of organizational-specific infrastructure and facilities information. The current version of CISN Display is 1.4. Its primary enhancement over the previous version is the development of a kiosk-mode for public display purposes.

### Earthquake Information Distribution

The USGS hosted a workshop in October 2004 to develop plans for the installation and use of the EIDS software. Doug Neuhauser and Pete Lombard participated in this workshop, which resulted in a document outlining the steps necessary for the installation and migration of the earthquake notification system from the current Quake Data Distribution Services (QDDS) to EIDS.

### Outreach

Since FY05/06 the CISN Web site ([www.cisn.org](http://www.cisn.org)) has been supported by two servers located at Berkeley and Caltech. The Web servers are set up so that the load can be distributed between them, providing improved access during times of high demand. With the increased robustness provided by the new servers, the CISN provides access to certain earthquake products directly from [www.cisn.org](http://www.cisn.org). For example, ShakeMaps are now served directly from the CISN Web site, in addition to being available from several USGS Web servers and the CGS. The design and content of <http://www.cisn.org> continues to evolve. The Web site is an important tool for CISN outreach as well as for communication and documentation among the CISN partners.

The CISN continues to support the dedicated Web site for emergency managers. Following a suggestion from the Advisory Committee, we have designed a Web site

to provide personalized access to earthquake information. Known as “myCISN,” the Web site is available at [eoc.cisn.org](http://eoc.cisn.org). Access to the Web site is limited to registered users in order to provide highly reliable access. At present, “myCISN” is a single Web server located at UC Berkeley. However, modifications to the database are underway to allow for multiple servers in the future. A second computer, already purchased, will either be installed in Sacramento or in southern California.

As part of the CISN, the BSL is contributing to efforts to raise awareness of earthquakes and preparedness as the 140 anniversary of the 1868 Hayward Fault earthquake approaches on October 21, 2008. In particular, we will be co-hosting the *Third Conference on Earthquake Hazards in the Eastern Bay Area* as well as organizing and participating in other related activities.

### 3.2.5 Acknowledgements

CISN activities at the BSL are supported by funding from the Governor’s Office of Emergency Services.

Barbara Romanowicz and Peggy Hellweg are members of the CISN Steering Committee. Peggy Hellweg is a member of the CISN Program Management Group, and she leads the CISN project at the BSL with support from Doug Neuhauser. Doug Neuhauser is chair of the CISN Standards Committee, which includes Peggy Hellweg, Pete Lombard and Stephane Zuzulevski as members.

Because of the breadth of the CISN project, many BSL staff have been involved including: John Friday, Jarrett Gardner, Peggy Hellweg, Bill Karavas, Alexei Kireev, Rick Lelling, Pete Lombard, Doug Neuhauser, Charley Paffenbarger, Bob Uhrhammer and Stephane Zuzlewski. Peggy Hellweg contributed to this chapter. Additional information about the CISN is available through reports from the Program Management Committee.

### 3.2.6 References

Hok, S., and D. J. Wald, Spatial Variability of Peak Strong Ground Motions: Implications for ShakeMap Interpolations, *EOS. Trans. AGU*, 84(46), F1121, 2003.

Lin, K-W., D. Wald, B. Worden and A.F. Shakal, Progress toward quantifying CISN ShakeMap uncertainty, *Eighth National Conference on Earthquake Engineering, San Francisco, California, April 18-21, 2006*.

### 3.3. Northern Hayward Fault Network

#### 3.3.1 Introduction

Complementary to the regional broadband network, the Hayward Fault Network (HFN) (Figure 3.10 and Table 3.5) is a deployment of borehole-installed, wide-dynamic range seismographic stations along the Hayward Fault and throughout the San Francisco Bay toll bridges network. Development of the HFN initiated through a cooperative effort between the BSL and the USGS, with support from the USGS, Caltrans, EPRI, the University of California Campus/Laboratory Collaboration (CLC) program, LLNL, and LBNL. The project's objectives included both an initial characterization period followed by longer-term monitoring effort using a backbone of stations from among the initial characterization set. Subsequent funding from Caltrans, however, has allowed for continued expansion of the backbone station set for additional coverage in critical locations.

The HFN consists of two components. The Northern Hayward Fault Network (NHFN) is operated by the BSL and currently consists of 28 stations with various operational status. These include stations located on Bay Area bridges and now at borehole sites of the Mini-PBO (MPBO) project, which were installed with support from NSF and the member institutions of the MPBO project. The NHFN is considered part of the BDSN and uses the network code BK. The Southern Hayward Fault Network (SHFN) is operated by the USGS and currently consists of 5 stations. This network is considered part of the NCSN and uses the network code NC. The purpose of the HFN is threefold: 1) to increase substantially the sensitivity of seismic data to low amplitude seismic signals, 2) to increase the recorded bandwidth for seismic events along the Hayward fault, and 3) to obtain bedrock ground motion signals at the bridges from more frequent smaller earthquakes.

Data with these attributes contribute significantly to a variety of scientific objectives including: a) the investigation of bridge responses to stronger ground motions from real earthquakes, b) obtaining a significantly lower detection threshold for microearthquakes and nonvolcanic tremor signals, c) increasing the resolution of the fault-zone seismic structure (e.g., in the vicinity of the Rodgers Creek/Hayward Fault step over), d) improving monitoring of spatial and temporal evolution of seismicity (to magnitudes approaching  $M \sim -1.0$ ) that may signal behavior indicative of the nucleation of large damaging earthquakes, e) the investigation of earthquake scaling, physics and related fault processes, f) improving working models for the Hayward fault, and g) using these models to make source-specific response calculations for estimating strong ground shaking throughout the Bay Area.

This chapter is primarily focused on the NHFN and activities associated with the BSL operations.

#### 3.3.2 NHFN Overview

The initial characterization period ended in 1997. During that period, the NHFN sensors provided signals to on-site, stand-alone Quanterra Q730 and RefTek 72A-07 dataloggers, and manual retrieval and download of data tapes was required. Also in that year, the long-term monitoring phase of the project began, involving the installation of 24-bit data acquisition and communication platforms and data telemetry to the BSL archives for a backbone of the initial NHFN stations.

Over the years, CalTrans has provided additional support for the upgrade of two non-backbone sites to backbone operational status and for the addition of several new sites to the monitoring back-bone. These expansion efforts are ongoing. Also since the transition to the long-term monitoring phase, the 5 stations of the MPBO project have been folded into the NHFN.

Of the 28 stations now considered part of the NHFN history, 14 of the stations are currently operational, with telemetered data streams flowing continuously into the BSL's BDSN processing stream with subsequent archival in the Northern California Earthquake Data Center (NCEDC) archive. These include the 5 MPBO sites. Nine of the original 28 are non-backbone stations that have not been upgraded to continuous telemetry. Though collection of data from these sites has been discontinued, their borehole sensor packages are still in place (having been grouted in), and efforts to find funding for upgrade of these sites with Quanterra Q4120, Q730 or Q330 dataloggers and continuous telemetry continues. The remaining 5 sites are in the process of being added to the NHFN backbone. Four of the sites have been drilled and instrumented and are awaiting installation of their electronics and infrastructures. Equipment has been purchased for the 1 remaining site, which is awaiting final land-use agreement from the Regional Parks district and drilling by CalTrans.

*Installation/Instrumentation:* The NHFN Sensor packages are generally installed at depths ranging between 100 and 200 m, the non-backbone non-operational Dumbarton bridge sites being exceptions with sensors at multiple depths (Table 3.5).

The five former MPBO sites that are now part of the NHFN have 3-component borehole geophone packages. Velocity measurements for the MPBO sites are provided by Mark Products L-22 2 Hz geophones (Table 3.6). All the remaining backbone and non-backbone NHFN sites have six-component borehole sensor pack-

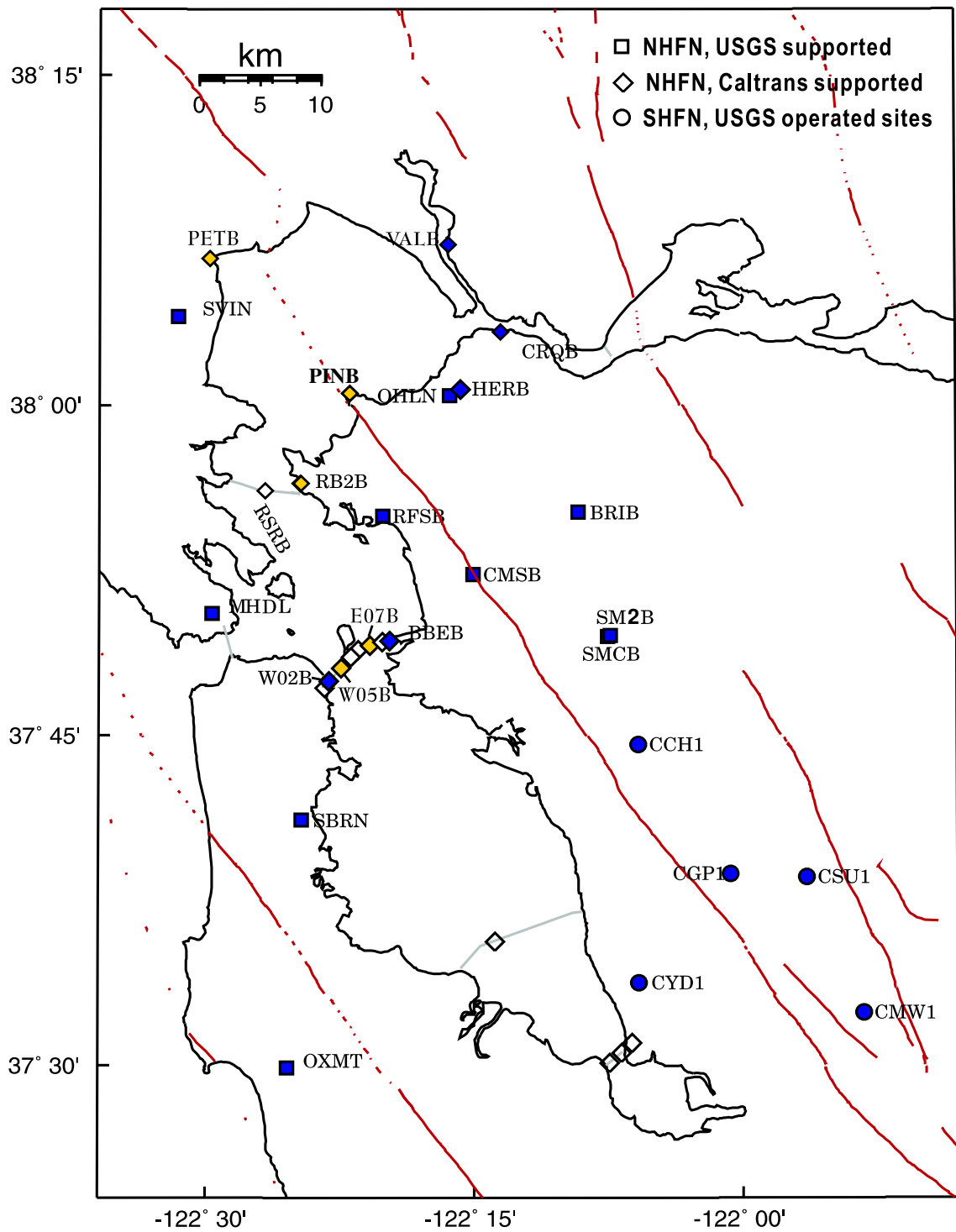


Figure 3.10: Map showing the locations of the HFN stations operated by the BSL (NHFN - squares and diamonds) and the USGS (SHFN - circles). Operational sites are filled blue/black, while sites in progress are yellow/grey. Other instrumented but currently non-operational boreholes are indicated as open symbols.

ages. The six-component packages were designed and fabricated at LBNL's Geophysical Measurement Facility and have three channels of acceleration, provided by Wilcoxon 731A piezoelectric accelerometers, and three channels of velocity, provided by Oyo HS-1 4.5 Hz geophones.

The 0.1-400 Hz Wilcoxon accelerometers have lower self-noise than the geophones above about 25-30 Hz, and remain on scale and linear to 0.5 g. In tests performed in the Byerly vault at UC Berkeley, the Wilcoxon is considerably quieter than the FBA-23 at all periods, and is almost as quiet as the STS-2 between 1 and 50 Hz.

All 14 NHFN backbone sites have Quanterra dataloggers with continuous telemetry to the BSL. Signals from these stations are digitized at a variety of data rates up to 500 Hz at 24-bit resolution (Table 3.7). The dataloggers employ causal FIR filters at high data rates and acausal FIR filters at lower data rates.

*Data Rates and Channels:* Because of limitations in telemetry bandwidth and disk storage, 8 of the 9 (excluding VALB) six-component NHFN stations transmit one channel of geophone data continuously (i.e., their vertical geophone channels) and an additional 3 channels of triggered data in 90 sec. snippets. A Murdock, Hutt, and Halbert (MHH) event detection algorithm (*Murdock and Hutt, 1983*) is operated independently at each station on 500 sps data for trigger determinations. Because of they are quieter, the 3 triggered channels are taken from the Wilcoxon accelerometers when possible. However, there is a tendency for these powered sensors to fail and in such cases, geophone channels are substituted for the failed accelerometers. Station VALB also transmits data from only 4 channels; however, all channels are transmitted continuously. Continuous data for all channels at reduced rates (20 and 1 sps) are also transmitted to and archived at the BSL. The five MPBO sites transmit their 3-component continuous geophone data streams at 100, 20 and 1 sps, which are also archived at BSL.

## Station Maintenance

Ongoing network maintenance involves regular inspection of the collected seismic waveform data and spectra for nearby seismic events, and also from noise samples. Other common problems include changes to background noise levels due to ground loops and failing preamps, as well as power and telemetry issues. Troubleshooting and remediation of problems often require a coordinated effort, with a technician at the BSL to examine seismic waveforms and spectra while the field technicians are still on site. BSL technicians and researchers regularly review data and assist in troubleshooting.

The NHFN station hardware has proven to be relatively reliable. Nonetheless, numerous maintenance and performance enhancement measures are still carried out. In particular, when a new station is added to the

backbone, extensive testing and correction for sources of instrumental noise (e.g., grounding related issues) and telemetry through-put are carried out to optimize the sensitivity of the station. Examples of maintenance and enhancement measures that are typically performed include: 1) tests on radio links to ascertain reasons for unusually large numbers of dropped packets, 2) trouble shooting sporadic problems with numerous frame relay telemetry dropouts, 3) manual power recycle and testing of hung Quanterra data loggers, 4) replacement of blown fuses or other problems relating to dead channels identified through remote monitoring at the BSL, 5) repair of frame relay and power supply problems when they arise, and 6) correcting antenna problems that arise due to various causes, such as weather or cultural activity.

## Quality Control

- PSD and Real Event Displays: Our commonly used quality checks on the performance of the borehole installed network include assessments of the power spectral density (PSD) distributions for background noise and quick checks following large teleseismic and moderate local earthquakes of the data records across the NHFN stations. Shown in Figure 3.11 is such a display for NHFN geophone channels from a recent Bay Area earthquake (20 July 2007, M4.2 Piedmont, CA). It is immediately apparent from this simple display that station MHDL was dead and needed immediate attention.

It is also apparent from the buzz underlying the earthquake signal in this display that the grounding schemes for stations SBRN and HERB may be in need of modification. One of the most pervasive problems at NHFN stations is power line noise (60 Hz and its harmonics at 120, 180, and 240 Hz). This noise reduces the sensitivity of the MHH detectors, and at any given station this type of noise source changes over periods of weeks to months, requiring continued vigilance and adaptability of the grounding scheme in order to maintain the desired high sensitivity to low amplitude seismic signals.

- Geophone Calibration Tests: Comparisons of the inferred ground accelerations generated by local earthquakes from co-sited NHFN geophone and accelerometer pairs show that the waveforms generally are quite coherent in frequency and phase response, but that their inferred ground accelerations differ significantly. At times, the amplitudes differ by up to a factor of 2 while the times of the peak amplitudes are identical. This implies that the free period and damping of the geophones are well characterized. However, it also indicates that the generator constant is not accurate (assuming that the

Code	Net	Latitude	Longitude	Elev (m)	Over (m)	Date	Location
VALB	BK	38.1215	-122.2753	-24	155.8	2005/11 - current	Napa River Bridge
PETB	BK	38.1189	-122.5011	-30	113	in progress	Petaluma River Bridge
CRQB	BK	38.05578	-122.22487	-25	38.4	1996/07 - current	CB
HERB	BK	38.01250	-122.26222	-25	217.9	2000/05 - current	Hercules
PINB*	BK	38.0113	-122.3653	tbd	tbd	in progress	Point Pinole
BRIB	BK	37.91886	-122.15179	219.7	108.8	1995/06 - current	BR, Orinda
RFSB	BK	37.91608	-122.33610	-27.3	91.4	1996/01 - current	RFS, Richmond
CMSB	BK	37.87195	-122.25168	94.7	167.6	1994/12 - current	CMS, Berkeley
SMCB	BK	37.83881	-122.11159	180.9	3.4	1997/12 - 2007/06	SMC, Moraga
SM2B	BK	37.8387	-122.1102	200	150.9	2007/06 - current	SMC, Moraga
SVIN	BK	38.03325	-122.52638	-21	158.7	2003/08 - current	MPBO, St. Vincent's school
OHLN	BK	38.00742	-122.27371	-0	196.7	2001/07 - current	MPBO, Ohlone Park
MHDL	BK	37.84227	-122.49374	94	160.6	2006/05 - current	MPBO, Marin Headlands
SBRN	BK	37.68562	-122.41127	4	157.5	2001/08 - current	MPBO, San Bruno Mtn.
OXMT	BK	37.4994	-122.4243	209	194.2	2003/12 - current	MPBO, Ox Mtn.
BBEB	BK	37.82167	-122.32867	-31	150.0	2002/05 - current	BB, Pier E23
E17B	BK	37.82086	-122.33534		160.0	1995/08 - current *	BB, Pier E17
E07B	BK	37.81847	-122.34688	tbd	134.0	1996/02 - current *	BB, Pier E7
YBIB	BK	37.81420	-122.35923	-27.0	61.0	1997/12 - current *	BB, Pier E2
YBAB	BK	37.80940	-122.36450		3.0	1998/06 - current *	BB, YB Anchorage
W05B	BK	37.80100	-122.37370	tbd	36.3	1997/10 - current *	BB, Pier W5
W02B	BK	37.79120	-122.38525	-45	57.6	2003/06 - current	BB, Pier W2
SFAB	BK	37.78610	-122.3893		0.0	1998/06 - current *	BB, SF Anchorage
RSRB	BK	37.93575	-122.44648	-48.0	109.0	1997/06 - current *	RSRB, Pier 34
RB2B	BK	37.93	-122.41	tbd	133.8	2003/07 - current *	RSRB, Pier 58
SM1B	BK	37.59403	-122.23242		298.0	not recorded	SMB, Pier 343
DB3B	BK	37.51295	-122.10857		1.5	1994/09 - 1994/11	DB, Pier 44
					62.5	1994/09 - 1994/09	
					157.9	1994/07 - current *	
DB2B	BK	37.50687	-122.11566			1994/07 - current *	DB, Pier 27
					189.2	1992/07 - 1992/11	
DB1B	BK	37.49947	-122.12755		0.0	1994/07 - 1994/09	DB, Pier 1
					1.5	1994/09 - 1994/09	
					71.6	1994/09 - 1994/09	
					228.0	1993/08 - current *	
CCH1	NC	37.7432	-122.0967	226		1995/05 - current	Chabot
CGP1	NC	37.6454	-122.0114	340		1995/03 - current	Garin Park
CSU1	NC	37.6430	-121.9402	499		1995/10 - current	Sunol
CYD1	NC	37.5629	-122.0967	-23		2002/09 - current	Coyote
CMW1	NC	37.5403	-121.8876	343		1995/06 - current	Mill Creek

Table 3.5: Stations of the Hayward Fault Network. Each HFN station is listed with its station code, network id, location, operational dates, and site description. The latitude and longitude (in degrees) are given in the WGS84 reference frame. The elevation of the well head (in meters) is relative to the WGS84 reference ellipsoid. The overburden is given in meters. The start dates indicate either the upgrade or installation time. The abbreviations are: BB - Bay Bridge; BR - Briones Reserve; CMS - Cal Memorial Stadium; CB - Carquinez Bridge; DB - Dumbarton Bridge; MPBO - mini-Plate Boundary Observatory; RFS - Richmond Field Station; RSRB - Richmond-San Rafael Bridge; SF - San Francisco; SMB - San Mateo Bridge; SMC - St. Mary's College; and, YB - Yerba Buena. The \* for station PINB indicates that this station name has been requested but has not yet been approved and may change. The \* in the Date column indicates the stations that have recorded data from an earlier period of manually retrieved tapes, but that are currently off-line.

Site	Geophone	Accelerometer	Z	H1	h2	datalogger	Notes	Telem.
VALB	Oyo HS-1	Wilcoxon 731A	TBD	TBD	TBD	Q330		FR
PETB	Oyo HS-1	Wilcoxon 731A	TBD	TBD	TBD	TBD		TBD
CRQB	Oyo HS-1	Wilcoxon 731A	-90	251	341	Q4120		FR
HERB	Oyo HS-1	Wilcoxon 731A	-90	TBD	TBD	Q4120		FR
PINB	Oyo HS-1	Wilcoxon 731A	TBD	TBD	TBD	TBD		TBD
BRIB	Oyo HS-1	Wilcoxon 731A	-90	79	349	Q4120	Acc. failed, Dilat.	FR
RFSB	Oyo HS-1	Wilcoxon 731A	-90	256	346	Q4120		FR
CMSB	Oyo HS-1	Wilcoxon 731A	-90	19	109	Q4120		FR
SMCB	Oyo HS-1	Wilcoxon 731A	-90	76	166	Q4120	Posthole	FR
SM2B	Oyo HS-1	Wilcoxon 731A	TBD	TBD	TBD	Q4120		FR
SVIN	Mark L-22		-90	298	28	Q4120	Tensor.	FR/Rad.
OHLN	Mark L-22		-90	313	43	Q4120	Tensor.	FR
MHDL	Mark L-22		-90	TBD	TBD	Q4120	Tensor.	FR
SBRN	Mark L-22		-90	347	77	Q4120	Tensor.	FR
OXMT	Mark L-22		-90	163	253	Q4120	Tensor.	FR
BBEB	Oyo HS-1	Wilcoxon 731A	-90	TBD	TBD	Q4120	Acc. failed	Radio
E17B	Oyo HS-1	Wilcoxon 731A	-90	TBD	TBD	None at present		
E07B	Oyo HS-1	Wilcoxon 731A	-90	TBD	TBD	None at present		
YBIB	Oyo HS-1	Wilcoxon 731A	-90	257	347	None at present	Z geop. failed	FR/Rad.
YBAB	Oyo HS-1	Wilcoxon 731A	-90	TBD	TBD	None at present		
W05B	Oyo HS-1	Wilcoxon 731A	-90	TBD	TBD	None at present		
W02B	Oyo HS-1	Wilcoxon 731A	-90	TBD	TBD	Q4120		Radio
SFAB	None	LLNL S-6000	TBD	TBD	TBD	None at present	Posthole	
RSRB	Oyo HS-1	Wilcoxon 731A	-90	50	140	None at present	2 acc. failed	FR
RB2B	Oyo HS-1	Wilcoxon 731A	-90	TBD	TBD	None at present	1 acc. failed	
SM1B	Oyo HS-1	Wilcoxon 731A	-90	TBD	TBD	None at present		
DB3B	Oyo HS-1	Wilcoxon 731A	-90	TBD	TBD	None at present	Acc. failed	
DB2B	Oyo HS-1	Wilcoxon 731A	-90	TBD	TBD	None at present		
DB1B	Oyo HS-1	Wilcoxon 731A	-90	TBD	TBD	None at present	Acc. failed	
CCH1	Oyo HS-1	Wilcoxon 731A	-90	TBD	TBD	Nanometrics HRD24	Dilat.	Radio
CGP1	Oyo HS-1	Wilcoxon 731A	-90	TBD	TBD	Nanometrics HRD24	Dilat.	Radio
CSU1	Oyo HS-1	Wilcoxon 731A	-90	TBD	TBD	Nanometrics HRD24	Dilat.	Radio
CYD1	Oyo HS-1	Wilcoxon 731A	-90	TBD	TBD	Nanometrics HRD24	Dilat.	Radio
CMW1	Oyo HS-1	Wilcoxon 731A	-90	TBD	TBD	Nanometrics HRD24	Dilat.	Radio

Table 3.6: Instrumentation of the HFN as of 06/30/2007. Every HFN downhole package consists of co-located 3-component geophones and accelerometers, with the exception of MPBO sites which have only 3-component geophones and are also collecting tensor strainmeter data. Six HFN sites (5 of the SHFN and 1 of the NHFN) also have dilatometers (Dilat.). Currently, 14 NHFN sites have Quanterra dataloggers with continuous telemetry to the BSL. The remaining backbone sites are either still being developed with support from Caltrans or are being upgraded to Quanterra dataloggers. The 5 SHFN sites have Nanometrics dataloggers with radio telemetry to the USGS. The orientation of the sensors (vertical - Z, horizontals - H1 and H2) are indicated where known or identified as "to be determined" (TBD).

corresponding ground accelerations inferred from the accelerometers are accurate).

Generally speaking, the accelerometers, being an active device, are more accurate and also more stable than the geophones, so it is reasonable to assume that the most likely reason for the difference is that the assumed generator constants for the geophones are inaccurate. *Rodgers et al.* (1995) describe a way to absolutely calibrate the geophones

in situ and to determine their generator constant, free period and fraction of critical damping. The only external parameter that is required is the value of the geophone's inertial mass.

We have built a calibration test box which allows us to routinely perform the testing described by *Rodgers et al.* whenever site visits are made. The box drives the signal coil with a known current step and rapidly switches the signal coil between the

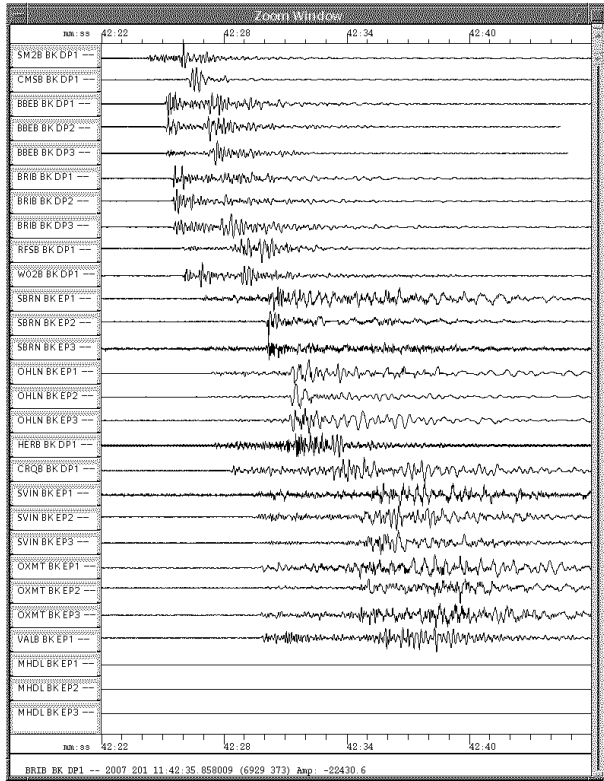


Figure 3.11: Plot of unfiltered P-wave seismograms, recorded on the geophones of the 14 operational NHFN borehole stations for a recent Bay Area earthquake (20 July 2007, M4.2 Piedmont, CA). The stations have been ordered by increasing distance from the event (top to bottom). It is immediately apparent from this simple display that station MHDL was dead and needed immediate attention.

current source and the datalogger input. From this information, expected and actual sensor response characteristics can be compared and corrections applied. Also, changes in the sensor response over time can be evaluated so that adjustments can be made, and pathologies arising in the sensors due to age can be identified. Once a geophone is absolutely calibrated, we also check the response of the corresponding accelerometer.

### 3.3.3 2006-2007 Activities

In addition to routine maintenance, operations, quality control and data collection, activities of the NHFN project over the past year have also included efforts at ensuring more stable operations and maintenance (O&M) funding support, upgrading and expanding the NHFN and developing procedures to enhance quality control and data analysis.

Sensor	Channel	Rate (sps)	Mode	FIR
Accelerometer	CL?	500.0	T	Ca
Accelerometer	HL?	200.0	C	Ca
Accelerometer	BL?	20.0	C	Ac
Accelerometer	LL?	1.0	C	Ac
Geophone	DP?	500.0	T,C	Ca
Geophone	EP?	200.0	C	Ca
Geophone	EP?	100.0	C	Ca
Geophone	BP?	20.0	C	Ac
Geophone	LP?	1.0	C	Ac

Table 3.7: Typical data streams acquired at NHFN sites, with channel name, sampling rate, sampling mode and FIR filter type. C indicates continuous, T triggered, Ca causal, and Ac acausal. Typically the DP1 continuous channel is archived and the remaining high sample rate data (i.e., CL and DP channels) are archived as triggered snippets. Prior to Sept. 2004, however, only triggered data was archived for all high sample rate channels.

### 3.3.4 Stable O&M Funding

In past years, support for NHFN O&M has been obtained on a yearly basis through competitive proposals to the USGS's external National Earthquake Hazard Reduction Program (NEHRP) program. Our requests for operating and maintaining a network were at a disadvantage in many regards since they had to compete against other proposals in the program that were focused on research. To help offset this disadvantage, we would also typically propose not only support for O&M but also support for research to be performed using NHFN data. For years the results of our proposal requests were funding grants that were roughly half the requested support and that were barely able to support the O&M of the network, without any moneys left over to do research. The need to compete competitively each year also contributed a significant level of uncertainty to the prospects for continued operation of the NHFN over longer time periods, and long-term planning of enhancement and expansion of the network were difficult.

This year, finally, after several years of negotiation and administrative and operational adaptations, we were able to propose and obtain a 3-year funding grant (cooperative agreement) through the ANSS (Advanced National Seismic System). Though this grant supports O&M for only 9 NHFN stations, it is more stable in the long-term, allowing for long-term planning and action to take place. It has also allowed us to fold the 5 MPBO stations into the network, which provide an excellent complement to the NHFN's borehole seismic coverage of the Bay Area. This year, we have also obtained a 3-year funding agreement with Caltrans for the O&M of 10 additional NHFN stations, bringing the total number of stations with long-term O&M support to 19 (14 currently operational and 5

near operational). We anticipate future long-term O&M support for the new planned NHFN stations to also receive long-term Caltrans support.

### 3.3.5 Upgrade of SMCB to SM2B

This year, we have completed our agreements with Caltrans and St. Mary's College to replace the post hole installation at St. Mary's College (SMCB) with a deep borehole installation (SM2B). Last year the hole was drilled by Caltrans as a hole of opportunity (i.e., when the schedule of a Caltrans drilling crew had an opening) to a depth of 151 m and a few hundred meters away from the post-hole (SMCB) site. The sensor package was also installed at that time. This year, with assistance from Caltrans and the St. Mary's College grounds crew, the site infrastructure was completed and 79 days of coincident data from both SMCB and SM2B was collected and analysed. SMCB was decommissioned and SM2B data acquisition began on June 26 of this year.

#### New Installations

As originally conceived, the Hayward Fault Network was to consist of 24 to 30 stations, 12-15 each north and south of San Leandro, managed respectively by UCB and USGS. Due to USGS funding limitations, however, the original plan has been significantly modified. The USGS component, for example, is now limited to 5 stations. With additional Caltrans support, however, development of the NHFN component of the project has continued. Currently, 14 NHFN sites are now operational and 4 more sites should come on-line soon (PETB, RB2B, E07B and W05B) having downhole sensors in place and surface equipment ready for installation. Activation of PETB (expected the 2nd week of October, 2007) and RB2B are planned first, with the addition of W05B and E07B as progress on the Bay-Bridge retrofit project allows.

With Caltrans funding, we have also purchased sensors and instrumentation for 2 additional sites, and Caltrans will provide drilling for these sites as spare drilling crew time becomes available (i.e., holes of opportunity). Permit negotiations for these two sites (PINB, shown in Figure 3.10; and a site at Cal Maritime Academy, not shown) are in their final stages, and the availability of Caltrans drilling is anticipated later this year or early next. We have also been asked by Caltrans to submit a proposal for the addition of 3 more NHFN sites in the coming years, an opportunity we are pursuing with vigor.

#### Quality Control and Data Analysis

In order to monitor and capture the source spectrum of moderate down to micro-scale earthquakes, it is essential that the NHFN instruments operate at high precision and in an extremely low noise environment. Therefore, the stations record at high sample rate, and their sensors

are emplaced in deep boreholes to reduce noise contamination originating in the near surface weathered zone and from cultural noise sources. In addition, the reduction of noise at these stations through vigilant monitoring of actual seismic events plays a central part of our quality control effort.

As mentioned, a key aspect of quality control of the NHFN data is the analysis of actual seismic events. Seismic events of larger magnitude are relatively rare and generally provide more energy at lower frequencies. Hence, in order to provide more frequent real events and quality control in the higher frequency band of the NHFN stations, analysis of recordings from the much more frequent microearthquakes are needed. Because real event analyses are relatively labor intensive and because of inadequate insufficient funding, traditional methods of event analysis have proven financially infeasible. To help circumvent these problems, efforts to develop new and improved analysis techniques are ongoing. We have developed and are currently testing some promising techniques that are particularly well suited to the analysis of similar and repeating microearthquakes. The advantages of similar and repeating event analyses for both quality control and scientific purposes are numerous, and the nature of the seismograms from these types of events make automated, rapid and robust analysis possible.

Towards this end, we are continuing to develop our new pattern scanning recognition scheme to detect, pick, locate and determine magnitudes for small and very small similar events recorded either continuously or from among large volumes of noisy triggered data snippets and our phase coherency method for identification of characteristically repeating events sequences from among groups of similar event multiplets.

*Pattern Scanning:* The pattern scanning recognition approach we are developing enhances the effective signal to noise for event detection, picking and locating by using the high amplitude information available in the full waveform of earthquake's signals. This is done by using a cross-correlation based scanning approach, which scans known waveform patterns through either continuous or collections triggered event snippets (regardless of the triggered event noise levels). With this approach, continuous or triggered waveform data that does not match selected patterns are ignored while waveforms that approximately match selected reference event patterns are flagged as newly identified earthquakes.

This approach is less comprehensive in that it only detects events that are somewhat similar in waveform character to the reference patterns. However, it can be generalized significantly by increasing the number of event patterns scanned or by using fairly low maximum cross-correlation thresholds for event flagging. Preliminary tests of our scanning code show that scans of 100 distinct event patterns can be scanned through a day's

worth of waveform data in 75 minutes on one 900Mhz SPARC cpu when continuous seismic data is used. Scanning through collections of all triggered snippets is substantially faster, in proportion to the inverse fraction of total time spanned by the snippet data.

The approach also provides automated cross-correlation pick alignments that can be used for high precision relative locations and for automated low-frequency spectral ratio determinations for magnitude estimates. Clearly the method has potential for automatically cataloging a large fraction of the more numerous microearthquakes, and, in conjunction with the special attributes of similar event groups, updates of the catalogs in an automated monitoring mode can provide near-real-time microearthquake information that can be a powerful tool for monitoring network performance of real event data. Future plans include development and implementation of an automated similar event scanning and cataloging scheme that will provide real-event data from similar small magnitude events for assessment of network health on a much more frequent basis (every few days).

Perhaps more significantly, the approach can also capture and rapidly catalog some of the most scientifically relevant events (e.g. repeats of characteristically repeating microearthquakes used for deep slip rate monitoring and swarms of similar events typically associated with foreshocks and aftershocks). The approach is also surprisingly good at detecting events over a wide magnitude range. Hence there is clear potential for using patterns from larger aftershocks (e.g. flagged by REDI) to rapidly and automatically develop a high-resolution picture of foreshock and aftershock activity associated with large mainshocks. Tests so far using waveform patterns from an aftershock from the Parkfield magnitude 6 event (2.2Ml) have been able to detect and fully process similar events as low as Ml - 1.2 (a range of 3.4 magnitude units). Testing in this regard is continuing, but clearly the 3.4 magnitude range is a lower bound on the potential magnitude range attainable.

*Phase Coherency:* In order to enhance even further the resolution and scientific value of the similar events identified using the pattern scanning approach, we are continuing to refine and test our spectral phase coherency algorithm. This algorithm allows for detailed quantification of the similarities and differences between highly similar Hayward fault events to provide characterization of the subsets of similar events known as characteristically repeating microearthquakes. These subsets form groups or sequences of events that are believed to represent recurring ruptures of the same small patch of fault through time, and, once recongnized, such sequences provide a new dimension of constraint on earthquake physics and deep fault deformation through the recurrence intervals and magnitudes of the events comprising the sequences.

The complex spectral phase coherency methodology can be carried out in various frequency bands geared appropriately to the magnitude dependence of frequency for earthquakes and is generally an order of magnitude better in its discrimination power than the simple cross correlation method. The goal of the testing and refinement is ultimately to develop a scheme for rapid and objective discrimination and identification of characteristically repeating microearthquakes sequences down to the lowest magnitude possible (where recurrence times are short and hence temporal resolutions are higher) along the Hayward fault, and to use the information from these sequences to gain a better picture of the time evolution of creep deep in the fault zone.

### 3.3.6 Acknowledgments

Thomas V. McEvelly, who passed away in February 2002, was instrumental in developing the Hayward Fault Network, and without his dedication and hard work the creation and continued operation of the NHFN would not have been possible.

Under Bob Nadeau's and Doug Dreger's general supervision, Rich Clymer, Doug Neuhauser, Bob Uhrhammer, Bill Karavas, John Friday, and Rick Lellingner all contribute to the operation of the NHFN. Bob Nadeau prepared this chapter.

Support for the NHFN is provided by the USGS through the NEHRP grant program (grant no. 07HQAG0014) and by Caltrans through grant no. 59A0245. Pat Hipley of Caltrans has been instrumental in the effort to continue to upgrade and expand the network. Larry Hutchings and William Foxall of LLNL have also been important collaborators on the project in years past.

### 3.3.7 References

Rodgers, P.W., A.J. Martin, M.C. Robertson, M.M. Hsu, and D.B. Harris, Signal-Coil Calibration of Electromagnetic Seismometers, *Bull. Seism. Soc. Am.*, 85(3), 845-850, 1995.

Murdock, J., and C. Hutt, A new event detector designed for the Seismic Research Observatories, *USGS Open-File-Report 83-0785*, 39 pp., 1983.

## 3.4. Parkfield Borehole Network (HRSN)

### 3.4.1 Introduction

The operation of the High Resolution Seismic Network (HRSN) at Parkfield, California began in 1987, as part of the United States Geological Survey (USGS) initiative known as the Parkfield Prediction Experiment (PPE) (*Bakun and Lindh, 1985*).

Figure 3.12 shows the location of the network, its relationship to the San Andreas fault, sites of significance from previous and ongoing research using the HRSN, double-difference relocated earthquake locations from 1987-1998, routine locations of seismicity from August 2002 to July 2003, some preliminary nonvolcanic tremor locations from January 2006 through June 2007, and the epicenter of the 1966 and 2004 M6 earthquakes that motivated much of the research. The HRSN records exceptionally high-quality data, owing to its 13 closely spaced three-component borehole sensors (generally emplaced in the extremely low attenuation and background noise environment at 200 to 300 m depth (Table 3.8), its high-frequency wide bandwidth recordings (0-100 Hz; 250 sps), and its low magnitude detection threshold (below magnitude 0.0 Ml).

Several aspects of the Parkfield region make it ideal for the study of small earthquakes and nonvolcanic tremors and their relationship to tectonic processes and large earthquakes. These include the fact that the network spans the SAFOD (San Andreas Fault Observatory at Depth) experimental zone, the nucleation region of earlier repeating magnitude 6 events and a significant portion of the transition from locked to creeping behavior on the San Andreas fault, the availability of three-dimensional P and S velocity models (*Michelini and McEvilly, 1991*), a long-term HRSN seismicity catalogue (complete to very low magnitudes and that includes at least half of the M6 seismic cycle), a well-defined and simple fault segment, the existence of deep nonvolcanic tremor (NVT) activity, and a relatively homogeneous mode of seismic energy release as indicated by the earthquake source mechanisms (over 90% right-lateral strike-slip).

In a series of journal articles and Ph.D. theses, the cumulative, often unexpected, results of UC Berkeley's HRSN research efforts (see: [http://www.seismo.berkeley.edu/seismo/faq/parkfield\\_bib.html](http://www.seismo.berkeley.edu/seismo/faq/parkfield_bib.html)) trace the evolution of a new and exciting picture of the San Andreas fault zone responding to its plate-boundary loading, and they are forcing new thinking on the dynamic processes and conditions within the fault zone at the sites of recurring small earthquakes and deep nonvolcanic tremors (*Nadeau and Dolenc, 2005*).

The Parkfield area has also become an area of focus of the EarthScope Project (<http://www.earthscope.org>)

through the SAFOD experiment (<http://www.icdp-online.de/sites/sanandreas/news/news1.html>), and the HRSN is playing a vital role in this endeavor. SAFOD is a comprehensive project to drill into the hypocentral zone of repeating M ~ 2 earthquakes on the San Andreas Fault at a depth of about 3 km. The goals of SAFOD are to establish a multi-stage geophysical observatory in close proximity to these repeating earthquakes, to carry out a comprehensive suite of down-hole measurements in order to study the physical and chemical conditions under which earthquakes occur, and to monitor and exhume rock, fluid, and gas samples for extensive laboratory studies (*Hickman et al., 2004*).

### 3.4.2 HRSN Overview

#### 1986 - 2001

Installation of the HRSN deep (200-300m) borehole sensors initiated in 1986, and recording of triggered 500 sps earthquake data began in 1987. The HRSN sensors are 3-component geophones in a mutually orthogonal gimbaled package. This ensures that the sensor corresponding to channel DP1 is aligned vertically and that the others are aligned horizontally. Originally a 10 station network, completed in 1988, the HRSN was expanded to 13 borehole stations in 2001, and the original recording systems (see previous BSL Annual Reports) were upgraded to 24 bit acquisition (Quanterra 730s) and 56K frame relay telemetry to UCB. Properties of the sensors are summarized in Table 3.9.

The 3 2001 borehole stations were added, with NSF support, at the NW end of the network as part of the SAFOD project to improve resolution of the structure, kinematics and monitoring capabilities in the SAFOD drill-path and target zones. Figure 3.12 illustrates the location of the drill site, the new borehole sites, and locations of earthquakes recorded by the initial and upgraded/expanded HRSN.

The three newest SAFOD stations have a similar configuration to the original upgraded 10 station network and include an additional channel for electrical signals. Station descriptions and instrument properties are summarized in Tables 3.8 and 3.9. All HRSN Q730 dataloggers employ FIR filters to extract data at 250 and 20 Hz (Table 3.10).

The remoteness of the drill site and new stations required an installation of an intermediate data collection point at Gastro Peak, with a microwave link to the CDF facility. The HRSN stations use SLIP to transmit TCP and UDP data packets over bidirectional spread-spectrum radio links between the on-site data acquisition

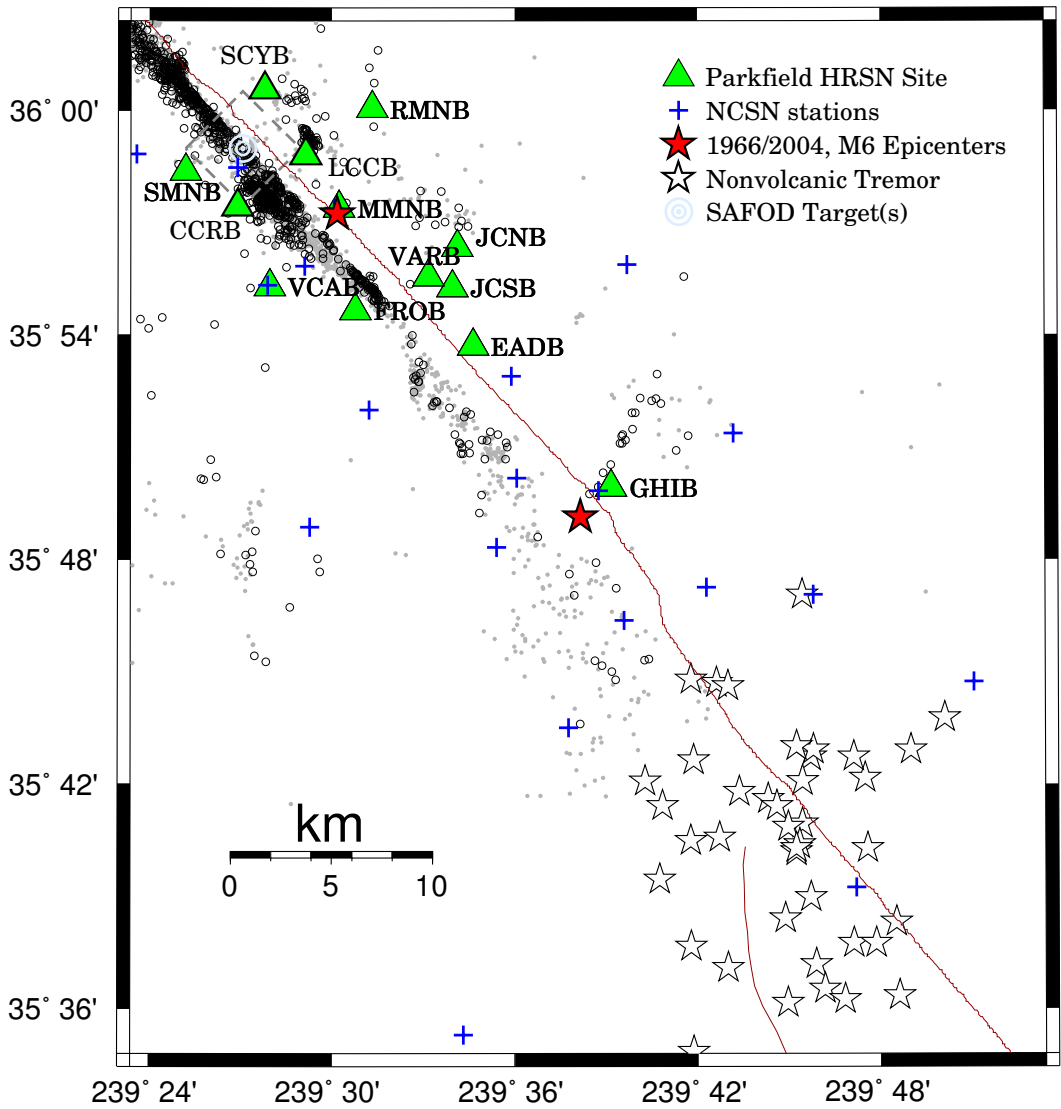


Figure 3.12: Map showing the San Andreas Fault trace and locations of the 13 Parkfield HRSN stations, the repeating M2 SAFOD targets (a 4 km by 4 km dashed box surrounds the SAFOD zone), and the epicenters of the 1966 and 2004 M6 Parkfield main shocks. Also shown are preliminary locations of some recently detected nonvolcanic tremors in the Cholame, CA area (January 2006 to June 2007), routine locations of earthquakes recorded by the expanded and upgraded 13 station HRSN (small open circles) and locations of events recorded by the earlier vintage 10 station HRSN relocated using an advanced 3-D double-differencing algorithm applied to a cubic splines interpolated 3-D velocity model (*Michelini and McEvilly, 1991*).

Site	Net	Latitude	Longitude	Surf. (m)	Depth (m)	Date	Location
EADB	BP	35.89525	-120.42286	466	245	01/1988 -	Eade Ranch
FROB	BP	35.91078	-120.48722	509	284	01/1988 -	Froelich Ranch
GHIB	BP	35.83236	-120.34774	400	63	01/1988 -	Gold Hill
JCNB	BP	35.93911	-120.43083	527	224	01/1988 -	Joaquin Canyon North
JCSB	BP	35.92120	-120.43408	455	155	01/1988 -	Joaquin Canyon South
MMNB	BP	35.95654	-120.49586	698	221	01/1988 -	Middle Mountain
RMNB	BP	36.00086	-120.47772	1165	73	01/1988 -	Gastro Peak
SMNB	BP	35.97292	-120.58009	699	282	01/1988 -	Stockdale Mountain
VARB	BP	35.92614	-120.44707	478	572	01/1988 - 08/19/2003	Varian Well
VARB	BP	35.92614	-120.44707	478	298	08/25/2003 -	Varian Well
VCAB	BP	35.92177	-120.53424	758	200	01/1988 -	Vineyard Canyon
CCRB	BP	35.95718	-120.55158	595	251	05/2001 -	Cholame Creek
LCCB	BP	35.98005	-120.51424	640	252	08/2001 -	Little Cholame Creek
SCYB	BP	36.00938	-120.53660	945	252	08/2001 -	Stone Canyon

Table 3.8: Stations of the Parkfield HRSN. Each HRSN station is listed with its station code, network id, location, date of initial operation, and site description. The latitude and longitude (in degrees) are given in the WGS84 reference frame. The surface elevation (in meters) is relative to mean sea level, and the depth to the sensor (in meters) below the surface is also given. Coordinates and station names for the 3 new SAFOD sites are given at the bottom.

Site	Sensor	Z	H1	H2	RefTek 24	RefTek 72-06	Quanterra 730
EADB	Mark Products L22	-90	170	260	01/1988 - 12/1998	12/1998 - 07/1999	03/2001 -
FROB	Mark Products L22	-90	338	248	01/1988 - 12/1998	12/1998 - 07/1999	03/2001 -
GHIB	Mark Products L22	90	failed	unk	01/1988 - 12/1998	12/1998 - 07/1999	03/2001 -
JCNB	Mark Products L22	-90	0	270	01/1988 - 12/1998	12/1998 - 06/2001	03/2001 -
JCSB	Geospace HS1	90	300	210	01/1988 - 12/1998	12/1998 - 07/1999	03/2001 -
MMNB	Mark Products L22	-90	175	265	01/1988 - 12/1998	12/1998 - 06/2001	03/2001 -
RMNB	Mark Products L22	-90	310	40	01/1988 - 12/1998	12/1998 - 07/1999	03/2001 -
SMNB	Mark Products L22	-90	120	210	01/1988 - 12/1998	12/1998 - 06/2001	03/2001 -
VARB	Litton 1023	90	15	285	01/1988 - 12/1998	12/1998 - 07/1999	03/2001 -
VCAB	Mark Products L22	-90	200	290	01/1988 - 12/1998	12/1998 - 06/2001	03/2001 -
CCRB	Mark Products L22	-90	N45W	N45E	-	-	05/2001 -
LCCB	Mark Products L22	-90	N45W	N45E	-	-	08/2001 -
SCYB	Mark Products L22	-90	N45W	N45E	-	-	08/2001 -

Table 3.9: Instrumentation of the Parkfield HRSN. Most HRSN sites have L22 sensors and were originally digitized with a RefTek 24 system. After the failure of the WESCOMP recording system, PASSCAL RefTek recorders were installed. In July of 1999, 6 of the PASSCAL systems were returned to IRIS and 4 were left at critical sites. The upgraded network uses a Quanterra 730 4-channel system. For the three new stations (bottom) horizontal orientations are approximate (N45W and N45E) and will be determined more accurately as available field time permits.

Sensor	Channel	Rate (sps)	Mode	FIR
Geophone	DP?	250.0	T and C	Ca
Geophone	BP?	20.0	C	Ac

Table 3.10: Data streams currently being acquired at each HRSN site. Sensor type, channel name, sampling rate, sampling mode, and type of FIR filter are given. C indicates continuous; T triggered; Ac acausal; Ca causal. “?” indicates orthogonal, vertical, and 2 horizontal components.

systems and the central recording system at the CDF. Six of the sites transmit directly to a router at the central recording site. The other seven sites transmit to a router at Gastro Peak, where the data are aggregated and transmitted to the central site over a 4 MBit/second digital 5.4 GHz microwave link. All HRSN data are recorded to disk at the CDF site.

The upgraded and expanded system is compatible with the data flow and archiving common to all the elements of the BDSN/NHFN and the NCEDC (Northern California Earthquake Data Center), and is providing remote access and control of the system. It has also provided event triggers with better timing accuracy and is also now recording continuous 20 and 250 sps data for all 38 channels of the HRSN, which flow seamlessly into both the USGS automated earthquake detection system and into the Berkeley’s NCEDC for archiving and online access to the community. The new system also helps minimize the problems of timing resolution, dynamic range, and missed detections, in addition to providing the added advantage of conventional data flow (the old system recorded SEG Y format).

Another feature of the new system that has been particularly useful both for routine maintenance and for pathology identification has been the Internet connectivity of the central site processing computer and the station dataloggers with the computer network at BSL. Through this connection, select data channels and on-site warning messages from the central site processor are sent directly to BSL for evaluation by project personnel. If, upon these evaluations, more detailed information on the HRSN’s performance is required, additional information can also be remotely accessed from the central site processing computer at Parkfield. Analysis of this remotely acquired information has been extremely useful for trouble shooting by allowing field personnel to schedule and plan the details of maintenance visits to Parkfield. The connectivity also allows certain data acquisition parameters to be modified remotely when needed, and commands can be sent to the central site computer and dataloggers to modify or restart processes when necessary.

The network connectivity and seamless data flow to the NCEDC also provides near-real-time monitoring ca-

pabilities that are useful for rapid evaluation of significant events as well as the network’s overall performance level. For example, shown in Figure 3.13 are P-wave seismograms of the  $M_w$  8.1 Solomon Islands earthquake of April 1, 2007 20:39:56 (UTC) (9892 km S54E of Parkfield, CA; depth 10 km) recorded on the DP1 (vertical) channels of the 13 HRSN borehole stations. This event killed 54 people. The seismic data from the quake was telemetered to Berkeley and available for analysis within a few seconds of being recorded by the HRSN. The consistency of the first motions and subsequent arrivals across all the stations of the local HRSN for this global event also show that the entire ensemble of stations for the network was performing well at this time. By routinely performing PSD analyses of the HRSN data, rapid assessment of the HRSN seismometer responses across their wide bandwidth is also easily done and corrective measures applied in a relatively short time-frame.

## Data Flow

*Initial Processing Scheme.* Continuous data streams on all 38 HRSN components are recorded at 20 and 250 sps on disk on the local HRSN computer at the CDF facility. These continuous data are transmitted in near-real-time to the Berkeley Seismological Laboratory (BSL) over a T1 link and then archived at the NCEDC. In addition, in large part in support of the SAFOD experiment taking place at Parkfield, the near-real-time data are being transmitted over the T1 circuit to the USGS at Menlo Park, CA and are also integrated into their NCSN (Northern California Seismic Network) trigger detection scheme to increase the sensitivity of the NCSN in the SAFOD area.

Shortly after being recorded to disk on the central site HRSN computer, event triggers for the individual station data are also determined, and a multi-station trigger association routine then processes the station triggers and generates a list of potential earthquakes. For each potential earthquake that is detected, a unique event identification number (compatible with the NCEDC classification scheme) is also assigned. Prior to the San Simeon earthquake of December 22, 2003, 30 second waveform segments were then collected for all stations and components and saved to local disk as an event gather, and event gathers were then periodically telemetered to BSL and included directly into the NCEDC earthquake database (dbms) for analysis and processing.

Because of its mandate to detect and record very low magnitude events in the Parkfield area, the HRSN is extremely sensitive to changes in very low amplitude seismic signals. As a consequence, in addition to detecting very small local earthquakes at Parkfield, the HRSN also detects numerous regional events and relatively distant and small amplitude nonvolcanic tremor events. For example, spot checks of aftershocks following the M6.5 San

Simeon earthquake of December 22, 2003 using continuous data and HRSN event detection listings have revealed that the overwhelming majority of HRSN detections following San Simeon resulted from seismic signals generated by San Simeon's aftershocks, despite the HRSN's  $\sim 50$  km distance from the events. Data from the California Integrated Seismic Network (CISN) show that there were  $\sim 1,150$  San Simeon aftershocks with magnitudes  $> 1.8$  in the week following San Simeon, and during this same period, the number of HRSN event detections was  $\sim 10,500$  (compared to an average weekly rate before San Simeon of 115 detections). This suggests that, despite the  $\sim 50$  km distance, the HRSN is detecting San Simeon aftershocks well below magnitude 1.

*Current Processing.* Since the beginning of the network's data collection in 1987, and up until recently, the local and regional events were discriminated based on analyst assessment of S-P times, and only local events with S-P times less than  $\sim 2.5$  sec at the first arriving station were picked and located as part of the HRSN routine catalog. However, because of the networks extreme sensitivity to the large swarm of aftershocks from the San Simeon and M6 Parkfield earthquakes of September 2004 (e.g., in the first 5 months following the San Simeon mainshock, over 70,000 event detections were made by the HRSN system, compared to an average 5 month detection rate of 2500 prior to San Simeon) and because of ever declining funding levels, this approach has had to be abandoned.

The dramatic increase in event detections vastly exceed the HRSN's capacity to process both the continuous and triggered event waveform data. To prevent the loss of seismic waveform coverage, processing of the triggered waveform data has been suspended to allow archiving of the 250 sps continuous data to tape to continue uninterrupted. Cataloging of the event detection times from the modified REDI real-time system algorithm is also continuing, and the continuous 250 sps waveform data is currently being periodically uploaded from the DLT tape archive onto the NCEDC for access to the research community.

Funding to generate catalogs of local events from the 10s of thousands of aftershock detections has not been forthcoming, and, as a consequence, major changes in our approach to cataloging events have had to be implemented, which involves integration of HRSN data into NCSN automated event detection and cataloging (with no analyst review) combined with a high resolution procedure now being developed to automatically detect, pick, locate, and determine magnitudes for similar and repeating events down to very low magnitudes (i.e., below magnitude -1.0Ml). These new schemes are discussed in more detail in the activities section below.

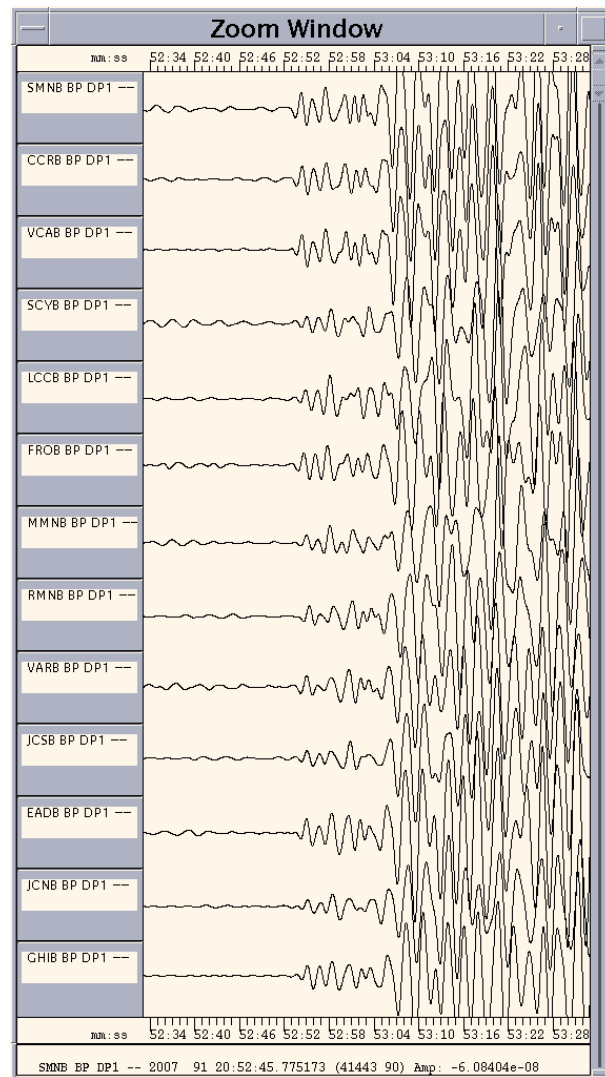


Figure 3.13: Plot of P-wave seismograms of the  $M_w$  8.1 Solomon Islands earthquake of April 1, 2007 20:39:56 (UTC) (9892 km S54E of Parkfield, CA; depth 10 km) recorded on the DP1 (vertical) channels of the 13 HRSN borehole stations. Here vertical component geophone data have been deconvolved to absolute ground velocity, 0.5-5 Hz, BP filtered. All the P waveforms have the same first motions and their subsequent arrivals are highly similar.

### 3.4.3 2006-2007 Activities

In addition to the routine operations and maintenance of the HRSN (California's first and longest operating borehole seismic network), research into: 1) how to process ongoing similar and repeating seismicity to very low magnitudes, 2) ongoing non-volcanic tremors in the Parkfield-Cholame area, 3) SAFOD related activities and 4) various approaches to lowering operational (primarily landowner fee) costs have been the primary driving forces behind most of the HRSN project's activities this year.

#### Operations and Maintenance

Routine maintenance tasks required this year to keep the HRSN in operation include cleaning and replacement of corroded electrical connections; grounding adjustments; cleaning of solar panels; re-seating, resoldering and replacement of faulty pre-amp circuit cards; testing and replacement of failing batteries; and insulation and painting of battery and datalogger housings to address problems with low power during cold weather. Remote monitoring of the network's health using the Berkeley Seismological Laboratory's SeisNetWatch software is also performed to identify both problems that can be resolved over the Internet (e.g. rebooting of data acquisition systems due to clock lockups) and more serious problems requiring field visits. Over the years, such efforts have paid off handsomely by providing exceptionally low noise recordings of very low amplitude seismic signals produced by microearthquakes (below magnitude 0.0MI) and non-volcanic tremors.

#### Reducing Operational costs

The increased scientific activity in the rural Parkfield area due to SAFOD has led to an increased demand for site access and development on privately owned property and a corresponding increase in access fees charged by private land owners. As a result land use fees paid by the HRSN project have increased dramatically from less than \$1000 annually prior to the SAFOD effort to over \$13,000. This represents over 15% of the entire HRSN budget with no corresponding increase in support from the project's funding agency. To compensate for the increased landowner costs, maintenance efforts have had to be cut back, and network performance has suffered.

To help alleviate the problem, this year we have developed plans to minimize our dependence on access to private lands. This has primarily involved developing alternative telemetry schemes for the HRSN sites in such a way as to minimize the additional effort and equipment needed to implement the schemes. Also central to this effort has been reaching cooperative agreements with other agencies involved in research in the area (i.e., USGS and UNAVCO). Initial field efforts to implement the plan have recently begun and are expected to be completed

before the end of summer 2008.

#### Tremor Monitoring

The HRSN data played an essential role in the discovery of nonvolcanic tremors along the San Andreas Fault (SAF) below Cholame, CA (*Nadeau and Dolenc, 2005*). The location of the Cholame tremors occupies a critical location between the smaller Parkfield ( $\sim$  M6) and much larger Ft. Tejon ( $\sim$  M8) rupture zones of the SAF. Because the time-varying nature of tremor activity is believed to reflect time-varying deep deformation and presumably episodes of accelerated stressing of faults, and because an anomalous increase in the rate of Cholame tremor activity preceded the 2004 Parkfield M6 by  $\sim$  21 days, we are continuing to monitor the tremor activity observable by the HRSN to look for anomalous rate changes that may signal an increased likelihood for another large SAF event to the SE. Results of monitoring effort are described further in the "Research" section of this report.

#### Similar Event Catalog

The increased microseismicity rates resulting from the San Simeon M6.5 and Parkfield M6 events and the increased interest in even smaller events in the SAFOD target zone have required new thinking on how to detect and catalog microearthquakes recorded by the HRSN. One action taken to help address this problem has been to integrate HRSN data streams into the NCSN event detection and automated cataloging process (described below). This approach has been successful at discriminating small events in the local Parkfield area from other types of event detections and for providing automated locations of a significantly increased number of small events in the local area (approx. double that of the NCSN network alone). However, the rate of local events from the HRSN sensitized NCSN catalog is still only catching about 1/2 the number of local events previously cataloged by the HRSN, and waveforms for the small events are not typically made available. In addition, unlike the previous HRSN catalog, the additional events added by the NCSN-HRSN integration are not reviewed by an analyst, nor do they generally have magnitude determinations associated with them. In some cases, the selection rules used for the integrated catalog also result in exclusion of events that are otherwise included by the NCSN.

These limitations severely hamper efforts relying on similar and characteristically repeating microearthquakes. They also reduce the effectiveness of research relying on numerous very small magnitude events in the SAFOD zone (e.g. for targeting the SAFOD targets). To help overcome these limitations, we have continued our efforts to develop an automated similar event cataloging scheme based on cross-correlation and pattern scanning of the continuous HRSN data now being

# SAFOD TARGET CLUSTERS (112 events since July 2001)

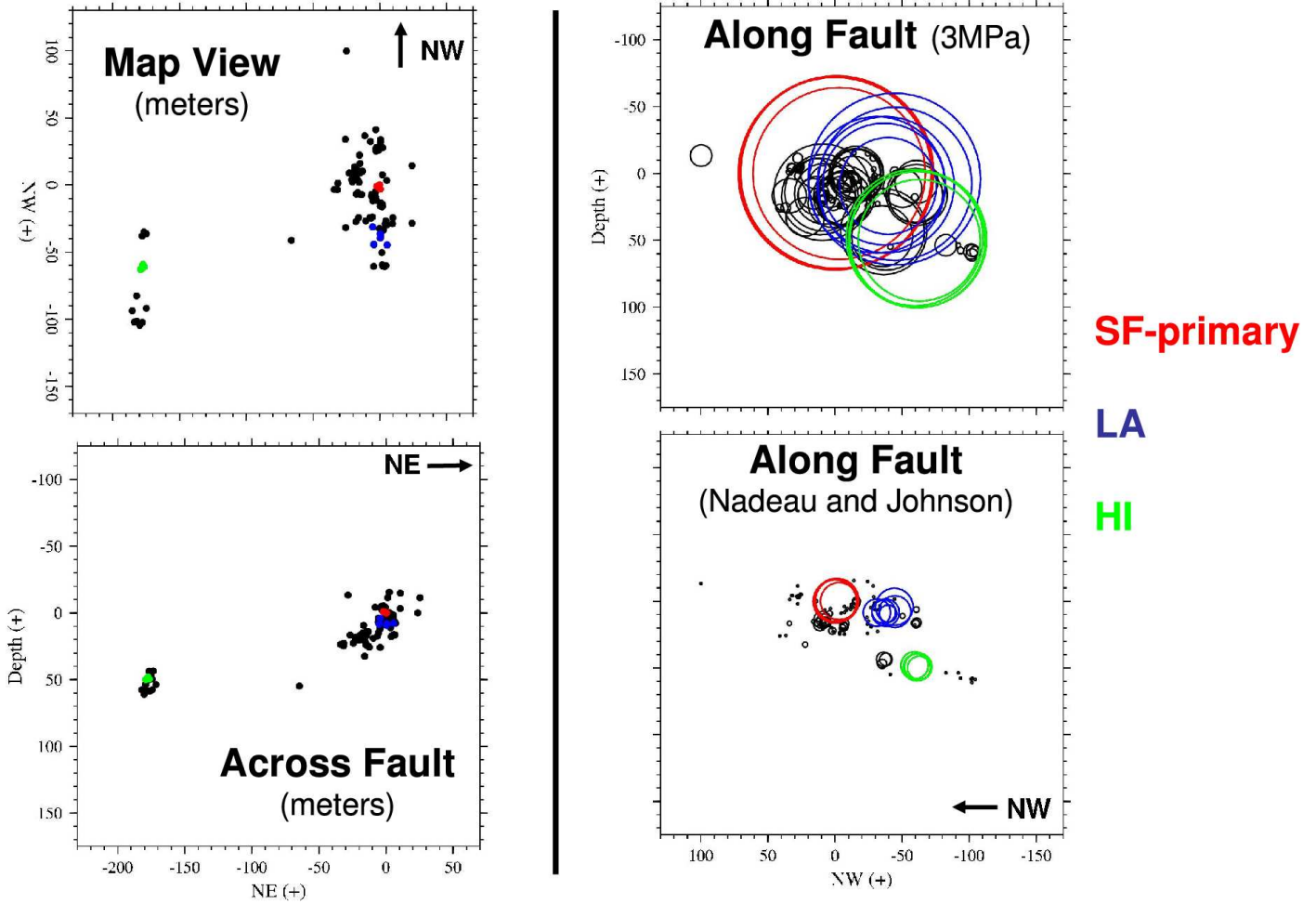


Figure 3.14: Map view (top, left), and across (bottom, left) and along SAF depth sections (top and bottom, right) of double-difference locations resulting from application of the similar event pattern scanning and automated cataloging method using one event from each of the SAFOD HI and SF target sequences as a reference. The magnitudes of the 112 events ranged from 2.2 down to -1.4 ML. In the across fault sections at the right, inferred circular dimensions of the event ruptures in the SAFOD zone are shown as open circles assuming a 3MPa constant stress-drop model (top) and an increasing stress-drop with decreasing magnitude model inferred from recurrence interval information (*Nadeau and Johnson, 1998*).

archived. The method uses a small number of reference events whose waveforms, picks, locations, and magnitudes have been accurately determined, and it automatically detects, picks, locates and determines magnitudes for events similar to the reference event to the level of accuracy and precision that only relative event analysis can bring.

The similar event detection is also remarkably insensitive to the magnitude of the reference event used, allowing similar events ranging over several magnitude units to be fully cataloged using a single reference event. It also does a remarkably good job even when seismic energy from multiple events is superposed. Once a cluster of similar events has been cataloged, it is a relatively straightforward process to identify characteristically repeating microearthquake sequences within the cluster (frequently a single similar event "cluster" will contain several sequences of repeating events).

Application of the method using two of the SAFOD target events as references is illustrated in Figure 3.14. One reference event is a member of the so-called Hawaii sequence (HI), and one is from the San Francisco sequence (SF), and their magnitudes are  $\sim 2.1$  and  $1.8$  (respectively). These events were scanned through 5 years of continuous data, and 110 other events occurring within the target region were identified and fully cataloged to high precision. Their magnitudes ranged down to magnitude  $-1.4$  Ml, and in addition to the SAFOD target sequence from which the reference was derived, several other repeating sequences within the 150m zone were also identified (5 of which had not previously been known to exist).

This high level of precision and low magnitude completeness has already proven useful to SAFOD for helping to delineate and constrain the active fault structure in the target zone. It has also proven vital for helping to resolve a long-standing debate in the seismologic community regarding the stress-drop scaling issues (*Dreger et al.*, 2007).

The automated cataloging procedure for similar events is still being refined to capture even smaller events and events over a larger area, as well as for increased processing speed. Eventually, a composite catalog of similar event groups from throughout the HRSN coverage zone is planned.

The approach also holds promise in other applications where automated and precise monitoring of bursts of seismic activity to very low magnitudes is desirable (e.g. in aftershock zones or in volcanic regions) or where automated updates of preexisting repeating sequences and their associated deep slip estimates are desired.

### Efforts in Support of SAFOD

An intensive and ongoing effort by the EarthScope component called SAFOD (San Andreas Fault Obser-

vatory at Depth) is underway to drill through, sample and monitor the active San Andreas Fault at seismogenic depths and in very close proximity (within a few 10s of km or less) of a repeating magnitude 2 earthquake site. The HRSN data plays a key role in these efforts by providing low noise and high sensitivity seismic waveforms from active and passive sources, and by providing a backbone of very small earthquake detections and continuous waveform data.

As of early September, 2007, SAFOD drilling had penetrated the fault at the HI repeating target sequence and collected core samples both in the presumed rupture zone of the repeating events and in the fault region that presumably creeps and surrounds the repeatedly rupturing HI patch. Future efforts will be focused on attempting to confirm that the drill penetration and coring efforts did indeed hit the target rupture zone and on long-term monitoring of the ongoing chemical, physical, seismologic and deformational properties in the zone (particularly any signals that might be associated with the next repeat of the HI sequence).

HRSN Activities this year have contributed in three principal ways to these and longer-term SAFOD monitoring efforts:

- 1) In collaboration with the USGS, we have completely integrated the HRSN data streams into the NCSN triggering scheme (described above) to increase the sensitivity of NCSN detection in the SAFOD area. This has effectively doubled the number of small events the target location working group has for constraining the relative location of ongoing seismicity in the target zone.

- 2) Again in collaboration with the USGS, we have completed a telemetry upgrade begun last year. Now all 39 channels of the HRSN data (both 20 sps and 250 sps data streams) flow directly from Parkfield, through the USGS Parkfield T1 and the NCEMC T1 to the BSL for near-real-time processing and archiving on the web-based NCEDC. This is now providing near immediate access of the HRSN data to the community without the week- or month-long delay associated with the previous procedure of having to transport DLT tapes to Berkeley to upload, and quality check the data. A copy of the 250 sps data stream is also processed for redundancy by the USGS Parkfield Earthworm node.

- 3) We have also continued to apply our prototype similar event automated catalog approach to the primary, secondary and tertiary SAFOD target zones and to provide the SAFOD event location working group with on-demand precise double-difference and relative magnitude catalogs of ongoing similar event activity in the SAFOD target zone.

During the past year, our SAFOD similar event detections and catalogs have been used by the working group to extract data from the corresponding PASO array, Pilot Hole, NCSN, and mainhole data sets for integration with

the HRSN data in order to provide the detailed information that was needed by drill crews for the final targeting of the HI target penetration and coring.

#### 3.4.4 Acknowledgments

Thomas V. McEvelly, who passed away in February 2002, was the PI on the HRSN project for many years. Without his dedication, continued operation of the HRSN would not have been possible. Under Bob Nadeau's and Doug Dreger's general supervision, Rich Clymer, Bob Uhrhammer, Doug Neuhauser, Don Lippert, Bill Karavas, John Friday, Rick Lellinger and Pete Lombard all contribute to the operation of the HRSN. Bob Nadeau prepared this chapter. During this reporting period, operation, maintenance, and data processing for the HRSN project was supported by the USGS, through grant 07HQAG0014.

#### 3.4.5 References

Bakun, W. H., and A. G. Lindh, The Parkfield, California, prediction experiment, *Earthq. Predict. Res.*, *3*, 285-304, 1985.

Daley, T.M. and T.V. McEvelly, Shear wave anisotropy in the Parkfield Varian Well VSP, *Bull. Seism. Soc. Am.*, *80*, 857-869, 1990.

Dreger, D., R.M. Nadeau, and A. Morrish, Repeating Earthquake Finite-Source Models: Strong Asperities Revealed on the San Andreas Fault, *Geophys. Res. Lett.*, revised version submitted, 2007.

Hickman, S., M.D. Zoback and W. Ellsworth, Introduction to special section: Preparing for the San Andreas Fault Observatory at Depth, *Geophys. Res. Lett.*, *31*, L12S01, doi:10.1029/2004GL020688, 2004.

Karageorgi, E., R. Clymer and T.V. McEvelly, Seismological studies at Parkfield. IV: Variations in controlled-source waveform parameters and their correlation with seismic activity, 1987-1994, *Bull. Seismol. Soc. Am.*, *87*, 39-49, 1997.

Michellini, A. and T.V. McEvelly, Seismological studies at Parkfield: I. Simultaneous inversion for velocity structure and hypocenters using B-splines parameterization, *Bull. Seismol. Soc. Am.*, *81*, 524-552, 1991.

Nadeau, R.M. and D. Dolenc, Nonvolcanic Tremors Deep Beneath the San Andreas Fault, *SCIENCE*, *307*, 389, 2005.

Nadeau, R. M., and L. R. Johnson, Seismological Studies at Parkfield VI: Moment Release Rates and Estimates of Source Parameters for Small Repeating Earthquakes, *Bull. Seismol. Soc. Amer.*, *88*, 790-814, 1998.

## 3.5. Bay Area Regional Deformation Network

### 3.5.1 Introduction

This year was the first of the newly funded BARD NEHRP project for the period 2007-2010. In consequence, this year, the field efforts have been focused on the permitting and preparation of the sites. Additionally, the upgrade to 1Hz of the BARD network has been pursued. The scientific efforts have focused on the processing of the high-rate GPS data in order to include the GPS solutions (static offsets and dynamic waveforms) in the existing monitoring system for the seismic activity in northern California (magnitude determination, moment tensor and Elarms system). Additionally, static solutions have been estimated and will be released in a peer review journal before the end of the year. This year was noteworthy because this was the last year of operation of the PBO installation in the San Francisco Bay Area (SFBA).

### 3.5.2 BARD overview

#### Description of the network

The BSL currently maintains and operates 30 BARD stations (twenty-six bi-frequency sites and four L1 sites). The sampling rate varies from 1 to 30 seconds, and the data are transmitted continuously over a serial connection. Most stations use frame relay technology, either alone or in combination with radio telemetry.

Of the 30 sites, ten (BRIB, CMBB, FARB, HOPB, MHCB, ORVB, PKDB, SAOB, SUTB, YBHB) are co-located with broadband seismic stations of the BDSN with which they share continuous frame-relay telemetry to UC Berkeley. These sites use the Quanterra data loggers to store and retrieve the GPS data converted to MiniSEED format (it Perin et al., 1998). The MiniSEED approach provides more robust data recovery from on-site backup on the Quanterra disks following telemetry outages.

Another five stations (SVIN, MHDL, OHLN, OXMT and SBRN) have been installed in the last 3 years in the SFBA and along the Hayward fault as the Berkeley part of a multi-institutional effort funded by the NSF/MRI program to improve strain monitoring in the SFBA using an integrated approach, with significant participation of the USGS/MP (Murray et al., 2002). These stations include borehole tensor strainmeters, three-component borehole seismic velocity sensors, downhole pore pressure and tilt sensors, and GPS receivers. This project served as a prototype for the strainmeter installations planned for PBO, which faces many of the same station installation, configuration, and data retrieval issues we have addressed. Consequently, these 5 stations have received the nickname *mini-PBO*. From July 2001 to Au-

gust 2002, five boreholes were drilled to about 200-m depth and equipped with tensor strainmeters recently developed by CIW and 3-component L22 (velocity) seismometers. For this project, we developed a self-centering GPS antenna mount for the top of the borehole casings, which are mechanically isolated from the upper few meters of the ground, to provide a stable, compact monument that allows access to the top of the borehole casing for downhole maintenance. The 5 GPS receivers were progressively installed and connected to Quanterra 4120 data loggers, which provide backup and telemetry capabilities. The completion of the last station (MHDL), located in the Marin Headlands, took longer because it required AC power, which PG&E installed in December 2005. The site is operational since Sept 1, 2006. In addition, 10-minute interval data, which are retrieved from all the sites by the USGS via a backup GOES satellite system, show that all the sites are successfully measuring strains due to tidal effects and to local and teleseismic earthquakes. The remaining BSL/BARD stations only record C-GPS data. Each BSL/BARD station uses a low-multipath choke-ring antenna, most of which (except the mini-PBO ones discussed above) are mounted to a reinforced concrete pillar approximately 0.5-1.0 meter above the ground level. The reinforcing steel bars of the pillar are drilled and cemented into a rock outcrop to improve long-term monument stability. A low-loss antenna cable is used to minimize signal degradation on the longer cable setups that normally would require signal amplification. Low-voltage cutoff devices are installed to improve receiver performance following power outages. Most stations are equipped with aging Z-12 receivers, which were originally programmed to record data once every 30 s and observe up to 12 satellites simultaneously at elevations down to the horizon. The antennas are equipped with SCIGN antenna adapters and hemispherical domes, designed to provide security and protection from weather and other natural phenomena, and to minimize differential radio propagation delays. The BSL acquired 7 Ashtech MicroZ-CGRS ( $\mu$ Z) receivers with NSF funding for the Mini-PBO project. These have been installed at the mini-PBO stations, and two have been used to replace failing Z12s at other stations (CMBB and MODB). At these sites, the data are collected using only direct serial connections and are susceptible to data loss during telemetry outages.

There is growing interest in collecting higher rates of data for a variety of applications. For example, GPS measurements can accurately track the propagation of earthquake dynamic motions both on the ground (*e.g.*, Larson et al., 2003) and in the atmosphere (*e.g.*, Artru et al.,

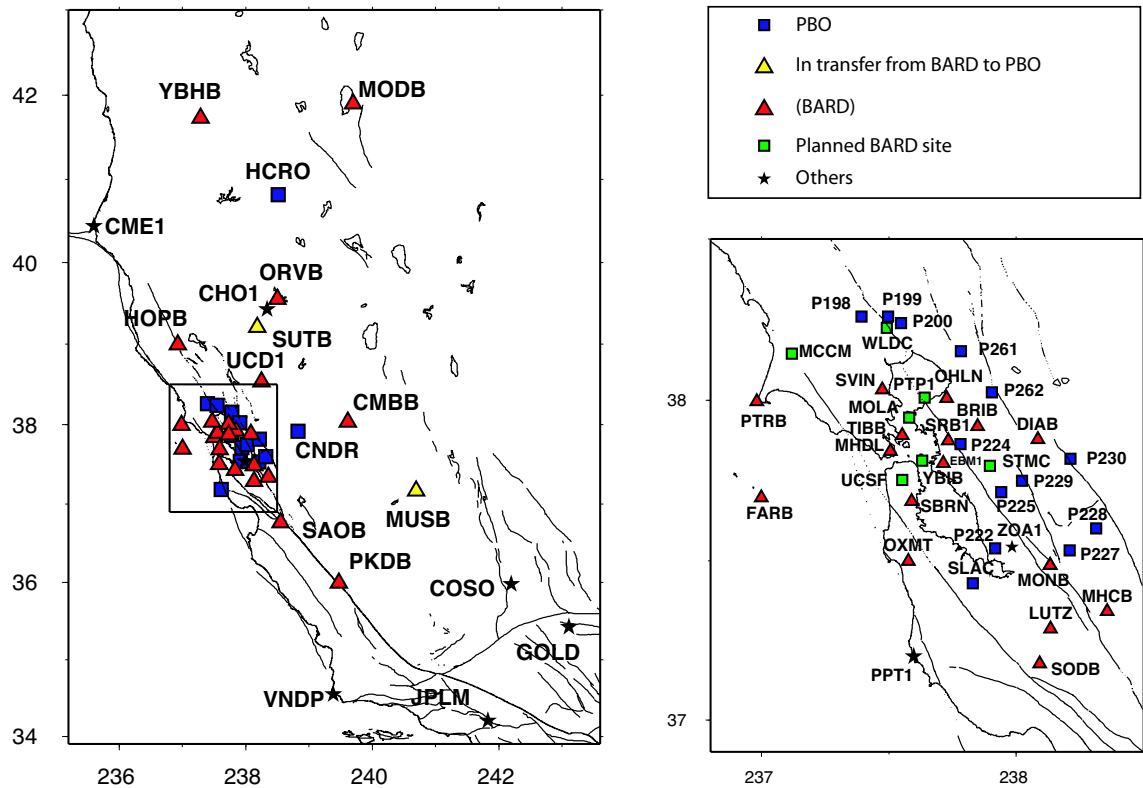


Figure 3.15: Operational BARD stations (dark triangles) in northern California (top) and in the San Francisco Bay area (bottom), including an 18-station network near the Long Valley Caldera (LVC) and a 14-station network near Parkfield (PKFD). In the oblique Mercator projection expected Pacific–North America relative plate motion is parallel to the horizontal. Circled stations use continuous real-time telemetry. The small black triangles near BRIB are the experimental L1 stations. Light triangles are PBO and Nucleus (previously existing continuous stations now part of PBO) stations operating in July 2005.

2001, *Ducic et al., 2003*), providing complementary information to seismic observations (calibration of integrated acceleration and velocity sensor data) and estimates of earth structure (direct observation of surface wave propagation over the oceans). We started collecting 1 Hz observations at 2 stations (DIAB and MONB) in 2003. In the last year, we have progressively upgraded the telemetry to continuous 1 Hz telemetry at 3 additional stations (BRIB, HOPB and PTRB), where the bandwidth of the existing telemetry system allowed it. At stations collocated with broadband seismic sensors, the seismic data has priority for telemetry, because it is used in the Northern California real-time earthquake notification system (see <http://www.cisn.org/ncmc/>), making this upgrade more difficult and in general not feasible with the current Z12 receivers because of insufficient data compression. All data collected from BARD/BSL are publicly available at the Northern California Earthquake Data Center (NCEDC; <http://www.ncedc.org/bard/>).

Between 1993 and 2001, the BSL acquired 29 Ashtech Z-12 and Micro-Z receivers from a variety of funding sources, including from federal (NSF and USGS), state (CLC), and private (EPRI) agencies. The network enhances continuous strain measurements in the Bay Area and includes several profiles between the Farallon Islands and the Sierra Nevada in order to better characterize the larger scale deformation field in northern California (Figure 3.15). During the last two years, 10 NETRS have been purchased via the UNAVCO purchase program. These receivers will help to upgrade the network to full high-rate capabilities. Three receivers are operating today (BRIB, MHDL and DIAB).

The number of continuous GPS stations in northern California is significantly increasing, with over 250 new site installations planned by 2008 as part of the Plate Boundary Observatory (PBO) component of the NSF-funded Earthscope project. UNAVCO and researchers from BARD and the other regional networks, such as SCIGN, BARGEN, and PANGA, are funded by NSF to fold operation and maintenance of about 200 existing stations, which constitute the PBO Nucleus network, into the PBO array by 2008. Two BSL-maintained stations (SUTB and MUSB) are included in the PBO Nucleus network. The other BSL stations are either collocated with seismic instrumentation or are located near the San Andreas Fault where real-time processing of the GPS data for earthquake notification is a high priority. Another 23 northern California stations, including most of the Parkfield network, will be included in the PBO Nucleus, and we are working with UNAVCO to facilitate their transition to UNAVCO control.

### **BARD Stations**

The majority of the BSL BARD stations use a low-multipath choke-ring antenna, most of which are

mounted to a reinforced concrete pillar approximately 0.5–1.0 meter above local ground level. The reinforcing steel bars of the pillar are drilled and cemented into a rock outcrop to improve long-term monument stability. A low-loss antenna cable is used to minimize signal degradation on the longer cable setups that normally would require signal amplification. Low-voltage cutoff devices are installed to improve receiver performance following power outages. Most use Ashtech Z-12 receivers that are programmed to record data once every 30 seconds and observe up to 12 satellites simultaneously at elevations down to the horizon. The antennas are equipped with SCIGN antenna adapters and hemispherical domes, designed to provide security and protection from weather and other natural phenomena, and to minimize differential radio propagation delays.

Data from most BSL-maintained stations are collected at 15 or 30-second intervals and transmitted continuously over serial connections (Table 3.5.2). Station TIBB uses a direct radio link to Berkeley, and MODB uses VSAT satellite telemetry. Most stations use frame relay technology, either alone or in combination with radio telemetry. Fourteen GPS stations are collocated with broadband seismometers and Quanterra data loggers (Table 3.2). With the support of IRIS, we developed software that converts continuous GPS data to MiniSEED opaque blockettes that are stored and retrieved from the Quanterra data loggers (*Perin et al., 1998*), providing more robust data recovery from onsite disks following telemetry outages.

Data from BRIB, CMBB, DIAB, HOPB, MHCBB, MHDL, MONB, OHLN, OXMT, PTRB, SBRN, SRB1, SVIN, TIBB and UCD1 in the Bay Area, and 13 stations in the Parkfield region (all but PKDB), are now being collected at 1-second intervals. All high-rate observations collected by these stations are currently available from the NCEDC. Collecting at such high frequency (for GPS) allows dynamic displacements due to large earthquakes to be better measured; however, this 30-fold increase in data can pose telemetry bandwidth limitations. We are planning to convert additional stations to 1-second sampling where possible during the next year. The acquisition of the 5 NETRS bundles will help to complete this project (see Subsection 3.5.3). In the Bay Area, we have converted stations that have sufficient bandwidth and are currently assessing bandwidth issues at other stations. Prior to the September 28, 2004 M6 Parkfield earthquake, data from the Parkfield stations were collected on an onsite computer, written to removable disk once per month, and sent to SOPAC for long-term archiving (decimated 30-sec data is acquired daily via the BSL frame relay circuit). In response to the earthquake, we modified the procedures to download 1-second data converted to compact RINEX format at hourly intervals, which does not significantly impact the telemetry bandwidth.

	Sites	Lat. (deg.)	Lon. (deg)	Receiver	Telem.	Sampling rate	Collocated Network	Location
1	BRIB	37.91	237.84	<b>NETRS</b>	T1	<b>1Hz</b>	BDSN	Briones Reservation, Orinda
2	CMBB	38.03	239.61	A-UZ12	FR	1Hz	BDSN	Columbia College, Columbia
3	DIAB	37.87	238.08	A-Z12	FR	1Hz		Mt. Diablo
4	FARB	37.69	236.99	A-Z12	R-FR/R	15 s	BDSN	Farallon Island
5	EBMD	37.81	237.71	T-SSI	R	1Hz		East Bay Mud Headquarter
6	HOPB	38.99	236.92	<b>TR 4000</b>	FR	<b>1Hz</b>	BDSN	Hopland Field Stat., Hopland
7	LUTZ	37.28	238.13	A-Z12	FR	30 s		SCC Comm., Santa Clara
8	MHCB	37.34	238.35	A-Z12	FR	1Hz	BDSN	Lick Obs., Mt. Hamilton
9	MHDL	37.84	237.50	T-NETRS	FR	1Hz	mini-PBO	Marin Headland
10	MODB	41.90	239.69	A-UZ12	NSN	15 s		Modoc Plateau
11	MONB	37.48	238.13	A-Z12	FR	1Hz		Monument Peak, Milpitas
12	MUSB	37.16	240.69	A-Z12	R-Mi-FR	30 s		Musick Mt.
13	OHLN	38.00	237.72	A-UZ12	FR	1Hz	mini-PBO	Ohlone Park, Hercules
14	ORVB	39.55	238.49	A-Z12	FR	15 s	BDSN	Oroville
15	OXMT	37.49	237.57	A-UZ12	FR	1Hz	mini-PBO	Ox Mountain
16	PKDB	35.94	239.45	A-Z12	FR	30 s	BDSN	Bear Valley Ranch, Parkfield
17	PTRB	37.99	236.98	A-Z12	R-FR	<b>1Hz</b>		Point Reyes Lighthouse
18	SAOB	36.76	238.55	A-Z12	FR	30 s	BDSN	San Andreas Obs., Hollister
19	SBRN	37.68	237.58	A-Z12	FR	1Hz	mini-PBO	San Bruno
20	SODB	37.16	238.07	A-Z12	R-FR	30 s		Soda Springs, Los Gatos
21	SRB1	37.87	237.73	T-SSE	FR	1Hz		SRB building, Berkeley
22	SUTB	39.20	238.17	A-Z12	R-FR	30 s	BDSN	Sutter Buttes
23	SVIN	38.03	237.47	A-UZ12	R-FR	1Hz	mini-PBO	St Vincents
24	TIBB	37.89	237.55	A-UZ12	R	1Hz		Tiburon
25	UCD1	38.53	238.24	<b>NETRS</b>	WEB	1Hz		UC - Davis
26	YBHB	41.73	237.28	A-Z12	FR	15 s	BDSN	Yreka Blue Horn Mine, Yreka
27	BDM	37.95	238.13	NETRS			BDSN	Black Diamond Mines Park, Antioch
28	MCCM	38.14	237.12	NETRS			BDSN	Marconi Conference Center, Marshall
29	PTP1	38.00	237.64	NETRS			NHFN	Point Pinole Regional Park
30	UCSF	37.75	237.55	NETRS				UC-San Francisco, San Francisco

Table 3.11: List of the BARD maintained by the BSL. Five models of receiver are operating now: Trimble 4000 SSE (T-SSE), Trimble 4000 SSI (T-SSI), Trimble NETRS, (T-NETRS), Ashtech Z12 and Ashtech Micro Z (A-UZ12). The replacement of the Ashtech Z12 by Trimble NETRS will make the receiver park more homogeneous. The telemetry types are listed in column 6. FR = Frame Relay, R = Radio, Mi= Microwave, WEB = DSL line. Some sites are transmitting data over several legs with different telemetry. Changes from last year's network table are highlighted in bold typography. **The sites 27 to 30 are in progress. For these 4 sites, the instrumentation is available and permit request procedures have been started.**

## Data archival

The Northern California Earthquake Data Center (NCEDC), operated jointly by the BSL and USGS, archives all permanent-site GPS data currently being collected in northern California. In the past months, and due to the transition to PBO, some sites are not present in the NCEDC archive (PPT1 for instance). All the sites available will be archived as in the past. We archive the Federal Aviation Administration (FAA) sites all over the west pacific coast (the closest one is ZOA1). Data importation and quality assurance are automated, although some manual correction of unusual data problems is still required. This year the volume of GPS data in raw format in the NCEDC storage facility has increased by 30% ( $\sim 525\text{Mb/day}$ ). This trend will continue with the installation of new sites (1Hz) and the conversion of the rest of the 15 sites of BARD.

As part of the activities funded by the USGS through the BARD network, the NCEDC has established an archive of the 7000+ survey-mode occupations collected by the USGS since 1992. The NCEDC continues to archive non-continuous survey GPS data. The initial dataset archived is the survey GPS data collected by the USGS Menlo Park for northern California and other locations. The NCEDC is the principal archive for this dataset. Significant quality control efforts were implemented by the NCEDC (*Romanowicz et al., 1994*) to ensure that the raw data, scanned site log sheets, and RINEX data are archived for each survey. All of the USGS MP GPS data has been transferred to the NCEDC, and virtually all of the data from 1992 to the present has been archived and is available for distribution. We are also archiving additional high-precision GPS data sets from northern California (mainly Parkfield measurements). Together with graduate students in the department who are now using the GAMIT software to process survey-mode data in the San Francisco Bay area, we are working to combine the survey-mode and C-GPS solutions into a self-consistent velocity field for northern California. The campaign velocity field computed from campaign measurements by UCB and USGS groups has been published by *d'Alessio et al., (2005)*.

Data from five of our sites (HOPB, MHCN, CMBB, OHLN, YBHB) are sent to the National Geodetic Survey (NGS) in the framework of the CORS (Continuous Operating Reference Stations) project (<http://www.ngs.noaa.gov/CORS/>). The data from these five sites are also distributed to the public through the CORS ftp site.

### 3.5.3 2006-2007 Activities

#### New stations and upgrades

**Permit requests:** We are in the process of permit agreement for the PTP1 site along the Hayward fault

and the BDM site located in Black Diamond Mine Park. The permit for this site will be retrieved by the EBPARK board during the month of September 2007.

Three sites have been upgraded to 1Hz (BRIB, HOPB, PTRB). The sites BRIB and HOPB are colocated with a broad-band seismometer (BRIB, HOPS) belonging to the BDSN network. The upgrade of these sites is an important step leading to the comparison of the GPS data with seismic records in the Bay Area.

**5Hz data in buffer.** We started to experiment with the use of 5Hz GPS data during August 2007. Today, the telemetry cost is too high to allow the transmission of these data in real-time. However, some delayed use of these data can occur after manual download, using the existing telemetry for a selection of sites. The storage capacity of NETRS receivers allows storing two days of data recorded at 5Hz.

**Real-Time Kinematic (RTK) service** In the framework of the collaboration with EBPARK, BSL is distributing RTK corrections at some sites. This experimental project aims at developing collaborations with private actors or local institutions in northern California. We hope to densify the network and reduce monumentation and telemetry costs associated with the installation and operations of new sites.

**Conversion of ten PBO sites:** Ten sites (P181, P222, P224, P225, P227, P228, P229, P230, P262, P256) of the PBO network will be included in the high rate processing under development at Berkeley Seismological Lab. These operations are carried out in close collaboration with East Bay Regional Parks (EBPARK) and East Bay Municipal Water District (EBMUD). These 10 sites will be operated through a radio network (Freewaves or Wi-LAN) using the existing telemetry paths. The cost of the installation will be supported by EBPARK and BSL (the Wi-LAN radio for the site P224). All sites will feed a NTRIP server installed this year on the BSL network by Doug Neuhauser. This server is providing RTK corrections while the streamed data is being converted into RINEX format.

**Upgrade of the EBMD site:** This site, operated in collaboration with EBMUD, is streaming RTK messages to Berkeley via a Wi-LAN link to the Space Science Lab. telemetry facility (Figure 3.16). This site is a prototype of the system that will be used for the 10 PBO sites (see above). This system is reliable and has proven its efficiency in terms of real-time localization (Jim Swanson and Janine Hampton, personal communication). The RTK system is not able to offer accurate displacements for basic science purposes. The RTK accuracy is estimated to 3 cm instantaneously. For this reason, all the RTK messages are converted by an NTRIP server at BSL.

**Parkfield area:** In February 2003, the BSL assumed responsibility for data telemetry from a 14-station GPS network in the Parkfield region, in addition to the BSL

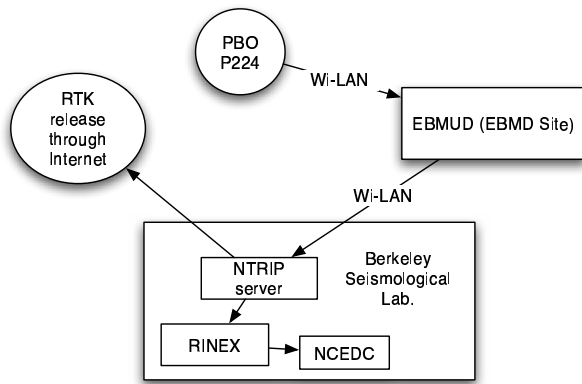


Figure 3.16: Present BSL operations at EBMD site and planned operations between the PBO site P224 and BSL. Since its installation in 2003, the EBMD site had been sending data to BSL using an internet DSL connection. The data collected (Trimble 5700 receiver) are now sent to BSL using a WI-LAN radio connection. The connection represents an upgrade of the quality of the radio link. The data collected here are thus more safely sent to BSL in case of a large seismic event.

station PKDB. Most of these stations were constructed using mini-PBO funding with contributions from the USGS and SCIGN. This project was continued during the year 2006-2007. All the Parkfield GPS sites have been transferred to the PBO network except the PKDB site, which remains a BSL/BARD site, as it is collocated with a long-term BDSN station. The PKDB sites have not been upgraded to 1Hz, which limits the comparison of data with seismic data. Last year, the site HUNT at Parkfield was upgraded to a Trimble NETRS receiver. We appreciated the good coordination with PBO (Freddy Blume) and San Diego teams during this last upgrade. Today, BSL is still in charge of the creation of the RINEX format files. These files are then downloaded daily by the PBO team to be archived at the UNAVCO facility in Boulder.

*Replacement and Upgrade of BARD and MPBO GPS receivers:* During 2006-2007, geodetic GPS hardware receivers of the BARD and MPBO arrays failed at a number of sites (CMBB, HOPB). Typically these sites had a crashed receiver that could not be rebooted. Electronics at these sites are twelve to 15 years old.

### 3.5.4 Data Analysis and Results

#### CALREF, a stable reference frame for northern California

The BARD dataset has been processed in the ITRF2000 (Altamimi *et al.*, 2002). The solutions (Houlié and Romanowicz, in prep) are in good agreement with campaign solutions (BAVU and USGS) previously re-

leased (d'Alessio *et al.*, 2005). The new coordinates release of the BARD network includes the presently operating sites and the velocity of the sites already transferred from BSL to PBO during the last two years.

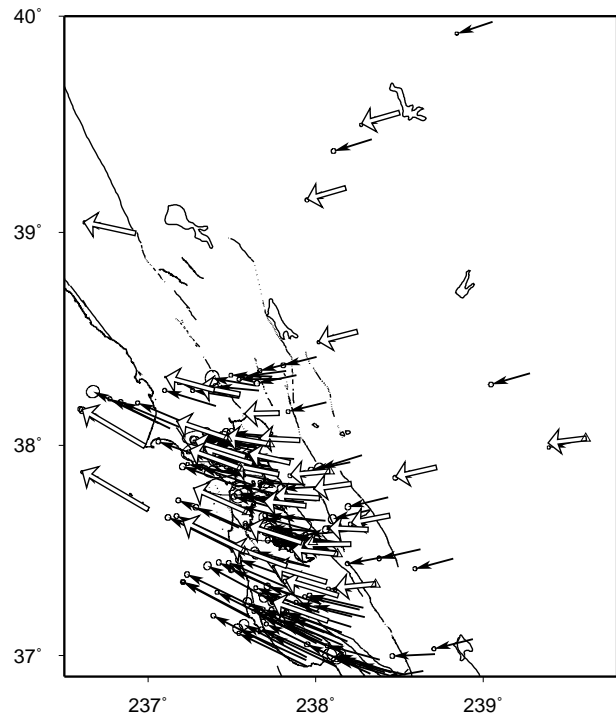


Figure 3.17: Comparison of the BARD solutions (white arrows) with the Bay Area Velocity Unification (BAVU) solutions (black arrows). All the data available at the BSL between 1994 and 2006 have been reprocessed (From Houlié and Romanowicz, in prep). BAVU website: <http://seismo.berkeley.edu/burgmann/RESEARCH/BAVU/>

All the BARD sites have been processed jointly with IGS sites in California. No *a priori* constraints have been assumed during the processing. All the velocities included in the first release of California Reference Frame (CALREF) are given in Table 3.13. The CALREF will provide velocities and coordinates of sites located in the bay area at specific epochs. Each solution will be associated with error estimations (formal and real). Every surveyor will be able to control the reference site coordinates for a given survey.

#### BARD products released on the web

A series of products will soon be released on the new BARD website (<http://www.ncedc.org/bard/>). The list of products released is still under discussion at BSL, but it will include various domains (from time-series (Figure 3.18) to troposphere studies) that can potentially benefit GPS studies and promote collaboration among BSL researchers or others. All products will be updated daily.

Sites	Lon. (deg.)	Lat. (deg.)	$dV_e$ (mm/y)	$dV_n$ (mm/y)
BAY1	197.293	55.19	-0.03	0.01
GOLD	243.111	35.425	1.20	-0.11
JPLM	241.827	34.205	0.50	0.59
PPT1	237.61	37.187	0.82	0.27
VNDP	239.384	34.556	-0.05	-0.81

Table 3.12: Comparison between previous published values and recomputed values. The adjustment with the ITRF2000 is good. The errors provided here are formal and cannot be qualified as realistic (From *Houlié and Romanowicz*, in prep).

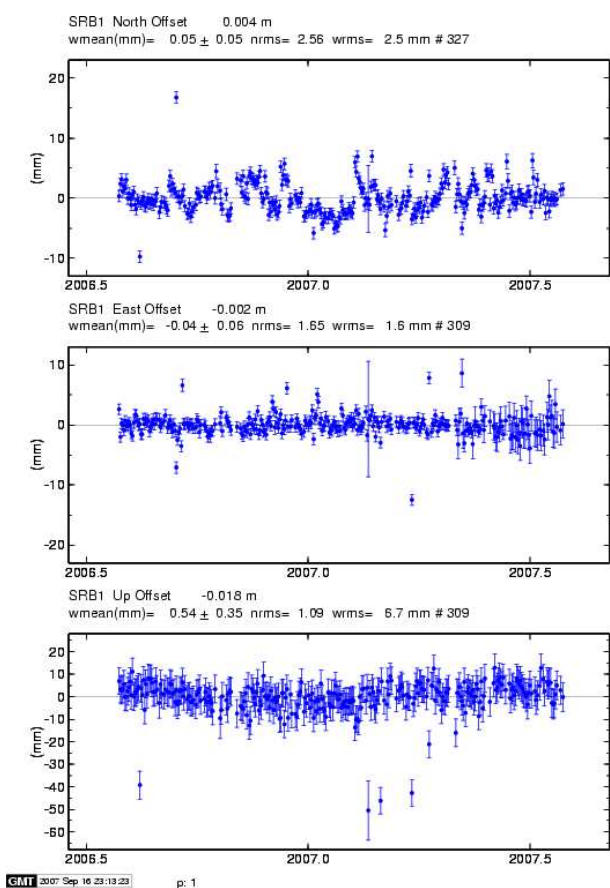


Figure 3.18: Time series of coordinates at the SRB1 site. Each day is processed automatically; then the time series is updated and BARD site coordinates in the ITRF2000 are adjusted.

### Troposphere study in southern California and in SFBA

Two distinct troposphere studies have been carried out this year. The first one, in collaboration with Gareth

Funning and Roland Bürgmann, focused on the uplift detected above the San Gabriel valley aquifer (Figure 2, Chapter 2) in southern California.

We propose including troposphere estimates from the GPS measurements into SAR data processing (in this case ROIPAC has been used).

Every day a troposphere map is estimated from the BARD dataset in order to increase the GPS accuracy and to correct the SAR scenes acquired in the San Francisco Bay Area. Twice a day, a map of troposphere delay is released for the previous day (See Figure 3.19). The troposphere maps will be released through the new version of the BARD website (see above). The next step of this research on the troposphere is now to manage the meteorological dataset jointly with GPS observations in real-time.

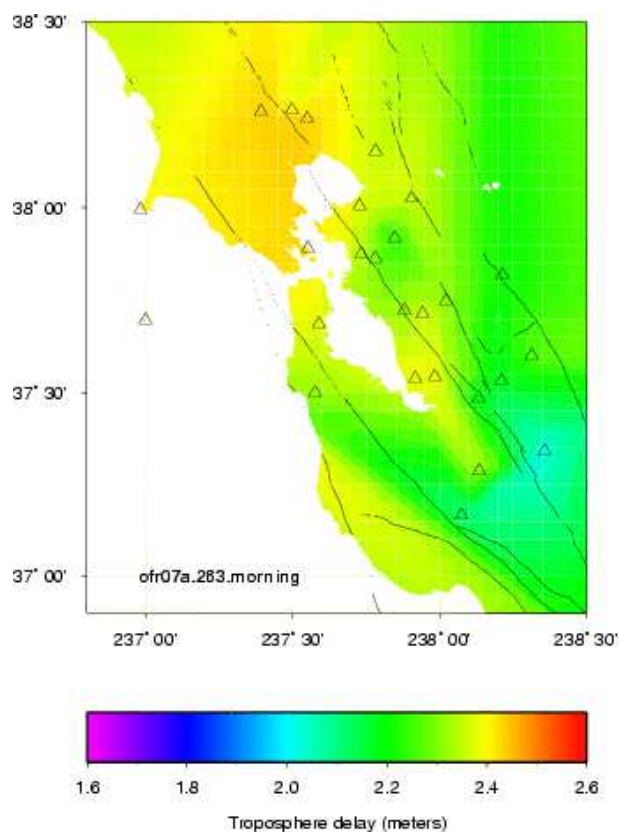


Figure 3.19: Interpolated troposphere delay at the acquisition time (5 am (PDT) of the SAR scene, 2007, Sep. 20th). The zenithal troposphere delay in the SFBA can experience up to 5 cm variation. This lateral troposphere effect can impact the SAR baseline estimation and the ongoing research on the slow creep deformation of the Hayward fault.

### 2004 Parkfield displacement field update

The Parkfield displacement field associated with the 2004 event has been reprocessed in order to better constrain the slip along the fault. A particular focus was on the near-fault observations. Indeed, as the other geodetic techniques (SAR and LiDAR)

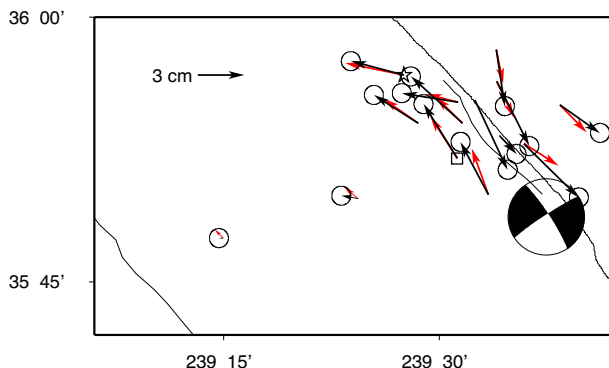


Figure 3.20: Coseismic displacements during the 2004 Parkfield earthquake. The displacement at the CRBT site is less than 3 mm. The displacement observed at PKDB (star) indicates the rupture along the fault is limited in the south.

cannot provide reliable information near the fault due to a lack of coherency, the accuracy of near-fault GPS displacements is crucial. The new computed displacement field will be published in two research articles (*Ahyi and Dreger, in press, JGR*) and (*Houlié, Dreger, and Romanowicz, in prep.*)

### 3.5.5 Acknowledgements

Since the departure of Mark Murray at the end of 2005, Barbara Romanowicz has overseen the BARD program. Rich Clymer, Bill Karavas, Rick Lellinger, John Friday, Nicolas Houlié and Doug Neuhauser contributed to the operation of the BARD network. The operation of the BARD network is partially supported by funding from the USGS/NEHRP program and funding from the NSF/UNAVCO *PBO nucleus* grant.

### 3.5.6 References

Altamimi, Z., P. Sillard, and C. Boucher, ITRF2000: A new release of the International Terrestrial Reference Frame for earth science applications, *J. Geophys. Res.*, 107(B10), 2214, doi:10.1029/2001JB000561, 2002

d'Alessio, M. A., I. A. Johanson, R. Bürgmann, D. A. Schmidt, and M. H. Murray, Slicing up the San Francisco Bay Area: Block kinematics from GPS-derived surface velocities, *J. Geophys. Res.*, 110, B06403, doi:10.1029/2004JB003496, 2005.

Houlié, N. and Romanowicz, B., CALREF, a stable reference frame for the Northern California, in prep.

Murray, M., Neuhauser D., Gee, L., Dreger, D., Basset, A., and Romanowicz, B., Combining real-time seismic and geodetic data to improve rapid earthquake information, *EOS. Trans. AGU*, 83(47), G52A-0957, 2002.

Perin, B. J., C. M. Meertens, D. S. Neuhauser, D. R. Baxter, M. H. Murray, and R. Butler, Institutional collaborations for joint seismic and GPS measurements, *Seismol. Res. Lett.*, 69, 159, 1998.

Romanowicz, B., B. Bogaert, D. Neuhauser, and D. Oppenheimer, Accessing northern California earthquake data via Internet, *EOS Trans. AGU*, 75, 257-260, 1994.

Site	Lon.	Lat	Ve (mm/y)	Vn (mm/y)	$\sigma_e$ (mm/y)	$\sigma_n$ (mm/y)	Start
BAY1*	197.29	55.19	-6.3	-25.5	0.0000	0.0000	1996.08
BAY2	197.29	55.19	-5.6	-25.2	0.0400	0.0300	1996.08
BRIB	237.85	37.92	-24.8	5.6	0.0100	0.0100	1993.58
CMBB	239.61	38.03	-22.9	-2.8	0.0100	0.0100	1993.92
CNDR	238.72	37.90	-24.4	-5.5	0.0200	0.0200	1999.27
DIAB	238.08	37.88	-23.7	-2.2	0.0100	0.0100	1998.33
FARB	237.00	37.70	-39.8	23.3	0.0100	0.0100	1994.00
GOLD*	243.11	35.43	-18.2	-5.4	0.0000	0.0000	1989.95
HCRO	238.53	40.82	-18.0	-8.7	0.1400	0.1500	2003.50
HOPB	236.93	39.00	-31.1	6.8	0.0100	0.0100	1995.58
JPLM*	241.83	34.21	-36.6	11.8	0.0000	0.0000	1989.44
LUTZ	238.14	37.29	-31.7	9.5	0.0100	0.0100	1996.33
MHCB	238.36	37.34	-24.2	-2.4	0.0100	0.0100	1996.33
MODB	239.70	41.90	-16.9	-9.1	0.0200	0.0200	1999.83
MOLA	237.58	37.95	-30.5	9.7	0.0100	0.0100	1993.75-2002.22
MONB	238.13	37.49	-27.5	2.7	0.0100	0.0100	1998.50
MUSB	240.69	37.17	-22.3	-4.0	0.0100	0.0100	1997.83
OHLN	237.73	38.01	-26.4	4.4	0.0200	0.0200	2001.83
ORVB	238.50	39.56	-22.7	-6.6	0.0100	0.0100	1996.83
OXMT	237.58	37.50	-36.9	18.0	0.0600	0.0600	2004.12
P181(PBO)	237.62	37.92	-29.0	9.6	0.3800	0.4000	2005.09
P198 (PBO)	237.39	38.26	-29.2	7.9	0.0900	0.1000	2004.77
P200 (PBO)	237.55	38.24	-24.3	4.7	0.2000	0.2200	2005.73
P222 (PBO)	237.92	37.54	-31.5	10.0	0.1100	0.1200	2005.26
P224 (PBO)	237.78	37.86	-26.9	5.5	0.1000	0.1100	2005.25
P225 (PBO)	237.94	37.71	-25.2	2.7	0.0900	0.1000	2005.14
P227 (PBO)	238.21	37.53	-28.6	-0.4	0.5800	0.6300	2006.20
P228 (PBO)	238.31	37.60	-23.5	1.0	0.4300	0.4700	2005.93
P229 (PBO)	238.02	37.75	-26.8	1.6	0.1100	0.1200	2005.29
P230 (PBO)	238.21	37.82	-22.5	-3.1	0.1100	0.1200	2005.15
P261 (PBO)	237.78	38.15	-21.0	-0.5	0.0900	0.1000	2004.50
P262 (PBO)	237.90	38.03	-24.2	1.2	0.1100	0.1200	2005.32
PKDB	239.46	35.95	-43.0	18.7	0.0100	0.0100	1996.67
PPT1*	237.61	37.19	-40.7	22.1	0.0000	0.0000	1996.14
PTRB	236.98	38.00	-37.7	22.2	0.0100	0.0100	1998.58
S300	238.44	37.67	-22.9	-4.4	0.0200	0.0200	1998.48
SAOB	238.55	36.77	-41.4	22.0	0.0100	0.0100	1997.58
SBRN	237.59	37.69	-32.0	14.2	0.0300	0.0300	2003.18
SODA	26.39	67.42	18.7	34.1	0.1400	0.1600	1994.70
SODB	238.07	37.17	-33.1	11.7	0.0100	0.0100	1996.33
SUAA	237.83	37.43	-33.7	12.4	0.0100	0.0100	1994.30
SUTB	238.18	39.21	-23.1	-6.7	0.0100	0.0100	1997.33
SVIN	237.47	38.03	-30.5	10.3	0.0400	0.0400	2003.89
THAL	238.07	37.35	-32.0	9.5	0.2000	0.2200	2003.00
TIBB	237.55	37.89	-30.8	11.2	0.0100	0.0100	1994.42
UCD1	238.25	38.54	-23.1	-6.0	0.0100	0.0100	1996.38
VNDP*	239.38	34.56	-42.2	20.9	0.0000	0.0000	1992.48
YBHB	237.29	41.73	-15.8	-6.7	0.0100	0.0100	1996.75

Table 3.13: CALREF 2006 official velocities. All velocities and estimated errors ( $\sigma$ ) are indicated in mm per year. For each site, the relevant time-span and the network are specified. The sites with a star are the sites for which the velocities have been used during the combination of the daily solutions.

## 3.6. Northern California Earthquake Data Center

### 3.6.1 Introduction

The Northern California Earthquake Data Center, a joint project of the Berkeley Seismological Laboratory (BSL) and the U.S. Geological Survey at Menlo Park, serves as an online archive for various types of digital data relating to earthquakes in central and northern California. The NCEDC is located at the Berkeley Seismological Laboratory, and has been accessible to users via the internet since mid-1992.

The primary goal of the NCEDC is to provide a stable and permanent archival and distribution center of digital geophysical data for networks in northern and central California. These data include seismic waveforms, electromagnetic data, GPS data, strain, creep, and earthquake parameters. The seismic data comes principally from the Berkeley Digital Seismic Network (BDSN) operated by the Seismological Laboratory, the Northern California Seismic Network (NCSN) operated by the USGS, the Berkeley High Resolution Seismic Network (HRSN) at Parkfield, the EarthScope USArray Transportable Array stations in northern California, the various Geysers networks, and selected stations from adjacent networks such as the University of Reno, Nevada network and the Southern California Seismic Network (SCSN). GPS data are primarily from the Bay Area Regional Deformation (BARD) GPS network and the USGS/Menlo Park GPS surveys. The collection of NCSN digital waveforms dates from 1984 to the present, the BDSN digital waveforms date from 1987 to the present, and the BARD GPS data date from 1993 to the present. The BDSN includes stations that form the specialized Northern Hayward Fault Network (NHFN) and the MiniPBO (MPBO) borehole seismic and strain stations in the SF Bay Region.

The NCEDC also provides support for earthquake processing and archiving activities of the Northern California Earthquake Management Center (NCEMC), a component of the California Integrated Seismic Network (CISN). The CISN is the California regional organization of the Advanced National Seismic Network (ANSS).

### 3.6.2 2006-2007 Activities

By its nature, data archiving is an ongoing activity. In 2006-2007, the NCEDC continued to expand its data holdings and enhance access to the data. Projects and activities of particular note include:

- Actively participated in the retirement of the NCSN CUSP earthquake review software, which allowed the NCEDC to begin receiving authoritative real-time earthquake data from the NCEMC database into the NCEDC database.

- Implemented real-time waveform collection of earthquake event waveforms for the NCEMC.
- Supported the NCEMC earthquake analysis by providing real-time access to earthquake parameters and waveforms from the NCEDC for the CISN Jiggle earthquake review software.
- Implemented software and procedures to read and archive continuous NCSN seismograms from tapes for 2001-2005, and began processing the NCSN data tapes.

These activities and projects are described in detail below.

### 3.6.3 Data Collections

The bulk of the data at the NCEDC consists of waveform and GPS data from northern California. Figure 3.21 shows the geographic distribution of data archived by the NCEDC. Figure 3.22 shows the relative proportion of each data set at the NCEDC. The total size of the datasets archived at the NCEDC is shown in Table 3.14. Figure 3.23 shows the amount of data for each year that is archived at the NCEDC.

### 3.6.4 BDSN/NHFN/MPBO Seismic Data

Archiving current BDSN (Section 3.1.), NHFN (Section 3.3.), and Mini-PBO (Section 3.3.) (all stations using the network code BK) seismic data is an ongoing task. These data are telemetered from 47 seismic data loggers in real-time to the BSL, where they are written to disk files, used for CISN real-time earthquake processing, and delivered in real-time to the DART (Data Available in Real Time) system on the NCEDC, where they are immediately available to anyone on the internet. In September 2004, the NCEDC began to archive continuous high frequency data (80 Hz and 100 Hz) from all of the BDSN broadband, strong motion, and strainmeter sensors. Previously, 20 Hz and lower rate data channels were archived continuously, and high frequency data was archived only for events. In early 2006, the NCEDC started to receive all of the BK stations in real-time and make them available to users through the DART. All timeseries data from the Berkeley networks continue to be processed and archived by an NCEDC analyst using *calqc* in order to provide the highest quality and most complete data stream to the NCEDC.

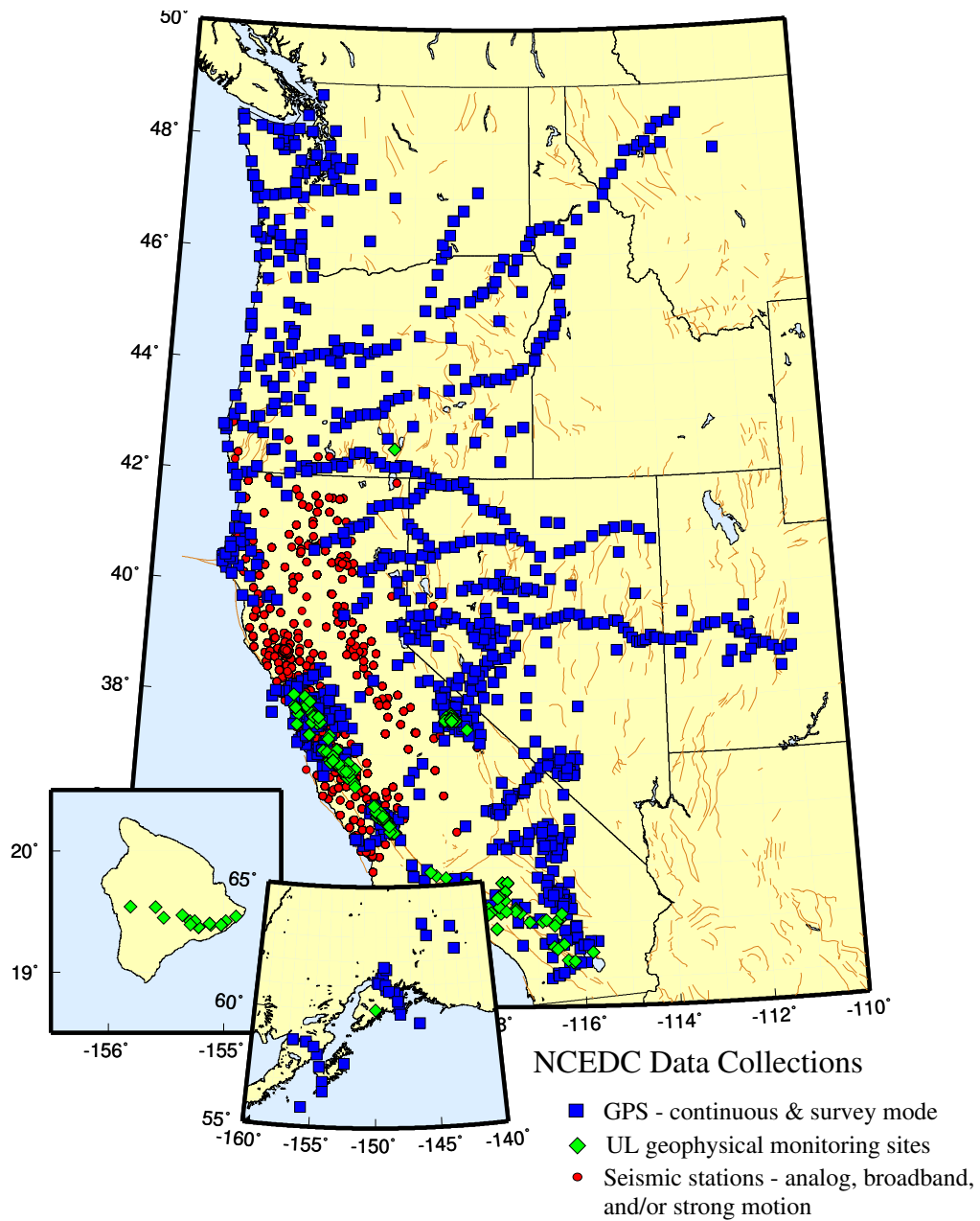


Figure 3.21: Map showing the location of stations whose data are archived at the NCEDC. Circles are seismic sites; squares are GPS sites, and diamonds are the locations of USGS low-frequency experiments.

## Volume of Data archived at the NCEDC

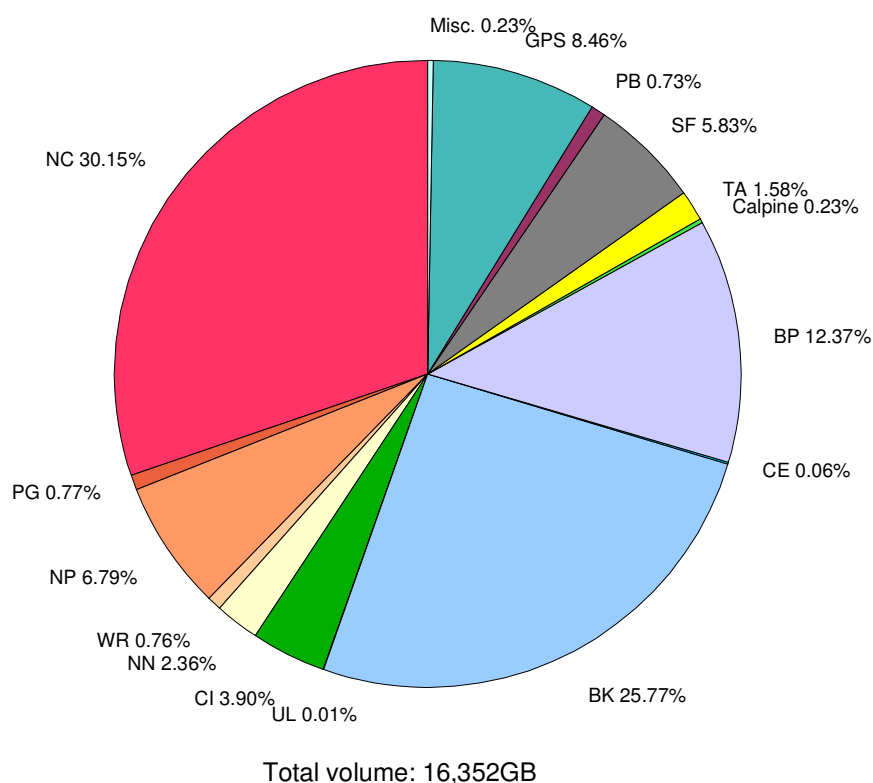


Figure 3.22: Chart showing the relative proportion of each data set at the NCEDC.

Data Type	GBytes
BDSN/NHFN/MPBO (broadband, electric and magnetic field, strain) waveforms	4,215
NCSN seismograms	6,300
Parkfield HRSN seismograms	2,023
BARD GPS (RINEX and raw data)	1,383
UNR Nevada seismograms	386
SCSN seismograms	638
Calpine/Unocal Geysers region seismograms	38
EarthScope SAFOD seismograms	954
EarthScope USArray seismograms	258
EarthScope PBO strain waveforms	119
USGS low frequency geophysical waveforms	2
Misc data	37
Total size of archived data	16,352

Table 3.14: Volume of Data Archived at the NCEDC by network

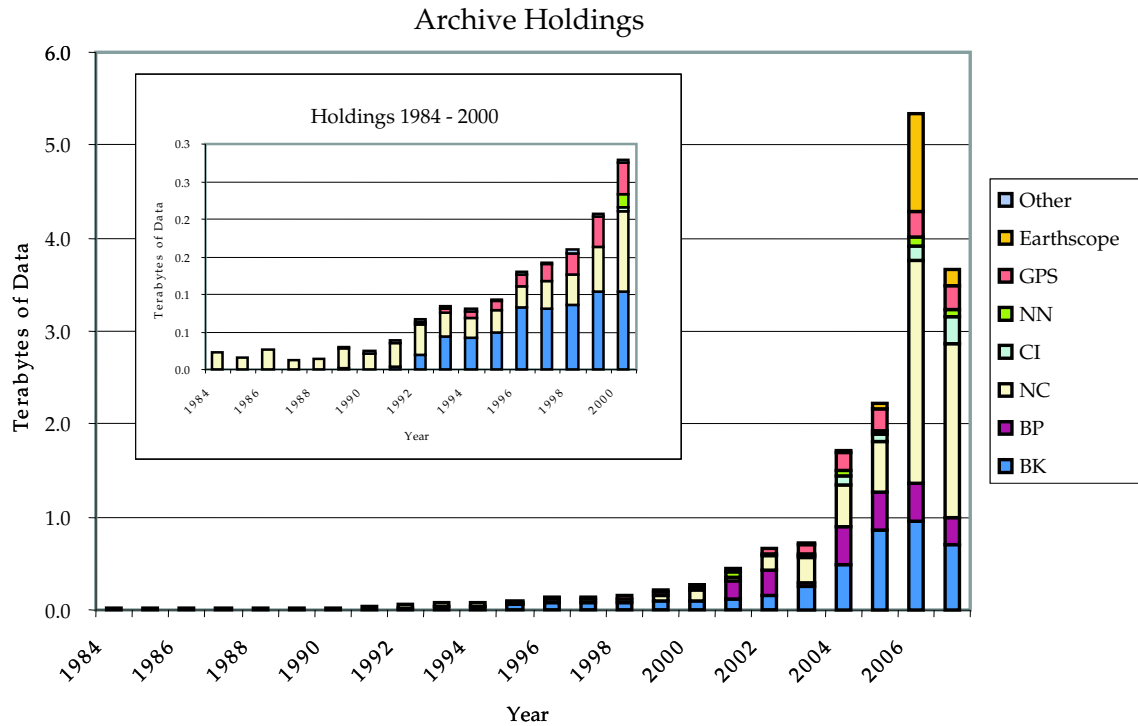


Figure 3.23: Figure showing the total volume of data archived at the NCEDC, broken down by data year.

### NCSN Seismic Data

NCSN continuous waveform data are sent in real-time to the NCEDC via the internet, and are made available to users in real-time through the NCEDC DART. NCSN event waveform data, as well as data from all other real-time BSL and collaborating networks, are automatically collected by the NCEMC waveform archiver and stored at the NCEDC for event review and analysis and for distribution to users. All NCSN and NCEMC data are archived in MiniSEED format.

The NCEDC also maintains a list of historic teleseismic events recorded by the NCSN, since these events do not appear in the NCSN catalog.

A description of the successive improvements in the acquisition of NCSN data, leading to the acquisition of complete NCSN waveform data in early 2006, can be found in the 2005-06 BSL annual report. We are currently working on completing the waveform data collection by reading and archiving NCSN seismograms from tapes for the period 2001-2005.

### Parkfield High Resolution Seismic Network Data

The history of upgrades to the acquisition and archival of HRSN data can be found in the 2005-06 BSL Annual Report.

In early 2006, the NCEDC started to receive the HRSN 20 Hz data and a subset of the 250 Hz data in real-time

for distribution through the DART. The NCEDC continued to archive continuous 250 Hz and 20 Hz data streams from the HRSN tapes written in Parkfield and processed at the NCEDC. In early 2007, the BSL established a radio telemetry link from the HRSN recording center at the California Department of Forestry (CDF) in Parkfield to Carr Hill, and started to telemeter all HRSN continuously to Carr Hill. These data are fed into the NCSN backup Earthworm system at Carr Hill, and are also routed through the USGS Parkfield and the NCEMC T1 between USGS/MP and the BSL for real-time processing by the NCEMC earthquake processing system. The data are also made available to users through the NCEDC DART, and are continuously archived at the NCEDC.

### EarthScope USArray Transportable Array

EarthScope began installing broadband stations for the Transportable Array component of USArray in California in 2005. The NCEDC started acquiring telemetered continuous data from the northern California and surrounding stations as they were installed, and is archiving these data to support users working with northern California seismic data. These data are made available to users using the same data request methods as all other continuous data waveform data at the NCEDC. The Transportable Array stations have a limited operational timespan of 18 to 24 months, after which they will

be relocated to new sites across the country. Data from these stations are delivered to the NCEDC as they are received by the BSL for distribution through the DART.

### **EarthScope Plate Boundary Observatory (PBO) strain data**

The NCEDC is one of two funded archives for PBO EarthScope borehole and laser strain data. Strain data are collected from all of the PBO strain sites and are processed by UNAVCO. MiniSEED data are delivered to the NCEDC using SeedLink, and raw and XML processed data are delivered to the NCEDC using Unidata's Local Data Manager (LDM). The MiniSEED data are inserted into the NCEDC DART, and are subsequently archived from the DART. UNAVCO provides EarthScope funding to the NCEDC to help cover the processing, archiving, and distribution costs for these data.

### **EarthScope SAFOD**

The NCEDC is designated as the primary archive center for the SAFOD event data, and will also process the continuous SAFOD data. Starting in July 2002, scientists from Duke University successfully installed a three component 32 level downhole-seismic array in the pilot hole at the EarthScope SAFOD site in collaboration with Steve Hickman (USGS), Mark Zoback (Stanford University) and the Oyo Geospace Engineering Resources International (GERI) Corporation. High frequency event recordings from this array have been provided by Duke University for archiving at the NCEDC. We converted data from the original SEG-2 format data files to MiniSEED, and have developed the SEED instrument responses for this data set. Continuous 4 KHz data from SAFOD are written to tape at SAFOD, and are periodically sent to the BSL to be converted, archived, and forwarded to the IRIS DMC. SAFOD EarthScope funding to the NCEDC is to cover the processing, archiving, and distribution costs for these data. A small subset of the continuous SAFOD data channels are also incorporated into the NCSN, are available in real-time from the NCEDC DART, are archived at the NCEDC, and are forwarded to the IRIS DMC.

### **UNR Broadband data**

The University of Reno in Nevada (UNR) operates several broadband stations in western Nevada and eastern California that are important for northern California earthquake processing and analysis. Starting in August 2000, the NCEDC has been receiving and archiving continuous broadband data from four UNR stations. The data are transmitted in real-time from UNR to UC Berkeley, where they are made available for CISEN real-time earthquake processing and for archiving. Initially, some of the stations were sampled at 20 Hz, but all stations are now sampled and archived continuously at 100

Hz.

The NCEDC installed Simple Wave Server (SWS) software at UNR, which provides an interface to UNR's recent collection of waveforms. The SWS is used by the NCEDC to retrieve waveforms from UNR that were missing at the NCEDC due to real-time telemetry outages between UNR and UC Berkeley.

In early 2006, the NCEDC started to archive continuous data from the UNR short-period stations that are contributed to the NCSN. Both the broadband and short-period UNR stations contributed to the CISEN are available in real-time through the NCEDC DART.

### **Electro-Magnetic Data**

The NCEDC continues to archive and process electric and magnetic field data acquired at several UC Berkeley sites. The BSL operates both magnetic and electric field sensors at PKD and SAO. Through a collaboration with Dr. Simon Klemperer at Stanford University, we acquire magnetic and electric field channels at BSL sites JRSC and BRIB, and magnetic field channels at site MHDL. The three magnetic field channels and either two or four electric field channels are digitized at 40 Hz, 1 Hz, and 0.1 Hz, and are telemetered in real-time along with seismic data to the Berkeley Seismological Laboratory, where they are processed and archived at the NCEDC in a similar fashion to the seismic data.

Using programs developed by Dr. Martin Fullerkrug at the Stanford University STAR Laboratory (now at the University of Bath), the NCEDC has computed and archived magnetic activity and Schumann resonance analysis using the 40 Hz data from this dataset. The magnetic activity and Schumann resonance data can be accessed from the Web. This processing was halted in mid 2005 due to problems with the code and will be resumed when the problems have been identified and corrected.

The NCEDC also archives data from a low-frequency, long-baseline electric field project operated by Dr. Steve Park of UC Riverside at site PKD2. These data are acquired and archived in an identical manner to the other electric field data at the NCEDC.

### **GPS Data**

The NCEDC continues to archive GPS data through the BARD (Bay Area Regional Deformation) network of continuously monitored GPS receivers in northern California (Section 3.5.). The NCEDC GPS archive now includes 67 continuous sites in northern California. There are approximately 50 core BARD sites owned and operated by UC Berkeley, USGS (Menlo Park and Cascade Volcano Observatory), LLNL, UC Davis, UC Santa Cruz, Trimble Navigation, and Stanford. Data are also archived from sites operated by other agencies including East Bay Municipal Utilities District, the City of Modesto, the Na-

tional Geodetic Survey, and the Jet Propulsion Laboratory.

In addition to the standard 15 second or 30 second continuous GPS datastream, the NCEDC is now privately archiving high-rate 1 Hz continuous GPS data from the 14 stations in Parkfield and from 10 BARD stations. The high-rate Parkfield data are collected by UNAVCO as part of the PBO Nucleus. The Parkfield data are available via anonymous FTP from the NCEDC but are currently not included in the GPS Seamless Archive (GSAC), since the GSAC does not currently handle both high-rate and low-rate data from the same site and day.

The NCEDC continues to archive non-continuous survey GPS data. The initial dataset archived is the survey GPS data collected by the USGS Menlo Park for northern California and other locations. The NCEDC is the principal archive for this dataset. Significant quality control efforts were implemented by the NCEDC to ensure that the raw data, scanned site log sheets, and RINEX data are archived for each survey. All of the USGS MP GPS data has been transferred to the NCEDC and virtually all of the data from 1992 to the present has been archived and is available for distribution.

### **Geysers Seismic Data**

The Calpine Corporation currently operates a microseismic monitoring network in the Geysers region of northern California. Prior to 1999 this network was operated by Unocal. Through various agreements, both Unocal and Calpine have released triggered event waveform data from 1989 through 2000 along with preliminary event catalogs for the same time period for archiving and distribution through the NCEDC. This dataset represents over 296,000 events that were recorded by Calpine/Unocal Geysers network, and are available via research accounts at the NCEDC.

The Lawrence Berkeley Laboratory (LBL), with funding from the California Energy Commission, operates a 22 station network in the Geysers region with an emphasis on monitoring seismicity related to well water injection. The earthquake locations and waveforms from this network are sent to the NCEDC, and the locations are forwarded to the NCSN so that they can be merged into the NCSN earthquake catalog. The LBL Geysers waveforms will be available at the NCEDC after the NCSN catalog has been migrated from flat files to the database. In 2007 the NCSN installed an Earthworm system at the Geysers to receive continuous LBL Geysers data, and this system provides event waveforms in real-time for the NCEMC earthquake processing and the NCEDC event archives.

### **USGS Low Frequency Data**

Over the last 30 years, the USGS at Menlo Park, in collaboration with other principal investigators, has col-

lected an extensive low-frequency geophysical data set that contains over 1300 channels of tilt, tensor strain, dilatational strain, creep, magnetic field, and water level as well as auxiliary channels such as temperature, pore pressure, rain and snow accumulation, and wind speed. In collaboration with the USGS, we assembled the requisite information for the hardware representation of the stations and the instrument responses for many channels of this diverse dataset, and developed the required programs to populate and update the hardware database and generate the instrument responses. We developed the programs and procedures to automate the process of importing the raw waveform data and convert it to MiniSEED format. Since these data are delivered to the NCEDC on a daily basis and immediately archived, these data are not inserted into the NCEDC DART.

We have currently archived timeseries data from 887 data channels from 167 sites, and have instrument response information for 542 channels at 139 sites. The waveform archive is updated on a daily basis with data from 350 currently operating data channels. We will augment the raw data archive as additional instrument response information is assembled by the USGS for the channels and will work with the USGS to clearly define the attributes of the "processed" data channels.

### **SCSN/Statewide seismic data**

In 2004 the NCEDC started to archive broadband and strong motion data from 15 SCSN (network CI) stations that are telemetered to the Northern California Management Center (NCEMC) of the California Integrated Seismic Network (CISN). These data are used in the prototype real-time state-wide earthquake processing system and also provide increased coverage for northern California events. Since the data are telemetered directly from the stations in real-time to both the SCSN and to the NCEMC, the NCEDC archives the NCEMC's copy of the data to ensure that at least one copy of the data will be preserved.

In early 2006, the NCEDC started to continuously archive all of the selected SCSN short-period stations that are contributed to the NCSN. All of these data are available in real-time from the NCEDC DART.

### **Earthquake Catalogs**

*Northern California:* The NCEDC provides searchable access to both the USGS and BSL earthquake catalogs for northern and central California. The "official" UC Berkeley earthquake catalog begins in 1910 and runs through 2003, and the "official" USGS catalog begins in 1966. Both of these catalogs are archived and available through the NCEDC, but the existence of 2 catalogs has caused confusion among both researchers and the public.

In late 2006, the NCEMC begun to archive and distribute a single unified northern California earthquake

catalog in real-time to the NCEDC through database replication from the NCEMC's real-time systems. The NCEDC has developed and is testing the required programs that will be used to enter all previous NCSN catalog data into the NCEDC database. We will then merge the BSL catalog with the NCEMC catalog to form a single unified northern California catalog from 1910 to the present. The BSL and the USGS have spent considerable effort over the past years to define procedures for merging the data from the two catalogs into a single northern and central California earthquake catalog in order to present a unified view of northern California seismicity. The differences in time period, variations in data availability, and mismatches in regions of coverage all complicate the task.

*Worldwide:* The NCEDC, in conjunction with the Council of the National Seismic System (CNSS), produced and distributed a world-wide composite catalog of earthquakes based on the catalogs of the national and various U.S. regional networks for several years. Each network updates their earthquake catalog on a daily basis at the NCEDC, and the NCEDC constructs a composite world-wide earthquake catalog by combining the data, removing duplicate entries that may occur from multiple networks recording an event, and giving priority to the data from each network's *authoritative region*. The catalog, which includes data from 14 regional and national networks, is searchable using a Web interface at the NCEDC. The catalog is also freely available to anyone via ftp over the internet.

With the demise of the CNSS and the development of the Advanced National Seismic System (ANSS), the NCEDC was asked to update its Web pages to present the composite catalog as a product of the ANSS. This conversion was completed in the fall of 2002. We continue to create, house, distribute, and provide a searchable web interface to the ANSS composite catalog, and to aid the regional networks in submitting data to the catalog.

### 3.6.5 NCEDC Operations

In 2005, the NCEDC relocated its archive and distribution system from McCone Hall to a new state-of-the-art computer facility in a new seismically braced building on the Berkeley campus. The facility provides seismically braced equipment racks, gigabit ethernet network, air conditioning, and power conditioning. The entire facility is powered by a UPS with generator backup.

The currently installed NCEDC facilities consist of a mass storage environment hosted by a Sun V240 host computer, a 100 slot LTO-2 tape library with two tape drives and a 20 TByte capacity, and 40 TBytes of RAID storage, all managed with the SAM-FS hierarchical storage management (HSM) software. A dual processor Sun Ultra 60 provides Web services and research account access to the NCEDC, a dual Sun 280R processor provide

data import and export services, and a Sun Ultra 450 computer is used for quality control procedures. Two AIT tape libraries are used to read NCSN continuous data tapes. A 64-bit Linux system hosts a database dedicated to providing data to external users. Two Sun Opteron processors provide additional data processing support for the NCEDC.

The hardware and software system is configured to automatically create multiple copies of each timeseries file. The NCEDC creates an online copy of each file on online RAID, a second copy on LTO-2 tape which is stored online in the tape library, and a third copy on LTO-2 tape which is stored offline and offsite. All NCEDC data are online and rapidly accessible by users.

The NCEDC operates two instances of its Oracle database, one for internal operations and one for external use for user data queries and data distribution programs. The databases are synchronized using multi-master replication.

### Data Quality Control

The NCEDC developed a GUI-based state-driven system *calqc* to facilitate the quality control processing that is applied to the continuously archived data sets at the NCEDC.

The quality control procedures for these datasets include the following tasks:

- data extraction of a full day of data,
- quickcheck program to summarize the quality and stability of the stations' clocks,
- determination if there is missing data for any data channel,
- provided procedures to retrieve missing data from the stations and incorporate it into the day's data,
- optional creation of multi-day timeseries plots for state-of-health data channels,
- optional timing corrections for data,
- optional extraction of event-based waveforms from continuous data channels,
- optional repacking of MiniSEED data,
- creating waveform inventory entries in the NCEDC database,
- publishing the data for remote access on the NCEDC.

*Calqc* uses previously developed programs to perform each function, but it provides a graphical point-and-click interface to automate these procedures, and to provide the analyst with a record of when each process was started, whether it executed correctly, and whether the analyst has indicated that a step has been completed. *Calqc* is used to process all data from the BDSN network, and all continuous broadband data from the NCSN, UNR, SCSN, and HRSN networks that are archived by the NCEDC. The remainder of the continuously archived data are automatically archived without any analyst interaction.

### 3.6.6 Database Development

Due to restrictions imposed by the USGS/MP NCSN CUSP event analysis system, the NCSN's authoritative catalog, phase data, amplitude, and coda readings were stored in flat files, rather than the NCEDC database. However, the NCEDC worked closely with the Northern California Earthquake Management Center (NCEMC) of the CISN to develop procedures allowing the USGS/MP to replace the CUSP analysis system with *jiggle*, the analysis tool developed by the SCSN, and to deliver earthquake parametric data in real-time to the NCEDC database. We developed the database tools to insert the NCEMC earthquake parametric information into databases in the real-time earthquake analysis systems, and extensively tested database replication between the NCEMC databases and the NCEDC database.

Starting in December 2006, the NCSN retired the CUSP system, and real-time earthquake parameters from the NCEMC has been inserted directly into the NCEMC and NCEDC databases, and reviewed with the *jiggle* analysis software. In collaboration with the NCSN, we developed the programs and procedures necessary to migrate the 1967-2006 NCSN catalog into the CISN parametric schema and have been performing quality control procedures on the data prior to entering the catalog into the database. During this time, we have continued to create flat-file hypoinverse files from the new data in the database in order to provide users with a single view of the entire NCSN catalog. Once the historic NCSN catalog has been entered into the database, the NCEDC will serve catalog and parametric searches from the database.

During 2002-2004, the NCEDC and NCSN jointly developed a system consisting of an extensive spreadsheet containing per-channel information that describes the hardware of each NCSN data channel and provides each channel with a SEED-compliant channel name. This spreadsheet, combined with a limited number of files that describe the central-site analog digitizer, FIR decimation filters, and general characteristics of digital acquisition systems, allows the NCSN to assemble its station history in a format that the NCEDC can use to populate the hardware tracking and instrument response database

tables for the NCSN.

The NCEDC instrument response schema represents full multi-stage instrument responses (including filter coefficients) for the broadband data loggers. The hardware tracking schema represents the interconnection of instruments, amplifiers, filters, and data loggers over time, and is used to describe all of the UC Berkeley and USGS stations and channels archived at the NCEDC. All NCSN event waveform and continuous timeseries data has been converted from CUSP and Earthworm format to MiniSEED, and is available along with the UC Berkeley data and data from the other networks archived at the NCEDC in full SEED format.

The NCEDC has developed XML import and export procedures to provide better maintenance of the hardware tracking information and resulting instrument responses for stations in our database. When changes are made to either existing hardware or to station configurations, we export the current view in XML format, use a GUI-based XML editor to easily update the information, and import the changes back into the database. When adding new stations or hardware, we can easily use information from existing hardware or stations as templates for the new information. This allows us to treat the database as the authoritative source of information, and to use off-the-shelf tools such as the XML editor and XML differencing programs as part of our database maintenance procedures.

Additional details on the joint catalog effort and database schema development may be found at <http://www.ncedc.org/db>

### 3.6.7 Data Distribution

The NCEDC continues to use the World Wide Web as a principal interface for users to request, search, and receive data from the NCEDC. In fall 2005 the NCEDC acquired the domain name *ncedc.org*. The NCEDC's Web address is now <http://www.ncedc.org/>

### Earthquake Catalogs

The NCEDC provides users with searchable access to northern California earthquake catalogs and to the ANSS world-wide catalog via the web. Users can search the catalogs by time, magnitude, and geographic region, and can retrieve either hypocenter and magnitude information or a full set of earthquake parameters including phase readings, amplitudes, and codas. Moment tensor results are now being added to the NCEMC California earthquake catalog.

### Station Metadata

In addition to the metadata returned through the various data request methods, the NCEDC provides dataless

SEED volumes and SEED RESP files for all data channels archived at the NCEDC. The NCEDC currently has full SEED instrument responses for 8462 data channels from 1379 stations in 14 networks. This includes stations from the California Geological Survey (CGS) strong motion stations that will contribute seismic waveform data for significant earthquakes to the NCEDC and SCEDC.

### SeismiQuery

We have ported and installed the IRIS *SeismiQuery* program at the NCEDC, which provides a common interface to query network, station, and channel attributes and query the availability of archived timeseries data. We have provided both IRIS and the SCEC Data Center with our modified version of *SeismiQuery*.

### DART (Data Available in Real Time)

The DART (Data Available in Real Time) represents the first step in NCEDC's effort to make current and recent timeseries data from all networks, stations, and channels available to users in real-time. The NCEDC developed DART in December 2005 to provide a mechanism for users to obtain access to real-time data from the NCEDC. All real-time timeseries data streams delivered to the NCEDC are placed in MiniSEED files in a web-accessible directory structure. The DART waveforms can be accessed by web browsers or http command-line programs such as *wget*, a *FISSURES* waveform server, and a Berkeley-developed Simple Wave Server (SWS) which provides programmatic access to the DART data by specified SEED channel and time interval. We will be providing users with a client program to retrieve data from the SWS in the near future. The DART currently provide access to the most recent 30 days of data.

We are using the Freeorb software, an enhanced version of the open-source orb software developed by the IRIS-funded Joint Seismic Project (JSP), as the primary method for delivering real-time data to the NCEDC and into the DART. The freeorb package implements an object ring buffer (ORB) and orbserver, which provides a reliable storage ring buffer and an interface for orb client programs to read, write, and query the orbserver. Orbserver clients running at the NCEDC computer connect to remote orbserver at the BSL and USGS/Menlo Park, retrieve the MiniSEED timeseries data records, and write them to daily channel files in the NCEDC DART. Strain data from the EarthScope PBO network are delivered to the NCEDC using SeedLink, and are inserted into the DART using a similar SeedLink client program.

The NCEDC developed an automated data archiving system to archive data from the DART on a daily basis. It allows us to specify which stations should be automatically archived, and which stations should be handled by the NCEDC's Quality Control program *calqc*,

which allows an analyst to review the waveforms, retrieve missing data from stations or waververs that may have late-arriving, out-of-order data, and perform timing corrections on the waveform data. The majority of data channels are currently archived automatically from the DART.

### NetDC

In a collaborative project with the IRIS DMC and other worldwide datacenters, the NCEDC helped develop and implement *NetDC*, a protocol which will provide a seamless user interface to multiple datacenters for geophysical network and station inventory, instrument responses, and data retrieval requests. The *NetDC* builds upon the foundation and concepts of the IRIS *BREQ\_FAST* data request system. The *NetDC* system was put into production in January 2000, and is currently operational at several datacenters worldwide, including NCEDC, IRIS DMC, ORFEUS, Geoscope, and SCEDC. The *NetDC* system receives user requests via email, automatically routes the appropriate portion of the requests to the appropriate datacenter, optionally aggregates the responses from the various datacenters, and delivers the data (or ftp pointers to the data) to the users via email.

### STP

In 2002, the NCEDC wrote a collaborative proposal with the SCEDC to the Southern California Earthquake Center, with the goal of unifying data access between the two data centers. As part of this project, the NCEDC and SCEDC are working to support a common set of 3 tools for accessing waveform and parametric data: *SeismiQuery*, *NetDC*, and *STP*.

The *Seismogram Transfer Program* or *STP* is a simple client-server program, developed at the SCEDC. Access to *STP* is either through a simple direct interface that is available for Sun or Linux platforms, or through a GUI Web interface. With the direct interface, the data are placed directly on a user's computer in several possible formats, with the byte-swap conversion performed automatically. With the Web interface, the selected and converted data are retrieved with a single ftp command. The *STP* interface also allows rapid access to parametric data such as hypocenters and phases.

The NCEDC has continued work on *STP*, working with the SCEDC on extensions and needed additions. We added support for the full SEED channel name (Station, Network, Channel, and Location), and are now able to return event-associated waveforms from the NCSN waveform archive.

### EVT\_FAST

In order to provide Web access to the NCSN waveform before the SEED conversion and instrument response for

the NCSN has been completed, the NCEDC implemented *EVT\_FAST*, an interim email-based waveform request system similar to the *BREQ\_FAST* email request system. Users email *EVT\_FAST* requests to the NCEDC and request NCSN waveform data based on the NCSN event id. Initially the NCSN waveform data was converted to either SAC ASCII, SAC binary, or AH format, and placed in the anonymous ftp directory for retrieval by the users. *EVT\_FAST* event waveforms can now also be provided in MiniSEED format, and are now named with their SEED channel names.

## FISSURES

The *FISSURES* project developed from an initiative by IRIS to improve earth scientists' efficiency by developing a unified environment that can provide interactive or programmatic access to waveform data and the corresponding metadata for instrument response, as well as station and channel inventory information. *FISSURES* was developed using CORBA (Common Object Request Broker Architecture) as the architecture to implement a system-independent method for the exchange of this binary data. The IRIS DMC developed a series of services, referred to as the *Data Handling Interface (DHI)*, using the *FISSURES* architecture to provide waveform and metadata from the IRIS DMC.

The NCEDC has implemented the *FISSURES Data Handling Interface (DHI)* services at the NCEDC, which involves interfacing the DHI servers with the NCEDC database schema. These services interact with the NCEDC database and data storage system, and can deliver NCEDC channel metadata as well as waveforms using the *FISSURES* interfaces. We have separate *FISSURES DHI* waveform servers to serve archived and DART data stream. Our *FISSURES* servers are registered with the IRIS *FISSURES naming services*, which ensures that all *FISSURES* users have transparent access to data from the NCEDC.

## GSAC

Since 1997, the NCEDC has collaborated with UNAVCO and other members of the GPS community on the development of the *GPS Seamless Archive Centers (GSAC)* project. This project allows a user to access the most current version of GPS data and metadata from distributed archive locations. The NCEDC is participating at several levels in the *GSAC* project: as a primary provider of data collected from core BARD stations and USGS MP surveys, and as a wholesale collection point for other data collected in northern California. We helped to define database schema and file formats for the *GSAC* project, and have produced complete and incremental monumentation and data holdings files describing the data sets that are produced by the BARD project or archived at the NCEDC so that other members of the

*GSAC* community can provide up-to-date information about our holdings. Currently, the NCEDC is the primary provider for over 138,000 data files from over 1400 continuous and survey-mode monuments. The data holdings records for these data have been incorporated into the *GSAC* retailer system, which became publicly available in late 2002.

In addition, the NCEDC is archiving and distributing high-rate 1 Hz GPS data from 10 BARD stations in addition to the normally sampled 15 second or 30 second data. These high-rate data are currently available only to UCB and USGS/MP researchers as we develop the appropriate techniques for processing these data.

### 3.6.8 Acknowledgements

The NCEDC is a joint project of the BSL and the USGS Menlo Park and is funded primarily by the BSL and the USGS. Additional funding for the handling and archiving of the EarthScope PBO and SAFOD data is provided through subawards from the respective NSF EarthScope projects.

Doug Neuhauser is the manager of the NCEDC. Stephane Zuzlewski, Rick McKenzie, Mario Aranha, Nicolas Houlie, Bob Uhrhammer, and Peggy Hellweg of the BSL and David Oppenheimer, Hal Macbeth, and Fred Klein of the USGS Menlo Park contribute to the operation of the NCEDC. Doug Neuhauser, Peggy Hellweg and Stephane Zuzlewski contributed to the preparation of this section.

## 3.7. Data Acquisition and Quality Control

### 3.7.1 Introduction

Stations from the networks operated by the BSL transmit data continuously to the BSL facilities on the UC Berkeley campus for analysis and archival. In this chapter, we describe activities and facilities which pertain to the individual networks described in Sections 3.1., 3.3. and 3.4., including procedures for data acquisition and quality control, and sensor testing capabilities and procedures. Some of these activities are continuous from year to year and have been described in prior BSL annual reports. In this section, we describe changes or activities which are specific to 2006-2007.

### 3.7.2 Data Acquisition Facilities

Before 2005-2006, both the BSL staff monitoring routine data acquisition and the computers and facilities to acquire, process and archive the data were located in McCone Hall. Since 2006, the computers and telemetry equipment associated with data acquisition reside in the new campus computer facility at 2195 Hearst Avenue. This building was constructed to current “emergency grade” seismic codes, and is expected to be operational even after a  $M$  7 earthquake on the nearby Hayward Fault. The hardened campus computer facility within was designed with special attention for post-earthquake operations. The computer center contains state-of-the-art seismic bracing, UPS power and air conditioning with generator backup, and extensive security and equipment monitoring. With the move of many BSL and NCEDC operations servers to the campus computer center, the generator power and air conditioning resources in the BSL server room in 237 McCone better match our needs for the infrastructure remaining in McCone Hall. The BSL generator is maintained by Physical Plant Capital Services and was run without load twice monthly.

### 3.7.3 Data Acquisition

Central-site data acquisition for data from the BDSN/NHFN/MPBO networks is performed by two computer systems in the 2195 Hearst Avenue data center (Figure 3.24). These acquisition systems also collect data from the Parkfield-Hollister electromagnetic array and for the BARD network. A third system is used primarily for data exchange with the USNSN and transmits data to the USNSN from HOPS, CMB, SAO, WDC, HUMO, MOD, MCCM, and YBH. Data acquisition for the HRSN follows a more complicated path, as described in Section 3.4.. During the year, we also collected data from US-Array travelling array stations deployed in Northern and

Central California from the orb-server of the Anza Network Facility at the University of California San Diego.

The BSL uses the program `comserv` developed by Quanterra for central data acquisition. This program receives data from a remote Quanterra data logger, and redistributes the data to one or more `comserv` client programs. The `comserv` clients used by REDI include `datalog`, which writes the data to disk files for archival purposes, `cdafill`, which writes the data to the shared memory region for REDI analysis, and other programs such as the seismic alarm process, the DAC480 system, and the feed for the Memento Mori Web page (Figure 3.25).

The two computers performing data acquisition also serve as REDI processing systems and hold the databases now used by these systems for storing earthquake information. In order to facilitate REDI processing, each system maintains a shared memory region that contains the most recent 30 minutes of data for each channel used by the REDI analysis system. All REDI analysis routines first attempt to use data in the shared memory region, and will only revert to retrieving data from disk files if the requested data is unavailable in the shared memory region.

Each BDSN datalogger that uses frame relay telemetry is configured to enable data transmission simultaneously to two different computers over two different frame relay T1 circuits to UCB. However, the BSL normally actively enables and uses only one of these data streams from each station at any given time. The `comserv` client program `cs2m` receives data from a `comserv` and multicasts the data over a private ethernet. The program `mcast`, a modified version of Quanterra’s `comserv` program, receives the multicast data from `cs2m`, and provides a `comserv`-like interface to local `comserv` clients. This allows each REDI system to have a `comserv` server for every station, and each of the two systems has a complete copy of all waveform data.

We have extended the multicasting approach to handle data received from other networks such as the NCSN and UNR. These data are received by Earthworm data exchange programs, and are then converted to MiniSEED and multicast in the same manner as the BSL data. We use `mserv` on both REDI computers to receive the multicast data, and handle it in an identical fashion to the BSL MiniSEED data.

In 2006, the BSL established a real-time data feed of all BSL waveforms between the BSL acquisition systems and the NCEDC computers using the open source Freeorb software. This allows the NCEDC to provide near-real-time access to all BSL waveform data through the

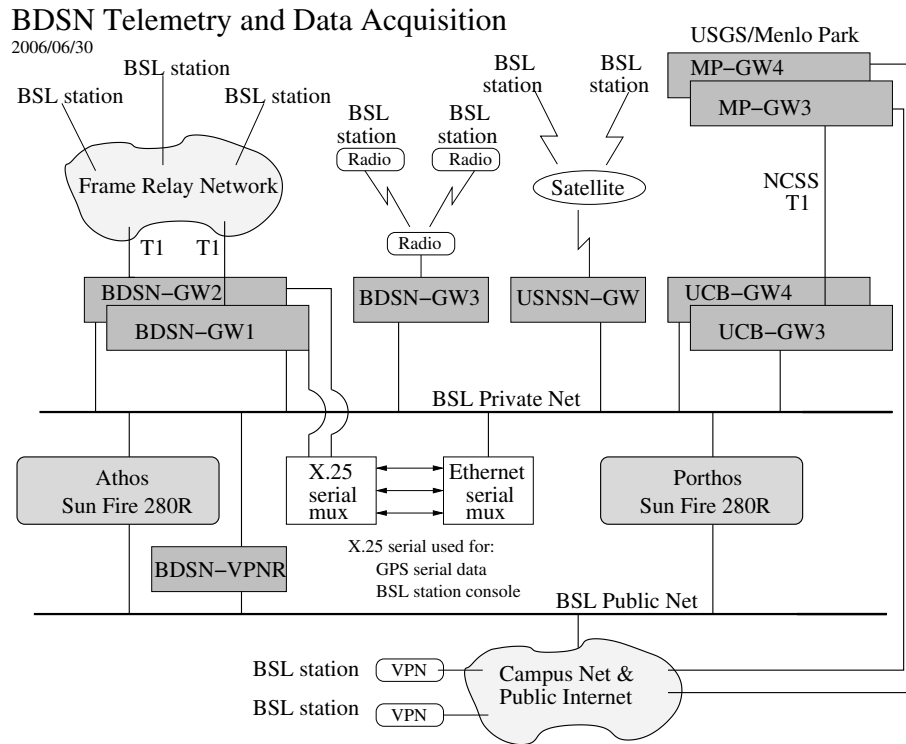


Figure 3.24: Data flow from the BDSN, NHFN, MPBO, HRSN, and BARD network into the BSL central processing facility.

NCEDC DART (Data Available in Real Time) system.

### 3.7.4 Seismic Noise Analysis

BSL seismic data are routinely monitored for state-of-health. An automated analysis is computed regularly to characterize the seismic noise level recorded by each broadband seismometer.

#### PSD Noise Analysis

The estimation of the Power Spectral Density (PSD) of the ground motion recorded at a seismic station, as documented in the 2000-2001 BSL annual report ([http://seismo.berkeley.edu/annual\\_report/ar00\\_01/](http://seismo.berkeley.edu/annual_report/ar00_01/)), provides an objective measure of background seismic noise characteristics over a wide range of frequencies. When used routinely, the PSD algorithm also provides an objective measure of seasonal and secular variation in the noise characteristics and aids in the early diagnoses of instrumental problems. A PSD estimation algorithm was developed in the early 1990's at the BSL for characterizing the background seismic noise and as a tool for quality control. As presently implemented, the algorithm sends the results via email to the engineering and some research staff members and generates a bar graph output which compares all the BDSN broadband stations by components. A summary of the results for

2006 is displayed in Figure 3.4. We also use the weekly PSD results to monitor trends in the noise level at each station. Figures showing the analysis for the current year are produced. These cumulative PSD plots are generated for each station and show the noise level in 5 frequency bands for the broadband channels. These plots make it easier to spot certain problems, such as failure of a sensor. In addition to the station-based plots, a summary plot for each channel is produced, comparing all stations. These figures are presented as part of a noise analysis of the BDSN on the WWW at <http://www.seismo.berkeley.edu/seismo/bdsn/psd/>.

#### PDF Noise Analysis

In addition to the PSD analysis developed by Bob Uhrhammer, the BSL has implemented the Ambient Noise Probability Density Function (PDF) analysis system developed by *McNamara and Buland* (2004). This system does its noise analysis over all the data of a given time period (week or year), including earthquakes, calibration pulses, and cultural noise. This is in contrast to Bob Uhrhammer's PSD analysis, which looks at only the quietest portion of data within a day or week. Pete Lombard of the BSL extended the McNamara code to cover a larger frequency range and support the many different types of sensors employed by the

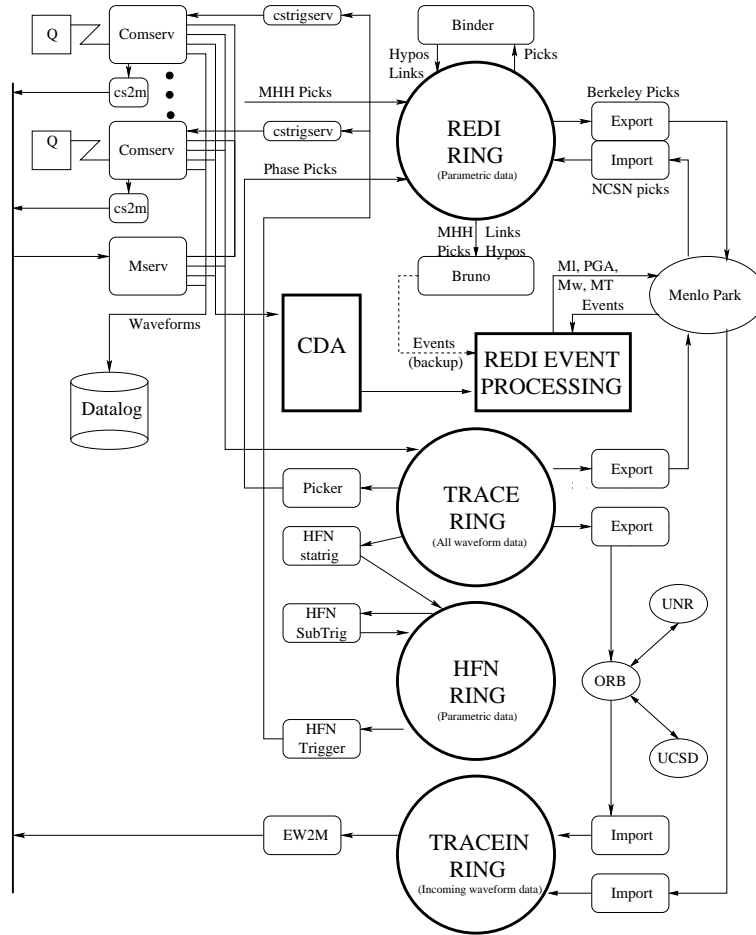


Figure 3.25: Dataflow in the REDI processing environment, showing waveform data coming in from the Quanterra data loggers (Q) into `comserv`. From `comserv`, data are logged to disk (via `datalog`), distributed to other computers (`mserv`), fed into the CDA for REDI processing, and spooled into a trace ring for export.

BSL. Besides the originally supported broadband sensors, our PDF analysis now includes surface and borehole accelerometers, strain meters, and electric and magnetic field sensors. These enhancements to the PDF code, plus a number of bug fixes, were provided back to the McNamara team for incorporation in their work. The results of the PDF analysis are presented on the web at <http://www.ncedc.org/ncedc/PDF/>. One difficulty with using these plots for review of station quality is that it is necessary to look at data from each component separately. To provide an overview, we have developed summary figures for all components in two spectral bands, 30 - 60 s and 0.125 - 0.25 s. Figure 3.26 shows these overviews for 2006. As the processing takes place shortly after the data arrives at the datacenter, data gaps may be present (white areas) in these plots. Most of these gaps have been filled by retrieving data from the stations.

### 3.7.5 Sensor Testing Facility

The BSL had set up an Instrumentation Test Facility in the Byerly Seismographic Vault in order to systematically determine and compare the characteristics of up to eight sensors at a time. The test equipment consists of an eight-channel Quanterra Q4120 high-resolution data logger and a custom interconnect panel that provides isolated power and preamplification, when required, to facilitate the connection and routing of signals from the sensors to the data logger with shielded signal lines. A GPS rebroadcaster has also been installed, so that all data loggers in the Byerly vault operate on the same time base. Upon acquisition of data at up to 200 samples-per-second (sps) from the instruments under test, PSD analysis, coherence analysis and additional ad hoc analysis algorithms are used to characterize and compare the performance of each sensor. Tilt tests and seismic signals with a sufficient signal level above the background

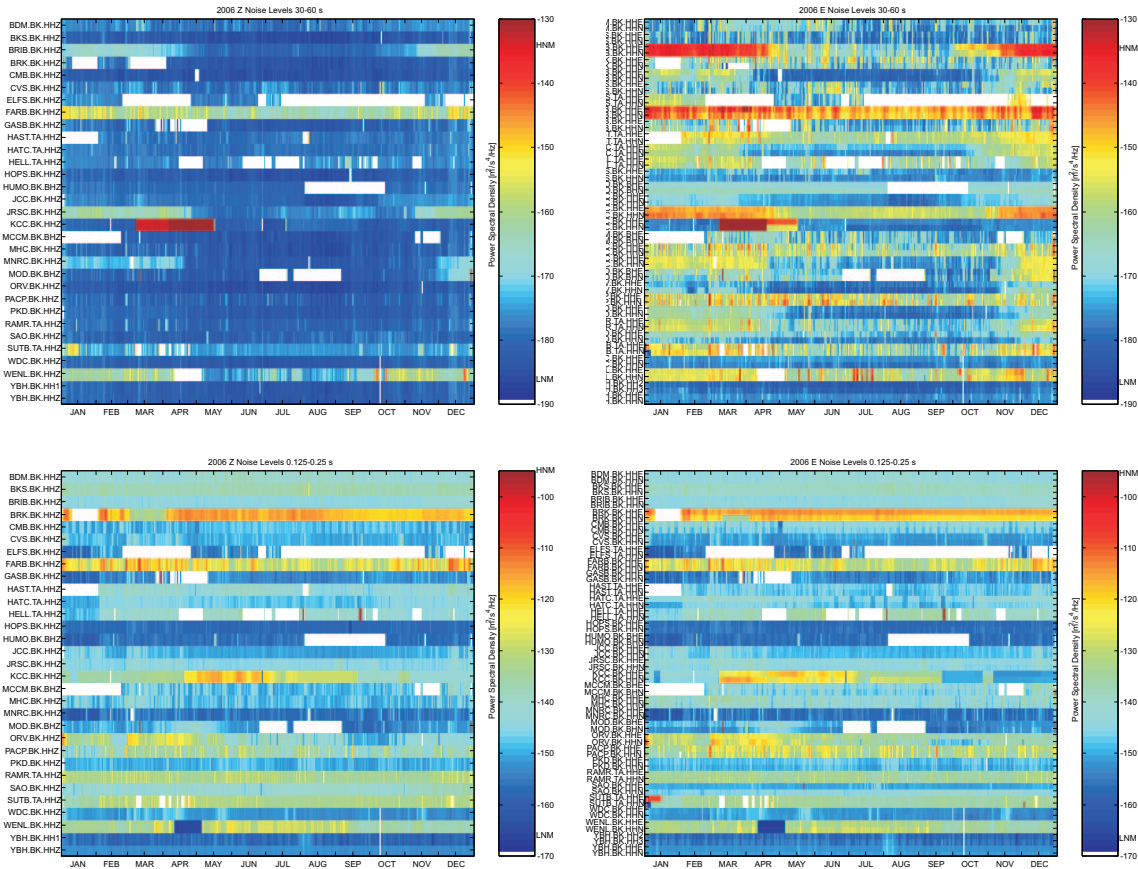


Figure 3.26: Noise overview taken from the PDF analysis for 2006 for BDSN stations. The top row shows daily minimum noise levels for the vertical (left) and horizontal (right) stations in the band 30 - 60 s. The lower row shows corresponding values in the band 0.125 - 0.25 s. White areas indicate times when realtime data are missing. Most such gaps have been filled in the datacenter archive by retrieving the data from the datalogger. The high noise level for KCC in the spring shows when water is running past the seismometers through the tunnel.

seismic noise are also used to verify the absolute calibration of the sensors. A simple vertical shake table is used to assess the linearity of a seismic sensor. The sensor testing facility of the BSL is described in detail in the BSL 2001-2002 Annual Report (available on-line at <http://www.seismo.berkeley.edu/>).

### 3.7.6 STS-1 Electronics Development

The STS-1 seismometer is currently the principal very broad-band (VBB) seismometer used in global or regional seismic networks operated by members of the Federation of Digital Broad-Band Seismograph Networks (FDSN). It is widely viewed as the finest VBB sensor in the world. Unfortunately, many of the STS-1's, which were manufactured and installed 10-20 years ago, are encountering both operational failures and age-related degradation. This problem is exacerbated by the fact that sensors are

no longer being produced or supported by the original manufacturer, G. Streckeisen AG. In a first step towards assuring continued high quality of VBB data for decades to come, we have developed and tested new electronics and methods for mechanical repair for the STS-1 very broadband seismometer. A primary goal of this effort was to develop a fully-tested, modern electronics module that will be a drop-in replacement for the original electronics. This new electronics design addresses environmental packaging problems that have led to operational errors and failures in the existing instruments. This effort also provided the opportunity to implement a set of electronic improvements that will make the installation and operation of the sensors more efficient. Metrozet developed the first prototype new electronics for the STS-1, while the BSL engineering staff prepared a test-bed at the Byerly Vault (BKS) and developed the capability to simultaneously test 6-8 STS-1 components. BSL staff then tested

and analysed results from successive versions of the electronics.

The first generation prototype electronics did not include centering or calibration functionality. The second generation prototype included remote centering functionality as well as calibration functions. After some observations and refinements, this generation of electronics was operated on two seismometers concurrently and successfully run through the swept and stepped calibration functions on four seismometers. During this final phase, the Metrozet electronics included the ability to initiate and operate the calibrations via a network (ethernet) connection. Most of the calibration testing was performed remotely from Metrozet's Southern California office over the BSL network. Metrozet was able to remotely log into the Berkeley network, establish a connection to the test bed in the Byerly seismic vault, and initiate control of the seismometer, including remote centering and calibration functions.

In the final stage of the project, once the BSL tests were completed and the development appeared complete and satisfactory, the new electronics were finally tested at the Albuquerque Seismological Laboratory's seismic vault, which is located in a quieter environment than BKS. The new electronics are currently being field tested at the BDSN broadband station HOPS.

### Data Logger Calibration

Prior to the tests on the new STS-1 electronics, the Instrumentation Test Facility eight-channel Quanterra Q4120 data logger (serial number 103064) was operated in the BDSN for 8 years. In July 2004, it was repaired, and the calibration was checked by the factory. At the beginning of these tests, the sensitivity, noise floor and crosstalk of the data logger were checked using a reference signal applied first simultaneously and then sequentially to all channels, with the non-driven channels terminated. The relative sensitivities of the data logger channels were checked by applying a high-level ( 19.8 V peak-to-peak) 1 Hz square wave signal simultaneously to all channels. The signal level on each channel was measured and the relative signal levels were compared to the sensitivities on the factory calibration sheet. The results are given in Table 3.15. The sensitivities of four of the channels have not changed by more than  $\pm 0.01\%$  from the factory calibration values. Of the remaining four channels, three changed by less than  $\pm 0.3\%$  and the fourth changed by  $-0.8\%$ .

The Q4120 data logger contains two 4-channel digitizer modules (HH1-HH4 and HH5-HH8). The inter-channel cross-talk was checked by connecting each of the channels in sequence with the high amplitude (20 V P-P) 1 Hz square-wave signal while terminating the other seven channels. The observed cross-talk signal on all channels is below the  $2.38 \mu\text{V}$  quantization level of the Q4120 data

logger. The cross-talk is thus more than 138.5 dB below the drive signal level. A check of the phase coherence between channels was performed by driving channel HH1 with a 20 V P-P 1 Hz square wave while terminating channels HH2-HH8 with 1k resistors. Spectral phase coherence analysis of the signal between selected channels (HH1-HH2, HH3-HH4, HH5-HH6, and HH7-HH8) shows that there is an inter-channel coherent phase comb present with peaks at 1 Hz and its odd harmonics, on channels within the same digitizer module, when HH1 is driven. At the same time, channels HH5-HH8, which are on a different digitizer module, exhibit no significant inter-channel phase coherence structure.

### Seismometer Acquisition and Alignment

After the data logger was calibrated, it was necessary to establish a stable seismometer subsystem test bed. Nine different STS1 instruments (six horizontal, and three vertical instruments) from a variety of sources were used. These sensors came from among the available BDSN sensors, from surplus sensors on loan from the Gräfenberg Array and from IGPP, UC San Diego. The instruments were set up and leveled, and the outputs to the Q4120 data logger were compared quantitatively. The sensors were systematically inspected and checked for nominal operation, and the ones that performed the best were selected for the testing procedures and installed in the test bed. The horizontal instruments were aligned along a single axis, toward the East, enabling coherency comparisons and evaluations. Misalignment of less than one degree across the six horizontal instruments caused unacceptable variances in signal coherency. It took a week to resolve these differences by rotating the individual instruments. Alignment of the vertical instruments was much easier. Only after all alignment incoherences were resolved were the new Metrozet electronics evaluated against the original Streckeisen factory electronics. The broadband STS-1 sensors listed in Table 3.16 were utilized during the testing procedures.

### Sensor Testing Timeline

The performance testing at BSL occurred in stages, with most work being performed between July 2006 and January 2007. The calibration of the data logger took over three weeks due to a number of back-to-back system failures, including the power supply, and dead data channels. During three weeks in August 2006, the initial six STS-1's (four horizontal, two vertical) were set-up as near identical (baseplates, cables, bell jars etc.) as possible.

It was during this portion of the testing that sensor to sensor coherency issues arose. The vertical sensors showed high levels of coherency, while the slightest misalignment of the horizontal instruments caused unacceptable incoherence in the horizontal instruments. All

Channel	Factory DU/V	P-P counts	Est P-P volts	Deviation %
1	403640	8012274	19.850050	-0.29
2	435388	8689678	19.958469	-0.83
3	437149	8651000	19.789591	+0.01
4	422829	8365690	19.785043	+0.01
5	420706	8314894	19.764144	+0.14
6	430613	8548404	19.851709	-0.30
7	438570	8680904	19.793657	-0.01
8	434817	8600236	19.778978	+0.01

Table 3.15: Quanterra Q4120 Calibration Check. Deviation is relative to the median inferred drive level of 19.791624 Volts.

Serial Number	Component	Source	Note
9	V	GRF	1
13	V	GRF	1
14	H	GRF	1
18	H	GRF	1
unknown	V	GRF	1
18718	H	IGPP/UCSD	2, 3
29201	H	BSL	4, 7
29212	H	BSL	4, 7
38502	V	BSL	3, 4, 7
38505	V	BKS Reference	3, 5
39010	H	BSL	4
39039	H	IGPP/UCSD	2, 3, 6, 7
48530	H	BSL	3, 4
48531	H	BKS Reference	3, 5
109112	V	BSL	4, 7
109124	V	BSL	4, 7

Table 3.16: STS-1 sensors. Notes: 1 - Gräfenberg (GRF) sent five seismometers total; three vertical, and two horizontal sensors. These BB instruments were some of the earliest produced by Streckeisen. While the sensors themselves are nearly identical to the later VBB instrument Streckeisen produced, the connector and electronics are sufficiently different that these were not used as part of the response test bed. These instruments were extremely useful in evaluation of the hinges, manufacture and assembly of these instruments. Gräfenberg also provided shielding, vacuum enclosures, and warpless base plates that were used. 2 - IGPP/UCSD sent two horizontal seismometers. 3 - These sensors were shipped from Streckeisen as 20 sec BB seismometers and later upgraded to 360 sec VBB seismometers. 4 - BSL provided STS-1 seismometers. 5 - These co-sited BKS STS-1's in the Byerly Seismic Vault are used as reference. 6 - Sensor was shipped with a mismatched Streckeisen electronics box (s/n 6824). 7 - These STS-1's were ultimately selected and used in the test bed.

possible causes for the incoherence were investigated and documented during the next 3-4 weeks. Possible causes included system timing, grounding, vacuum levels, and the seismometers themselves. Over a period of a week, the horizontal instruments were rotated slightly until the coherence began to improve in a predictable fashion.

Thus, seven weeks after BSL began to work on this project, the first meaningful tests of the Metrozet electronics began. Each set of electronics was paired with each of the seismometers in succession, with the pairing lasting at least twenty four hours. Approximately three

weeks after this initial rotation through the seismometers was completed, Metrozet produced the second set of prototype electronics. Progress continued in similar two to three week increments until January of 2007, at which time the new electronics and calibration systems had been paired with and evaluated on seven different STS1 seismometers.

### Coherence and Power Spectral Density

An algorithm "scn\_psd" to calculate the signal Power Spectral Density (PSD), the noise PSD and the coherence

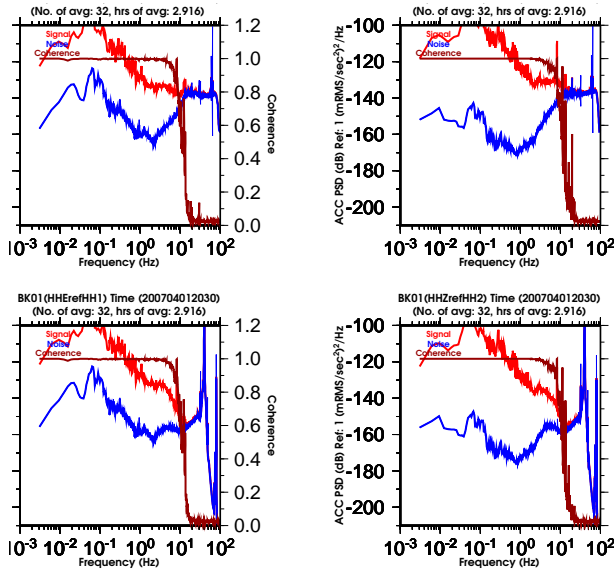


Figure 3.27: Results for two vertical component STS-1's (HHZ and HH2) and two horizontal component STS-1's (HHE and HH1) in the presence of a large seismic signal. The event is a Me 8.1 earthquake which occurred 87.9 degrees WSW of Berkeley at 20:39 UT on 2007/04/01. Shown are the signal PSD (red), the noise PSD (blue) and the coherence (brown) for each sensor. In all tests, the corresponding BKS STS-1's are used as the reference signals in the analysis. In the presence of large seismic signals, the coherence is typically close to unity at all frequencies below the 5 Hz high-frequency corner of the BKS reference STS-1's. Note the relatively high noise PSD level on the horizontal components in the vicinity of 0.1 Hz. This is due to a slight misalignment of the sensitive axes of the horizontal components. Several time consuming trial and error iterations in aligning the horizontal components are required to lower the horizontal component noise PSD. Three continuous hours of 200 Hz data are used by the `scn_psd` algorithm. `scn_psd` parses the data into 32 non-overlapping samples, applies a hanning window, corrects for the effects of the hanning window, scales the data to ground motion, calculates the FFT, and stores the resulting complex spectral values for each sample. At each frequency, the RMS signal PSD is calculated from the average of the complex spectral values, coherence is calculated from the averaged complex spectral cross product, and the RMS noise PSD is then determined from the product of the signal PSD and (1 - coherence). The method is described in detail in Gardner (1992).

between sensors has been developed as a tool for quantifying the performance differences between the seismic sensors under test. Two sample results of the algorithm are shown. Figure 3.27 shows the results for four seis-

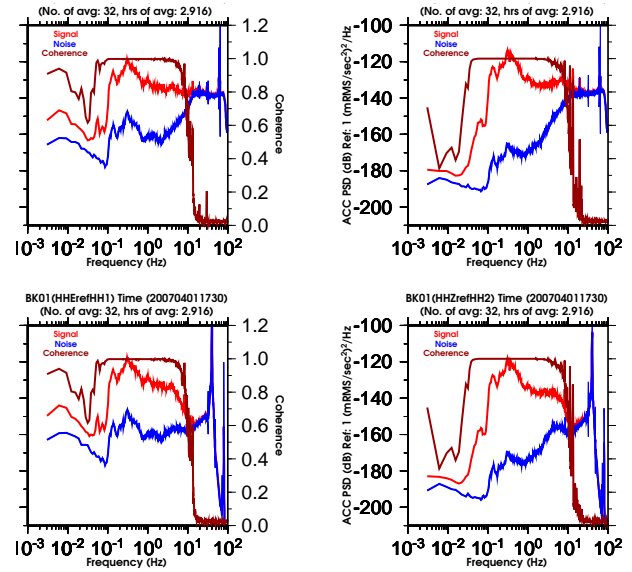


Figure 3.28: Results for the STS-1's in the presence of background noise. The traces are the same as in Figure 3.27. The lower and upper frequencies at which the coherence degrades from near unity varies among the sensors. Coherence bandwidth is a measure of the performance of the sensors.

ometers in the case of a large seismic event and Figure 3.28 shows the results for four seismometers in the case of background noise.

### Seismometer Frequency Response

Algorithms were developed to determine the free period ( $T_s$ ) and fraction of critical damping ( $h_s$ ) and to determine the high-frequency corner ( $f_g$ ) and fraction of critical damping ( $h_g$ ) parameters by measuring the frequency response of the seismometer to known stimuli. The free period ( $T_s$ ) and fraction of critical damping ( $h_s$ ), which describe the low-frequency response, were determined via a grid search for the maximum variance reduction between the observed response and the theoretical time series response to a 40-1100 second period swept sine wave. The high-frequency corner ( $f_g$ ) and fraction of critical damping ( $h_g$ ), which describe the high-frequency response, were determined via a grid search for the maximum variance reduction between the observed response and the theoretical phase response to a 0.5-40 Hz stepped sine wave. Both of these stimuli are generated by the Metrozet E300 electronics as well as output to the STS-1 calibration coils, and they can be remotely invoked. Figure 3.29 shows an example of the observed and theoretical time series response to the swept sine wave stimulus, and Figure 3.30 shows an example of the observed and theoretical phase response to the stepped sine wave stimulus.

Comp	S/N	Streckeisen BRB V/(m/s)	Streckeisen LP V/(m/s <sup>2</sup> )	Metrozet BRB V/(m/s)	Metrozet LP V/(m/s <sup>2</sup> )	Percent Change
Z	109114	2452	83.4	2386	80.5	-2.7
N	29219	2284	77.4	1984	66.9	-13.1
E	29215	2304	78.0	1993	67.0	-13.5

Table 3.17: Comparison of the sensitivities of the HOPS STS-1's with Streckeisen and with Metrozet electronics. The Streckeisen sensitivities were obtained from the factory calibration sheets supplied with each seismometer. The Metrozet sensitivities were calculated using the STS-1 Calibration Software Applet supplied by Metrozet.

Comp	$T_s$	$h_s$	$f_g$	$h_g$	C
Z	360.08	0.6768	15.00	0.371	0.00939
N	362.93	0.6889	16.28	0.328	0.00909
E	388.37	0.9920	16.29	0.343	0.00844

Table 3.18: HOPS STS-1 calibration results.

### Field Testing at BDSN Station Hopland (HOPS)

On June 7, 2007, a Metrozet STS-1-E300-10-005 electronics box was installed in place of the Streckeisen factory supplied electronics boxes on the three STS-1 broadband seismometers operating at HOPS. As a result of this change, the flat pass band sensitivities of the STS-1 BRB and LP outputs changed as shown in Table 3.17.

As described in the previous section, the frequency responses of the three STS-1 seismometers with Metrozet E300 electronics were determined from their measured responses to swept sine and stepped sine stimuli. The results are listed in Table 3.18.

The constant "C" in Table 3.18 is an empirically derived scaling factor which scales the stimulus signal so that the calculated times series best agrees with the observed time series in a least-squares sense. "C" is proportional to the product of the calibration coil generator constant, the flat passband velocity sensitivity of the seismometer and the sensitivity of the data logger. This and other tests allowed the development of recommendations for the use of the new remote calibration procedures provided with the Metrozet E300 electronics.

### Conclusions

The coherence analysis and the calibration analysis results are evidence that the Metrozet prototype E300 STS-1 electronics are working and that they can successfully replace the original Streckeisen electronics boxes. The new electronics also has the added advantages that it is web accessible and that it has built-in step and sinusoidal calibration stimuli which can be invoked remotely. Another advantage of the new electronics is that the high frequency corner is nominally 15 Hz while the Streckeisen high-frequency corner is 10 Hz.

### 3.7.7 Acknowledgements

Doug Neuhauser, Bob Uhrhammer, Peggy Hellweg, Pete Lombard, Rick McKenzie and Cyndy Bresloff are involved in the data acquisition and quality control of BDSN/NHFN/MBPO data. Development of the sensor test facility and analysis system was a collaborative effort of Bob Uhrhammer, Tom McEvelly, John Friday, and Bill Karavas. IRIS and DTRA provided, in part, funding for and/or incentive to set up and operate the facility, and we thank them for their support. Bob Uhrhammer, Peggy Hellweg, Pete Lombard, Doug Neuhauser, and Barbara Romanowicz contributed to the preparation of this chapter. The STS-1 project is funded by the NSF through the IRIS/GSN program (IRIS Subaward Agreement number 388). This is a collaborative project with Tom VanZandt of Metrozet, LLC (Redondo Beach, CA).

### 3.7.8 References

- Ekström, G. and M. Nettles, <http://www.seismology.harvard.edu/~ekstrom/Projects/WQC.html>, 2005.
- Gardner, W. A., A unifying view of coherence in signal processing, *Signal Processing*, 29, p. 113-140, 1992.
- Ingate, S. et al, Workshop Report from Broadband Seismometer Workshop, Lake Tahoe, CA, <http://www.iris.edu/stations/seisWorkshop04/report.htm>, 2004.
- McNamara, D. and R. Buland, Ambient Noise Levels in the Continental United States *Bull. Seism. Soc. Am.*, 94, 4, 2004.
- Scherbaum, Frank. Of Poles and Zeros: Fundamentals in Digital Seismology, Volume 15 of Modern Approaches in Geophysics, G. Nolet, Managing Editor, Kluwer Academic Press, Dordrecht, xi + 257 pp., 1996.
- Tapley, W. C. and J. E. Tull, SAC - Seismic Analysis

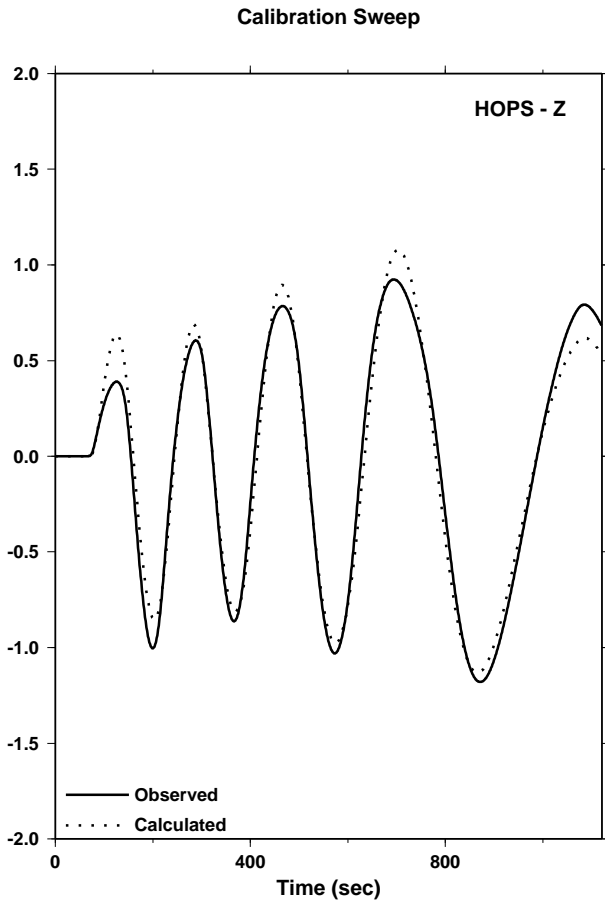


Figure 3.29: Plot of the HOPS STS-1 vertical seismometer observed time series response (solid line) and the corresponding theoretical time series response (dashed line). The best fitting theoretical response was determined via an adaptive migrating grid search to find the  $T_s$  and  $h_s$  which maximizes the variance reduction. The best fit was obtained for  $T_s = 360.08$  seconds and  $h_s = 0.6768$  critical.

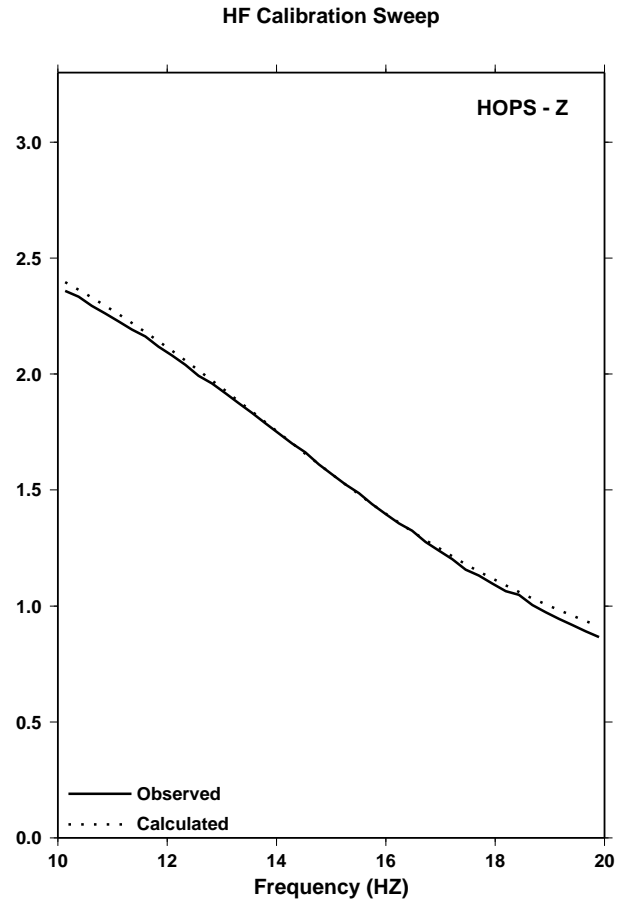


Figure 3.30: Plot of the HOPS STS-1 vertical seismometer observed phase response (solid line) and the corresponding theoretical phase response (dashed line). The best fitting theoretical response was determined via an adaptive migrating grid search to find the  $f_g$  and  $h_g$  which maximizes the variance reduction. The best fit was obtained for  $f_g = 14.998$  Hz and  $h_g = 0.371$  critical.

Code: Users Manual, *Lawrence Livermore National Laboratory*, Revision 4, 388 pp., March 20, 1992.

Wielandt, E. and G. Streckeisen, The leaf spring seismometer: design and performance, *Bull. Seis. Soc. Am.*, 72, 2349-2367, 1982.

Wielandt, E. and Steim, J. M., A digital very broad band seismograph, *Annales Geophysicae*, 4 B(3), 227-232, 1986.

## 3.8. Northern California Earthquake Monitoring

### 3.8.1 Introduction

Routine analysis of the data produced by BSL networks begins as the waveforms are acquired by computers at UC Berkeley, and ranges from automatic processing for earthquake response to analyst review for earthquake catalogs and quality control.

Starting in the mid 1990s, the BSL invested in the development of the hardware and software necessary for an automated earthquake notification system (*Gee et al.*, 1996; 2003a) called the Rapid Earthquake Data Integration (REDI) project. This system provides rapid determination of earthquake parameters: near real-time locations and magnitudes of northern and central California earthquakes, estimates of the rupture characteristics and the distribution of ground shaking following significant earthquakes, and tools for the rapid assessment of damage and estimation of loss. In 1996, the BSL and USGS began collaborating on a joint notification system for northern and central California earthquakes. This system merges the programs in Menlo Park and Berkeley into a single earthquake notification system, combining data from the NCSN and the BDSN. Today, the joint BSL and USGS system forms the Northern California Earthquake Management Center (NCEMC) of the California Integrated Seismic Network (Section 3.2.), and development is proceeding on the next generation of earthquake reporting software based on Southern California’s Trinet system.

With partial support from the USGS, the BSL has also embarked on the development and assessment of a system to warn of imminent ground shaking in the seconds after an earthquake has initiated but before strong motion begins at sites that may be damaged (Research Study 2.17.).

### 3.8.2 Northern California Earthquake Management Center

The details of the Northern California processing system and the REDI project have been described in previous annual reports. In this section, we describe how the Northern California Earthquake Management Center fits within the CISN system.

Figure 3.9 in Section 3.2. illustrates the NCEMC as part of the CISN communications ring. The NCEMC is a distributed center, with elements in Berkeley and in Menlo Park. The 35 mile separation between these two centers is in sharp contrast to the Southern California Earthquake Management Center, where the USGS Pasadena is located across the street from the Caltech Seismological Laboratory. As described in Section 3.2., the CISN partners are connected by a dedicated T1 communications link, with the capability of falling back to the

Internet. In addition to the CISN ring, the BSL and the USGS Menlo Park have a second dedicated communications link to provide bandwidth for shipping waveform data and other information between their processing systems.

Figure 3.31 provides more detail on the current system at the NCEMC. At present, two Earthworm-Earlybird systems in Menlo Park feed two “standard” REDI processing systems at UC Berkeley. One of these systems is the production or paging system; the other is set up as a hot backup. The second system is frequently used to test new software developments before migrating them to the production environment. The Earthworm-Earlybird-REDI systems perform standard detection and location, and estimate  $M_d$ ,  $M_L$ , and  $M_w$ , as well as processing ground motion data. The computation of ShakeMaps is also performed on two systems, one in Menlo Park and one in Berkeley. An additional system at the BSL performs finite-fault processing and computes higher level ShakeMaps.

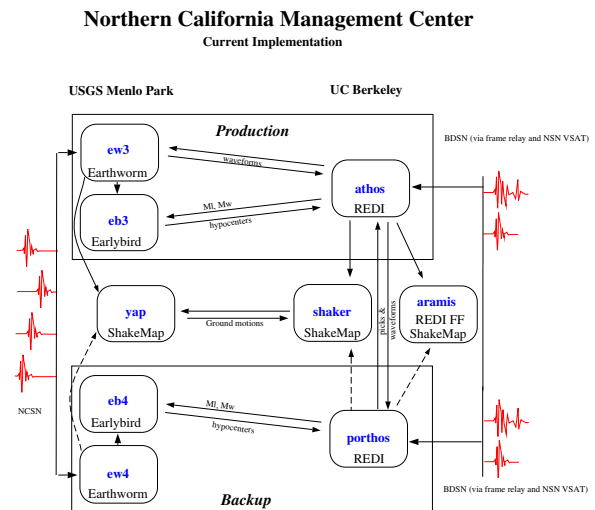


Figure 3.31: Detailed view of the current Northern California processing system, showing the two Earthworm-Earlybird-REDI systems, the two ShakeMap systems, and the finite-fault system.

The dense network and Earthworm-Earlybird processing environment of the NCSN provides rapid and accurate earthquake locations, low magnitude detection thresholds, and first-motion mechanisms for small quakes. The high dynamic range data loggers, digital telemetry, and broadband and strong-motion sensors of the BDSN along with the REDI analysis software provide

reliable magnitude determination, moment tensor estimation, peak ground motions, and source rupture characteristics. Robust preliminary hypocenters are available about 25 seconds after the origin time, while preliminary coda magnitudes follow within 2-4 minutes. Estimates of local magnitude are generally available 30-120 seconds later, and other parameters, such as the peak ground acceleration and moment magnitude, follow within 1-4 minutes (Figure 3.32).

Earthquake information from the joint notification system is distributed by pager/cellphone, e-mail, and the WWW. The first two mechanisms “push” the information to recipients, while the current Web interface requires interested parties to actively seek the information. Consequently, paging and, to a lesser extent, e-mail are the preferred methods for emergency response notification. The *recenteqs* site has enjoyed enormous popularity since its introduction and provides a valuable resource for information whose bandwidth exceeds the limits of wireless systems and for access to information which is useful not only in the seconds immediately after an earthquake, but in the following hours and days as well.

### 3.8.3 2006-2007 Activities

#### System Development

As part of ongoing efforts to improve the monitoring systems in northern California and to unify the processing systems within the CISN, the BSL and the USGS Menlo Park made progress in the development of the next generation of the northern California joint notification system of the Northern California Seismic System (NCSS). Figure 3.31 illustrates the current organization of the system. Although this approach functions reasonably well, there are potential problems associated with the separation of critical system elements by ~35 miles of San Francisco Bay.

Since FY01/02 we have been working to design and implement the software for Northern California operations so that identical, complete systems operate independently at the USGS and UC Berkeley. When CISN started, independently developed systems for monitoring earthquakes operated in Southern and Northern California, Trinet and Earthworm/REDI, respectively. Each of these systems has its strengths and weaknesses, and a choice had to be made. The current design for the new Northern California system draws strongly on the development of TriNet in Southern California (Figure 3.33), with modifications to allow for local differences (such as very different forms of data acquisition and variability in network distribution). In addition, the BSL and the USGS want to minimize use of proprietary software in the system. One exception is the database program. As part of the development of the Northern California Earthquake Data Center, the USGS and BSL have worked extensively with Oracle databases, and extending this to

the real-time system is not viewed as a major issue.

During the last few years, BSL staff members, particularly Pete Lombard, have become extremely familiar with portions of the TriNet software. We have continued to adapt the software for Northern California, making adjustments and modifications along the way. For example, Pete Lombard has adapted the TriNet magnitude module to northern California, where it is now running on a test system. Pete made a number of suggestions on how to improve the performance of the magnitude module and has worked closely with Caltech and the USGS/Pasadena on modifications.

The BSL and the USGS Menlo Park have implemented a system to exchange “reduced amplitude timeseries.” One of the important innovations of the TriNet software development is the concept of continuous processing (Kanamori *et al.*, 1999). Waveform data are constantly processed to produce Wood Anderson synthetic amplitudes and peak ground motions. A program called *rad* produces a reduced timeseries, sampled every 5 secs, and stores it in a memory area called an “Amplitude Data Area” or ADA. Other modules can access the ADA to retrieve amplitudes to calculate magnitude and ShakeMaps as needed. The BSL and the USGS Menlo Park have collaborated to establish the tools for ADA-based exchange. As part of the software development in northern California, a number of modules have been developed.

#### Event Review with Jiggle

CUSP was finally retired as the event review system in the NCEMC in late November, 2006. CUSP was initially developed in Southern California during the late 1970s - early 1980s and has been used to time earthquakes for a number of years in Northern California. However, the CUSP system became increasingly outdated, as it relied on obsolete hardware. The primary responsibility for the programming and development necessary has rested on BSL staff. They implemented the *RequestCardGenerator* (a module that decides which channels to archive, given a particular earthquake), a waveform archiving module, and *Jiggle* (the earthquake timing interface) within the Northern California system. The entry of all parameteric earthquake data from real-time processing into the Oracle database and the preparation of station and instrument metadata for insertion into the database were important prerequisites for the transition. The NCEMC and SCMC collaborated on modifications to *Jiggle* for use in Northern California, such as the computation of  $M_d$ .

#### $M_L$ and $M_w$

The REDI system has routinely produced automatic estimates of moment magnitude ( $M_w$ ) for many years. However, wary of complications caused by the publication of multiple magnitudes, these estimates were not

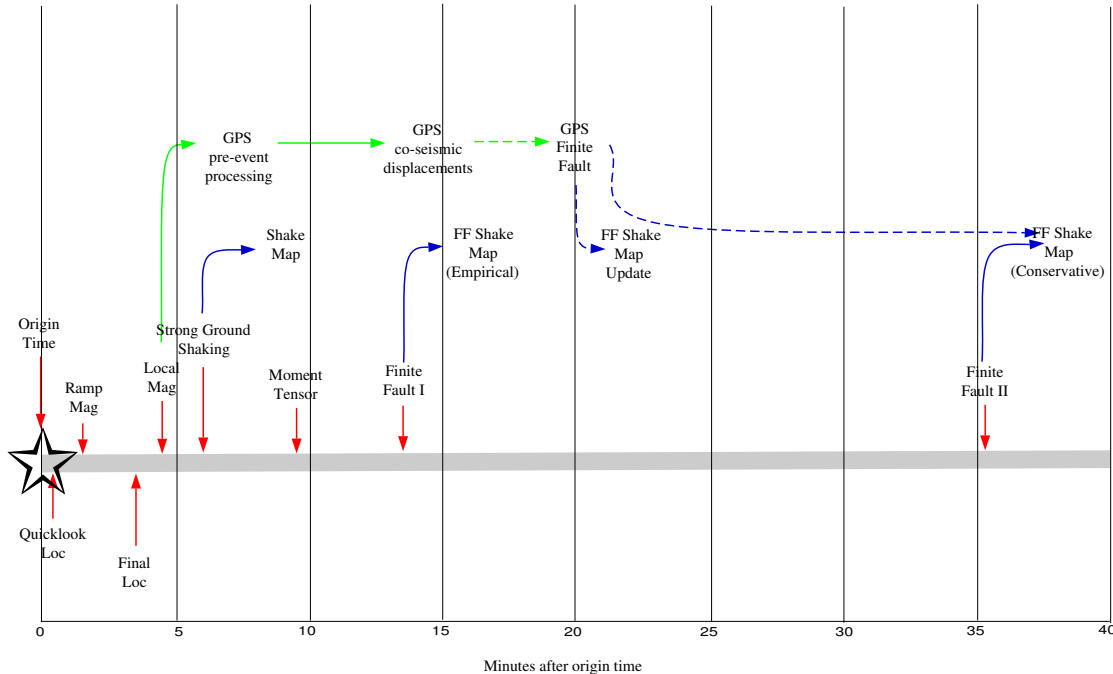


Figure 3.32: Illustration of the current (solid lines) and planned/proposed (dotted lines) development of real-time processing in northern California. The Finite Fault I and II are fully implemented within the REDI system at UC Berkeley and are integrated with ShakeMap. The resulting maps are still being evaluated and are not currently available to the public.

routinely used as the “official” magnitude until after the 05/14/2002 Gilroy earthquake ( $M_w$  4.9,  $M_L$  5.1). Since then, solutions that meet a minimum quality criterion are automatically reported (a variance reduction of 40% or higher). This criterion appears to work very well and screens out events contaminated by teleseisms. Over the last few years, nearly all events over 4.5 have met this criterion, as have a number of events in the  $M_{3.5}$ -4.5 range. As part of the effort to establish a statewide magnitude reporting hierarchy, we have looked more closely at the estimates of  $M_w$  (Gee *et al.*, 2003b; 2004) and the comparison between  $M_w$  and  $M_L$ .

Two methods of determining regional moment tensor (RMT) solutions were originally part of the REDI system - the complete waveform modeling technique (CW) of Dreger and Romanowicz (1994) and the surface wave inversion (SW) of Romanowicz *et al.* (1993). In FY05/06, processing for the SW algorithm was discontinued, however CW moment tensors continue to be calculated, reviewed and reported. Comparison between the results of the CW method and other regional moment tensor studies in northern California and the western United States show excellent agreement in the estimate of seismic moment and  $M_w$ .

As we transition toward statewide reporting of earthquake information, a comparison of magnitudes calculated for Southern and Northern California becomes important. We have collected a set of events recorded well by digital broadband and strong motion stations of the Northern California (NC), Berkeley (BK) and Southern California (CI) networks and are assessing the computation of local magnitude for each station. Research Study 2.13. reports on these activities.

### 3.8.4 Routine Earthquake Analysis

In fiscal year 2006-2007, more than 23,000 earthquakes were detected and located by the automatic systems in northern California. This compares with over 30,000 in 2005-2006 and 38,800 in 2004-2005. Many of the large number of events in 2004-2005 are aftershocks of the 2004 Parkfield earthquake. The number of events continues to remain high, because we now receive and process data from a network of seismometers in the Geysers, a region with a high level of small magnitude seismicity. Of the more than 23,000 events, over 208 had preliminary magnitudes of three or greater. Thirty one events had  $M_L$  greater than 4. The largest event recorded by the system occurred on 26 February 2007 with  $M_w$  5.4. This earth-

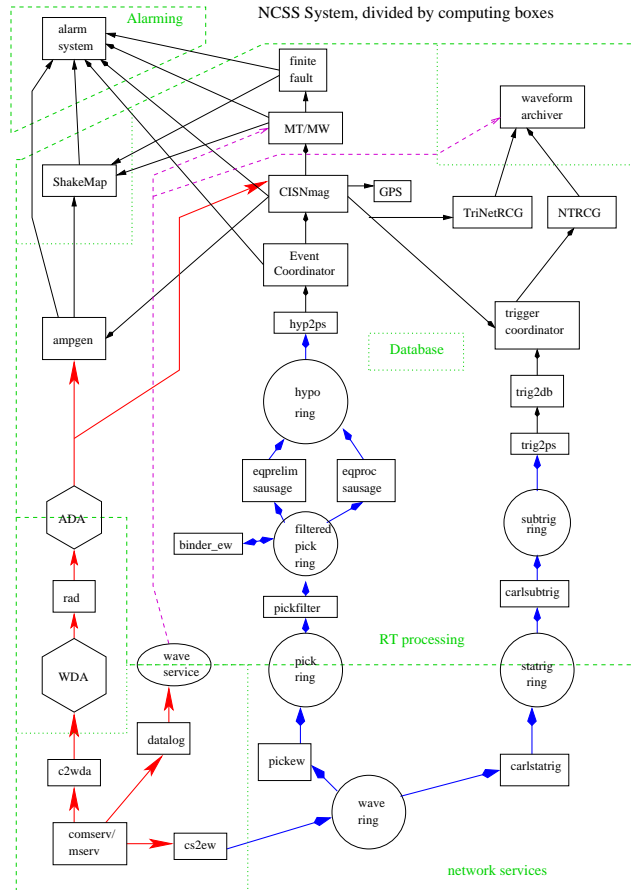


Figure 3.33: Schematic diagram of the planned NCSS system. The design combines elements of the Earthworm, TriNet, and REDI systems

quake, as well as the five events with the next largest magnitudes, occurred off the coast of northernmost California.

As described in the 2003-2004 Annual Report, the BSL staff are no longer reading BDSN records for local and regional earthquakes (as of March 2004). This decision was in part intended to reduce duplication of effort between Berkeley and Menlo Park.

The BSL continues to focus on the unique contributions that can be made from the broadband network. From July 2006 through June 2007, BSL analysts reviewed more than 40 earthquakes in northern California and adjoining areas of magnitude 3.2 and higher. Reviewed moment tensor solutions were obtained for 37 of these events (through 6/30/2007). Figure 3.34 and Table 3.19 display the locations of earthquakes in the BSL moment tensor catalog and their mechanisms.

### Seismic Background Noise PSD in Northern and Central California

The density and distribution of broadband seismic stations located in Northern and Central California increased during the past few years, with two new BK stations and additional broadband seismic stations installed as the USArray transportable array completes its station coverage in the region. One design goal of the transportable network has been to complement the existing BDSN broadband stations and cover the region with an average interstation spacing of  $\sim 70$  km. We have been using data from the USArray TA stations and monitoring station quality through the analysis of the seismic background noise PSD level observed at the transportable stations. This is, in part, so that we can choose the best sites to continue occupying after the transportable array moves out of the region, in order to improve the coverage of the BDSN network. Based on this analysis as well as criteria such as ownership and access to power and

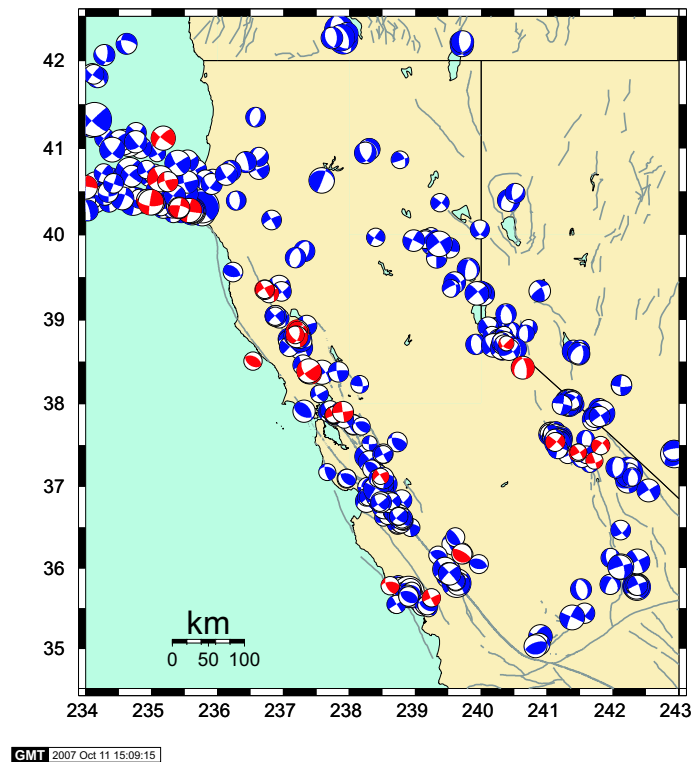


Figure 3.34: Map comparing reviewed moment tensor solutions determined by the BSL from past years (blue) with those from the fiscal year 2006-2007 (red).

telemetry, seven stations have been selected for upgrade to permanent sites within the next 18 months. These are: V04C (RAMR), HAST, P01C and S04C, as well as HATC, HELL and SUTB (see Figure 3.2).

### 3.8.5 Acknowledgements

Peggy Hellweg oversees the REDI system and directs the routine analysis. Peter Lombard and Doug Neuhauser contribute to the development of software. Rick McKenzie, Doug Dreger, Aimin Cao, Sean Ford, Aurelie Guilhem, Ayhi Kim, Ved Lekic, Junkee Rhie, Dennise Templeton, and Akiko Toh contribute to the routine analysis of moment tensors. Peggy Hellweg, Doug Neuhauser and Bob Uhrhammer contributed to the writing of this chapter. Partial support for the development and maintenance of the REDI system is provided by the USGS. The facilities of the IRIS Data Management System, and specifically the IRIS Data Management Center, were used by Bob Uhrhammer for access to the TA network (USArray) waveform and metadata required in the noise comparison study.

### 3.8.6 References

Dreger, D., and B. Romanowicz, Source characteristics of events in the San Francisco Bay region, *USGS Open*

*File Report 94-176*, 301-309, 1994.

Gee, L., J. Polet, R. Uhrhammer, and K. Hutton, Earthquake Magnitudes in California, *Seism. Res. Lett.*, *75(2)*, 272, 2004.

Gee, L., D. Neuhauser, D. Dreger, M. Pasyanos, R. Uhrhammer, and B. Romanowicz, The Rapid Earthquake Data Integration Project, *Handbook of Earthquake and Engineering Seismology*, IASPEI, 1261-1273, 2003a.

Gee, L., D. Dreger, G. Wurman, Y. Gung, B. Uhrhammer, and B. Romanowicz, A Decade of Regional Moment Tensor Analysis at UC Berkeley, *Eos Trans. AGU*, *84(46)*, Fall Meet. Suppl., Abstract S52C-0148, 2003b.

Gee, L., D. Neuhauser, D. Dreger, M. Pasyanos, B. Romanowicz, and R. Uhrhammer, The Rapid Earthquake Data Integration System, *Bull. Seis. Soc. Am.*, *86*, 936-945, 1996.

Pasyanos, M., D. Dreger, and B. Romanowicz, Toward real-time estimation of regional moment tensors, *Bull. Seis. Soc. Am.*, *86*, 1255-1269, 1996.

Romanowicz, B., D. Dreger, M. Pasyanos, and R. Uhrhammer, Monitoring of strain release in central and northern California using broadband data, *Geophys. Res. Lett.*, *20*, 1643-1646, 1993.

Location	Date	UTC Time	Lat.	Lon.	MT Depth	$M_l$	$M_w$	Str.	Dip	Rake	Mo
Offshore of Fort Ross	7/6/2006	20:43:24	38.508	-123.463	5	3.7	3.7	4.69E+21	295	46	84
Petrolia	7/19/2006	11:41:43	40.281	-124.426	30	4.7	5	3.53E+23	102	83	173
Glen Ellen	8/3/2006	3:08:12	38.363	-122.589	5	4.7	4.4	5.64E+22	256	86	19
Bishop	9/7/2006	1:38:59	37.31	-118.284	8	3.6	3.4	1.86E+21	342	86	158
Willits	9/26/2006	20:56:13	39.31	-123.217	8	3.9	3.9	9.52E+21	333	61	-171
Petrolia	10/17/2006	20:53:18	40.55	-126	11	4.9	4.8	2.03E+23	277	85	-166
Geysers	10/20/2006	17:00:08	38.867	-122.7873	5	4.5	4.6	9.88E+22	254	68	-39
Geysers	10/20/2006	23:31:39	38.867	-122.783	5	4.5	3.8	6.50E+21	240	55	-65
Petrolia	10/24/2006	14:26:43	40.403	-125.066	5	4	4.4	4.50E+22	99	85	182
Willits	11/9/2006	8:38:13	39.355	-123.285	8	4	4	1.49E+22	336	87	172
Willits	11/10/2006	5:05:56	39.357	-123.282	8	3.7	3.7	4.69E+21	329	90	-167
Paso Robles	11/30/2006	4:06:40	35.631	-120.754	8	4.7	3.8	5.33E+21	245	89	7
Coalinga	12/16/2006	6:14:05	36.174	-120.292	5	4.3	4.2	2.16E+22	299	71	89
Petrolia	12/17/2006	15:13:40	40.392	-125.023	5	3.9	4.3	3.57E+22	274	90	-159
Bishop	12/19/2006	15:21:42	37.493	-118.188	5	4	3.7	4.33E+21	221	86	-27
Berkeley	12/21/2006	3:12:28	37.86	-122.237	8	3.7	3.6	2.85E+21	49	80	-14
Berkeley	12/23/2006	6:49:57	37.862	-122.237	11	3.7	3.6	2.82E+21	139	89	-153
Berkeley	12/23/2006	17:21:15	37.861	-122.235	11	3.5	3.4	1.63E+21	148	86	-169
Glen Ellen	1/12/2007	11:27:50	38.391	-122.615	11	3.8	3.7	3.27E+23	236	89	34
Bishop	1/17/2007	14:01:08	37.408	-118.531	5	4	3.6	3.66E+21	37	83	17
Morgan Hill	1/17/2007	17:43:22	37.12	-121.523	8	3.5	3.4	1.38E+21	328	89	-159
Petrolia	1/24/2007	13:42:52	40.312	-124.584	18	3.7	4.4	5.05E+22	187	85	25
San Simeon	2/20/2007	16:46:13	35.78	-121.382	8	3.7	3.7	4.96E+21	151	59	137
Berkeley	2/24/2007	23:46:15	37.865	-122.241	11	3.4	3.3	1.15E+21	154	88	-176
Ferndale	2/26/2007	12:19:54	40.647	-124.864	8	5	5.4	1.48E+24	60	89	-4
Lafayette	3/2/2007	4:40:00	37.901	-122.098	14	4.4	4.2	2.77E+22	82	89	-1
Bridgeport	3/9/2007	3:17:32	38.428	-119.367	11	5	4.7	1.29E+23	349	65	-114
Petrolia	4/5/2007	22:54:29	40.311	-124.578	18	3.8	4.1	1.93E+22	12	88	18
Ferndale	4/7/2007	23:55:03	40.616	-124.753	18	3.7	4.1	2.00E+22	256	78	21
Geysers	4/24/2007	21:08:28	38.796	-122.794	5	4.4	4.4	4.62E+22	342	82	-160
Geysers	4/30/2007	15:51:28	38.82	-122.823	5	3.1	3.7	3.89E+21	136	58	-133
Markleeville	4/30/2007	21:57:32	38.72	-119.62	5	3.5	3.1	5.66E+20	226	87	47
Petrolia	5/9/2007	7:50:05	40.376	-125.014	11	5	5.2	7.81E+23	188	85	24
Bishop	5/26/2007	8:04:12	37.416	-118.525	8	3.5	3.3	1.24E+21	59	81	10
Mammoth	6/12/2007	7:22:36	37.5425	-118.8677	11	3.6	3.6	3.14E+21	140	82	-143
Mammoth	6/12/2007	7:23:43	37.539	-118.876	14	5.1	4.6	9.96E+21	310	82	172
Offshore of McKinleyville	6/25/2007	2:32:25	41.1155	-124.825	18	5	5	3.36E+23	128	84	160

Table 3.19: Moment tensor solutions for significant events from July 1, 2006 through June 30, 2007 using a complete waveform fitting inversion. Epicentral information is from the UC Berkeley/USGS Northern California Earthquake Management Center. Moment is in dyne-cm and depth is in km.

## 3.9. Outreach and Educational Activities

### 3.9.1 Introduction

The BSL is involved in a variety of outreach activities ranging from lectures to lab tours and educational displays. Recorded information on current earthquake activity is updated regularly on our information tape (510-642-2160). Additional basic information on earthquakes and seismic hazards for northern and central California, as well as other information seismology and our research, can be found on an extensive set of web pages.

### 3.9.2 Highlights of 2006-2007

This year's Lawson Lecture introduced the Parkfield segment of the San Andreas Fault to the wider community. Andy Michaels of the United States Geological Survey in Menlo Park spoke about "Parkfield 2004: Lessons from the Best-Recorded Earthquake in History". This section of the fault, currently the target of the "San Andreas Fault Observatory at Depth" drilling project, has been the object of intense research since the Parkfield Earthquake Prediction Experiment began in the mid-1980s. Then, the goal was to acquire high-quality measurements close to, and in advance of, a large earthquake. This goal was finally met when the September 28, 2004, magnitude 6, Parkfield, California, earthquake finally occurred on the San Andreas fault in the middle of the dense and diverse network of instruments designed by the scientists for the Parkfield Earthquake Prediction Experiment. The resulting data reveal aspects of the earthquake process never before seen, providing important insights into earthquake processes, prediction, and the hazards assessments that underlie important policies such as building codes.

### 3.9.3 On-Going Activities

#### Tours and Presentations

As every year, tours and presentations formed an important part of BSL's public relations activities. Each month, several groups, ranging from middle-school students to scientists and engineers, tour our laboratory under the guidance of a graduate student or a member of the staff.

The BSL hosted several special groups during 2006-2007. The geology class from Bishop Stopford School in England made its annual stop for a tour of the laboratory and the Hayward Fault. Several classes at different grade levels received tours. In addition, BSL graduate students visited local elementary, middle and high schools to talk about earthquakes and how we measure them. In addition to the tours, Drs. Romanowicz, Allen, Dreger, Hellweg, and Uhrhammer presented talks on earthquakes and

related phenomena to public groups and the media.

#### Open House

The BSL participated in *CalDay* this year. The attendance for the open house was, as always, good. The visitors learned about UC Berkeley's role in earthquake monitoring, watched a streaming feed of earthquake data, jumped up and down to "make a quake," played with the earthquake machine, made P and S-waves with springs, learned about earthquake preparedness, and were given sample seismograms. The BSL also co-sponsored lectures with the Earth and Planetary Science department on "Geology of the Berkeley and East Bay Hills", "Geology of San Francisco Bay Area" and "Why do Volcanoes Erupt Explosively."

#### Educational Displays

The BSL continues to make REDI earthquake data available to certain schools, universities, colleges, and museums for educational displays. Participating organizations receive a REDI pager and the Qpager software to display the earthquake information. The Qpager program maps the previous seven days of seismicity, with each earthquake shown as a dot. The size of the dot indicates the magnitude of the event, while the color of the dot indicates its age. These educational displays have been installed at UC Berkeley (McCone Hall, Earthquake Engineering Research Center, LHS), California Academy of Sciences, CSU Fresno, CSU Northridge, CSU Sacramento, Caltech, College of the Redwoods, Fresno City College, Humboldt State University, San Diego State University, Sonoma State University, Stanford University (Blume Engineering Center, Department of Geophysics), UC Davis, UC Santa Cruz, UC San Diego, and USC. For the past three years, middle schools of the San Francisco Unified School District have participated in the program.

In addition to the seismicity displays, the BSL provides local waveform feeds for helicorders at visitor centers associated with BDSN stations (CMB and MHC). Organizations such as LHS, KRON, and KPIX receive feeds from BKS via dedicated phone lines for display, while the USGS Menlo Park uses data from CMB for display in the lobby of the seismology building. The BSL has also loaned a seismometer and helicorder display to the San Leandro Unified School District for their use in science classes.

#### WWW

We continue to maintain and update our presence on the WWW. The webpages are intended to provide a

source of earthquake information for the public. They also present information about the networks we operate, including station profiles. This benefits the research community as well. The BSL web pages publicize seminar schedules, advertise courses, and describe our research, as well as our operations. They offer updates on recent earthquake activity, details on Bay Area seismicity and hazards, and links to other earthquake and earth science servers. We also use the WWW server to distribute information internally among BSL personnel, with such details as the computing and operational resources, rosters, and schedules for various purposes.

### **Earthquake Research Affiliates Program**

The UC Berkeley Earthquake Research Affiliates (ERA) Program is an outreach project of the BSL, the Department of Earth and Planetary Science, and the Earthquake Engineering Research Center. The purpose is to promote the support of earthquake research while involving corporations and governmental agencies in academic investigation and education activities such as conferences and field trips. The ERA program provides an interface between the academic investigation and practical application of earthquake studies.

#### **3.9.4 Acknowledgements**

Peggy Hellweg oversees the outreach activities at the BSL. Barbara Romanowicz, Bob Uhrhammer, Rick McKenzie, and many other faculty, staff, and students at the BSL contribute to the outreach activities. Peggy Hellweg contributed to the preparation of this chapter.

# Glossary of Common Acronyms

Table 3.20: Standard abbreviations used in this report.

Acronym	Definition
AGU	American Geophysical Union
ANSS	Advanced National Seismic System
BARD	Bay Area Regional Deformation
BDSN	Berkeley Digital Seismic Network
BSL	Berkeley Seismological Laboratory
BSS	Berkeley Seismographic Station
CISN	California Integrated Seismic Network
CGS	California Geological Survey
CLC	Campus Laboratory Collaboration
CNSS	Council of the National Seismic System
CSRC	California Spatial Reference Center
DART	Data Available in Real Time
DRC	Disaster Resistent California
EM	Electromagnetic
EPRI	Electric Power Research Institute
EERI	Earthquake Engineering Research Institute
FBA	Force Balance Accelerometer
FEMA	Federal Emergency Management Agency
FIR	Finite Impulse Response
FRAD	Frame Relay Access Device
GPS	Global Positioning System
GSAC	GPS Seamless Archive Center
HFN	Hayward Fault Network
HRSN	High Resolution Seismic Network
IGS	International Geodetic Service
IMS	International Monitoring System
InSAR	Interferometric Synthetic Aperture Radar
IRIS	Incorporated Research Institutions for Seismology
ISC	International Seismological Center
ISTAT	Integrating Science, Teaching, and Technology
JPL	Jet Propulsion Laboratory
LBNL	Lawrence Berkeley National Laboratory
LLNL	Lawrence Livermore National Laboratory
MBARI	Monterey Bay Aquarium Research Institute
MHH	Murdock, Hutt, and Halbert
MOA	Memorandum of Agreement
MOBB	Monterey Ocean Bottom Broadband observatory
MOISE	Monterey Bay Ocean Bottom International Seismic Experiment
MPBO	Mini-Plate Boundary Observatory
MRI	Major Research Initiative

*continued on next page*

Table 3.20: *continued*

Acronym	Definition
MRE	Major Research Equipment
MT	Magnetotelluric
NCEDC	Northern California Earthquake Data Center
NCEMC	Northern California Earthquake Management Center
NCSN	Northern California Seismic Network
NCSS	Northern California Seismic System
NEHRP	National Earthquake Hazards Reduction Program
NEIC	National Earthquake Information Center
NHFN	Northern Hayward Fault Network
NGS	National Geodetic Survey
NOAA	National Oceanic and Atmospheric Administration
NSMP	National Strong Motion Program
NSF	National Science Foundation
NSN	National Seismic Network
OES	California Governor's Office of Emergency Services
ORU	Organized Research Unit
PBO	Plate Boundary Observatory
PEER	Pacific Earthquake Engineering Center
PH	Pilot Hole
PMG	CISN Program Management Group
PPE	Parkfield Prediction Experiment
PREM	Preliminary Reference Earth Model
PSD	Power Spectral Density
QDDS	Quake Data Distribution System
REDI	Rapid Earthquake Data Integration
RTK	Real Time Kinematic Data
SAF	San Andreas Fault
SAFOD	San Andreas Fault Observatory at Depth
SAR	Synthetic Aperture Radar
SCEC	Southern California Earthquake Center
SCEDC	Southern California Earthquake Data Center
SCIGN	Southern California Integrated GPS Network
SCMC	Southern California Management Center
SCSN	Southern California Seismic Network
SEED	Standard for the Exchange of Earthquake Data
SEM	Spectral Element Method
SHFN	Southern Hayward Fault Network
SIO	Scripps Institutions of Oceanography
SNCL	Station Network Channel Location
SSA	Seismological Society of America
STP	Seismogram Transfer Program
UCB	University of California at Berkeley
UNAVCO	University NAVSTAR Consortium
UNR	University of Nevada, Reno
UrEDAS	Urgent Earthquake Detection and Alarm System
USGS	United States Geological Survey

# Appendix I Publications, Presentations, and Panels 2006-2007

## Publications

- Allen, R.M., The ElarmS earthquake early warning methodology and its application across California. In "Earthquake Early Warning Systems", P. Gasparini, G. Manfredi, J. Zschau (Eds), p. 21-44, Springer, ISBN-13 978-3-540-72240-3, 2007.
- Banerjee, P., F. F. Pollitz, B. Nagarajan, and R. Bürgmann (2007), Coseismic slip distributions of the 26 December 2004 Sumatra-Andaman and 28 March 2005 Nias earthquakes from GPS static offsets, *Bull. Seism. Soc. Am.*, 97, S86-S102.
- Benetatos, C., D. Dreger, and A. Kiratzi (2007). Complex and segmented rupture associated with the 14 August 2003 Mw 6.2 Lefkada, Ionian Islands, Earthquake, *Bull. Seism. Soc. Am.*, 97, 35-51.
- Cao, A., and B. Romanowicz, Locating scatterers in the mantle using array analysis of PKP precursors from an earthquake doublet. *Earth. Planet. Sci. Lett.*, 255, 22-31, 2007.
- Cao, A., and B. Romanowicz, Test of the innermost inner core models using broadband PKIKP travel time residuals. *Geophys. Res. Lett.*, 34, L08303, 2007. doi:10.1029/2007GL029384
- Cao, A., Y. Masson, and B. Romanowicz, Short wavelength topography on the Inner Core Boundary. *Proc. Natl. Acad. Sci. U.S.A.*, 104, 31-35, 2007.
- Cammarano, F. and B. Romanowicz, Insights into the nature of the transition zone from physically constrained inversion of long period seismic data, *PNAS*, 104, 9139-9144
- Chen, K. H., R. M. Nadeau, and R.-J. Rau (2007), Towards a universal rule on the recurrence interval scaling of repeating earthquakes?, *Geophys. Res. Lett.*, 34, L16308, doi:10.1029/2007GL030554.
- Dolenc, D., B. Romanowicz, R. Uhrhammer, P. McGill, D. Neuhauser, and D. Stakes, Identifying and removing noise from the Monterey ocean bottom broadband seismic station (MOBB) data, *Geochem. Geophys. Geosys.*, 8, Q02005, doi:10.1029/2006GC001403, 2007.
- Freed, A. M., R. Bürgmann, E. Calais, and J. T. Freymueller (2006), Stress-dependent power-law flow in the upper mantle following the 2002 Denali, Alaska, earthquake, *Earth Planet. Sci. Lett.*, 252, doi:10.1016/j.epsl.2006.1010.1011.
- Freed, A. M., S. T. Ali, and R. Bürgmann (2007), Evolution of stress in Southern California for the past 200 years from coseismic, postseismic and interseismic stress changes, *Geophysical Journal International*, 169, doi: 10.1111/j.1365-1246X.2007.03391.x.
- Funning, G J, R Burgmann, A Ferretti, F Novali and A Fumagalli, 2007, Creep on the Rodgers Creek fault from a 10 year PS-InSAR dataset, *Geophys. Res. Lett.*, in press.
- Funning, G J, B Parsons and T J Wright, 2007, Fault slip in the 1997 Manyi, Tibet earthquake from linear elastic modelling of InSAR displacements, *Geophys. J. Int.*, 169, 988-1008.
- Handy, M. R., G. Hirth, and R. Bürgmann (2007), Continental fault structure and rheology from the frictional-to-viscous transition downward, in *Tectonic Faults: Agents of Change on a Dynamic Earth*, edited by M. R. Handy, et al., pp. 139-181, MIT Press, Cambridge, MA.

- Hellweg, M. and D. Seidl (2006): The contingency table - a powerful tool of multivariate statistics. In Eds. H.M. Mader, S.G. Coles and C.B. Conner, *Statistics in Volcanology*, Special Publications of IAVCEI, Geological Society of London, 1, 105-113.
- Houlié, N. and Montagner, J.-P., Hidden Dykes detected on Ultra Long Period (ULP) seismic signals at Piton de la Fournaise volcano, 261, 1-2, 10.1016/j.epsl.2007.04.018, *Earth Planetary Science Letters* (2007).
- Jackson, J., M Bouchon, E Fielding, G Funning, M Ghorashi, D Hatzfeld, H Nazari, B Parsons, K Priestley, M Talebian, M Tatar, R Walker and T Wright, 2006, Seismotectonic, rupture process and earthquake hazard aspects of the 26 December 2003 Bam earthquake, *Geophys. J. Int.*, 166, 1270-1292.
- Johnson, K. M., R. Bürgmann, and K. Larson (2006), Frictional properties on the San Andreas fault near Parkfield, California, inferred from models of afterslip following the 2004 earthquake, *Bull. Seism. Soc. Am.*, 96, 321-338.
- Johnson, K., G. Hilley, and R. Bürgmann (2007), Influence of lithosphere viscosity structure on estimates of fault slip rate in the Mojave region of the San Andreas fault system, *Journal of Geophysical Research*, 112, doi:10.1029/2006JB004842.
- Lockman, A.B. and R.M. Allen. Magnitude-period scaling relations for Japan and the Pacific Northwest: Implications for earthquake early warning. *Bull. seism. Soc. Am.* 97 (1), 140-150, doi: 10.1785/0120040091, 2007.
- Malagnini, L., P. Bodin, K. Mayeda, A. Akinci, Unbiased moment-rate spectra and absolute site effects in the Kachachh Basin, India, from the analysis of the aftershocks of the 2001 Mw 7.6 Bhuj earthquake, *Bull. Seismol. Soc. Am.*, 96, doi:10.1785/0120050089, 2006.
- Malagnini, L., K. Mayeda, R. Uhrhammer, A. Akinci, and R.B. Herrmann, A regional ground motion excitation/attenuation model for the San Francisco region, *Bull. Seism. Soc. Am.*, 97, 843-862, doi:10.1785/0120060101, 2007.
- Marone, F. and B. Romanowicz, On the depth distribution of azimuthal anisotropy in the continental upper mantle, *Nature*, 447, 198-201, 2007.
- Marone, F. and B. Romanowicz, Non-linear crustal corrections in high-resolution waveform seismic tomography, *Geophys. J. Int.*, 170, 460-467, 2007.
- Marone, F., Y. C. Gung and B. Romanowicz, High resolution 3D radial anisotropic structure of the North American upper mantle from inversion of surface waveform data, *Geophys. J. Int.*, in press; online: doi: 10.1111/j.1365-246X.2007.03465.x, 2007.
- Mayeda, K., L. Malagnini, W.R. Walter, A new spectral ratio method using narrow band coda envelopes: Evidence for non-self-similarity in the Hector Mine sequence, *Geophys. Res. Lett.*, 34, L11303 doi:10.1029/2007GL030041, 2007.
- Morasca, P., K. Mayeda, R. Gök, W.S. Phillips, L. Malagnini, 2-D coda and direct wave tomography in northern Italy, *Geophys. J. Int.* (in press)
- E Nissen, B Emmerson, G J Funning, A Mistrukov, B Parsons, D P Robinson and T J Wright, 2007, Combining InSAR and seismology to study the 2003 Siberian Altai earthquakes - dextral strike-slip and anticlockwise rotations in the northern India-Eurasia collision zone, *Geophys. J. Int.*, 169, 216-232.
- Nolet, G., R.M. Allen and D. Zhao, Mantle plume tomography, *Chemical Geology* 241, 248-263, doi: 10.1016/j.chemgeo.2007.01.022, 2007.
- Olson, E.L., and R.M. Allen. Is earthquake rupture deterministic? (Reply) *Nature*, 442, E6, doi:10.1038/nature04964, 2006.
- Phillips, W.S., R.J. Stead, G.E. Randall, H.E. Hartse and K. Mayeda, Source effects from broad area network calibration of regional distance coda waves, *Scattering of Short Period Waves in the Heterogeneous Earth*, H. Sato and M.C. Fehler, Editors (in press)
- Pollitz, F., R. Bürgmann, and P. Banerjee (2006), Postseismic relaxation following the great 2004 Sumatra-Andaman earthquake on a compressible self-gravitating Earth, *Geophysical Journal International*, 167, doi: 10.1111/j.1365-1246X.2006.03018.x.

- Rhie, J., D. S. Dreger, R. Bürgmann, and B. Romanowicz (2007), Slip of the 2004 Sumatra-Andaman earthquake from joint inversion of long period global seismic waveforms and GPS static offsets, *Bull. Seism. Soc. Am.*, 97, S115-S127.
- Rolandone, F., D. S. Dreger, M. H. Murray, and R. Bürgmann (2006), Coseismic Slip Distribution of the 2003 Mw 6.5 San Simeon earthquake, California, determined from GPS measurements and seismic waveform data, *Geophys. Res. Lett.*, 33, doi:10.1029/2006GL027079.
- Romanowicz, B. and B. Mitchell (2007) Q in the Earth from crust to core, *Treatise of Geophysics*, Vol. 1, to be published by Elsevier, in press.
- Ryder, I., B Parsons, T J Wright and G J Funning, Post-seismic motion following the 1997 Manyi (Tibet) earthquake: InSAR observations and modelling, *Geophys. J. Int.*, 169, 1009–1027, 2007.
- Simons, F.J., B.D.E. Dando and R.M. Allen. Automatic detection and rapid determination of earthquake magnitude by wavelet multiscale analysis of the primary arrival. *Earth Planet. Sci. Lett.* 250, 214-223, doi:10.1016/j.epsl.2006.07.039, 2006.
- Sol, S., A. Meltzer, R. Bürgmann, R. D. van der Hilst, R. King, Z. Chen, P. Koons, E. Lev, Y. P. Liu, B. P. K. Zeitler, X. Zhang, J. Zhang, and B. Zurek, Geodynamics of the southeastern Tibetan plateau from seismic anisotropy and geodesy, *Geology*, 35, 563-566, 2007.
- Tullis, T. E., R. Bürgmann, M. Cocco, G. Hirth, G. C. P. King, O. Oncken, K. Otsuki, J. R. Rice, A. Rubin, P. Segall, S. A. Shapiro, and C. A. J. Wibberley, Rheology of Fault Rocks and Their Surroundings, in *Tectonic Faults: Agents of Change on a Dynamic Earth*, edited by M. R. Handy, et al., pp. 183-204, MIT Press, Cambridge, MA., 2007
- Walter, W. R., K. Mayeda, R. Gök, A. Hofstetter, The scaling of seismic energy with moment: Simple models compared with observations, *Earthquakes: Radiated Energy and the Physics of Faulting*, *AGU Geophysical Monograph Series*, 170, 2006.
- Walter, W.R., K. Mayeda, L. Malagnini, and L. Scognamiglio, Regional body-wave attenuation using a coda source normalization method: Application to MEDNET records of earthquakes in Italy, *Geophys. Res. Lett.*, 34, L10308, doi:10.1029/2007GL029990, 2007.
- Wu, Y.-M., H. Kanamori, R.M. Allen and E. Hauksson, Determination of earthquake early warning parameters, tau-c and Pd, for southern California. *Geophys. J. Int.*, 241, 248-263 doi: 10.1016/j.chemgeo.2007.01.022, 2007.
- Wurman, G., R.M. Allen and P. Lombard, Toward earthquake early warning in northern California, *J. Geophys. Res.* 112, B08311, doi:10.1029/2006JB004830, 2007.

## Presentations

### **SAFER (Seismic Early Warning for Europe) Kickoff Meeting, Capri, Italy, July, 2006**

Allen, R.M. Toward earthquake early warning for California.

### **High Lava Plains Workshop, Bend, Oregon, July, 2006**

Allen, R.M. and M. Xue. The origins of the Newberry hotspot.

### **SCEC Annual Meeting, Palm Springs, CA, September, 2006**

Allen, R.M. and G. Wurman. Earthquake early warning in northern California.

Allen, R.M. Subduction and upwelling in Cascadia: Development of a velocity model for the Pacific Northwest. (California 3D Velocity Model Workshop)

### **Montessus de Balore Conference in Santiago de Chile, November, 2006**

Romanowicz, B., "Real-time seismology at UC Berkeley" (invited)

**American Geophysical Union, 2006 Fall Meeting, San Francisco, CA, December 11-15, 2006**

- Brudzinski, M.R. and R.M. Allen. Segmentation in Episodic Tremor and Slip All Along Cascadia. *Eos Trans. AGU*, 87(52), Fall Meet. Suppl., Abstract T53G-05, 2006.
- Cammarano, F. and B. Romanowicz, Physically constrained inversion of long-period seismic waveforms: Insights on the nature of the transition zone *Eos Trans. AGU* 87, Fall Meet. Suppl., Abstract S41E-05, 2006
- Cao, A. and B. Romanowicz, Array analysis of small-scale mantle heterogeneity using PKP precursors from doublets *Eos Trans. AGU* 87, Fall Meet. Suppl., Abstract S43A-1355, 2006
- Chen, K.H., R.M. Nadeau, R. Rau, Evidence of off-fault deep creep from repeating seismicity along the northern Longitudinal Valley Fault in Taiwan *EOS Trans. AGU*, 87, Fall Meet. Suppl., Abstract, T31F-07, 2006
- Dando, B., F.J. Simons and R.M. Allen. Automatic detection and rapid determination of earthquake magnitude by wavelet multiscale analysis of the primary arrival. *Eos Trans. AGU*, 87(52), Fall Meet. Suppl., Abstract S11B-02, 2006.
- Dreger, D. and J. Rhie, A source representation of microseisms constrained by HV spectral ratio observations *EOS Trans. AGU*, 87(52), Fall Meeting Suppl., Abstract S23D-0200.
- Escalante, C., F. Cammarano, N. De Koker, A. Piazzoni, Y. Wang, F. Marone, C. Dalton, and B. Romanowicz, Seismic velocity gradients across the transition zone *Eos Trans. AGU* 87, Fall Meet. Suppl., Abstract U21A-0808, 2006
- Ford, S.R., D.S. Dreger, W.R. Walter, Full moment tensor analysis of Western US explosions, earthquakes, collapses, and volcanic events using a regional waveform inversion *EOS Trans. AGU*, 87(52), Fall Meeting Suppl., Abstract S43A-1352.
- Ford, S.R., V. Lekic, B.A. Romanowicz, and A. To, Analysis of Multiply Core-reflected Shear-waves from the M6.7 Kiholo Bay Earthquake *Eos Trans. AGU* 87, Fall Meet. Suppl., Abstract S51F-1794, 2006
- Funning, G.J., R. Bürgmann, A. Ferretti, F. Novali, and A. Fumagalli, Creep on the faults of the Northern San Francisco Bay Area documented by PS-InSAR *Eos Trans. AGU* 87, Fall Meet. Suppl., Abstract G52A-03, 2006
- Goltz, C., D.L. Turcott, S. Abaimov and R.M. Nadeau, Universal Recurrence Time Statistics of Characteristic Earthquakes, *EOS Trans. AGU*, 87, Fall Meet. Suppl., Abstract, NG41A-03, 2006.
- Hellweg, M., J. Boatwright, H. Bundock, H. Haddadi, and P. Lombard, Reality check: Using the 1906 Simulations to Assess Performance of Northern California Networks *Eos Trans. AGU*, 87(52), Fall Meet. Suppl., Abstract S51B-1272.
- Houlié, N. and B. Romanowicz, B, CALREF, a stable reference frame for the Northern California *Eos Trans. AGU*, 87(52), Abstract G43A-0982, 2006.
- Kim, A., and D. Dreger (2006). Rupture process of the 2004 Parkfield earthquake from near-fault seismic and geodetic data, *EOS Trans. AGU*, 87(52), Fall Meeting Suppl., Abstract S23C-0166, 2006
- Komorowski, J., N. Houlié, C.M. Kasereka, H. Ciraba, Early detection of eruptive dykes revealed by Normalized Difference Vegetation Index (NDVI) on Nyiragongo and Etna volcanoes: Implications for dyke wedge emplacement, monitoring, and risk assessment. *Eos Trans. AGU*, 87(52), Abstract T41B-1573, 2006.
- Larsen, S., D. Dreger, and D. Dolenc, Simulations of the 1906 San Francisco earthquake and scenario earthquakes in Northern California, *Eos Trans., AGU*, 87 (52), Fall Meet. Suppl., Abstract S51B-1269, 2006.
- Lekic, V. and B. Romanowicz, Applying the spectral element method to model 3D attenuation in the upper mantle, *EOS Trans AGU* 87 (52) Fall Meeting Suppl. Abstract S51A-1257, 2006.
- Lekic, V., Reif, C., Dziewonski, A. M., Sheehan, A., and van Summeren, J., Seismic Constraints on Slab Interaction With the Transition Zone *Eos Trans., AGU*, 87 (52), Fall Meet. Suppl., Abstract U21A-0809, 2006.

- Masson, Y., A. Cao, and B. Romanowicz, Test of innermost inner core models using broadband absolute PKIKP travel time residuals *Eos Trans. AGU 87*, Fall Meet. Suppl., Abstract U43A-0843, 2006
- Marone, F. and B. Romanowicz, 3D radial and azimuthal anisotropic structure of the North American upper mantle *Eos Trans. AGU 87*, Fall Meet. Suppl., Abstract S53A-1295, 2006
- Neuhauser, D., L. Dietz, P. Lombard, F. Klein, S. Zuzlewski, W. Kohler, M. Hellweg, J. Luetgert, D. Oppenheimer, and B. Romanowicz, The Northern California Earthquake Management System: A Unified System From Realtime Monitoring to Data Distribution *Eos Trans. AGU, 87(52)*, Fall Meet. Suppl., Abstract S11A-0198.
- Nissen, E., B. Emmerson, G. Funning, A. Mistrukov, B. Parsons, D. Robinson, E. Rogozhin, and T. Wright, Studying the 2003 Siberian Altai earthquakes with InSAR and seismology - Dextral strike-slip and anticlockwise rotations in the Northern India-Eurasia Collision Zone. *Eos Trans. AGU 87*, Fall Meet. Suppl., Abstract T43D-1660, 2006
- Novali, F., G.J. Funning, R. Bürgmann, A. Ferretti, and C. Giannico, ASF RADARSAT data reveal rates and mechanisms of contemporary surface deformation in the San Francisco Bay Area *Eos Trans. AGU 87*, Fall Meet. Suppl., Abstract H24C-04, 2006
- Panning, M.P., F. Marone, A. Kim, Y. Capdeville, P. Cupillard, Y. Gung, B. Romanowicz, Improvements in mode-based waveform modeling and application to Eurasian velocity structure *Eos Trans. AGU 87*, Fall Meet. Suppl., Abstract S51A-1254, 2006
- Porritt, R.W., R. Allen, R. Nadeau, and M. Brudzinski, Automated Search for Tremor in Parkfield and the Bay Area, CA. *Eos Trans. AGU, 87(52)*, Fall Meet. Suppl., Abstract T41A-1549, 2006.
- Rhie, J., V. Lekic, and B. Romanowicz, An assessment of surface wave and normal mode spheroidal Q models by forward modeling of Rayleigh waves, *EOS Trans AGU 87 (52)*, Fall Meeting Suppl. Abstract, S23D-0201, 2006.
- Rodgers, A. Petersson, S. Nilsson, B. Sjogreen, and K. McCandless, Broadband waveform modeling to evaluate the USGS seismic velocity model for the San Francisco Bay Area *Eos Trans. AGU 87*, Fall Meet. Suppl., Abstract S51B-1270, 2006
- Romanowicz, B., A. Cao, and Y. Masson, Short wavelength topography on the inner core boundary *Eos Trans. AGU 87*, Fall Meet. Suppl., Abstract U41D-04, 2006
- Scognamiglio, L., E. Tinti, A. Michelini, L. Malagnini, and D.S. Dreger, Near real-time regional moment tensor estimation using Italian broadband stations *EOS Trans. AGU, 87(52)*, Fall Meeting Suppl., Abstract S31B-0197.
- Taira, T., P.G. Solver, F. Niu, and R.M. Nadeau, Direct Detection of Temporal Variations in Seismic Scatterers at Seismogenic Depth Attributed to the 2004 Parkfield earthquake *EOS Trans. AGU, 87*, Fall Meet. Suppl., Abstract S23C-0185, 2006.
- Templeton, D. and R. Nadeau, R. Bürgmann, Distribution of slip at the juncture of the San Andreas and Calaveras Faults from repeating earthquakes *EOS Trans. AGU, 87*, Fall Meet. Suppl., Abstract, S31A-0173, 2006.
- To, A. and B. Romanowicz, Constraints on lateral S wave velocity gradients around the Pacific superplume *Eos Trans. AGU 87*, Fall Meet. Suppl., Abstract S51C-1288, 2006
- Wurman, G., R.M. Allen, and P. Lombard, Toward earthquake early warning in Northern California *Eos Trans. AGU 87*, Fall Meet. Suppl., Abstract S42C-07, 2006.
- Xue, M. and R.M. Allen, The fate of the Juan de Fuca Plate, *Eos Trans. AGU, 87(52)*, Fall Meet. Suppl., Abstract S51D-06, 2006.

**USGS/NEHRP Annual Workshop on Earthquake Hazards, Menlo Park, CA, January 18-19, 2007**

- Allen, R.M., M. Hellweg, A. Kireev, P. Lombard, D. Neuhauser, and G. Wurman, Earthquake early warning in Northern California

- Bürgmann, R., G. Funning, and N. Houlié, Space geodetic constraints on fault slip rates and the distribution of aseismic slip on Bay Area faults
- Bürgmann, R., G. Funning, G. Hilley, A. Ferretti, and F. Novali, Active uplift and thrust-fault strain accumulation rates from PS-InSAR and GPS data
- Hellweg, M., The Orinda Events
- Hellweg, M., P. Lombard, J. Boatwright, H. Bundock, and H. Haddadi, Using 1906 simulations to assess performance of Northern California networks
- Houlié, N. and B. Romanowicz, the BARD Continuous GPS Network: Monitoring Active Deformation and Strain Accumulation in Northern California and the San Francisco Bay Area
- Kim, A. and D. Dreger, Determination of Finite-Source Parameters: ShakeMap Applications
- Romanowicz, B., D. Neuhauser, D. Oppenheimer, F. Klein, H. Macbeth, Operation of the NCEDC
- Romanowicz, B., M. Hellweg, P. Lombard, D. Neuhauser, D. Oppenheimer, L. Dietz, and F. Klein, Operation of the joint earthquake notification system in Northern California
- Uhrhammer, R., M. Hellweg, P. Lombard, K. Hutton, E. Hauksson, A. Walter, and D. Oppenheimer, Recalibrating  $M_L$  for CISM

### **2007 Earthscope Annual Meeting, Monterey, California, March 27-30, 2007.**

- Allen, R.M. and M. Xue. Convective interactions in the mantle beneath the Pacific Northwest: The fate of the Juan de Fuca plate.
- Hellweg, M., D. Dreger and B. Romanowicz, Regional Moment Tensors in Northern California: Adding Data from USArray Stations
- Marone, F. and B. Romanowicz, 3D radial and azimuthal anisotropic structure of the North American upper mantle
- Nadeau, R.M. (Invited), Effect of Parkfield Earthquake on Tremor Activity Below the San Andreas Fault Near Cholame, CA, EarthScope National Meeting, March 27-30, 2007, Monterey, CA.
- Nadeau, R.M. and K.H. Chen, A Microseismic View of the Immediate SAFOD Target Zone, POSTER, EarthScope National Meeting, March 27-30, 2007, Monterey, CA.
- Uhrhammer, R., M. Hellweg, B. Romanowicz and P. Lombard, Assessment of Station Performance: Noise levels at BDSN, TA and NC.
- Neuhauser, D., L. Dietz, P. Lombard, F. Klein, S. Zuzlewski, W. Kohler, M. Hellweg, J. Luetgert, D. Oppenheimer and B. Romanowicz, The Northern California Earthquake Management System: A Unified System From Realtime Monitoring to Data Distribution.

### **101st Annual Meeting of the Seismological Society of America, Kona, Hawaii, April 11-13, 2007**

- Bürgmann, R., A.M. Freed, and T.A. Herring, Probing the Rheology of the Upper Mantle Using Far-field GPS Transients Following the 1999 Hector Mine, California Earthquake, *Seism. Res. Lett.*, 78(2), 299, 2007
- Dreger, D.S., E. Tinti, and A. Cirella, Slip Velocity Function Parameterization for Broadband Ground Motion Simulation *Seism. Res. Lett.*, 78(2), 308, 2007
- Dolenc, D., D. Dreger, and S. Larsen, Simultaneous inversion of the teleseismic, local, and microseism observations for the velocity structure within the Santa Clara Valley basins, *Seism. Res. Lett.*, 78(2), 310, 2007.
- Dolenc, D., B. Romanowicz, and W.S.D. Wilcock, Observations of infragravity Waves at the Endeavour ocean bottom broadband station (KEEB) *Seism. Res. Lett.*, 78(2), 261, 2007
- Ellsworth, W., L. Dietz, S. Hickman, G. Jensen, W. Kohler, J. Luetgert, C. Weiland, M. Zoback, E. Davis, R. Krug, E. Samson, M. Aranha, D. Neuhauser, R. Uhrhammer, V. Oye, G.F.Z. Prevedel,

and M. Zumberge, The San Andreas Fault Observatory at Depth: Monitoring Earthquakes and Fault Movement Inside the Fault *Seism. Res. Lett.*, 78(2), 266, 2007

Ford, S.R., D.S. Dreger, and W.R. Walter, Full Moment Tensor Analysis of Nevada Test Site Explosions and Earthquakes, and Western US Collapses and Volcanic Events Using a Regional Waveform Inversion, *Seism. Res. Lett.*, 78(2), 240, 2007

Frey Mueller J.T., A. Freed, E. Calais, and R. Bürgmann, Denali Earthquake Postseismic Deformation: Implications for Postseismic Mechanisms *Seism. Res. Lett.*, 78(2), 299, 2007

Hellweg, M., Complexity at Small Magnitudes: Earthquakes in the Orinda Sequence *Seism. Res. Lett.*, 78(2), 285, 2007

Johanson, I.A., R.M. Nadeau, D. Templeton, and R. Bürgmann, Heterogeneous Creep at San Juan Bautista from GPS, InSAR and Repeating Earthquakes *Seism. Res. Lett.*, 78(2), 289, 2007

Kim, A., D.S. Dreger, and S. Larsen, Broadband Modeling of 3D Velocity Structure in the San Francisco Bay Area *Seism. Res. Lett.*, 78(2), 257, 2007

Nadeau, R.M., Borehole Seismic Observations of Deep Fault Deformation Associated with the 2004 Parkfield Mainshock: Nonvolcanic Tremor and Repeating Micro-earthquakes *Seism. Res. Lett.*, 78(2), 266, 2007

Neuhauser, D.S., S. Zuzlewski, R. Uhrhammer, N. Houlié, M. Aranha, B. Romanowicz, F. Klein, L. Dietz, S. Silverman, and D. Oppenheimer, Diverse Geophysical Data Available through the Northern California Earthquake Data Center *Seism. Res. Lett.*, 78(2), 283, 2007

Sammis, C.G., R.L. Biegel, and L.R. Johnson, Effect of Rock Damage on Seismic Waves generated by Explosions *Seism. Res. Lett.*, 78(2), 240, 2007

Wurman, G., R.M. Allen, P. Lombard, D. Neuhauser, A. Kireev, and M. Hellweg, Real-time implementation of ElarmS for earthquake early warning in northern California *Seism. Res. Lett.*, 78(2), 241, 2007

### **Computational Geosciences Symposium (DOE office of BS), Gaithersburg, MD, May 3-4, 2007**

Romanowicz, B. "Towards regional tomography of South East Asia using the Spectral Element Method" (invited)

### **American Geophysical Union, 2007 Spring Meeting, Acapulco, Mexico, May 2007**

Houlié, N., B. Romanowicz and M. Hellweg, A Contribution to Mitigating Seismic Risk in the Bay Area: The Bay Area Regional Deformation (BARD) GPS Network, *Eos Trans. AGU*, 88(23), Jt. Assem. Suppl., Abstract G43A-03.

B. Romanowicz, D. Dreger, D. Neuhauser, W. Karavas, M. Hellweg, R. Uhrhammer, P. Lombard, J. Friday, R. Lellinger, J. Gardner, R. McKenzie and C. Bresloff, The Berkeley Digital Seismic Network. *Eos Trans. AGU*, 88(23), Jt. Assem. Suppl., Abstract S33C-03.

Hellweg, M., D. Given, E. Hauksson, D. Neuhauser, D. Oppenheimer and A. Shakal, The California Integrated Seismic Network, *Eos Trans. AGU*, 88(23), Jt. Assem. Suppl., Abstract S33C-07.

### **SAFER (Seismic Early Warning for Europe) Meeting, Athens, Greece, June, 2007**

Allen, R.M. Toward earthquake early warning for California.

### **Gordon Research Conference, Mt. Holyoke MA, June 2007**

Allen, R.M. and M. Xue. The Fate of the Juan de Fuca plate: Implications for a Yellowstone plume head.

Cammarano, F. and B. Romanowicz, L. Stixrude and C. Lithgow-Bertelloni, Thermal and compositional models of the upper mantle as constrained by long period seismic waveforms and mineral physics data

Cao, A. and Barbara Romanowicz, Array analysis of small-scale mantle heterogeneity using PKP precursors from doublet

Lekic, V. and B. Romanowicz, Applying the Coupled Spectral Element Method to Tomography: Crustal Effects

## Speaking Engagements

- Allen, R.M. "Earthquake early warning in California: Current development and future plans.", Istituto Nazionale di Geofisica e Vulcanologia, Rome, Italy, July 2006.
- Allen, R.M. "CISN Earthquake Early Warning: Real-time testing of algorithms statewide.", California Integrated Seismic Network Advisory Board Meeting, August 2006.
- Allen, R.M. "Warning before shaking: Rapid hazard assessment across California." Institut de Physique du Globe de Paris, January 2007.
- Allen, R.M. "Segmentation in episodic tremor and slip along the length of the Cascadia forearc." Institut de Physique du Globe de Paris, January 2007.
- Allen, R.M. "Earthquake?" College of Letters and Sciences Faculty Forum, UC Berkeley, CA, February 2007.
- Allen, R.M. "Passive source seismology: Resolvable scales using various techniques." GeoSwath Workshop, Boise, Idaho, April 2007.
- Allen, R.M. "Episodic tremor and slip along the length of Cascadia: Observations and implications for seismic hazard." National Earthquake Prediction Evaluation Council, Portland, OR, May 2007.
- Allen, R.M. "Earthquake early warning: Current progress and future prospects." Advanced National Seismic System Steering Committee, Salt Lake City, UT, June 2007.
- Bürgmann, R., "Geodetic Imaging of Lithosphere Rheology", IGP, Paris, January 8, 2007
- Bürgmann, R., "Active Tectonics of the San Francisco Bay Area", Konferenz der Geologische Vereinigung, Potsdam, Germany, September 29, 2006
- Dolenc, D. "Monterey Bay Broadband Seismic Observatory: Observation and Removal of Long-period Noise", Geological Sciences Seminar, University of Minnesota, Duluth, March 29, 2007
- Dreger, D., R. Nadeau and A. Morrish "Kinematic modeling of the SAFOD target events", EarthScope National Meeting, Monterey, California, March 27-30, 2007. (Invited)
- Funning, G., "Aseismic creep on the Hayward-Rodgers Creek fault zone" Crustal deformation in the Bay Area meeting, UC Berkeley, June 8, 2007
- Funning, G., "Space geodesy in the Bay Area: surface deformation, fault kinematics and creep" Earthquake Hazards Seminar, US Geological Survey, Menlo Park, CA, April 18, 2007
- Funning, G., "Studying surface deformation and fault creep in the Bay Area using satellite radar measurements" UC Berkeley, Berkeley Seismological Laboratory Seminar, November 14, 2006
- Funning, G., "Surface deformation monitoring in the Bay Area using space-based radar", Department of Civil Engineering, Geo-Engineering Seminar, UC Berkeley, November 8, 2006
- Hellweg, M. "Below Zero: Scaling and Complexity in Small Earthquakes"; Physics Colloquium, Universidad del Valle, Cali, Colombia, September 28, 2006
- Hellweg, M. "Listening Carefully: Learning from Earthquakes", Northern California Chapter of the "Achievement Awards for College", Francisca Club, San Francisco, CA, March 5, 2007
- Hellweg, M. "Earthquakes in and around Orinda, CA", Orinda Historical Society, Orinda, CA, March 21, 2007
- Hellweg, M. "Earthquakes in our backyard", North Pleasanton Rotary Club, Pleasanton, CA, June 15, 2007
- Houlié, N. "Tracking magma volumes on active basaltic volcanoes.", UC Santa Cruz (seminar), June 1, 2007

- Mayeda, K. "Why do we have earthquakes, and what do seismologists do?", Head-Royce School 6th Grade, Oakland, CA, March 2, 2007
- Nadeau, R.M., "Nonvolcanic Tremor Deep Beneath the San Andreas Fault near Cholame", California, University of California, Berkeley Seismological Laboratory, Summer Tremor Activity Seminar, July 13, 2006. (Invited)
- Nadeau, R.M., "Monitoring the SAFOD Target Earthquakes – Nov 2, 2006 Repeat of the NW (San Francisco) M2 sequence", Berkeley Seismological Laboratory, Earthquake of the Week, Berkeley, California, November 3, 2006.
- Nadeau, R.M., Internal structure of the targets: relative locations, SAFOD Earthquake Target Location Workshop, San Francisco, CA, December 12, 2006.(Invited)
- Romanowicz, B., "Elastic and anelastic waveform tomography at global and continental scales" Paris workshop on IGP/BSL collaboration, Paris, January 8-10, 2007
- Romanowicz, B., "The Earth's hum: bridging the gap between seismology and oceanography", B.Jardetsky Lecture, Lamont, September 22, 2006:
- Romanowicz, B. "Contraintes sismologiques sur la structure et la déformation au Tibet", Lecture at Collège de France, France, February 7, 2007
- Romanowicz, B., "Le bourdonnement de la terre: interactions dynamiques entre l'atmosphère, les océans et la terre solide", Université Paul Sabatier, Toulouse, France, February 2, 2007
- Romanowicz, B., "Tomographie élastique et anélastique à l'échelle globale et continentale", Ecole Normale Supérieure, Lyon, France, April 25, 2007
- Romanowicz, B., "Short Period topography on the inner core boundary", Ecole Normale Supérieure, Lyon, France, April 25, 2007
- Romanowicz, B., "Structure anisotrope, et dynamique du manteau à l'échelle continentale", Ecole Normale Supérieure, Paris, France May 29th, 2007
- Romanowicz, B., "The earth's hum: bridging the gap between seismology and oceanography", Department of Geophysics, Utrecht University, the Netherlands, June 5, 2007
- Romanowicz, B., "Structure anisotrope, et dynamique du manteau à l'échelle continentale" Université Joseph Fourier, Grenoble (LGIT), June 21, 2007
- Romanowicz, B., "Structure anisotrope, et dynamique du manteau à l'échelle continentale" Université Blaise Pascal, Strasbourg, France, June 25, 2007
- Romanowicz, B., "The earth's hum: bridging the gap between seismology and oceanography", Department of Geophysics, ETH, Zurich, June 27, 2007
- Romanowicz, B., "Towards large scale tomography using the Spectral Element Method", 4th SPICE workshop, held in Cargèse, Corsica, May 18-19, 2007 (invited)
- Uhrhammer, R. A., "Earthquakes and the Hayward Fault", Alameda County Emergency Operations Center, Dublin, CA, January 3, 2007.
- Uhrhammer, R. A., "Seismology", North Bay Amateur Radio Association, Mare Island Museum, March 26, 2007.
- Uhrhammer, R. A., "Seismology Update", West Berkeley Lions Club, Spengers Restaurant, Berkeley, CA, March 23, 2007.

## Panels and Professional Service

### Richard M. Allen

Briefed National Earthquake Prediction Evaluation Council, May 2007.

Briefed Advanced National Seismic System Steering Committee, June 2007.

U.S. participant in the European Commission project "Seismic Early Warning Across Europe," June 2006 to June 2009.

## **Roland Bürgmann**

Associate Editor, Bulletin of the Seismological Society of America  
Corresponding Editor, Eos  
Editorial Board, Earth and Planetary Science Letters  
Member, UNAVCO Nominations Committee  
Member, WinSAR Nominations Committee  
Elected member, SSA Board Of Directors  
Chair, EarthScope PBO Standing Committee  
2007 EarthScope Annual Meeting Organizing Committee  
Member, Tectonics Observatory at Caltech Review Committee  
Member, UC Berkeley Graduate Fellowship Committee  
Member of the AAAS, AGU, GSA, and SSA

## **Douglas S. Dreger**

COSMOS Board of Directors  
Golden Gate Bridge Instrumentation Committee

## **Margaret Hellweg**

Member, CISN Program Management Committee  
Member, CISN Standards Committee  
Member, CISN Steering Committee  
Member, CISN Outreach Committee  
Member, 1868 Commemoration Committee  
Member, 1868 Commemoration Executive Committee  
Member, IASPEI/IAVCEI Joint Commission on Volcano Seismology

## **Douglas S. Neuhauser**

Chair, Standards Group, California integrated Seismic network (CISN)  
Acting Member, CISN Program management CDommittee

## **Robert M. Nadeau**

Member, SAFOD target event location working group  
Member, UNAVCO Strategic Planning Committee

## **Barbara Romanowicz**

Member Advisory Committee to College de France, Paris (COSS)  
Member, Conseil d'administration of Institut de Physique du Globe in Paris  
Member, Conseil Scientifique, Institut de Recherche pour le Développement  
Member, National Earthquake Prediction Evaluation Council  
Member, Advisory committee, Geophysical Institute, Univ. of Alaska, Fairbanks  
Member, Cooperative Institute for Deep Earth Research (CIDER) Steering Committee  
CIDER 2006 Summer program - lead member of organizing team - July 16- Aug 4, 2006, Santa Barbara, CA  
Member, Fellows Committee, AGU  
Reviewing Editor for Science  
Member, BESR (Board on Earth Sciences and Resources)  
Member, CISN Steering Committee

## **Robert A. Uhrhammer**

Member, International Association of Seismology and Physics of the Earths Interior, Working Group on Magnitudes

Member, California Integrated Seismic Network, Magnitude Working Group

Member, American National Seismic System, Technical Integration Committee, Working Group D, Seismic Instrumentation

## Appendix II Seminar Speakers 2006-2007

JAMIE RECTOR  
UC Berkeley  
Earth and Planetary Science  
“*What is Q?*”  
Tuesday, August 29, 2007

ARCHIE PAULSON  
UC Berkeley  
“*Inference of the Earth’s Mantle Viscosity from Post-Glacial Rebound*”  
Tuesday, September 5, 2006

FELIX HERMANN  
University of British Columbia  
Earth and Ocean Sciences  
“*Stable Seismic Recovery with Curvetelets*”  
Tuesday, September 5, 2006

JOE DUFEK  
UC Berkeley  
Earth & Planetary Science  
“*Self-organization in turbulent multiphase flow: integrating the dynamics and deposits of volcanic eruptions*”  
Tuesday, September 19, 2006

DAVID DOLENC  
UC Berkeley  
Earth & Planetary Science  
“*Results from two studies in seismology: I. Seismic observations and modeling in the Santa Clara Valley, CA, II. Observations and removal of the long-period noise at the Monterey ocean bottom broadband station (MOBB)*”  
Tuesday, September 26, 2006

JESSE LAWRENCE  
IGPP  
UC San Diego  
“*What Can Body Waves Tell Us About the Mantle Transition Zone?*”  
Tuesday, October 5, 2006

CHARLIE SAMMIS  
Department of Earth Science  
USC  
“*Dynamic Triggering of Microearthquakes by P- and S-waves from the 1999 Chi-Chi, Taiwan Earthquake*”  
Tuesday, October 10, 2006

JUNKEE RHIE  
UC Berkeley  
Earth & Planetary Sciences  
“*Excitation of Earth’s Incessant Free Oscillations by Atmosphere-Ocean-Sea-floor Coupling*”  
Tuesday, October 17, 2006

CHRIS FULLER  
UC Berkeley  
Berkeley Seismological Laboratory  
“*Subduction-thrust Seismicity and the Structure of Accreting Margins*”  
Tuesday, October 24, 2006

HEIDI KUMZA  
UC Berkeley  
“*Support Vector machines for Geophysical Inversion*”  
Tuesday, October 31, 2006

GEORGE ZANDT  
University of Arizona  
Department of Geosciences  
“*Lower Crustal Seismic Anisotropy: Evidence for Mega Low-Angle Shear-Zones, Crust-Mantle Decoupling, and Delamination*”  
Tuesday, November 7, 2006

GARETH FUNNING  
UC Berkeley  
Berkeley Seismological Laboratory  
“*Studying Surface Deformation and Fault Creep in the Bay Area using Satellite Radar Measurements*”  
Tuesday, November 14, 2006

EMILY BRODSKY  
UC Santa Cruz  
Earth & Planetary Sciences  
“*Triggering Earthquakes Dynamically*”  
Tuesday, November 21, 2006

CHRISTINE REIF  
UC Santa Cruz  
Earth & Planetary Sciences  
“*What can seismic tomography really say about the temperature, composition, and mineralogy of the lowermost mantle?*”  
Tuesday, November 28, 2006

STEFANO GRESTA  
University of Catania  
“*The 2002 eruption of Mount Etna: seismological constraints on the eruptive mechanism*”  
Tuesday, September 5, 2006

SEOK GOO SONG  
Stanford University  
*"A unified source model for the 1906 San Francisco Earthquake"*  
Tuesday, December 19, 2006

JULIET BIGGS  
University of Oxford  
Department of Earth Sciences  
*"InSAR observations of the Denali fault earthquake cycle"*  
Tuesday, January 23, 2007

TAKUJI YAMADA  
Boston University  
Department of Earth Sciences  
*"Stress drop, radiated seismic energy, and rupture speed of microearthquakes: Analysis of borehole seismograms in the vicinity of the source region in a South African gold mine"*  
Tuesday, January 30, 2007

MARGARET BOETTCHER  
USGS, Menlo Park  
*"A synoptic model of slip on oceanic ridge transform faults- insights from earthquakes and laboratory experiments"*  
Tuesday, February 6, 2007

DENNISE TEMPLETON  
UC Berkeley  
Berkeley Seismological Laboratory  
*"Exotic Seismic Sources: A look at non-double-couple earthquakes and identically repeating events"*  
Tuesday, February 13, 2007

KEVIN MAYEDA  
UC Berkeley  
Berkeley Seismological Laboratory  
*"Broadband applications of coda waves to source, site, and path effects"*  
Tuesday, February 20, 2007

JIM RICE  
Harvard University  
Earth and Planetary Sciences  
*"Aseismic transients in subduction zones: What physical basis?"*  
Tuesday, February 27, 2007

SAEKO KITA  
USGS, Menlo Park  
*"Existence of a seismic belt in the upper plane of the double seismic zone extending in the along-arc direction at depths of 70-100 km beneath NE Japan"*  
Tuesday, March 6, 2007

GERMAN PRIETO  
UC San Diego  
IGPP  
*"Confidence intervals for earthquake source parameters"*  
Tuesday, March 13, 2007

AKIKO TO  
UC Berkeley  
Berkeley Seismological laboratory  
*"What we have learned about the D" layer in and around the Pacific superplume"*  
Tuesday, March 20, 2007

CHEN JI  
UC Santa Barbara  
Department Earth Science  
*"Very broadband studies of large earthquakes"*  
Tuesday, April 3, 2007

ALLAN RUBIN  
Princeton University  
Geosciences  
*"Theoretical earthquake nucleation, with implications for slow slip events and more"*  
Tuesday, April 17, 2007

ANDY MICHAEL  
USGS, Menlo Park  
*"The Parkfield 2004 earthquake: lessons from the best-recorded quake in history"*  
Tuesday, April 24, 2007  
2007 Lawson Lecture

STEPHEN MORRIS  
UC Berkeley  
Department of Mechanical Engineering  
*"The implications of (seismically) small density differences for mantle dynamics"*  
Tuesday, May 1, 2007

SUSAN HOUGH  
USGS, Pasadena  
*"California's biggest historical earthquake"*  
Tuesday, May 8, 2007

